

**ULTRA HIGH TIP SPEED (670.6 M/SEC) FAN STAGE WITH COMPOSITE ROTOR
AERODYNAMIC AND MECHANICAL DESIGN**

(NASA-CR-135122) ULTRA HIGH TIP SPEED N77-20101
(670.6 m/sec) FAN STAGE WITH COMPOSITE
ROTOR: AERODYNAMIC AND MECHANICAL DESIGN
(Pratt and Whitney Aircraft) 198 p Unclas
HC A09/MF A01 CSCL 21E G3/07 20560

by

J. E. Halle, G. D. Burger and R. E. Dundas

March 1977

UNITED TECHNOLOGIES CORPORATION
Pratt & Whitney Aircraft Group
Commercial Products Division

Prepared for

NATIONAL AERONAUTICS AND SPACE ADMINISTRATION
NASA-Lewis Research Center
Contract NAS3-15335

1. Report No. NAS CR-135122		2. Government Accession No.		3. Recipient's Catalog No.	
4. Title and Subtitle Ultra High Tip Speed (670.6 m/sec) Fan Stage With Composite Rotor—Aerodynamic and Mechanical Design				5. Report Date March 1977	
				6. Performing Organization Code	
7. Author(s) J. E. Halle, G. D. Burger, and R. E. Dundas				8. Performing Organization Report No. PWA 5487	
9. Performing Organization Name and Address Pratt & Whitney Aircraft Group Commercial Products Division United Technologies Corporation East Hartford, CT 06108				10. Work Unit No.	
				11. Contract or Grant No. NAS3-15335	
12. Sponsoring Agency Name and Address National Aeronautics and Space Administration Washington, D. C. 20546				13. Type of Report and Period Covered Contractor Report	
				14. Sponsoring Agency Code	
15. Supplementary Notes NASA Project Manager: Mr. R. D. Hager, Fluid System Components Division, Fan and Compressor Branch; NASA-Lewis Research Center, Cleveland, Ohio 44135					
16. Abstract <p>A highly loaded, single-stage compressor having a tip speed of 670.6 m/sec was designed for the purpose of investigating very high tip speeds and high aerodynamic loadings to obtain high stage pressure ratios at acceptable levels of efficiency. The design pressure ratio is 2.8 at an adiabatic efficiency of 84.4%. Corrected design flow is 83.4 kg/sec; corrected design speed is 15,200 rpm; and rotor inlet tip diameter is 0.853 m. The rotor uses multiple-circular-arc airfoils from 0 to 15% span, precompression airfoils assuming single, strong oblique shocks from 21 to 43% span, and precompression airfoils assuming multiple oblique shocks from 52% span to the tip. Because of the high tip speeds, the rotor blades are designed to be fabricated of composite materials. Two composite materials were investigated: Courtaulds HTS graphite fiber in a Kerimid 601 polyimide matrix and the same fibers in a PMR polyimide matrix. In addition to providing a description of the aerodynamic and mechanical design of the 670.6 m/sec fan, discussion is presented of the results of structural tests of blades fabricated with both types of matrices.</p>					
17. Key Words (Suggested by Author(s)) Single-Stage Fan Ultra-High Tip Speed High Stage Loading Composite Blades				18. Distribution Statement Unclassified — Unlimited	
19. Security Classif. (of this report) Unclassified		20. Security Classif. (of this page) Unclassified		21. No. of Pages 200	
22. Price*					

* For sale by the National Technical Information Service, Springfield, Virginia 22151

FOREWORD

This report describes an ultra high tip speed fan designed by the Pratt & Whitney Aircraft Group, Commercial Products Division, United Technologies Corporation under contract NAS3-15335 for the National Aeronautics and Space Administration, NASA-Lewis Research Center. The aerodynamic design section was written by J. E. Halle and G. D. Burger, and the mechanical design section was written by R. E. Dundas. The report also includes discussions of the structural test results of composite blades fabricated of graphite fibers in a PMR polyimide matrix by W. E. Winters of TRW, Inc. and in a Kerimid 601 polyimide matrix by J. A. Arnold of P&WA. During this program effort, Mr. R. D. Hager was the NASA Project Manager and Mr. H. V. Marman was the P&WA Program Manager.

TABLE OF CONTENTS

	<u>Page</u>
SUMMARY	1
INTRODUCTION	3
AERODYNAMIC DESIGN	4
Flowpath and Vector Diagram Design	5
Rotor Blade Design	5
Stator Vane Design	14
MECHANICAL DESIGN	15
Rotor Blade Design	15
Stage Vibration	23
Critical Speed	25
APPENDIXES	
A — NOMENCLATURE	113
B — STREAMLINE FLOWFIELD CALCULATION PROCEDURE	119
C — AERODYNAMIC SUMMARY	121
D — AIRFOIL GEOMETRY ON CONICAL SURFACES	129
E — COSINE VARIATION OF BLADE CHANNEL AREA	133
F — BLOCKAGE CALCULATIONS	135
G — CALCULATION OF INTRABLADE WORK DISTRIBUTION BASED ON BLADE CHANNEL STATIC PRESSURE DISTRIBUTION	136
H — MANUFACTURING COORDINATES FOR SECTIONS NORMAL TO STACKING LINE	141
I — EVALUATION OF KERIMID 601 POLYIMIDE ULTRA-HIGH TIP SPEED FAN BLADES	169
J — EVALUATION OF PMR POLYIMIDE ULTRA-HIGH TIP SPEED FAN BLADES	177
REFERENCES	190
DISTRIBUTION LIST	191

LIST OF ILLUSTRATIONS

<u>Figure</u>	<u>Title</u>	<u>Page</u>
1	Comparison of Design Spanwise Profiles of Rotor Inlet Meridional Mach Number	27
2	Comparison of Design Flowpaths	28
3	Relative Velocity at Rotor Inlet and Exit as a Function of Span	29
4	Absolute Velocity at Stator Inlet and Exit as a Function of Span	30
5	Rotor and Stator Solidity as a Function of Span	31
6	Rotor and Stator Diffusion Factor as a Function of Span	32
7	Rotor Inlet and Exit Meridional Velocity as a Function of Span	33
8	Rotor Inlet and Exit Relative Mach Number as a Function of Span	34
9	Multiple-Circular-Arc Airfoil Definition	35
10	Multiple-Circular-Arc Airfoil Cascade Relationships	35
11	Rotor Front and Total Camber Distribution for MCA Portion of Span	36
12	One-Shock Precompression Airfoil Terminology	37
13	Two-Shock Precompression Airfoil Terminology	38
14	General Design Procedure	39
15	Axial Distribution of Specific Flow Ratio for Design Streamlines	40
16	Spanwise Distribution of Shock and Total Recovery for the Rotor	42
17	Spanwise Distribution of Rotor Total Loss Coefficient	43
18	Axial Work Distribution for Design Streamlines	44
19	Axial Loss Distributions for Design Streamlines	47
20	Axial Blockage Distributions for Design Streamlines	50
21	Axial Static Pressure Distribution for Design Streamlines	52

LIST OF ILLUSTRATIONS (Cont'd)

<u>Figure</u>	<u>Title</u>	<u>Page</u>
22	Rotor Inlet and Exit and Stator Inlet Meridional Air Angles	54
23	Rotor Inlet and Exit Meanline Angles as a Function of Span	55
24	Rotor Meanline Incidence as a Function of Span	56
25	Rotor Deviation as a Function of Span	57
26	Rotor Cross-Sectional Area as a Function of Span	58
27	Rotor Leading and Trailing Edge Radii as a Function of Span	59
28	Rotor Leading Edge Wedge Angle as a Function of Span	60
29	Rotor Precompression Ramp Angle as a Function of Span	60
30	Rotor Thickness-to-Chord Ratio and Blade Chord as a Function of Span	61
31	Critical Area Ratios as Functions of Span for Precompression Sections	62
32	Stator Recovery and Loss Coefficient as a Function of Span	63
33	Stator Inlet and Exit Absolute Mach Numbers as Functions of Span	64
34	Stator Vane Front and Total Chords as Functions of Span	65
35	Stator Maximum Thickness-to-Chord Ratio and Chordwise Location as a Function of Span	66
36	Stator Vane Suction Surface Incidence as a Function of Span	66
37	Stator Channel Area Ratios as a Function of Axial Distance	67
38	Stator Minimum A/A^* as a Function of Span	69
39	Stator Vane Deviation and Comparison With Carter's Rule	70
40	Stator Vane Inlet and Exit Mean Camber Line	71
41	Stator Vane Front and Total Cambers	72
42	Strength as a Function of Ply Orientation	73

LIST OF ILLUSTRATIONS (Cont'd)

<u>Figure</u>	<u>Title</u>	<u>Page</u>
43	Tensile and Shear Moduli of Elasticity as a Function of Ply Orientation	74
44	Typical Blade Section	75
45	Blade Section in Root Area	76
46	Blade Construction Details	76
47	Centrifugal Stress, Suction Surface (0.1829 m [7.2 in.] radius)	77
48	Centrifugal Stress, Pressure Surface (0.189 m [7.2 in.] radius)	78
49	Centrifugal Stress, Section Surface (0.187 m [7.31 in.] radius)	79
50	Centrifugal Stress, Pressure Surface (0.1857 m [7.32 in.] radius)	80
51	Centrifugal Stress, Suction Surface (0.1923 m [7.57 in.] radius)	81
52	Centrifugal Stress, Pressure Surface (0.1923 m [7.57 in.] radius)	82
53	Centrifugal Stress, Suction Surface (0.2017 m [7.94 in.] radius)	83
54	Centrifugal Stress, Pressure Surface (0.2017 m [7.94 in.] radius)	84
55	Centrifugal Stress, Suction Surface (0.2182 m [8.59 in.] radius)	85
56	Centrifugal Stress, Pressure Surface (0.2182 m [8.59 in.] radius)	86
57	Centrifugal Stress, Suction Surface (0.2393 m [9.42 in.] radius)	87
58	Centrifugal Stress, Pressure Surface (0.2393 m [9.42 in.] radius)	88
59	Centrifugal Stress, Suction Surface (0.2769 m [10.9 in.] radius)	89
60	Centrifugal Stress, Pressure Surface (0.2769 m [10.9 in.] radius)	90
61	Centrifugal Stress, Suction Surface (0.3713 m [14.62 in.] radius)	91
62	Centrifugal Stress, Pressure Surface (0.3713 m [14.62 in.] radius)	92
63	Temperature Map of Composite Blade at 105 Percent of Design Speed for Standard Day Inlet Conditions	93

LIST OF ILLUSTRATIONS (Cont'd)

<u>Figure</u>	<u>Title</u>	<u>Page</u>
64	Blade Tilt to Offset Air Loads	94
65	Blade Untwist as a Function of Blade Radius	95
66	Loading Edge Uncamber as a Function of Inlet Pressure	96
67	Precamber Offset Curves for Tip Leading Edge	97
68	Six-Wedge Dovetail Configuration Analysis	98
69	Identification of Stress Location Areas	99
70	Campbell Diagram	100
71	Campbell Diagram, Tip Modes (With $2 \pm 75^\circ$ Plies)	101
72	Campbell Diagram	102
73	Stiff Bearing Critical Speed	103
74	Model of Dynamic System for Critical Speed Calculations	104
75	Mode Shapes of Criticals Having Significant Fan Rotor Motion (Natural Frequency = 5540 rpm)	105
76	Mode Shapes of Criticals Having Significant Fan Rotor Motion (Natural Frequency = 11481 rpm)	106
77	Mode Shapes of Criticals Having Significant Fan Rotor Motion (Natural Frequency = 12280 rpm)	107
78	Mode Shapes of Critical Having Significant Fan Rotor Motion (Natural Frequency = 17686 rpm)	108
79	Mode Sape of Criticals Having Significant Fan Rotor Motion (Natural Frequency = 18400 rpm)	109
80	Response of Rotor to 0.706 N-cm [1 oz-in.] Unbalance in the Plane of the Rotor	110
81	Response of Rotor to 0.706 N-cm [1 oz-in.] Unbalance in the Plane of the Coupling Diaphram	111

SUMMARY

A highly loaded, single-stage compressor having a tip speed of 670.6 m/sec [2200 ft/sec] has been designed under Contract NAS3-15335. The purpose of the program is to investigate the use of very high tip speeds and high aerodynamic loadings to obtain high stage pressure ratios at acceptable levels of efficiency. The rotor has been designed for precompression (compression ahead of the covered channel between blades) at radii where inlet supersonic relative Mach numbers are high enough to allow attached oblique shocks at the leading edge. No inlet-guide-vane is used, and the stator vanes are designed for zero exit swirl. The design pressure ratio is 2.8 at an adiabatic efficiency of 84.4%. Corrected design flow is 83.4 kg/sec [184.0 lbm/sec]; corrected design speed is 15,200 rpm; and rotor inlet tip diameter is 0.853 m [33.6 in.]. Because of the high tip speed, rotor blades are designed to be fabricated of composite materials.

The aerodynamic design of the rotor is the result of an iteration between airfoil design calculations and axisymmetric flowfield calculations. The flowfield calculation gave intrablade radial distributions of flow and aerodynamic conditions. Airfoil design calculations gave intrablade flow conditions on conical surfaces approximating stream surfaces of revolution. The iteration was performed to match work, loss, blockage, and static pressure distributions axially and radially through the rotor to obtain flowfield conditions compatible with the assumed low loss shock wave systems of the airfoil design calculations.

The rotor design uses multiple-circular-arc airfoil sections from the hub to 15 percent span, precompression airfoils assuming single, strong oblique shocks from 21 to 43 percent span, and precompression airfoils assuming multiple oblique shocks from 52 percent span to the tip. Each airfoil section is designed for the lowest possible shock losses. Normal shocks are assumed at radial locations where the leading edge angle of the airfoil is too large for an attached shock at the design relative Mach number. Strong oblique shocks are assumed where leading edge shocks can be attached and where subsonic diffusion is required downstream of the shock. Multiple weak oblique-shocks are assumed where leading edge shocks can be attached and where exit relative Mach numbers are compatible with an oblique shock at the exit of the channel between airfoils.

Rotor losses were estimated using a loss model in which shock and profile losses are considered separately. Shock losses were estimated based on relative Mach numbers and airfoil shape. Profile losses were estimated based on theoretical boundary layer calculations, modified to conform to cascade test results. Both loss components were calculated for each pass of the design iteration since they are a function of airfoil shape.

The stator airfoils are multiple-circular-arcs. Stator loss estimates are based on a correlation of loss parameter versus diffusion factor and percent span. The stator leading edge is located close behind the rotor. The calculated stator inlet Mach number reaches a maximum of 0.89 at the hub.

Courtaulds HTS graphite fiber in polyimide matrix Kerimid 601 is assumed for the rotor blade design — after completion of the design, a NASA developed polyimide resin matrix (designated PMR) with significantly superior qualities was investigated as an alternate composite. A typical rotor blade cross-section is composed of a core of radially oriented plies 0.0254 cm [0.01 in.] thick incased in a shell of 0.0127 cm [0.005 in.] thick plies oriented $\pm 40^\circ$. In addition, two cross-ply ($\pm 75^\circ$) at the tip are required to reduce tip flutter to acceptable levels. The blade is secured to the disk by a “dovetail” formed by fanning out blade fibers into bundles with aluminum wedges bonded to the bundles. The bearing surfaces are titanium pads bonded to the outer fiber bundles. The design vane material is AMS 5613 stainless steel.

A discussion of structural test results of blades both with Kerimid and with PMR matrix is presented in appendixes to the report.

Due to unsatisfactory materials performance, no aerodynamic performance tests will be conducted.

INTRODUCTION

Future aircraft powerplants require lightweight compressors that are efficient over a wide range of operation. Weight reductions can be obtained by increasing stage pressure ratio to reduce the number of fan and compressor stages. Pressure ratio per stage can be increased considerably above current levels by increasing rotor wheel speed and blade loadings. However, careful consideration must be given to blade element design in order to avoid severe aerodynamic losses. These losses result from strong shocks at high Mach numbers and from boundary layer growth due to shock impingement and high blade loadings. In addition, the higher tip speeds increase stress levels on blades and blade attachments, requiring new materials.

An extensive research program conducted by NASA on high-speed, highly loaded fan stages has proven that good performance can be obtained with these operating conditions. As part of the NASA program, P&WA successfully demonstrated the performance of a 487.7 m/sec [1600 ft/sec] and a 548.6 m/sec [1800 ft/sec] tip speed fan stage. The 487.7 m/sec fan produced a stage pressure ratio of 1.946 at an adiabatic efficiency of 84.5% with multiple-circular-arc (MCA) airfoil sections (ref. 1). The 548.6 m/sec fan produced a stage pressure ratio of 2.2 at an adiabatic efficiency of 82% with part MCA and part precompression airfoils with strong oblique shocks (ref. 2).

As part of this series of high tip speed, highly loaded, single-stage compressors, a 670.6 m/sec [2200 ft/sec] tip speed fan stage was designed. This report describes the aerodynamic and mechanical design of that fan. The results of structural tests of the blades are discussed in Appendixes I and J.

Symbols and abbreviations used in the report are defined in Appendix A.

AERODYNAMIC DESIGN

The 670.6 m/sec [2200 ft/sec] tip speed fan stage has a hub-tip ratio of 0.5 and a design flow per inlet annulus area of 195.1 kg/m²-sec [40.0 lbm/ft²-sec] at the rotor inlet. The design pressure ratio is 2.8, and the predicted stage adiabatic efficiency is 84.4%. The rotor has supersonic relative Mach numbers for the entire inlet span and supersonic exit flow from 65 percent span to the tip. The blade design incorporates three airfoil shapes: MCA airfoils, single oblique-shock precompression airfoils, and multiple oblique-shock precompression airfoils. The stage has no inlet guide vanes and a zero exit swirl. In addition the rotor aerodynamic design must be compatible with mechanical design criteria, including the requirement for fabrication of composite material.

A summary of overall performance and blade vane design parameters is presented in Table I.

TABLE I – OVERALL PERFORMANCE AND BLADE AND VANE DESIGN PARAMETERS

FAN DESIGN OVERALL PERFORMANCE PARAMETERS

Rotor Pressure Ratio	2.88
Rotor Efficiency (adia.), %	87.1
Stage Pressure Ratio	2.80
Stage Efficiency (adia.), %	84.4
Corrected Flow, kg/sec	83.4 [184.0 lbm/sec]
Corrected Speed, rpm	15,200

BLADE AND VANE DESIGN PARAMETERS

Rotor Inlet Tip Diameter, meter	0.853 [33.6 in.]
Rotor Tip Speed, m/sec	670.6 [2200 ft/sec]
Rotor Tip Relative Mach Number	2.15
Rotor Tip Diffusion Factor (90% span from hub)	0.435
Rotor Inlet Hub-Tip Ratio	0.5
Rotor Tip Solidity	1.413
Number of Rotor Blades	19
Rotor Aspect Ratio (average length/axially projected hub chord)	1.63
Stator Hub Mach Number (10% span from hub)	0.845
Number of Stator Vanes	60
Stator Aspect Ratio (average length/axially projected hub chord)	1.58

FLOWPATH AND VECTOR DIAGRAM DESIGN

The flowpath is designed to utilize existing ducts and casings from the 548.6 m/sec [1800 ft/sec] compressor, (ref. 2) with modifications for optimum performance with the higher rotor tip speed. Contract requirements established the hub-tip ratio, rotor tip speed, and approximate pressure ratio. The design pressure ratio, specific flow, and blade and vane solidities and aspect ratios evolved from a study of blade element loadings and fan flow capacity using an axisymmetric streamline analysis program (described in Appendix B) for the flowfield calculation.

The first objective of the study was to raise specific flow from the 180.5 kg/sec-m² [38.7 lbm/sec-ft²] of the reference 3 flowpath to a higher value more compatible with advanced engine designs. Rotor aspect ratio was reduced to give larger streamline radii of curvature at the rotor inlet and to increase the axial component of meridional Mach number near both endwalls. This change gives a more even distribution of meridional velocity at the rotor inlet, permitting specific flow to be increased to 195.1 kg/sec-m² [40.0 lbm/sec-ft²] without choking and with the same annulus convergence across the rotor. Profiles of meridional Mach number at the rotor inlet are compared in Figure 1, and the flowpath modification is shown in Figure 2.

The second objective was to determine the maximum pressure ratio consistent with reasonable values of stall margin and exit Mach number. The desired 2.8 pressure ratio could not be obtained with the reference 3 flowpath without excessive stator loadings. Therefore, stator hub convergence was increased and the stator chord was lengthened to increase solidity. Acceptable loadings were calculated for a 2.8 pressure ratio with the revised flowpath (solid-line configuration in Figure 2).

The stator stacking line is at the same location as in the stator of reference 3. The higher hub solidity of the 670.6 m/sec stator relative to the reference 3 stator results in a longer chord axial projection which forces the rotor forward in the flowpath to obtain a suitable rotor-stator spacing.

Spanwise distributions of velocity at the inlet and exit for the rotor and stator as calculated by the streamline program are shown in Figures 3 and 4. Figure 3 shows the distributions of relative velocity for the rotor, and Figure 4 shows the distributions of absolute velocity for the stator. Blade and vane solidities are shown in Figure 5, and the corresponding loadings are shown in Figure 6. The estimated stall margin of the stage is 12 percent.

ROTOR BLADE DESIGN

A quasi three-dimensional, intrablade design technique was used in which blade-to-blade aerodynamic conditions from airfoil design calculations were matched to meridional plane aerodynamic conditions from the axisymmetric flowfield that would be compatible with the airfoil design intrablade shock system. The technique consisted of an iteration in which: 1) flow conditions at the leading and trailing edges and the intrablade stream tube convergence from the axisymmetric flowfield calculation were used as input to airfoil design calculations and 2) intrablade losses, blockages, and energy input from the airfoil design calculations were used as input to the flowfield calculation. Since the flowfield calculation was axisymmetric, it was necessary to average cross-channel flow conditions from airfoil design calculations for input into the flowfield calculation.

Axisymmetric Flowfield Calculations

Flowfield calculations were made using a relaxation program based on the Marsh method (ref. 4) of solution of Wu's equations (ref. 5). This calculation method gives a solution for steady, compressible, and inviscid axisymmetric flow in axial-flow turbomachinery for specified intrablade distributions of work, loss, and blockage. Fluid properties were compared with gap-averaged values from the blade-to-blade calculations.

The relaxation program provides a more complex specification of intrablade flow conditions (i.e., flow conditions at a greater number of points) than the streamline calculation. Some discrepancy was noted between the relaxation and streamline solutions. The relaxation solution had higher meridional velocities at the tip and lower velocities at the hub and mid-span, as shown by Figure 7. The relaxation calculation is believed to be more accurate because of the more detailed specification of blockage, work, and loss.

Rotor inlet and exit relative Mach numbers from the relaxation calculation are compared with values from the streamline calculation in Figure 8. Inlet relative flow is supersonic from hub to tip, and exit relative flow is supersonic from 65 percent span to the tip.

The design velocity vector data calculated along streamlines at the rotor leading and trailing edges is tabulated in Appendix C, Rotor Aerodynamic Summary. The streamline calculation values are also presented.

Airfoil Design Calculations

The rotor blading utilizes three types of airfoils, all having supersonic relative flow. The leading edge wedge-angle of the blade and the relative inlet and exit Mach number (Figure 8) determined the type of airfoil. Each airfoil section was chosen to provide the lowest possible shock losses. The undefined portions of the blade are used to blend between adjacent airfoil types and do not represent a definite airfoil shape.

Multiple-circular-arc airfoils are specified where the combination of leading edge wedge-angle of the airfoil and the relative Mach number does not allow the formation of an attached oblique shock. MCA section shock losses were calculated assuming a normal shock at the channel inlet. The sections are MCA from 0 to 10 percent flow (0 to 15.1 percent span) from the hub.

Single-shock, precompression airfoils are specified from 15 to 35 percent flow (21.3 to 42.6 percent span) from the hub. These airfoils were designed assuming a strong, attached oblique-shock at the channel entrance, which gives subsonic relative flow at the exit with a lower calculated shock loss than for a normal-shock MCA blade.

From 45 to 100 percent flow (52.5 to 100 percent span) from the hub, multiple-shock precompression airfoils are used. This blade design assumes one oblique shock at the channel inlet and another at the channel exit. Other compression (or expansion) waves can exist in the fully supersonic flow in the channel. A detailed explanation of the design system for each of the three airfoils is presented in the following sections. Rotor blade geometry on conical surfaces is tabulated in Appendix D.

Multiple-Circular-Arc Design

MCA sections extend from the hub to 15.1 percent span. Airfoil sections were defined by specifying total and front chord, total and front camber, maximum thickness and its location, and leading and trailing edge radii, as shown by Figure 9.

For the MCA blade sections, a normal shock was assumed at the first covered section of the blade passage, as shown in Figure 10. Mach number upstream of the assumed normal shock was calculated in two steps. First a free-streamline relationship was used to calculate flow conditions and relative air angle at the shock position midway between blades. This free-stream flow calculation accounted for stream tube contraction and radius change. In the second step, the critical area ratio (A/A^*) of the free-stream flow was multiplied by the ratio of blade-channel entrance width to the width of a free-stream channel ($S \cos \beta'$). The resulting A/A^* established the upstream shock Mach number.

Rotor incidence for the MCA portion of the blade is +1.5 deg to the suction surface of the blade at a location halfway between the leading edge and the emanation point of the first captured Mach wave.

Front camber was used in conjunction with incidence to control the blade channel width. Front and total camber distributions are shown in Figure 11. The ratio of minimum blade-channel flow area to critical area, A/A^* , was set at $1.04 \pm 1\%$ to prevent choking, except at the very hub where 1.02 was used. Thickness requirements at the hub limited the area margin available.

The calculation of critical area ratio $(A/A^*)_{\min}$ includes determining the flow area (A) from the channel width between blades and from stream-tube contraction or expansion as determined by the axisymmetric flow calculation. The critical area (A^*) was determined from the inlet relative Mach number with correction for radius change, shock losses, a distribution of profile loss, and endwall loss where applicable.

Deviation was estimated using Carter's Rule and a correlation of test data from references 1, 2, and 6.

One-Shock Precompression Airfoil Design

A single, strong oblique-shock precompression airfoil is specified where the combination of supersonic relative Mach number at the inlet and the wedge angle at the airfoil leading edge allows the formation of an attached oblique shock and where the relative Mach number at the exit is too low for an oblique shock at the channel exit. This shock pattern blends between the normal shock MCA sections and the multiple-shock precompression sections which use a weak oblique-shock at the channel inlet. A schematic of the one-shock precompression airfoil is illustrated in Figure 12. Aerodynamic surfaces were generated from which metal surfaces were defined by subtracting the boundary layer displacement thickness as calculated by the method presented in reference 7.

The single-shock, precompression design system assumes that the strong shock across the channel entrance is oblique and attached to the leading edge of the airfoil. Flow conditions upstream of the first captured Mach line are adjusted to account for losses in the bow-shock

system which propagates upstream of the rotor inlet plane. The suction surface, inlet section (A-B in Figure 12) was designed to provide an aerodynamic surface (blade surface plus boundary layer displacement thickness) that is aligned with a constant-angular-momentum streamline from the leading edge to the first captured Mach wave. The concave surface (B-C) is the pre-compression ramp. The curvature of this ramp generates a series of compression waves which diffuse the supersonic flow. The wave system is designed to coalesce near A', slightly downstream of the rotor inlet plane. The precompression wave system lowers the Mach number of the flow across the passage entrance, reducing the total pressure loss associated with the oblique shock (A'-D). The flow deflection across this oblique shock at the pressure surface is equal to the leading edge aerodynamic wedge angle (blade wedge angle plus the angle corresponding to the growth of the boundary layer displacement thickness) plus the precompression angle.

The shock A'-D was constructed in increments across the gap to account for gapwise changes in flow conditions upstream of the shock. Shock losses were calculated for each increment and mass averaged across the gap to obtain the oblique shock loss of the blade element. Channel flow downstream of the oblique shock is subsonic; and turning and stream tube area were made compatible with exit aerodynamic conditions. Suction surface curvature in segment C-D was designed to adjust the supersonic flow upstream of the shock to be compatible with the shock deflection and subsonic flow conditions downstream of the shock. Iterations were made on surface shape until compatibility was achieved, accounting for effect of radius change and stream tube convergence (or divergence).

The suction surface immediately behind the shock impingement point, D, is aligned with the flow direction downstream of the shock. The surface is rounded at D to allow for boundary layer thickness changes in the region of shock impingement. The channel area is blended from the value at D to the desired value at the channel exit. A cosine variation of stream tube area determined the locus of points that define the suction surface (D-G). The cosine variations are given in Appendix E.

The pressure surface segment A-E follows a free streamline downstream of the oblique shock. Segment F-G of the pressure surface is designed to guide the flow to the desired exit angle. Segment E-F blends smoothly between A-E and F-G. The chordwise locations of the pressure surface points, E and F, are tabulated in Appendix D.

Multiple-Shock Precompression Blade Design

A multiple-shock precompression airfoil is specified in the outer region where exit relative Mach numbers are sufficiently high for the existence of an oblique shock at the channel exit. A schematic of this type of precompression blade, including terminology, is shown in Figure 13. The aerodynamic surfaces were determined by means of the multiple-shock airfoil, design system, and the metal surfaces were obtained by subtracting the boundary layer displacement thickness.

The multiple-shock precompression design system assumes a weak oblique shock across the channel entrance attached to the leading edge of the airfoil. Another oblique shock emanates from the suction surface trailing edge to adjust the flow to exit conditions, which can have either a supersonic or high subsonic velocity. In the supersonic flowfield generated by adjacent airfoils, the waves emanating from the pressure surface (A'-E-F-J in Figure 13) are right running and the waves from the suction surface (A-B-C-D-G-H) are left running.

Flow conditions upstream of the first captured Mach line were adjusted to account for the bow-shock system which propagates upstream of the rotor inlet plane. Development of the blade suction surface up to the shock impingement point (A-D) was the same as in the model for the single, strong oblique-shock. Segment C-D provides compatibility between supersonic flow conditions upstream and downstream of the weak oblique shock. The weak oblique right shock wave A'-D was constructed in increments across the gap to account for gapwise changes in flow conditions upstream of the shock. Shock losses were calculated for each increment and mass averaged across the gap to obtain the right-shock loss of the blade element. Flow deflection of this oblique shock at the pressure surface is equal to the leading edge aerodynamic wedge angle (blade wedge angle plus boundary layer displacement) plus the precompression angle. Channel flow downstream of this right oblique-shock is supersonic and contains at least one right expansion or compression wave (E-G) whose strength was set along with the left oblique-shock strength (F-H) to satisfy exit aerodynamic conditions. The left shock was assumed to originate at the aerodynamic suction surface trailing edge. Suction surface elements D-G and G-H align respectively with the supersonic flow directions downstream of the right shock and right expansion or compression wave. The surface is rounded at D to allow for boundary layer thickness changes in the region of the shock impingement.

The pressure surface segments A-E and E-F are aligned respectively with the supersonic flow directions downstream of the right shock and right expansion or compression wave. The remaining segment F-J is a free streamline at the desired exit angle. Chordwise locations of the pressure surface points, E and F, are tabulated in Appendix D.

General Design Procedure

The final rotor design is the result of matching the intrablade axisymmetric flow calculation to the airfoil blade design calculation. The matching, performed by an iterative procedure, provided static pressure distributions consistent with the assumed shock patterns at each design streamline. Both calculations provided solutions for conditions in the core flow (i.e., between boundary layers) in the blade channel. The iteration procedure is outlined in Figure 14; the input and output of each program is shown.

Intrablade Flowfield Program Input

Input for the intrablade flowfield calculation program consisted of flowpath boundary specifications, blade edge locations, weight flow, rotor speed, axial and radial distributions of total pressure, total temperature and blockage, and a radial distribution of stator exit air angle. The pressures, temperatures, and blockages were core flow values which assumed shock and endwall losses only and were compatible with the blade design programs.

Intrablade values of work and loss were input for each design airfoil section at 0, 20, 40, 60, and 80 percent of the axially projected rotor chord. Intrablade work distributions were obtained from the cross-channel force resulting from the static pressure difference between blade surfaces as calculated by the airfoil design programs. The calculation procedure for work distribution is described in Appendix F. Loss distributions were obtained by applying the shock losses from the blade design programs linearly from the point of intersection on the suction surface to the point of intersection on the pressure surface. The bow-wave loss was applied at the leading edge. Endwall losses were applied linearly from the leading to trailing edge.

Blockage was distributed between the rotor leading and trailing edges to account for profile loss as well as blade metal blockage. The equivalent blockages were determined by adding boundary layer displacement thickness to the metal thickness. Both thicknesses were obtained from the output of the blade design calculation. Blockage of endwall boundary layers was accounted for by additional increments. These endwall blockage increments were input as constant values at a particular calculation station, varying from two percent at the rotor leading edge to three percent at the rotor trailing edge. Intrablade blockage terms, required because of nonaxisymmetric flow and the interaction of shock and boundary layer, were also included. Total blockage amounted to about 40 percent near the thickest part of the blade (see Figure 20). Blockage terms are further discussed in Appendix G.

Airfoil Design Input

Blade inlet and exit aerodynamic conditions and flow per unit annulus area (specific flow ratio) distribution were obtained from the intrablade axisymmetric calculation. Specific flow ratio is a measure of streamtube convergence and is defined by

$$\frac{(\rho V_m \bar{K}_{\text{airfoil}})_{\text{inlet}}}{(\rho V_m \bar{K}_{\text{airfoil}})_{\text{local}}} = \frac{A_{\text{annulus local}}}{A_{\text{annulus inlet}}}$$

where ρ = density

V_m = meridian velocity

\bar{K} = $\frac{\text{effective area}}{\text{actual area}}$

and where \bar{K}_{airfoil} is the accumulation of all blockage factors except the endwall boundary layer blockage factor. Annulus convergence through the rotor and stator was used together with solidity to control blade and vane loadings. Spanwise distributions of diffusion factor for the rotor and stator are shown in Figure 6.

The distribution of specific flow ratio for design streamlines are presented in Figure 15. The locally high value of specific flow ratio at approximately 17 percent of chord on the hub is due to streamline curvature where flow direction must conform to the hub wall slope.

Loss Determination

The total rotor loss is the sum of shock, profile, and endwall losses, and is a function of the airfoil shape. The rotor loss estimation was determined as part of the iteration procedure.

Shock losses were calculated for each particular-airfoil blade element, depending on the shock model assumed (i.e., normal shock, single strong-oblique-shock, or multiple oblique shocks). Bow wave loss was included in the calculation. The shock losses in the transition regions between the three airfoil types were estimated by blending the calculated losses for the adjacent sections.

Profile loss estimates for precompression airfoils were based on the airfoil design calculations and the results of cascade tests. Analytical estimates of profile loss were based on boundary layer calculations on blade surfaces. The calculation method of Reshotko and Tucker (ref. 7) was utilized. The calculated losses were compared with cascade results of similar airfoil shapes, and values at each chordwise location were multiplied by a constant amount at each span to bring the calculations into agreement with the test results. The blade design programs used this profile loss estimate to obtain core-flow aerodynamics for designing the aerodynamic surfaces of the blade channel.

Endwall losses were calculated from 0 to 20 percent and 80 to 100 percent of span. The calculations were based on correlations of experimental, single-stage compressor data.

The total loss used to design the airfoils was obtained by summing the three component losses (i.e., shock, profile, and endwall). Figure 16 shows the radial distribution of total pressure recovery due to shock loss and to all losses. Figure 17 shows the corresponding spanwise distribution of total loss coefficient.

Convergence Criteria

The design iteration was assumed to be covered when the intrablade axisymmetric flow-field (Wu-Marsh) and blade design programs had intrablade distributions of static pressure which gave values of minimum A/A^* within 0.5 percent and a similar pressure slope through the channel. Work, loss, and blockage distributions were calculated by the blade-to-blade programs, but some smoothing in the radial direction was required before input to the axisymmetric program. For example, Figure 18 shows that the strong oblique shock, precompression sections (streamlines 4, 5, and 6) had calculated work distributions concentrated near the front half of the blade while the outboard, multiple shock, precompression sections had work concentrated in the rear half of the blade. The work schedules input to the axisymmetric program had to be modified to avoid flow discontinuities in the radial direction. This resulted in sizeable differences in input from the strong oblique shock blade calculations; however, excellent agreement occurred for the multiple shock sections where the highest Mach numbers occurred. No work distributions were calculated for the MCA blade sections (streamlines 1, 2, and 3) since surface static pressures were not available to calculate work as was done for the precompression sections (see Appendix F).

The loss distributions presented in Figure 19 include only shock and endwall loss since the core-flow design procedure replaced profile (airfoil boundary layer) loss with an equivalent blockage. All loss for the normal-shock MCA and strong oblique shock, precompression blades occurs between the leading edge and the point where the shock intersects the suction surface. Streamlines 1, 2, and 3 have endwall loss linearly superimposed from the leading to trailing edge. Radial smoothing to prevent discontinuities in shock losses resulted in the revised axial distributions input to the axisymmetric program. Figure 20 shows the distribution of blockage through the blade consisting of the metal plus airfoil boundary layer displacement thicknesses.

Since static pressures calculated by the intrablade flowfield program represent axisymmetric values, it was necessary to calculate a cross-channel gap average static pressure from the airfoil design calculations for comparison at axial locations along each streamline. The gap average static pressure was calculated based on the A/A^* distribution in the aerodynamic channel using area weighted average of subsonic and supersonic static pressures across any shocks that intersected an axial location where an average was desired. Static pressure comparisons are shown in Figure 21 for design streamlines.

Blade Geometry

The relative air angles of rotor blade leading and trailing edges are presented in Figure 22; two curves are shown for each angle. One curve is based on the streamline calculation; the other, on the intrablade axisymmetric flow calculation. The values from the intrablade calculation were used to design the blades. Angle differences are small in the high Mach number portion of the blades. The meanline metal angles (Figure 23) used in the calculation of incidence and deviation angles are the averages of pressure and suction surface metal angles at the leading and trailing edges of the developed blade sections. The meanline incidence and deviation angles for the entire blade are shown in Figures 24 and 25, respectively. The determination of incidence and deviation was discussed in the Airfoil Design Calculations section (page 5). As shown by the data included in Figure 25a, the deviation falls within the experience of other successful MCA precompression blade designs. The increment added to Carter's rule in the MCA portion was based on a correlation of test data from references 1, 2, and 6. The present design falls within this band, as shown in Figure 25b.

Precompression blade sections were designed for a radial distribution of cross-sectional area determined from the preliminary mechanical design. The main purpose of this requirement is to provide the required mechanical properties and to smooth blending of the MCA and precompression blades. A spanwise distribution of blade cross-sectional areas is shown in Figure 26. The precompression airfoil cross-sectional areas were obtained primarily by controlling the leading edge radius, blade leading edge wedge-angle, and precompression ramp angle, as shown respectively in Figures 27, 28, and 29. The leading edge wedge-angle and the location of the pressure surface point, E, (Figure 12), were chosen to avoid local chordwise narrowing of blade elements which could result in concentrations of vibrational stress. Blade chord versus span is shown in Figure 30a. The ratio of maximum thickness to chord is shown in Figure 30b.

The region of the blade from 13.4 to 19.4 percent span provides transition from the MCA to strong-shock precompression sections. The outermost MCA conical section is at 13.4 percent span, and the first precompression section is at 19.4 percent span. The region of the blade from 40.84 to 50.63 percent span provides transition from strong-shock precompression to multiple-shock precompression sections, in a similar manner.

The blade section "stacking" program interpolates between conical sections to define stacked sections on planes normal to a radial line, for manufacturing purposes. This program provides interpolated stacked sections in the transition region. Significant chordwise variations in the center of gravity locations of the sections on either side of the transition regions caused undesirable leading and trailing edge radial profile discontinuities when the interpolated sections were stacked on their centers of gravity. To avoid these discontinuities, the design conical

airfoils were shifted axially and tangentially to smooth the edge profiles. This resulted in manufacturing sections in the transition regions which are not stacked exactly on their centers of gravity. Stress calculations were made recognizing these offset centers of gravity. The resulting blade coordinates are presented in Appendix H.

Shock Starting

Shock systems assumed in the design of these airfoils can be attained only if the channel between blades is capable of swallowing stronger shocks during the "starting" process. Starting criteria were based on results from the reference 2 fan stage which achieved a started shock system. Critical area ratios ($A/A^*_{\min.}$) in channels between blades were analyzed to determine throat area requirements. Critical area ratios for the subject fan design were compared with ratios at which starting was achieved in the reference 2 test.

Critical area ratios were calculated based upon channel width between blades, bow-wave losses, profile losses, streamline radius changes, specific flow ratio (stream tube contraction), and different assumed shock systems. The minimum A/A^* ratios for the subject design pre-compression blade sections are plotted versus span in Figure 31 for three types of assumed shock loss. The corresponding curves for the reference 3^(a) fan design are also presented. The minimum A/A^* ratio occurs just downstream of the right shock for the single-shock airfoils and at the last covered section for the multiple-shock airfoils. Curve A in Figure 31 was computed on the basis of the design shock loss (i.e., the one or two oblique-shock models shown in Figures 12 and 13). The $A/A^*_{\min.}$ ranged from 1.02 to 1.36. Curve B in Figure 31 is the minimum A/A^* distribution based on a normal shock at the channel entrance Mach number (after the precompression ramp) with design total loss held constant. Curve C is also based on a normal shock at the channel entrance, but the design profile loss is held constant so that the overall total loss is higher than design.

(a) Reference 2 and reference 3 are reports for the same fan stage, the 548.6 m/sec [1800 ft/sec] tip speed fan.

STATOR VANE DESIGN

The stator has 60 vanes — the same as for the reference 2 stator — and all have MCA airfoil sections from root to tip. Airfoil sections were designed on conical surfaces approximating stream surfaces of revolution. The design procedure did not involve the intrablade analysis performed for the rotor. Inlet and exit aerodynamics came from the streamline flowfield program which has been used successfully in earlier fan programs. The design velocity vector data calculated along streamlines at the stator leading and trailing edges is tabulated in Appendix C. Stator losses were calculated by means of a correlation of loss parameter versus diffusion factor and percent span. Figure 32 shows the final radial distribution of stator loss coefficient. Spanwise distributions of absolute flow angle and Mach number are shown in Figures 22 and 33.

Vane chord length varies from 7.44 cm [2.93 in.] at the hub to 6.33 cm [2.61 in.] at the tip, which gives a hub solidity of 2.5. The high solidity is necessary to keep the hub diffusion factor below 0.5. Aspect ratio is 1.58, based on average blade length and axially projected chord at the hub. Figure 34 shows front and total chords for the MCA airfoils versus span. Maximum thickness-to-chord ratio is 0.07 at the tip, tapering linearly to 0.05 at the hub. This stator blade thickness distribution was selected to provide mechanical integrity and low blade-element loss. Figure 35 shows the maximum thickness-to-chord ratio and its chord-wise location versus span.

Incidence to the suction surface varies from zero degrees at the hub to -3 degrees at the tip (Figure 36) based on minimum loss data from similar stators. Camber distributions was employed to control throat area in the channel between adjacent vanes. The optimum ratio of capture-area to throat-area, defined in reference 8, was used to set throat area. Figure 37 shows axial distributions of A/A^* in channels between stator blades, and Figure 38 shows the minimum A/A^* versus span.

Stator deviation angles were determined using Carter's rule plus an adjustment based on data from references 1 and 9. The spanwise distribution of Carter's rule and design deviation-angles are given in Figure 39.

Figure 40 presents mean camber-line metal-angles versus span, and Figure 41 presents front and total camber angles. All angles in these figures are measured on conical surfaces on which the airfoils were designed. Stator geometry on conical surfaces is summarized in Appendix D.

For manufacturing purposes, airfoil sections were defined on planes normal to a radial line which passes through the center of gravity of the hub section. Coordinates of these sections are tabulated in Appendix H.

MECHANICAL DESIGN

The 670.6 m/sec [2200 ft/sec] fan was designed to utilize the existing hubs, drive shaft, cases, bearings, and bearing supports of the earlier 548.6 m/sec [1800 ft/sec] fan (ref 3). Because of the severe stresses due to the high tip speed, a rotor fabricated of a high strength, composite material is required. The original choice of a composite was Courtaulds HTS graphite fiber in the polyimide matrix Kerimid 601. However, about midway through the contract, consideration was given to the substitution of a NASA-Lewis developed matrix material PMR. This new material is a polyimide resin with improved temperature capability, ductility, and translation of fiber properties in graphite fiber composites. Substitution of the material does not affect airfoil shape since the shape was primarily developed to satisfy aerodynamic considerations. Only the original material is discussed in this section of the report. A discussion of the results of structural tests of the Kerimid 601 matrix blades by J. A. Arnold of P&WA is presented in Appendix I. An evaluation of the PMR polyimide blade by W. E. Winters of TRW Inc. including a discussion of structural test results is presented in Appendix J.

The vane material is conventional AMS 5616 stainless steel.

ROTOR BLADE DESIGN

The minimum specification properties of the original prepreg are:

Ultimate tensile strength: 124,000 N/cm² [180,000 lbm/in.²]
Flexure strength (amb.): 138,000 N/cm² [200,000 lbm/in.²]
Flexure strength (260°C [500°F]): 103,000 N/cm² [150,000 lbm/in.²]
Short beam shear strength: 7,580 N/cm² [11,000 lbm/in.²]
Flexure modulus of elasticity x 10⁻⁶: 11.7 N/cm² [17 lbm/in.²]

The strength of the composite is a function of the orientation of the fibers to the direction of loading, assuming an equal number of plies tilted at a given angle in each direction from the direction of loading. The ability of a composite material to retain high strength when loaded off-axis is a result of a complex interaction of shear in the matrix and of the transverse tension in the prepreg, and is a function of the material strength in those modes.

Curves of minimum tensile and shear strengths are presented in Figure 42 as functions of ply orientation angle. The solid line curves show the values originally assumed in the design. The values are based on typical strength-loss curves for similar materials. However, tests conducted by TRW, Inc. (broken-line curve) indicate that the strength of plies oriented at $\pm 10^\circ$ fall far below the solid-line curve. Thus, limiting the ply orientation in the core to only radial plies was believed necessary for adequate strength.

Curves of elastic modulus and shear modulus are presented in Figure 43 as a function of ply orientation angle. These curves are also based on typical data on similar composites.

A typical cross-section of the blade is presented in Figure 44. The figure shows a core of radially oriented plies 0.0254 cm [0.01 in.] thick encased in a shell of 0.0177 cm [0.005 in.] thick plies arranged alternately at angles of $+40^\circ$ and -40° from the radial. The core provides radial strength and stiffness while the shell absorbs untwist effects and provides torsional stiffness. A criterion of 15 percent of the maximum blade thickness at any station, or as nearly so as consistent with good ply layup, was used to establish shell thickness for each radial station.

The airfoil cross-sections change to parallelogram sections between the inner flowpath and the top of the dovetail attachment. Figure 45 shows this section, and identifies the location and magnitude of some of the critical stresses. The dovetail is oriented to minimize the severity of the transition bends from the airfoil leading edge, and is as close as feasible to an axial direction to minimize design difficulties in the area of the disk rim, difficulties inherent in highly staggered broach angles. Figure 46 shows the transition at the leading edge. This eccentricity contributes heavily to high stresses calculated in the root area.

The centrifugal stresses were calculated by means of an ASKA program (a finite element program). The blade material was assumed to be an isotropic, nonuniform, wrapped plate in a centrifugal field; and complete stress distributions on both the pressure and suction sides were obtained. This distribution includes all centrifugal, twistup, untwist, nonradial stacking, and local eccentricity effects.

The stress distributions over the cross sections at various radial stations were converted to direct radial load and transverse bending moment distributions. These in turn were distributed between the core and the shell at each axial location in proportion to the local radial and flexural stiffness, and the resulting stresses in each were calculated. This procedure is believed to give good representation of peak stresses and stress gradients although the actual distribution of stresses may be off because of the assumption of isotropy.

Curves of stresses over the cross sections at eight radial calculation stations¹ are presented in Figures 47 through 62. Curves are given for radial tensile stresses in the core and on the outer surface of the shell for both pressure and suction sides of the blade.

The peak calculated stress in the core is $61,400 \text{ N/cm}^2$ [$89,000 \text{ lbm/in.}^2$] at the leading edge on the pressure side in the attachment area (18.29 cm [7.2 in.] radial station). The radial stress in the shell at this point is $16,500 \text{ N/cm}^2$ [$24,000 \text{ lbm/in.}^2$]. The local temperature in this region is expected to be about 100° C (see Figure 63). At this temperature there is a reduction in ultimate tensile strength from $124,000 \text{ N/cm}^2$ to about $114,000 \text{ N/cm}^2$ [$165,000 \text{ lbm/in.}^2$]. It is a normal P&WA practice to limit the calculated stresses in composite blades to 70 percent of the ultimate tensile strength to allow for vibratory stresses and any deterioration in the strength of the plies. Based on this criterion, the blade is safe since it would be stressed to about 55 percent of the ultimate strength.

The ideal ultimate tensile strength of $\pm 40^\circ$ fibers is about $27,600 \text{ N/cm}^2$ [$40,000 \text{ lbm/in.}^2$]; see the solid-line curve in Figure 42. If this ideal value were reliable, the blade would be assumed to be safe since the maximum stress is $16,500 \text{ N/cm}^2$, providing a stress-strength ratio of 60 percent which is within the P&WA 70 percent criterion. However, the TRW tests indicate that the tensile strength at this orientation angle may be considerably below the ideal value; in which case the shell would be overstressed. Local overstressing in the shell could lead to cracking of the matrix, but the load would redistribute accordingly. P&WA has operation experience with microcracks and has not seen any evidence that the basic integrity of the blade is compromised by these cracks for the relatively short operational time typical of the current program. Therefore, any such cracking can be expected to be confined to very local areas and not endanger the blade.

Bending stresses at the blade root due to air loads can be reduced significantly by tilting the blade axially (forward) and tangentially (opposite the direction of rotation). In this way, centrifugal forces on the blade have bending moments about the blade root that counteract the bending moments caused by the air loads.

The rig is intended to be operated at approximately 50.8 cm Hg [20 in. Hg], and this pressure was used to determine tilt offsets. The calculated air pressures were integrated chordwise at the various blade radial stations to establish a spanwise distribution of air load. In determining the bending moments, stresses, and deflections resulting from air loads and from the tilt centrifugal forces, the blade was treated as a beam with rigid (unwrapped) sections.

The air-load bending stress calculated at the root is $10,300 \text{ N/cm}^2$ [$15,000 \text{ lbm/in.}^2$] at 50.8 cm Hg inlet pressure. The tip of the blade is offset. The axial offset is 0.140 cm

1. The radial calculation stations are measured from the centerline of the rig.

[0.055 in.], and the tangential offset is 0.089 cm [0.035 in.] opposite the direction of rotation. These offsets cancel the air load stresses at the root at the operating inlet pressure.

If the air load were to drop to zero during a surge, the peak root centrifugal stress would actually be reduced by the tilt centrifugal stresses. Figure 64 shows the tilt directions and magnitudes and the air load, tilt, and centrifugal stresses at the root and net operating and net surge stresses.

Rotor Untwist and Tip Uncamber

The untwist of the entire blade due to twist-up and varying stagger in the centrifugal field was calculated. Each section was assumed to be rigid and stacked with the centroids on a radial line. Based on these assumptions, the untwist at the tip was calculated to be 0.45 degrees.

A calculation was also made by NASA, using a NASTRAN simulation of the blade as a distorted, nonuniform composite plate in a centrifugal field; and the tip untwist was found to be 0.7 degrees. The 0.7 degree untwist is believed to be more realistic since the effect of the eccentricities of the centroids from the radial were accounted for. The 0.7 degree figure was therefore adopted. A curve of the manufacturing pretwist required to achieve the desired aerodynamic stagger at speed is shown in Figure 65.

The rotor tip is reinforced by two 0.017 cm [0.005 in.] plies oriented $+75^\circ$ and -75° (shown in Figure 46) to the radial direction in order to provide chordwise stiffness in this area. This is done both to avoid the possibility of tip chordwise flutter in the high Mach number stream and to minimize uncambering or overcambering of the thin leading edge at the tip in the centrifugal field and as a consequence of the air loads. The uncambering-overcambering phenomenon is a result of three effects:

- 1) The untwist action, due to centrifugal loading and the varying stagger from root to tip, results in transverse forces along the chord which tend to uncamber the leading edge.
- 2) The centrifugal twist-up action on a staggered blade which results in components of centrifugal force transverse to the blade chord at the tip. This is an overcambering action at the leading edge.
- 3) The air loads transverse to the blade which tend to uncamber the tip.

A NASTRAN calculation was used to determine the deflection lines of the blade tip resulting from the above effects. The blade was represented by an "equivalent thickness" isotropic blade having a uniform value of modulus of elasticity (E). The equivalent thickness was established by calculating the actual composite bending stiffness (ΣEI) at every point, dividing it by the adopted value of E , and establishing a thickness to give the ensuing equivalent inertia. The tip deflections are dependent both on the chordwise stiffness (particularly in the tip area and in connection with the twist-up and air load actions) and on the radial stiffness (particularly in connection with untwist effects). A review of the chord-

wise and radial stiffnesses at the tip indicated that they are sufficiently close to permit the use of chordwise stiffness throughout, and this is the way the calculation was completed.

An equivalent uniform density was used to ensure that realistic centrifugal forces were applied, particularly at the tip leading edge. This equivalent density was based on the average density of the leading outer 5.1 cm x 5.1 cm [2 in. x 2 in.] portion of the blade and was corrected for the equivalent thickness.

A curve of uncamber as a function of fan inlet pressure is presented in Figure 66.

The rig design includes a window in the case to permit high speed photography of the blade tip. The photographs thus obtained would permit the operating camberline of the blade tips to be determined and the inlet throttle to be adjusted for optimum air angles. To provide maximum latitude for adjustment, the precamber specified corresponds to that calculated for an inlet pressure of 50.8 cm Hg. This precamber extends 5.1 cm [2 in.] in from the leading edge and from the tip inward to about the 0.33 m [13.0 in.] radial station. Curves of the precamber offset are presented in Figure 67 for various radial stations. The average precamber is 0.45 degrees over the first 5.1 cm of chord.

Dovetail Design

The blade is secured in the disk by means of a dovetail, shown in Figure 46. The blade fibers fan out in bundles and together with aluminum wedges bonded between bundles provide the dovetail shape. The bearing surfaces consist of two titanium pads bonded to the outermost fiber bundles.

The dovetail was stress analyzed by means of a two-dimensional, finite element model. The exact geometry and stiffness of the shell fibers, pressure pads, and wedges were defined. One-half the dovetail was analyzed with the boundary conditions shown in Figure 68. A uniform displacement on boundary "A" was applied, and the strains and stresses throughout the dovetail and the normal forces on the other two boundaries were computed. The pull of the foil and dovetail per inch of dovetail length was divided by the integral of the stresses on boundary "A" to determine a factor by which the solution is multiplied.

The stresses in the dovetail cannot be accurately analyzed, and reliable criteria for composite dovetails are not yet available. Furthermore, the two-dimensional model utilized assumes a uniform dovetail symmetrically loaded along its length, which is not valid because of the eccentricities of the airfoil relative to the dovetail and because of the high angle of the dovetail from the axial (approximately 40 degrees). The new design could only be validated by comparison with successfully demonstrated dovetails that had been analyzed by means of the same two-dimensional, finite model.

After iterating to reduce the shear stresses between the composite and the aluminum wedges, a six-wedge configuration was adopted (Figure 68). The direct, transverse, and bond shear stresses throughout the six-wedge dovetail configuration are shown respectively in Tables II, III, and IV (see Figure 69 for identification of stress location areas).

TABLE II – DIRECT STRESSES IN DOVETAIL
(Stresses in N/cm² [lbf/in.²] x 10⁻³)

See Figure 69 for identification

	<u>A</u>	<u>B</u>	<u>C</u>	<u>D</u>	<u>E</u>	<u>F</u>	<u>G</u>	<u>H</u>	<u>I</u>	<u>J</u>	<u>K</u>	<u>L</u>	<u>M</u>	<u>N</u>	<u>O</u>
1	- 6.87 [- 9.96]	-10.4 [-15.1]	-14.8 [-21.5]	-14.0 [-20.3]	-15.4 [-22.3]	-14.8 [-21.5]	-14.3 [-20.8]	-12.8 [-18.5]	-10.1 [-14.7]	- 5.0 [- 7.3]	- 3.4 [- 4.9]	8.41 [12.2]	21.3 [31.0]	21.6 [31.3]	17.7 [25.7]
2	- 6.69 [- 9.71]	-11.1 [-16.1]	-12.5 [-18.1]	-10.7 [-15.5]	-10.1 [-14.6]	- 8.34 [-12.1]	- 7.17 [-10.4]	- 6.5 [- 9.4]	- 4.4 [- 6.4]	- 0.41 [- 0.6]	4.1 [6.0]	6.96 [10.1]	10.6 [15.4]		
3	1.3 [1.9]	7.31 [10.6]	12.7 [18.4]	10.9 [15.8]	14.9 [21.6]	17.8 [25.8]	18.5 [26.9]	24.1 [35.0]	29.5 [42.8]	32.8 [47.6]	34.7 [50.4]	33.3 [48.3]	32.7 [47.4]		
4	0 [4.1]	2.8 [4.1]	6.96 [10.1]	10.6 [15.4]	13.8 [20.0]	15.9 [23.1]	17.7 [25.7]	20.2 [29.3]	22.6 [32.8]	24.6 [35.7]	26.9 [39.0]	26.4 [38.3]	27.0 [39.2]		
5	- 1.4 [- 2.0]	- 0.41 [- 0.6]	2.8 [4.0]	4.3 [6.3]	10.5 [15.3]	15.2 [22.0]	17.7 [25.6]	21.9 [31.8]	25.0 [36.3]	26.8 [38.8]	25.5 [37.0]	25.0 [36.3]	25.4 [36.8]		
6	0.07 [0.1]	1.65 [2.4]	4.55 [6.6]	8.07 [11.7]	11.3 [16.4]	13.8 [20.0]	11.4 [23.9]	18.0 [26.1]	20.1 [29.2]	21.9 [31.7]	22.8 [33.1]	22.8 [33.0]	22.8 [33.1]		
7	2.8 [0.4]	2.41 [3.5]	6.69 [9.7]	11.0 [15.9]	13.9 [20.2]	15.9 [23.0]	17.7 [25.7]	19.9 [28.8]	21.6 [31.4]	22.3 [32.3]	22.3 [32.4]	22.1 [32.0]	22.1 [32.0]		
8	1.44 [2.1]	4.55 [6.6]	8.34 [12.1]	11.8 [17.1]	13.9 [20.2]	15.5 [22.5]	17.0 [24.7]	18.3 [26.6]	19.4 [28.1]	16.5 [23.9]	20.4 [29.6]	20.4 [29.6]	20.7 [30.0]		

TABLE III – TRANSVERSE STRESS IN DOVETAIL
(Stresses in N/cm² [lbf/in.²] x 10⁻³)

See Figure 69 for identification

	<u>A</u>	<u>B</u>	<u>C</u>	<u>D</u>	<u>E</u>	<u>F</u>	<u>G</u>	<u>H</u>	<u>I</u>	<u>J</u>	<u>K</u>	<u>L</u>	<u>M</u>
1	-17.6 [-25.5]	-17.6 [-25.5]	-16.1 [-23.4]	-15.4 [-22.4]	-15.6 [-22.6]	-15.4 [-22.3]	-15.2 [-22.1]	-15.5 [-22.5]	-17.0 [-24.6]	-19.8 [-28.7]	-20.2 [-29.3]	-16.6 [-21.4]	- 5.45 [- 7.9]
2	-11.6 [-16.8]	-16.1 [-23.4]	-15.8 [-22.9]	-15.7 [-22.7]	-15.4 [-22.4]	-15.7 [-22.7]	-15.6 [-22.6]	-15.7 [-22.8]	-16.4 [-23.8]	-17.0 [-24.6]	-15.9 [-23.0]	-11.4 [-16.6]	- 6.27 [- 9.1]
3	- 7.45 [-10.8]	-10.2 [-14.8]	-12.8 [-18.6]	-14.1 [-20.4]	-14.3 [-20.8]	-14.8 [-21.4]	-14.6 [-21.2]	-14.8 [21.4]	-15.2 [-22.1]	-15.3 [-22.2]	-14.1 [-20.4]	-10.8 [-15.6]	- 5.93 [- 8.6]
4	- 7.10 [-10.3]	- 9.79 [-14.2]	-11.8 [-17.1]	-13.2 [-19.2]	-14.1 [-20.4]	-13.7 [-19.9]	-13.8 [-20.0]	-14.1 [20.4]	-13.7 [-19.8]	-12.6 [-18.3]	-11.4 [-16.5]	- 9.31 [-13.5]	- 6.07 [- 8.8]
5	- 5.65 [- 8.2]	- 8.55 [-12.4]	-10.8 [-15.7]	-12.7 [-18.4]	-12.3 [-17.9]	-12.5 [-18.2]	-12.8 [-18.5]	-13.1 [-19.0]	-12.8 [-18.6]	-11.5 [-16.7]	-10.5 [-15.3]	- 8.76 [-12.7]	- 6.07 [- 8.8]
6	-12.7 [- 8.4]	- 8.55 [-12.4]	-10.7 [-15.5]	-11.9 [-17.2]	-12.3 [-17.8]	-12.1 [-17.6]	-12.3 [-17.8]	-12.5 [-18.1]	- 7.03 [-10.2]	-10.5 [-15.2]	- 9.38 [-13.6]	- 8.14 [-11.2]	- 6.14 [- 8.9]
7	- 6.62 [- 9.6]	- 8.34 [-12.1]	-10.0 [-14.5]	-11.1 [-16.1]	-11.7 [-16.9]	-11.8 [-17.1]	-11.9 [-17.3]	-12.0 [-17.4]	-11.4 [-16.6]	10.2 [-14.8]	- 9.17 [-13.3]	- 7.93 [-11.5]	- 6.14 [- 8.9]
8	- 6.76 [- 9.8]	- 8.41 [-12.2]	-10.0 [-14.5]	-11.1 [-16.1]	-11.6 [-16.8]	-11.8 [-17.1]	-11.9 [-17.2]	-11.8 [-17.1]	-11.2 [-16.2]	-10.1 [-14.7]	- 9.10 [-13.2]	- 7.72 [-11.2]	- 6.14 [- 8.9]

TABLE IV – SHEAR STRESS IN DOVETAIL
(Stresses in N/cm^2 [lbf/in.^2] $\times 10^{-3}$)

See Figure 69 for identification

	<u>A</u>	<u>B</u>	<u>C</u>	<u>D</u>	<u>E</u>	<u>F</u>	<u>G</u>	<u>H</u>	<u>I</u>	<u>J</u>	<u>K</u>	<u>L</u>	<u>M</u>
1	0.896 [1.3]	2.42 [3.51]	2.76 [4.0]	0.676 [0.98]	-0.39 [-0.56]	-0.758 [-1.1]	-1.86 [-2.7]	-2.62 [-3.8]	-3.10 [-4.5]	-2.46 [-4.3]	-5.31 [-7.7]	-0.552 [-0.8]	2.07 [3.0]
2	-3.31 [-4.8]	-0.483 [-0.7]	1.45 [2.1]	0.552 [0.8]	~ -	0.276 [0.4]	-0.414 [-0.6]	-0.207 [-0.3]	1.10 [1.6]	2.21 [3.2]	-0.896 [-1.3]	2.34 [3.4]	3.59 [5.2]
3	-2.55 [-3.7]	-2.14 [-3.1]	-0.758 [-1.1]	-2.76 [-4.0]	-2.14 [-3.1]	1.72 [2.5]	3.24 [4.7]	-2.62 [-3.8]	-1.17 [-1.7]	0.689 [1.0]	-1.52 [-2.2]	2.00 [2.9]	2.90 [4.2]
4	-1.31 [-1.9]	0.552 [0.8]	0.689 [1.0]	-1.10 [-1.6]	-0.552 [-0.8]	0.138 [0.2]	-1.03 [-1.5]	-0.207 [-0.3]	1.17 [1.7]	2.14 [3.1]	-0.827 [-1.2]	1.03 [1.5]	1.59 [2.3]
5	0.621 [0.9]	-0.965 [-1.4]	-1.24 [-1.8]	2.83 [4.1]	-2.69 [-3.9]	-2.34 [-3.4]	-2.83 [-4.1]	-2.00 [-2.9]	-0.689 [-1.0]	0.483 [0.7]	-0.758 [-1.1]	0.689 [1.0]	1.10 [1.6]
6	-0.552 [-0.8]	-0.414 [-0.6]	0 -	-0.896 [-1.3]	-0.621 [-0.9]	-0.345 [-0.5]	-0.689 [-1.0]	-0.207 [-0.3]	0.483 [0.7]	0.965 [1.4]	-0.345 [-0.5]	0.345 [0.5]	0.552 [0.8]
7	-0.896 [-1.3]	-1.31 [-1.9]	-1.65 [-2.4]	-1.79 [-2.6]	-1.72 [-2.5]	-1.59 [-2.3]	1.52 [2.2]	-1.31 [-1.9]	-0.758 [-1.1]	-0.345 [-0.5]	0.276 [0.4]	0.138 [0.2]	0.276 [0.4]
8	-2.07 [-0.3]	-0.276 [-0.4]	-0.345 [-0.5]	-0.345 [-0.5]	-0.345 [-0.5]	-0.345 [-0.5]	-0.345 [-0.5]	-0.276 [-0.4]	-1.38 [-0.2]	-1.38 [-0.2]	-0.069 [-0.1]	0 -	0.069 [0.1]

The highest direct tensile stress calculated for the radial plies is $34,750 \text{ N/cm}^2$ [$50,400 \text{ lbm/in.}^2$], and in the $\pm 40^\circ$ plies it is $21,400 \text{ N/cm}^2$ [$31,000 \text{ lbm/in.}^2$]. The $\pm 40^\circ$ ply stress is of concern since it is 77.5% of the tensile strength using the ideal (solid line) curve of Figure 42. It is, however, a local stress attributable to shear lag with large stress gradients. This material can therefore be expected to yield sufficiently in this region to redistribute the load.

The peak stress is $20,200 \text{ N/cm}^2$ [$29,300 \text{ lbm/in.}^2$] (compressive) and should not present a problem.

The calculated peak bond shear stress is $5,300 \text{ N/cm}^2$ [$7,700 \text{ lbm/in.}^2$] between the $\pm 40^\circ$ plies and the titanium pad. This peak stress is due to shear lag and cannot be evaluated directly because available test data are related to the average stress over a bonded surface. Figure 68 shows selected average shear stresses over areas where direction of the shear stress is essentially constant (i.e., over the full wedge surface in the case of the core plies and over the upper portion of the titanium pad in the case of the shell plies). These average values are consistent with P&WA experience. In addition, TRW has developed a bond system (Kerimid 501) capable of developing $1,380 \text{ N/cm}^2$ [$2,000 \text{ lbm/in.}^2$] in sandwich specimens. The TRW experiments did not employ transverse loading. All bond surfaces in the present design have transverse stresses of about $13,800 \text{ N/cm}^2$ [$20,000 \text{ lbm/in.}^2$] which should help significantly.

STAGE VIBRATION

Rotor Vibration

Even when advanced composite materials are used, the first bending resonance by second order engine excitation (2E) is unavoidable with fan blades of moderate size with a dovetail attachment and no shrouds. Elimination of the shroud reduces the bending frequency more than is compensated by the high modulus-to-density ratio of advanced composites. As a result, the composite fibers must be oriented and distributed so as to reduce first bending frequency to a level where the 2E excitation is reasonably safe.

The blade frequencies were calculated by assuming that the blade is a beam with unwrapped cross sections. Equivalent section properties of the composite sections were generated and used in a vibration program which considered bending and torsion modes to be uncoupled. Simultaneously, calculations were made of the frequencies of an isotropic blade, taking into account torsion-bending coupling and the offsets of the centroids of the actual blade sections from the radial stacking line. These calculations provided factors by which the composite blade results could be modified to represent true geometric conditions.

A Campbell diagram is presented in Figure 70 for the coupled blade-disk system. By proper ply-orientation and core-to-shell sizing, the blade-disk system was tuned to avoid critical resonances in the operating range. The first coupled bending mode 2E resonance is at 65 percent of design speed and the second bending mode 4E resonance is at 117 percent speed. The first torsional mode 3E resonance is at 117 percent of design speed, and the 4E resonance is at 86 percent design speed.

Figure 71 shows the tip chordwise bending mode resonance diagram for the first two modes. Vane passing order (60E) will not excite the first or second tip modes.

Rotor Blade Flutter

In addition to avoiding critical resonances, bending and torsion frequencies were kept high enough to achieve adequate bending and torsional stall flutter parameters. Reduced velocity parameters were calculated and compared with successful experience. The value of the reduced velocity parameter is 2.7 for bending and 1.2 for torsion; both are within the successful (no flutter) area determined through experience. Figure 70 shows the calculation.

The reduced velocity parameter for tip mode flutter is 5.3 which is consistent with successful (no flutter) experience. Two cross-ply (75° orientation) are required at the tip to reduce the tip mode flutter parameter to the level of comparable successful experience. Figure 71 shows the calculation of the tip mode parameter.

Stator Vane Vibration

Stator vane bending and torsion frequencies were calculated considering: a) the coupling between bending and torsion modes and b) the complete variable-vane system-vane, rotation spindle, and actuation arm. As shown in Figure 72, stator vane first bending and first torsional frequencies will not be excited by blade passing order (19E) in the operating range. The first torsion mode 4E resonance is at 83 percent speed; however, there is no anticipated source of 4E resonance. The second or third torsion could be excited by the fan rotor passing order (19E). But these modes are not expected to be easily excited, and the resonances occur low in the operating speed range (at or below 75 percent speed).

Stator Vane Flutter

Reduced velocity flutter parameters were calculated and compared with correlated test data. The definition and method of calculation are shown on Figure 72. The value of the reduced velocity parameter for bending flutter is 1.55 and for torsional flutter is 1.59; both are within the successful (no flutter) area determined through experience.

Stator Vane Stresses

The stator stresses due to air loads were calculated by assuming the stator to be simply supported at the ID and OD. The maximum stress was 5,200 N/cm² [7,500 lbf/in.²] at ambient inlet pressure. At the supported ends, the airfoil overhangs the button at the leading and trailing edge. In particular the variable spindle at the OD may be tight enough in its bushing to provide end fixity for the vane, and the stress at the junction of the vane and button, therefore, is of concern. Assuming the vane is fixed-fixed, the air-load moment of 6.04 m-N [53.5 in.-lbf] about the minor axis of the vane and 1.76 m-N [15.6 in.-lbf] about the major axis at the OD. Considering only the section of the vane covered by the button, the maximum stress due to these moments is 7,900 N/cm² [11,500 lbf/in.²].

The vane material is MAS 5613 stainless steel having a yield stress of 80,000 N/cm² [116,000 lbf/in.²] at the estimated metal temperature of 149°C [300°F]. The nominal stresses are substantially below this value and no problem is anticipated.

CRITICAL SPEED

Stiff bearing critical speed is a basic P&WA criterion which P&WA requires to be as high as practical, preferably 25 to 35 percent above maximum operating speed. This is done to ensure that critical speeds in the operating range as a consequence of bearing support flexibility in conjunction with rotor flexibility have a high percentage of the total strain energy of the vibration system in the stationary components. As a result, structural damping is maximized and the critical speeds are tolerable. This criterion also ensures that at a critical speed the relative whirl between rotor and case is minimum, thus assisting in maintaining tip clearance.

For the subject rotor, the stiff bearing critical speed is at 15,400 rpm (101 percent speed). Although this is lower than had been desired, the dynamics of the system can be shown to be satisfactory. The mode-shape is shown in Figure 73. A model of the entire dynamic system used in the frame and rotor critical speed analyses is presented in Figure 74. The linear and torsional spring constants of the bearing supports are also shown.

Frame and rotor calculations were made up to 20,000 rpm (25 percent above maximum speed) to allow for the normal inaccuracy in calculating these complex modes. Table V lists the calculated criticals and information on the percentage of total strain energy in the rotor. Figures 75 through 79 show the mode shapes of the criticals that have significant motion of the fan rotor. The mode shapes and criticals are very similar to those obtained in the reference 3 fan. In particular, the critical at 11,480 rpm (76 percent speed) has 31 percent of the total strain energy in the rotor.

Pratt & Whitney Aircraft normally provides a bearing damper where there is a critical speed in the operating range having more than 25 percent strain energy in the rotating components. Therefore, a series of forced response analyses were conducted on the system, both with and without a damper at the front bearing and with unbalances at the rotor and at the flexible diaphragm behind the No. 2 bearing.

Figures 80 and 81 show the results of the forced response calculations. In the first figure, the response of the rotor to 0.706 N-cm [1 oz-in.] unbalance in its own plane is shown as a function of speed both with and without a damper at the front bearing. In the case without the damper, values of structural damping coefficients were used that are consistent with typical P&WA experience. These values are shown in Figure 73. The damping coefficient and damper spring rate were calculated based on geometry, clearance, and viscosity of the lubricant. The nonlinear characteristics of the damper were recognized in the calculation. The rotor would be balanced to better than 0.035 N-cm [0.05 oz-in.], but development of some additional unbalance during running must be assumed. A factor of five (for an operating unbalance of 0.883 N-cm [1.25 oz-in.]) is a reasonable assumption.

Figure 80 indicates, therefore, that without a damper at the front bearing the amplitude of the fan rotor due to an unbalance of 0.883 N-cm [1.25 oz-in.] in its plane would be 0.0750 mm [six mils] at the critical speed at 11,480 rpm, 0.0127 mm [0.5 mils] at 12,300 rpm, 0.0635 mm [2.5 mils] at the critical now estimated to occur at 116 percent speed. The addition of the damper would reduce these amplitudes to 0.0190, 0.0127, and 0.00444 mm [0.75, 0.5, & 0.175 mils], respectively. At the highest critical speed, the damper would reduce the amplitude at the diaphragm coupling from 0.108 to 0.0318 mm [4.25 to 1.25 mils].

The values of response without the damper are relatively high (0.610 mm [24 mils] at the rotor for 0.706 N-cm [1 oz-in.] unbalance at the lowest critical). Providing a damper in such a sensitive system is desirable. The damper would reduce this sensitivity to 0.108 mm per N-cm [3 mils per oz-in.], a much more reasonable value. For these reasons, the damper should be used in the rig.

Figure 81 shows the effect of unbalance in the plane of the diaphragm. Significant unbalance at this location is not expected, and the figure is mainly of interest to indicate the potential of balancing at this plane. A study of the figure shows that without a damper a 0.706N-cm [1 oz-in.] unbalance at the diaphragm would reduce the amplitude of the rotor by 0.432 mm [17 mils] at 11,480 rpm, 0.559 mm [2.2 mils] at 12,300 rpm, and 0.432 mm [17 mils] at 17,700 rpm. The corresponding values are 0.0127, 0.0114, and 0.127 mm [0.5, 0.45, & 5 mils] with a damper. These figures indicate good balancing potential at the highest critical, even in a damped system.

TABLE V – STRAIN ENERGY PERCENT FOR CALCULATED ROTOR CRITICALS

<u>Critical Speed (rpm)</u>	<u>Mode</u>	<u>Strain Energy (%)</u>			
		<u>Fan Rotor</u>	<u>Drive Shaft</u>	<u>Turboshaft</u>	<u>Total Rotor</u>
596	Mount	0	0.6	0	0.6
4,452	— —	0	1.6	0.2	1.8
5,540	OD Case	0.2	0.2	0	0.4
11,482	Fan Rotor	30.2	1.0	0	31.2
12,268	Inlet Fairing	9.6	0.3	0	9.9
17,685	Drive Shaft	10.2	15.1	3.6	28.9
18,435	OD Case	4.8	2.5	1.6	8.9
19,654	Drive Shaft	7.2	13.3	3.1	23.6

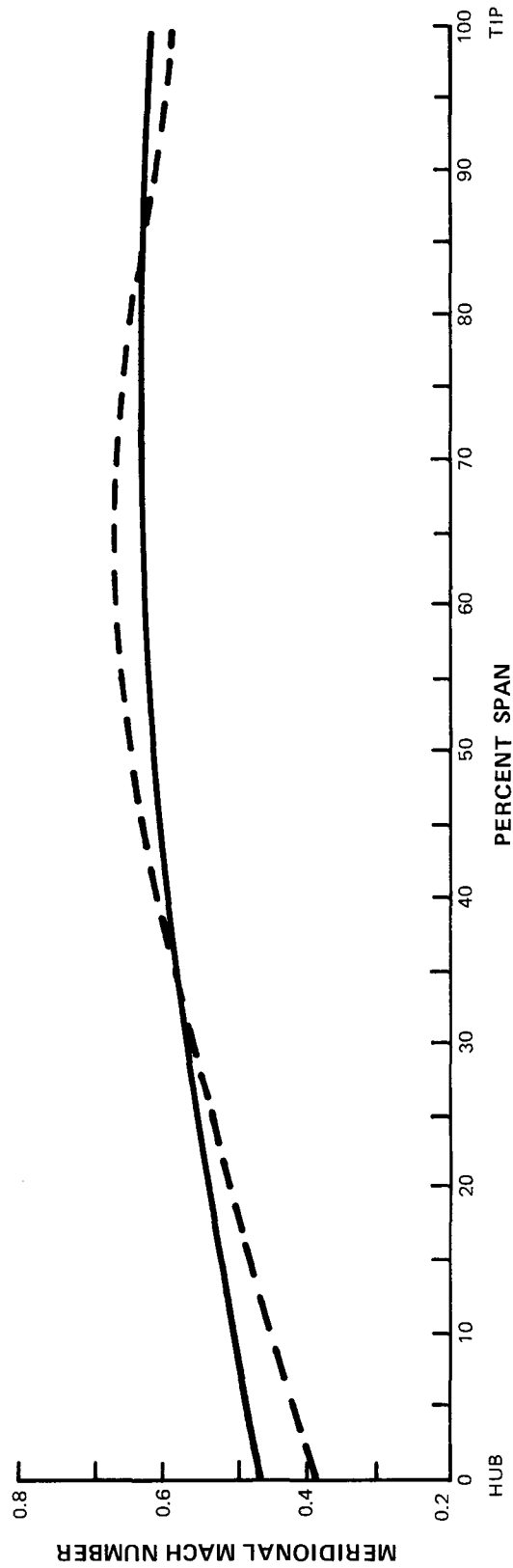


Figure 1 Comparison of Design Spanwise Profiles of Rotor Inlet Meridional Mach Number – Solid line curve shows profile for the 670.6 m/sec [2200 ft/sec] tip speed fan, and broken line curve shows profile for the 548.6 m/sec [1800 ft/sec] fan.

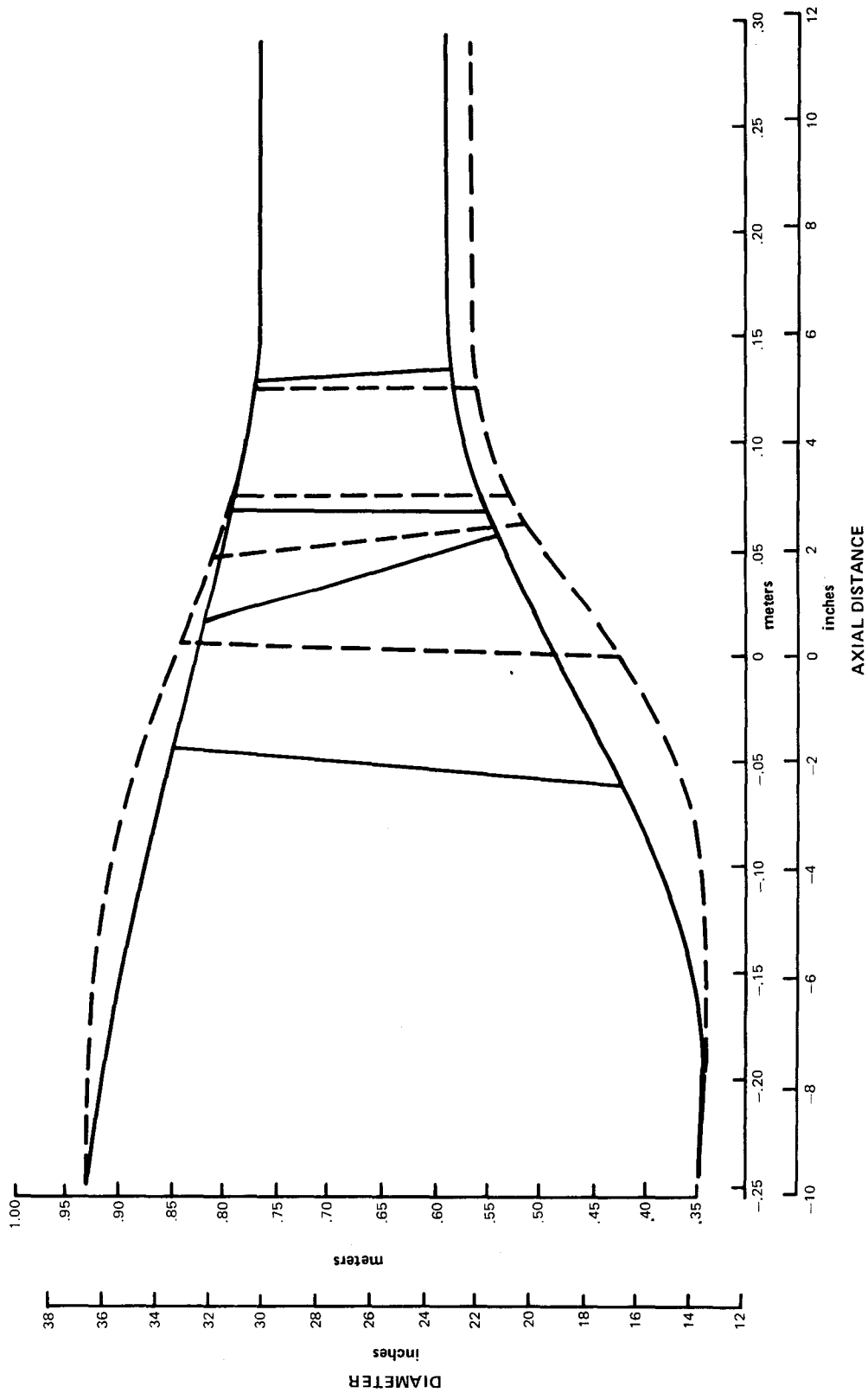


Figure 2 Comparison of Design Flowpaths -- Solid lines show flowpath of 670.6 m/sec [2200 ft/sec] tip speed fan, and broken lines show flowpath of 548.6 m/sec [1800 ft/sec] fan.

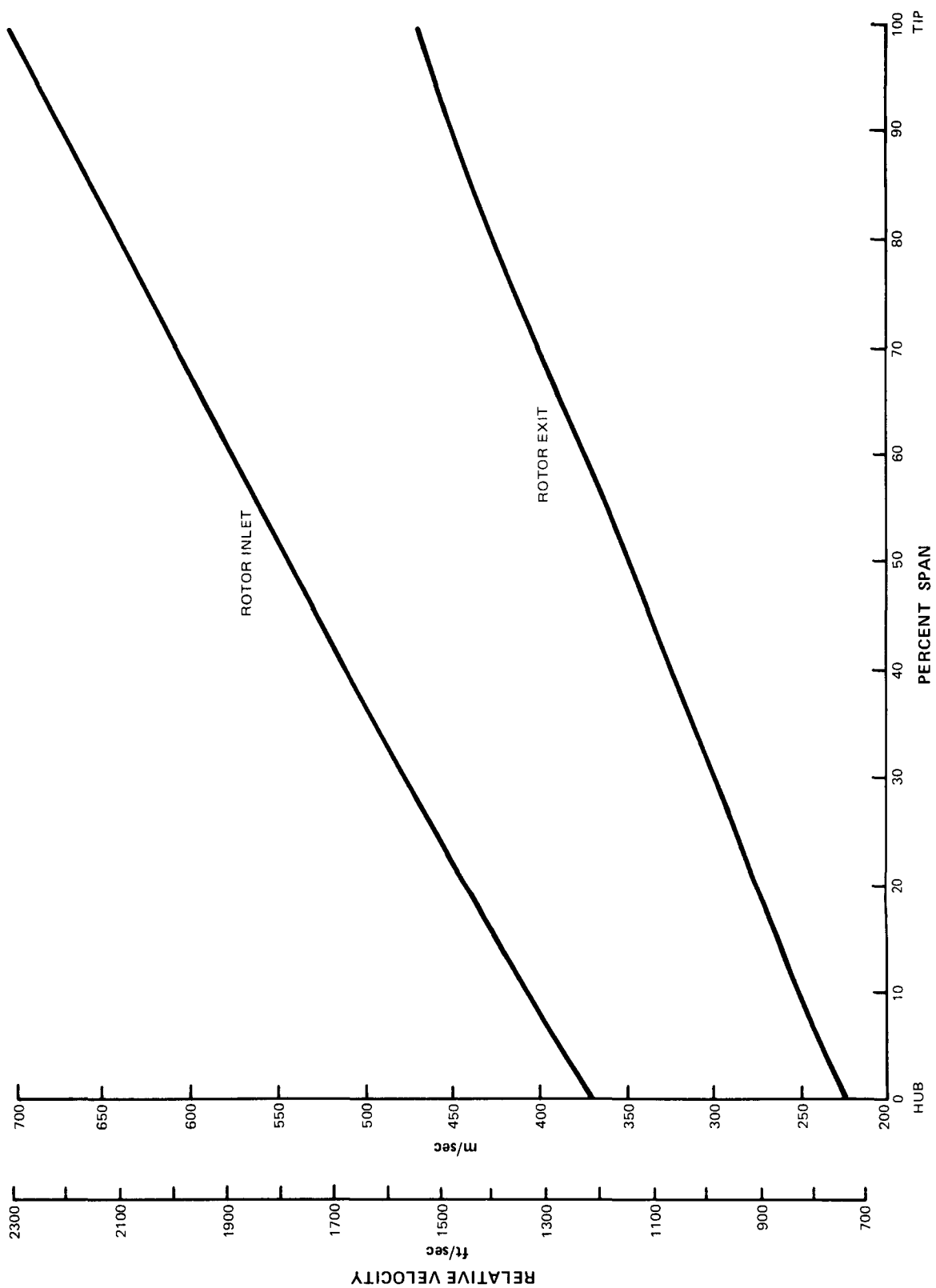


Figure 3 Relative Velocity at Rotor Inlet and Exit as a Function of Span

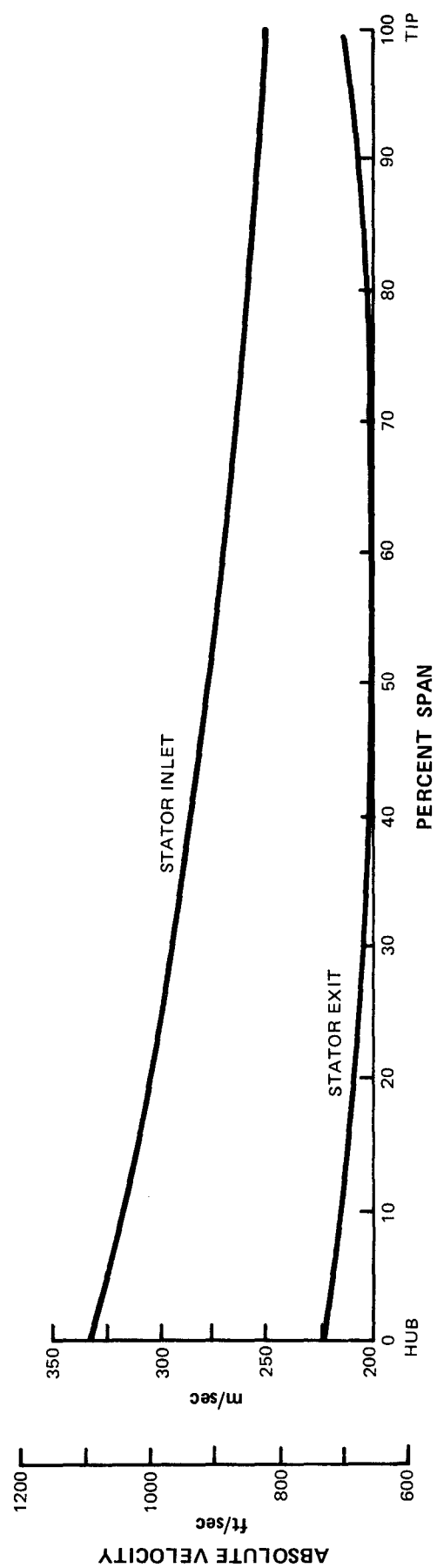


Figure 4 Absolute Velocity at Stator Inlet and Exit as a Function of Span

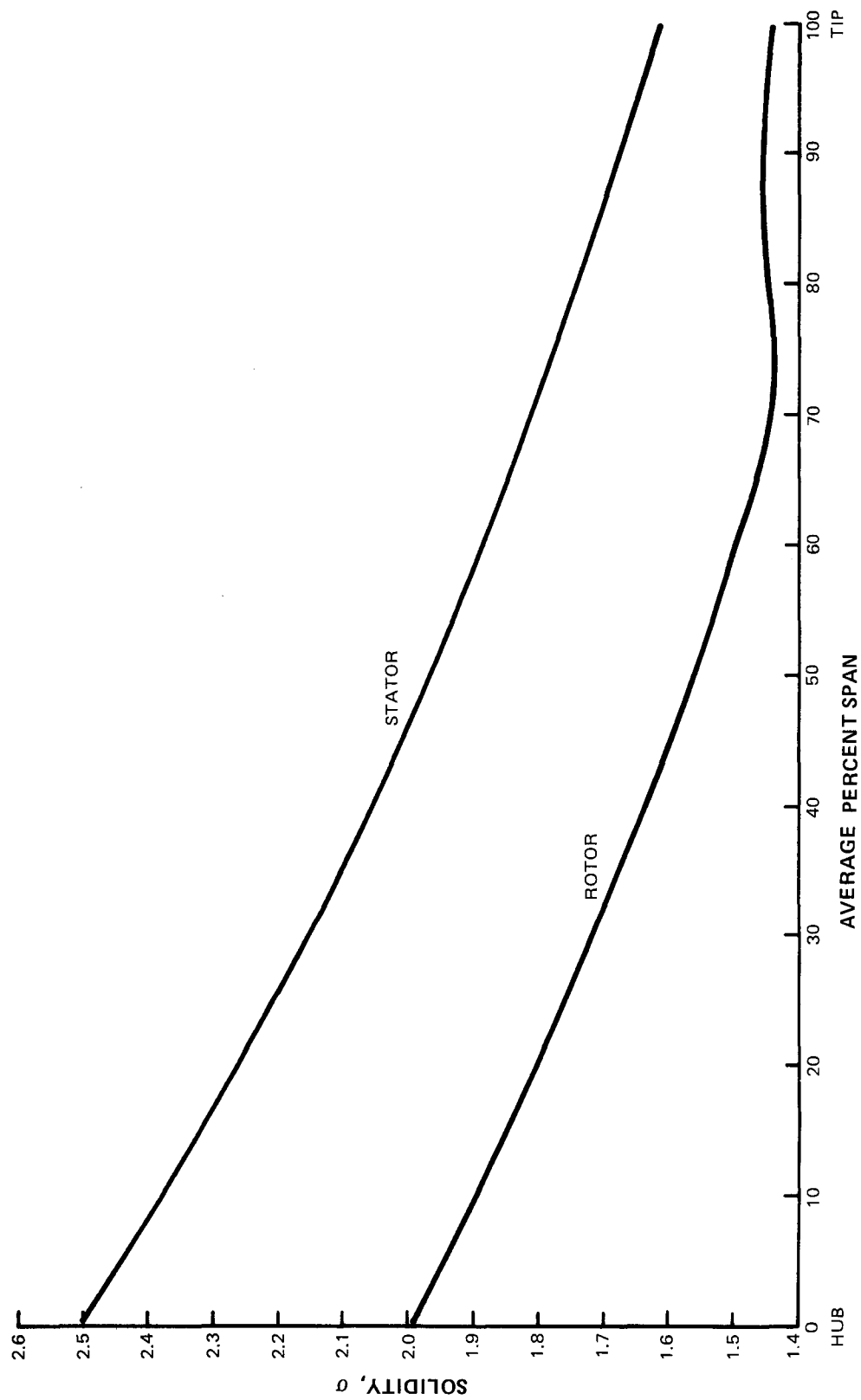


Figure 5 Rotor and Stator Solidity as a Function of Span

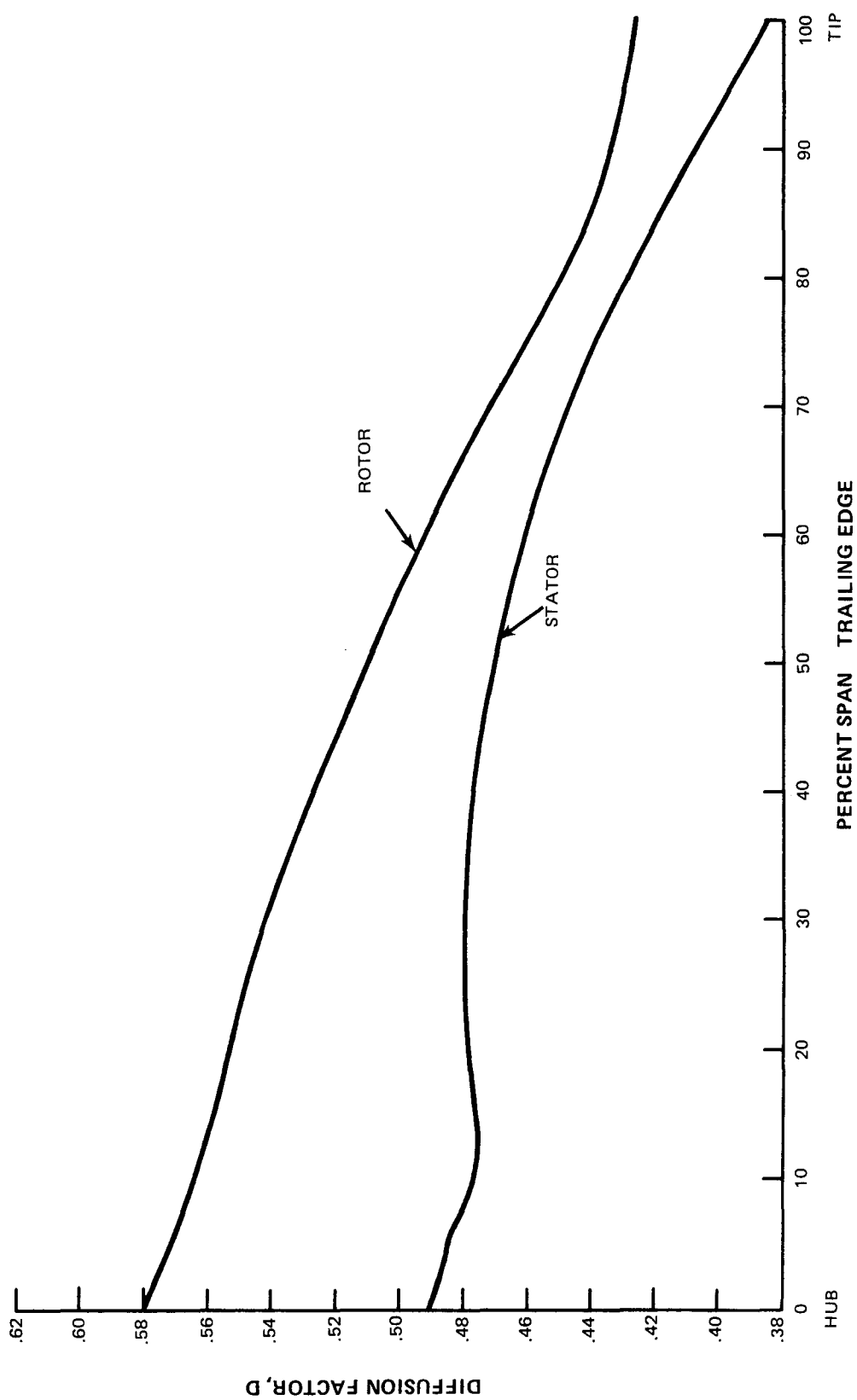


Figure 6 Rotor and Stator Diffusion Factor as a Function of Span

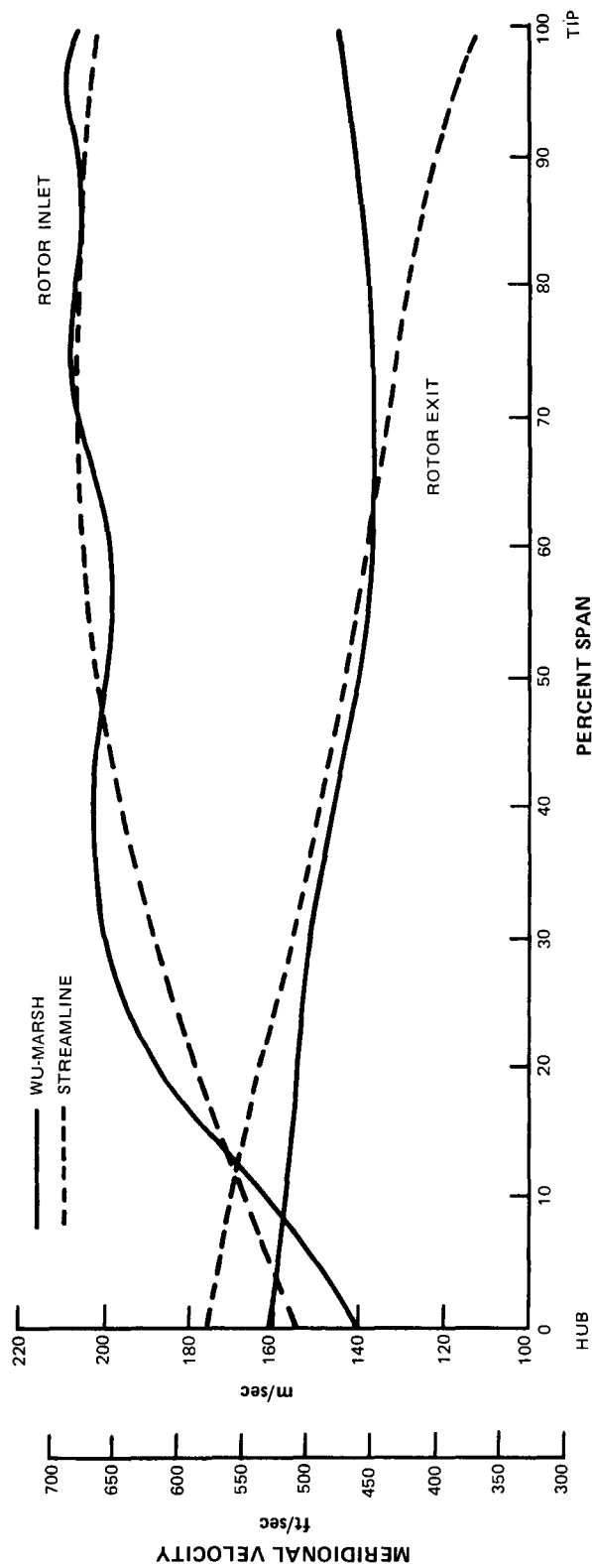


Figure 7 Rotor Inlet and Exit Meridional Velocity as a Function of Span

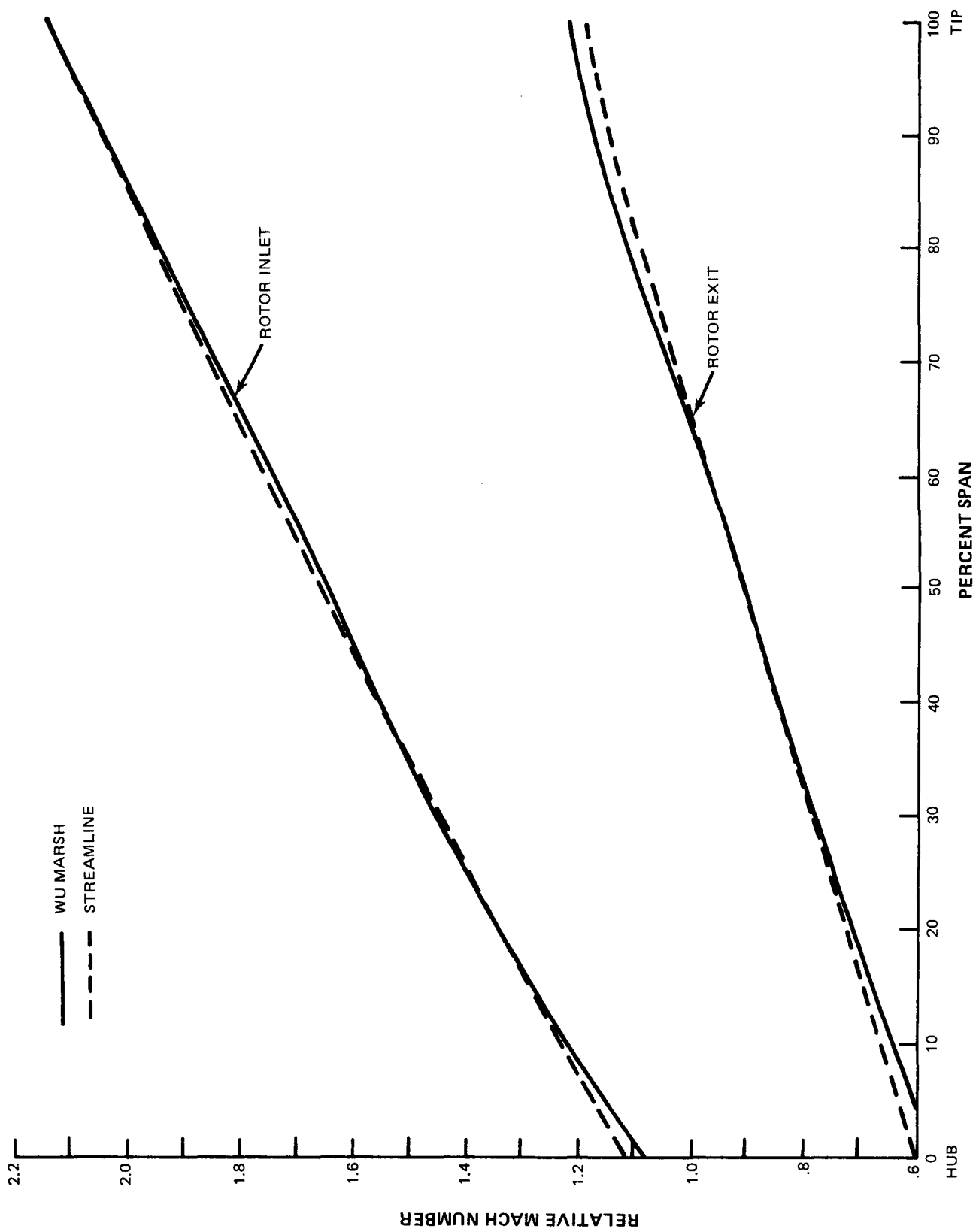


Figure 8 Rotor Inlet and Exit Relative Mach Number as a Function of Span

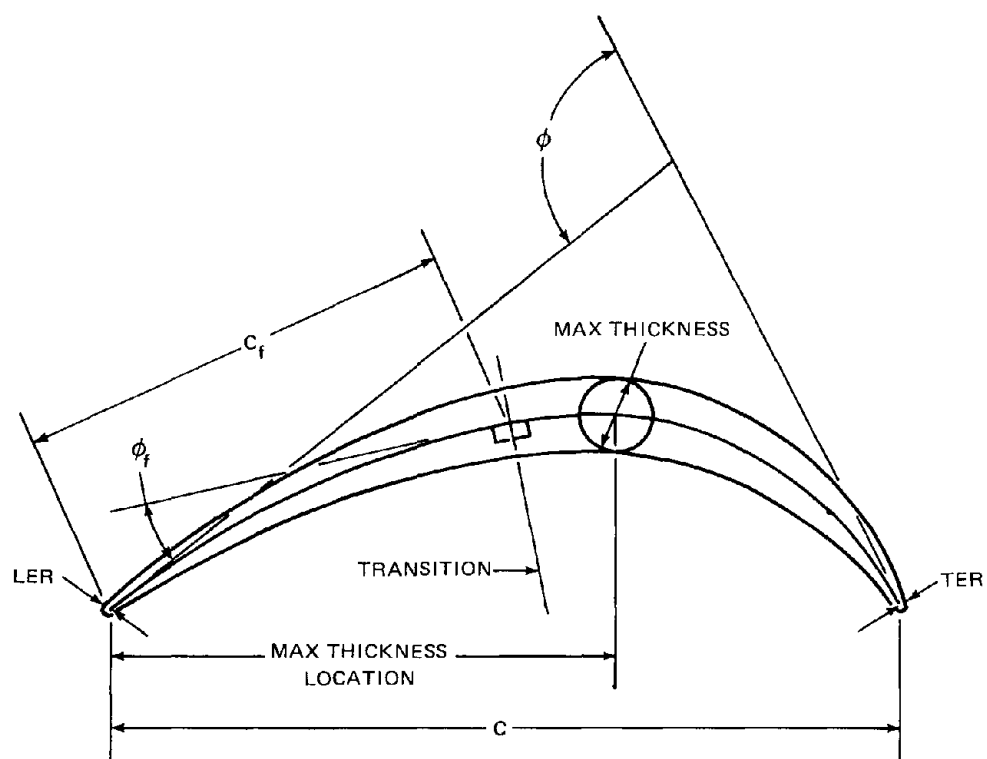


Figure 9 Multiple-Circular-Arc Airfoil Definition

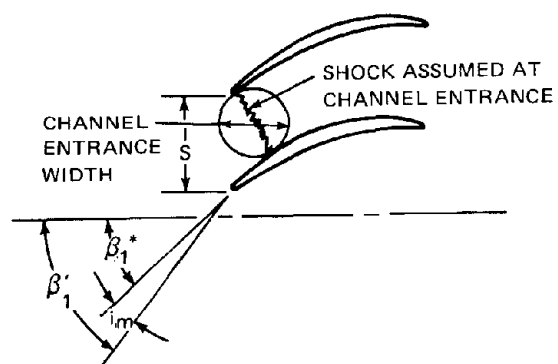


Figure 10 Multiple-Circular-Arc Airfoil Cascade Relationships

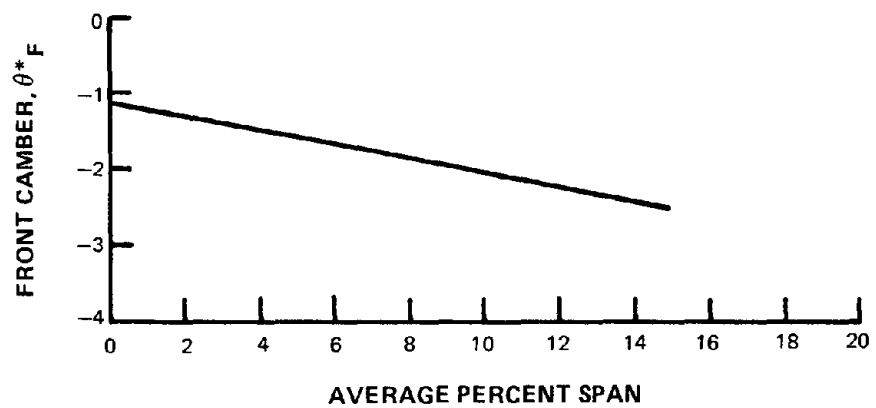
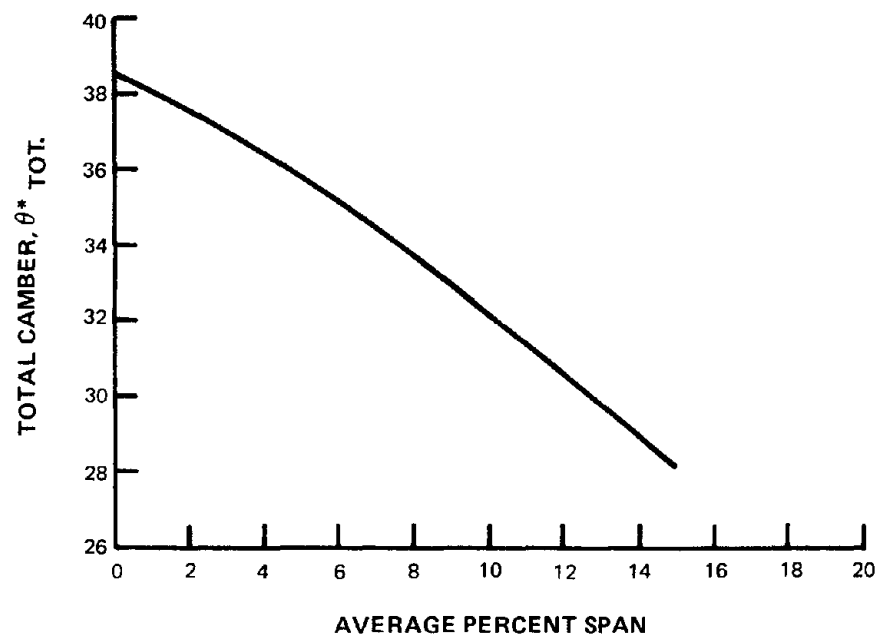


Figure 11 Rotor Front and Total Camber Distribution for MCA Portion of Span

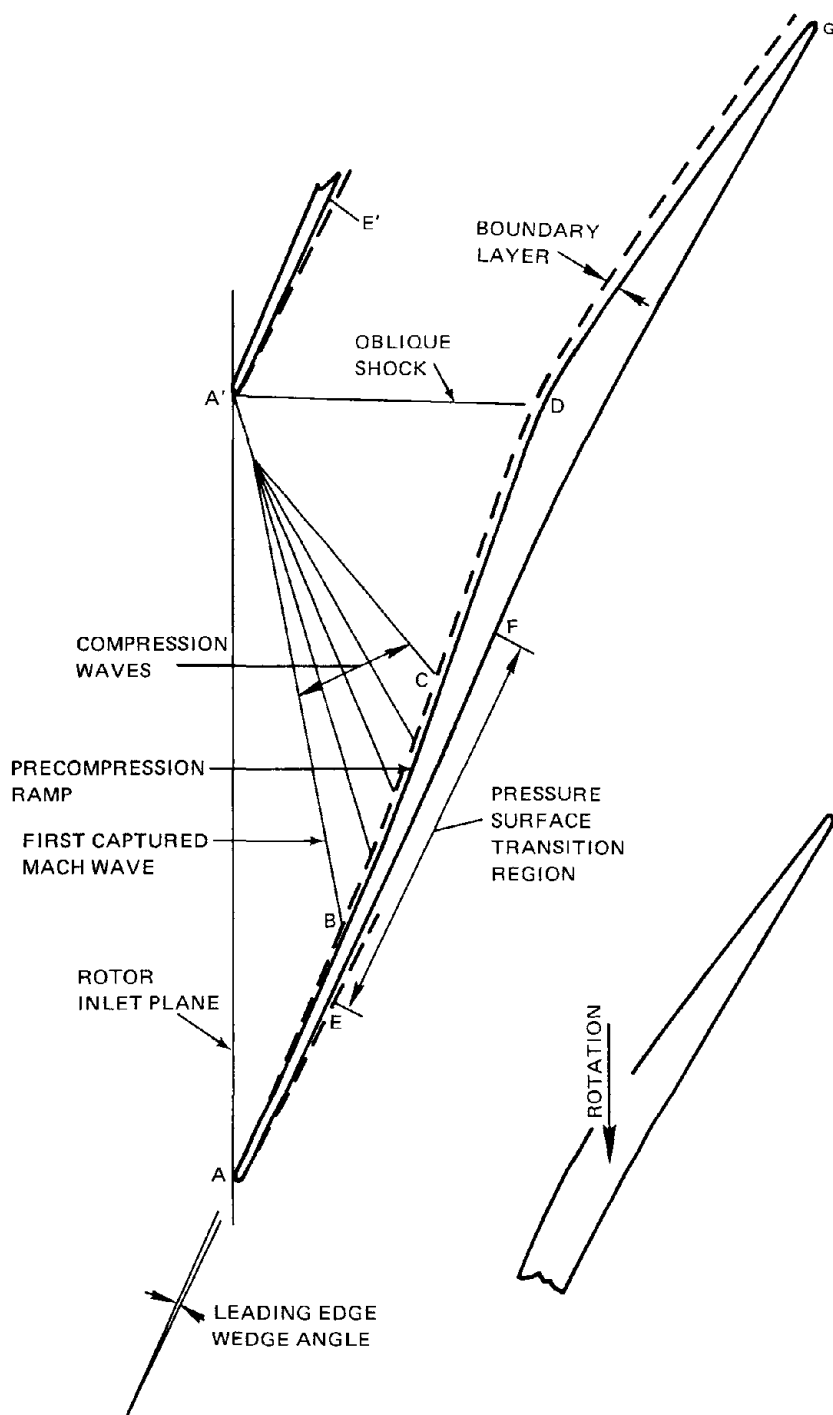


Figure 12 One-Shock Precompression Airfoil Terminology

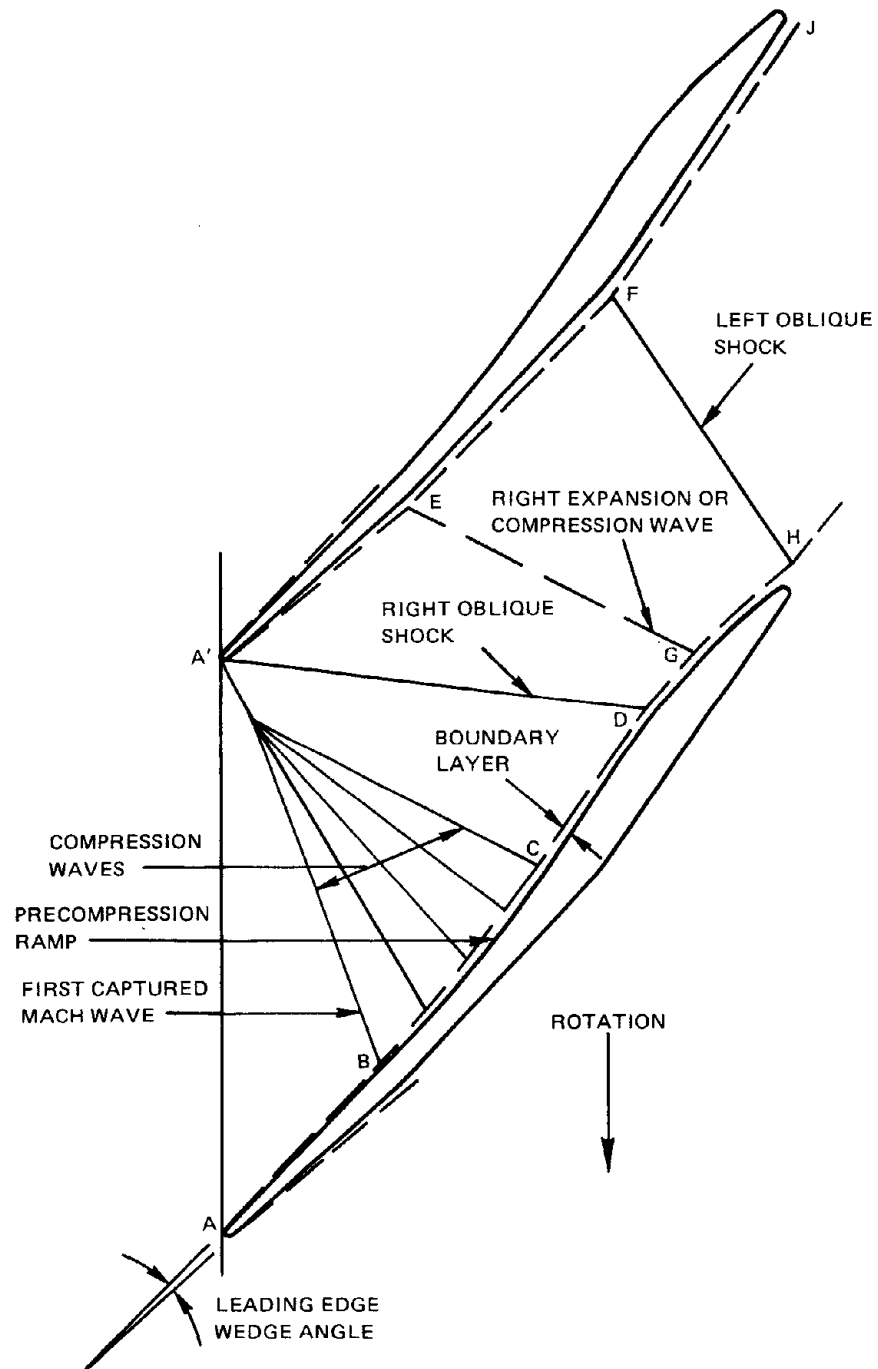


Figure 13 Two-Shock Precompression Airfoil Terminology

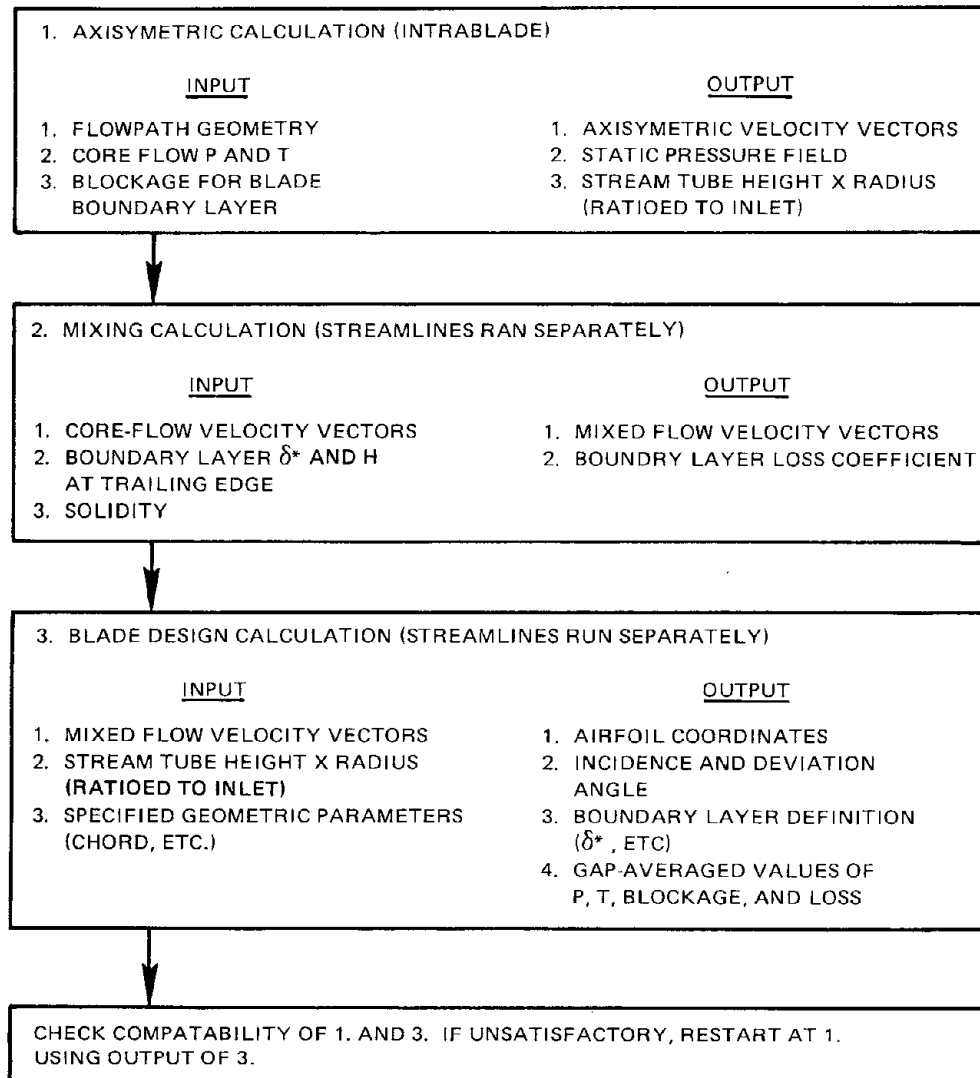


Figure 14 General Design Procedure

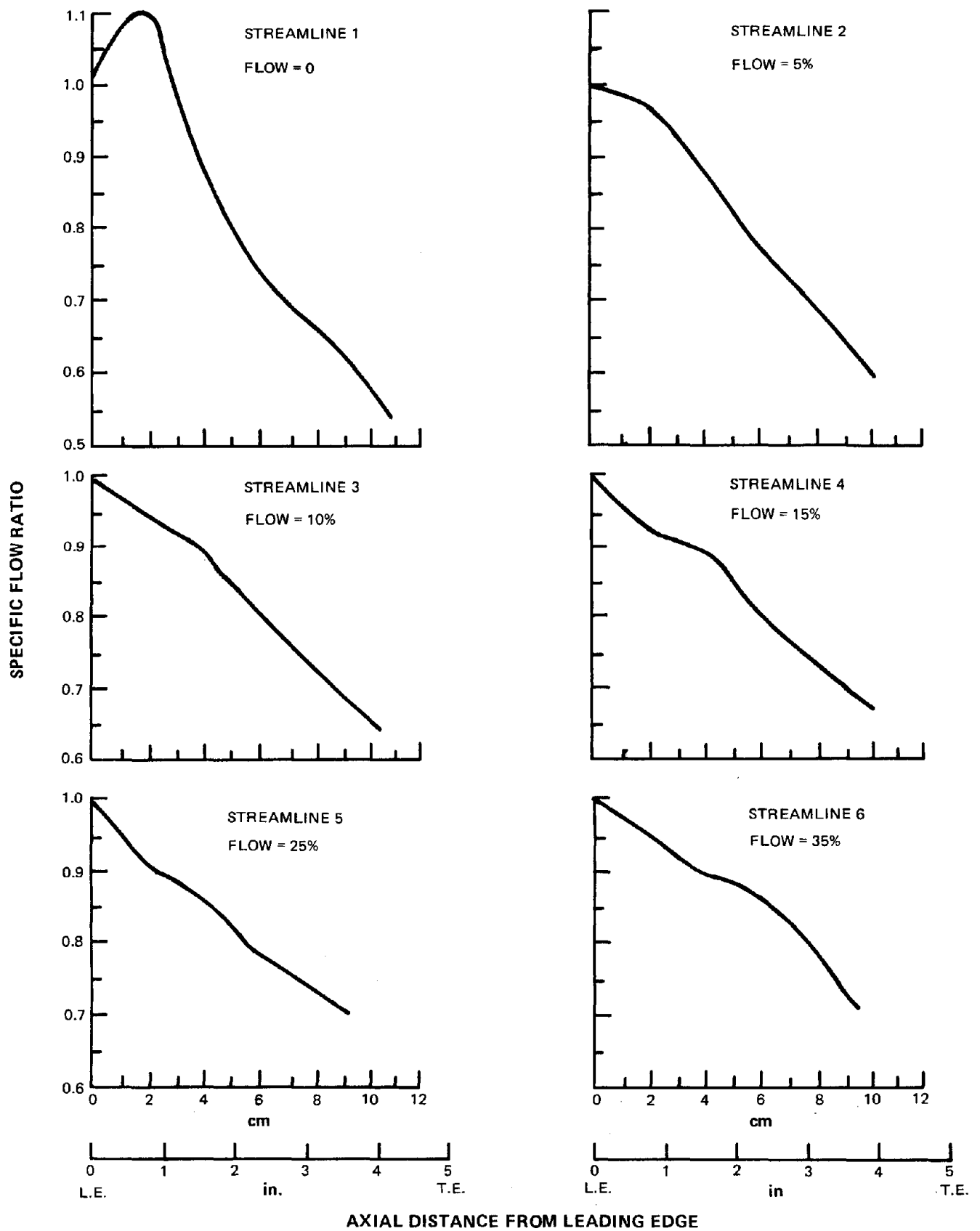


Figure 15 Axial Distribution of Specific Flow Ratio for Design Streamlines

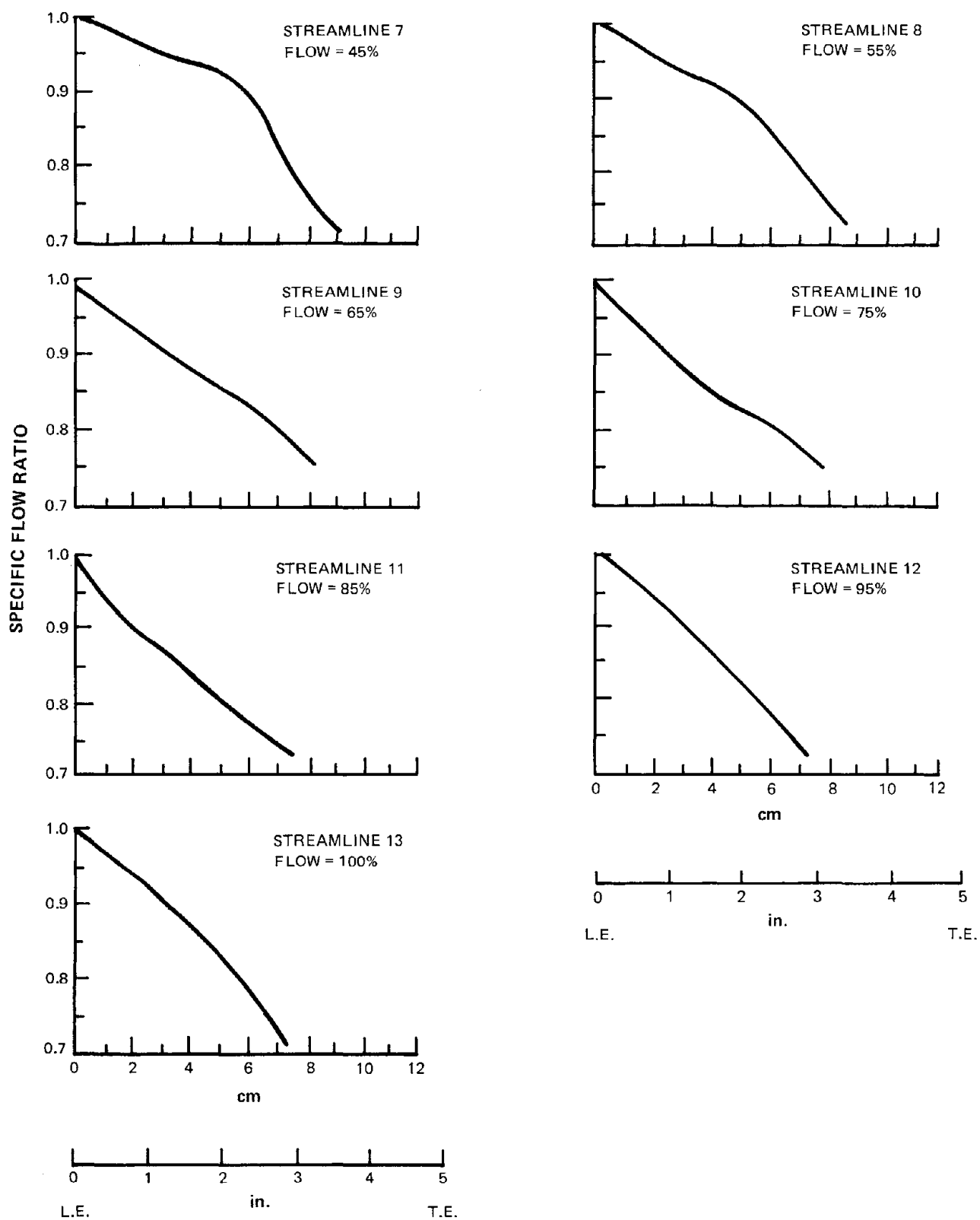


Figure 15 (Cont'd) Axial Distribution of Specific Flow Ratio for Design Streamlines

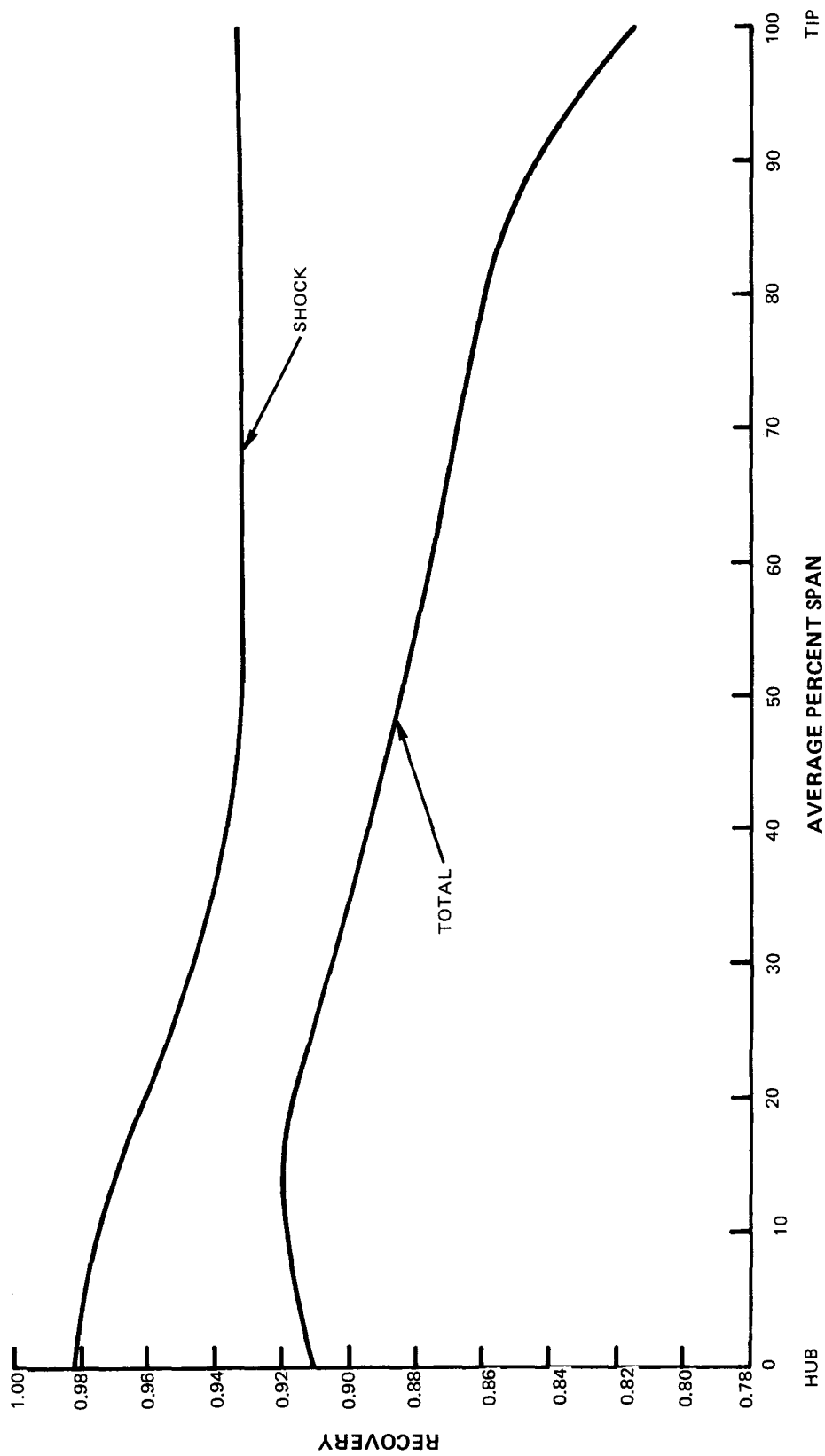


Figure 16 Spanwise Distribution of Shock and Total Recovery for the Rotor

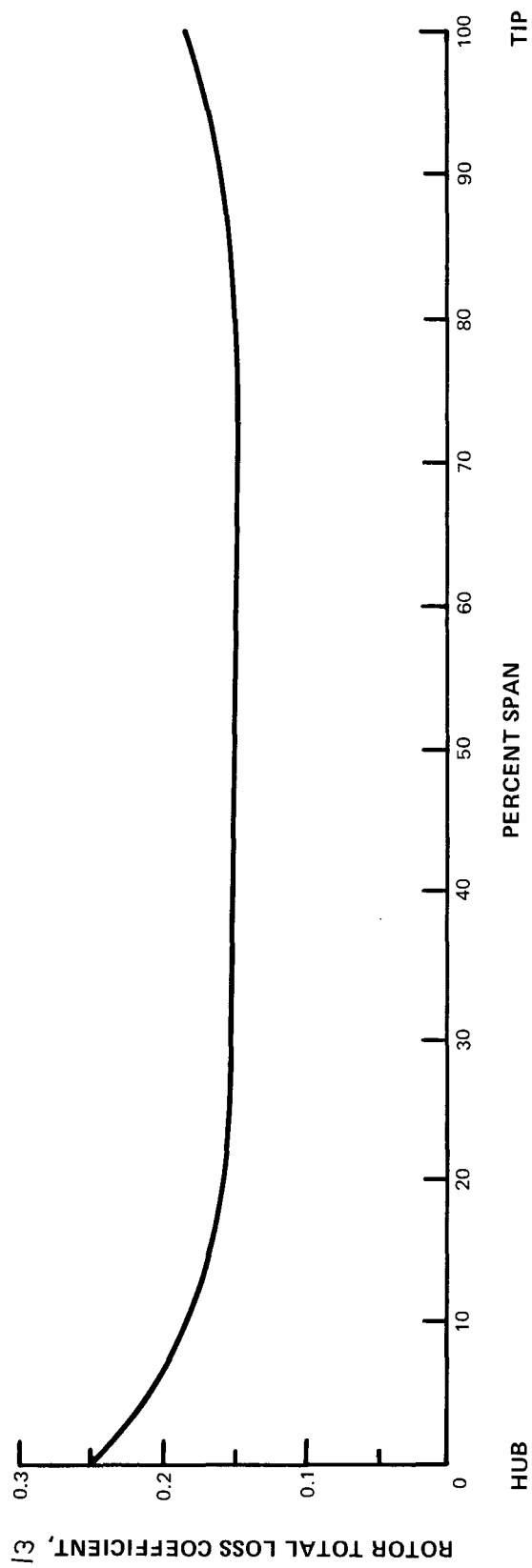


Figure 17 Spanwise Distribution of Rotor Total Loss Coefficient

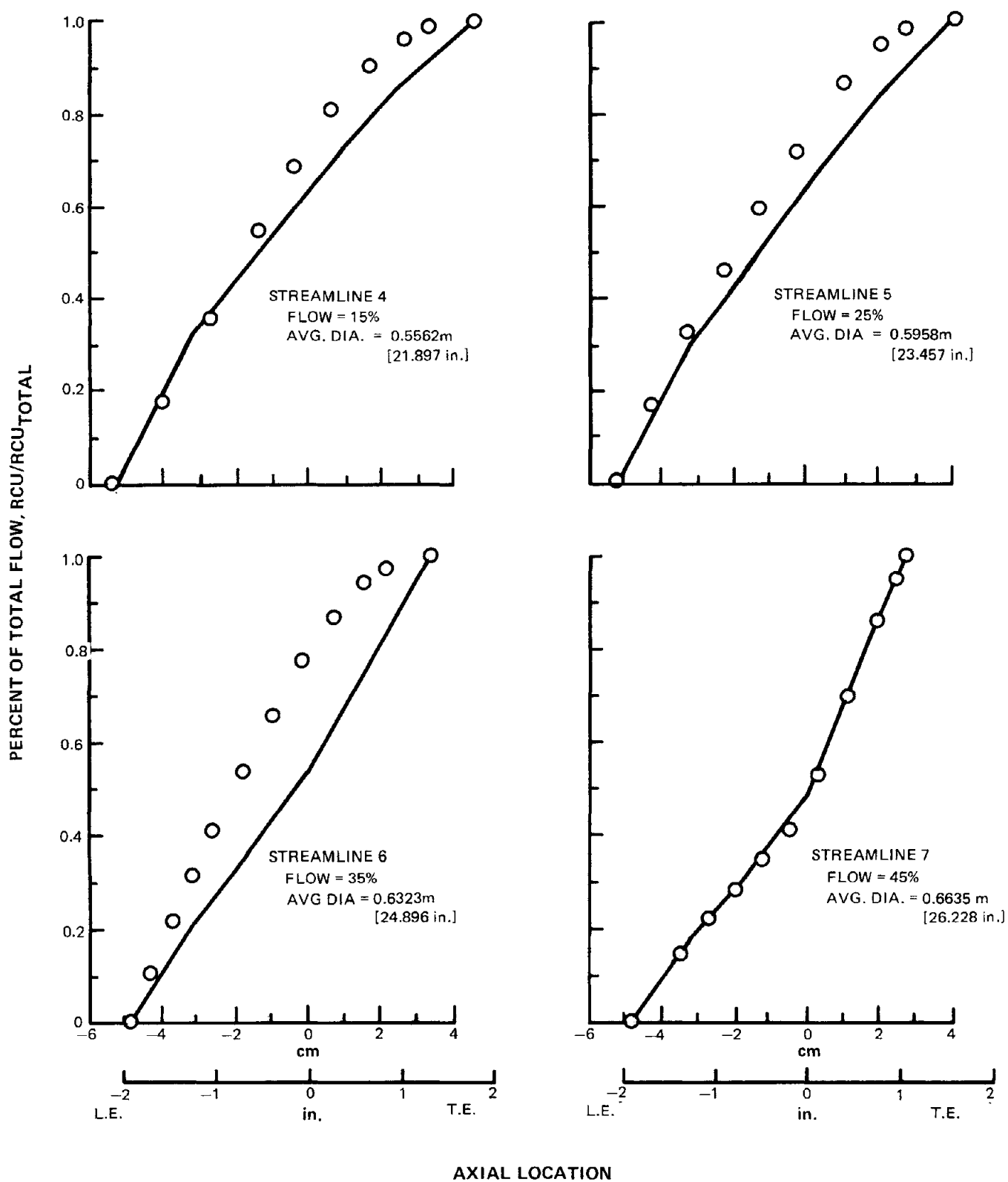


Figure 18 Axial Work Distribution for Design Streamlines. Curve shows Wu-Marsh, and circles indicate blade program values.

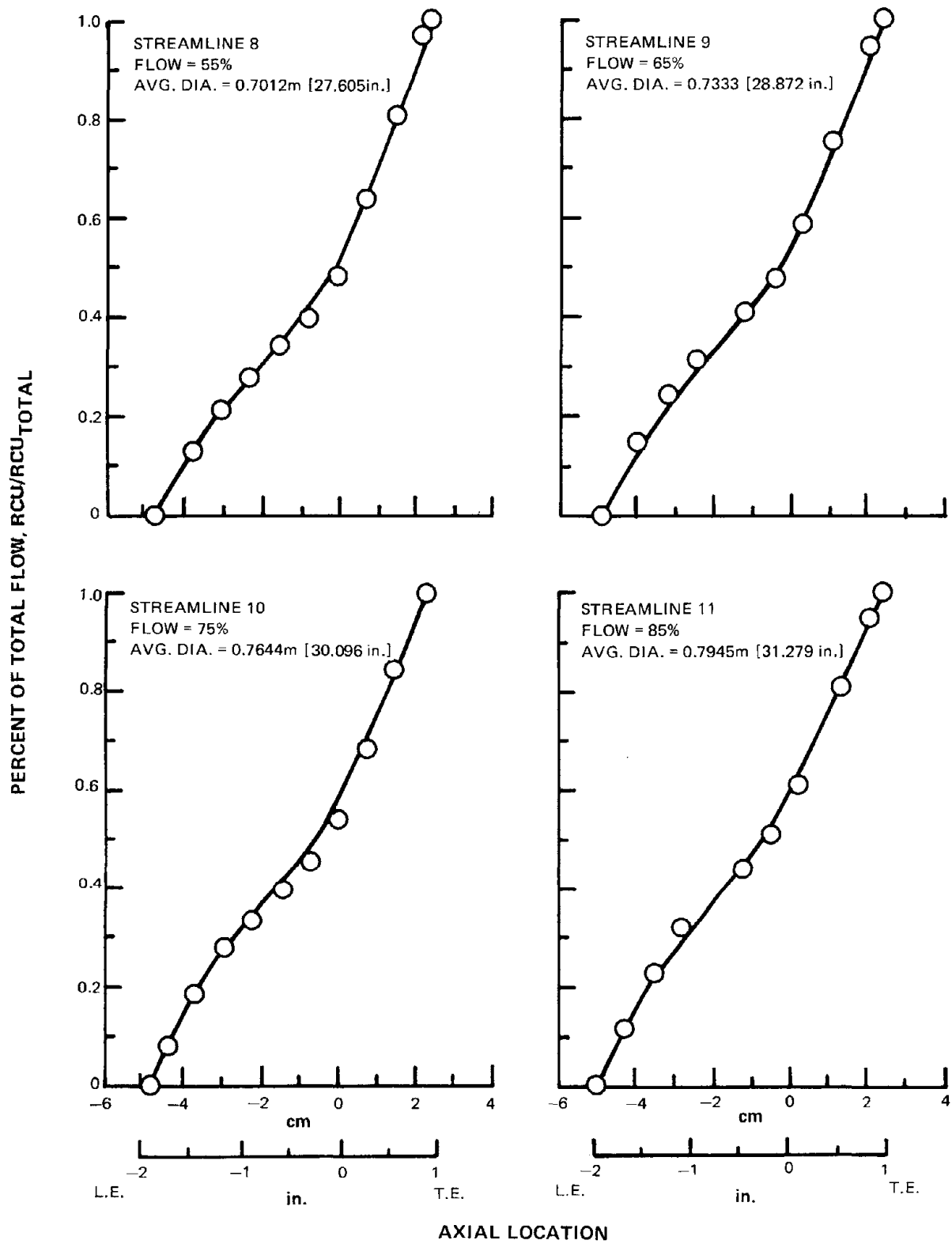


Figure 18 (Cont'd) Axial Work Distributions for Design Streamlines. Curve shows Wu-Marsh, and circles indicate blade values (metal + blade boundary + endwall blockage).

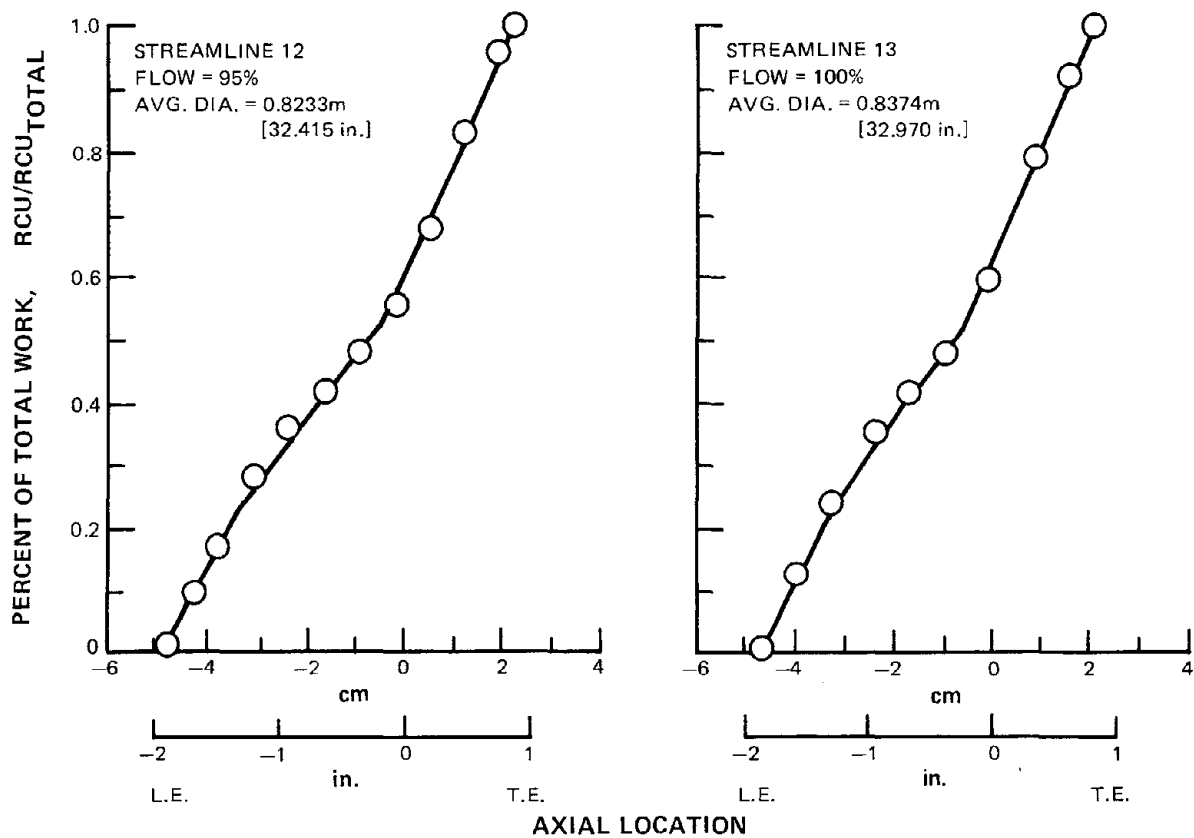


Figure 18 (Cont'd) Axial Work Distributions for Design Streamlines. Curve shows Wu-Marsh, and circles indicate blade values (metal + blade boundary + endwall blockage).

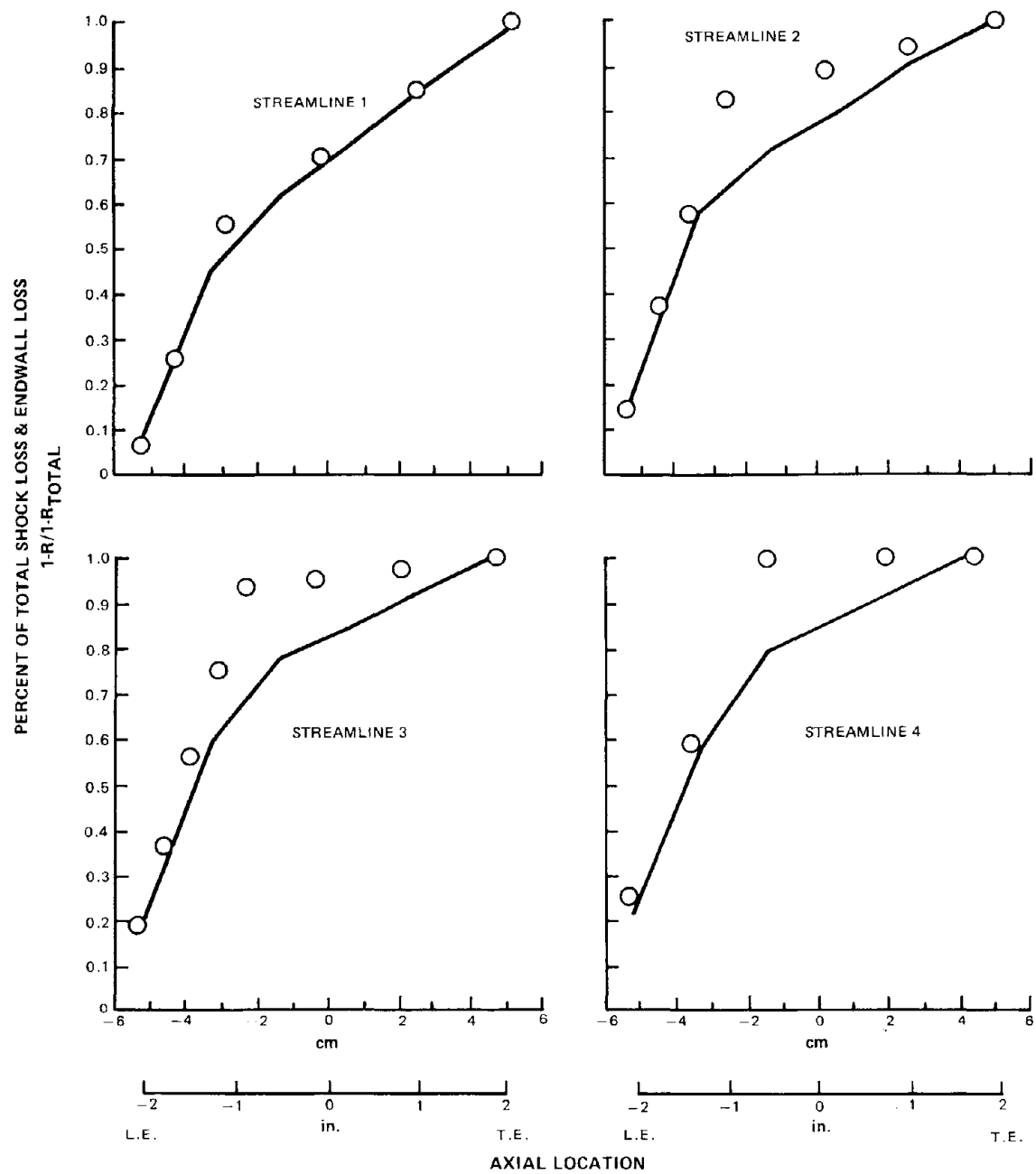


Figure 19 Axial Loss Distributions for Design Streamlines

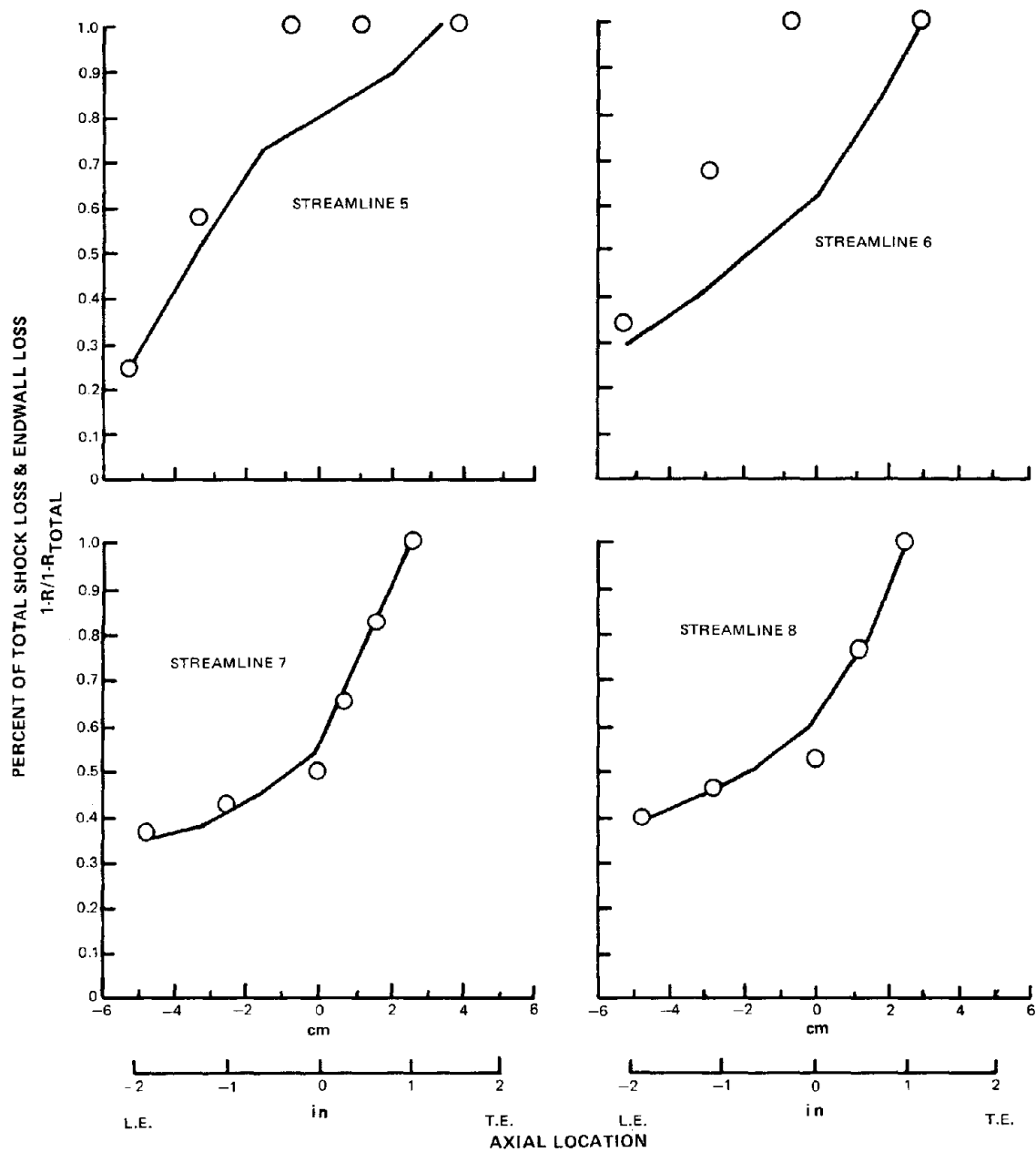


Figure 19 (Cont'd) Axial Loss Distributions for Design Streamlines

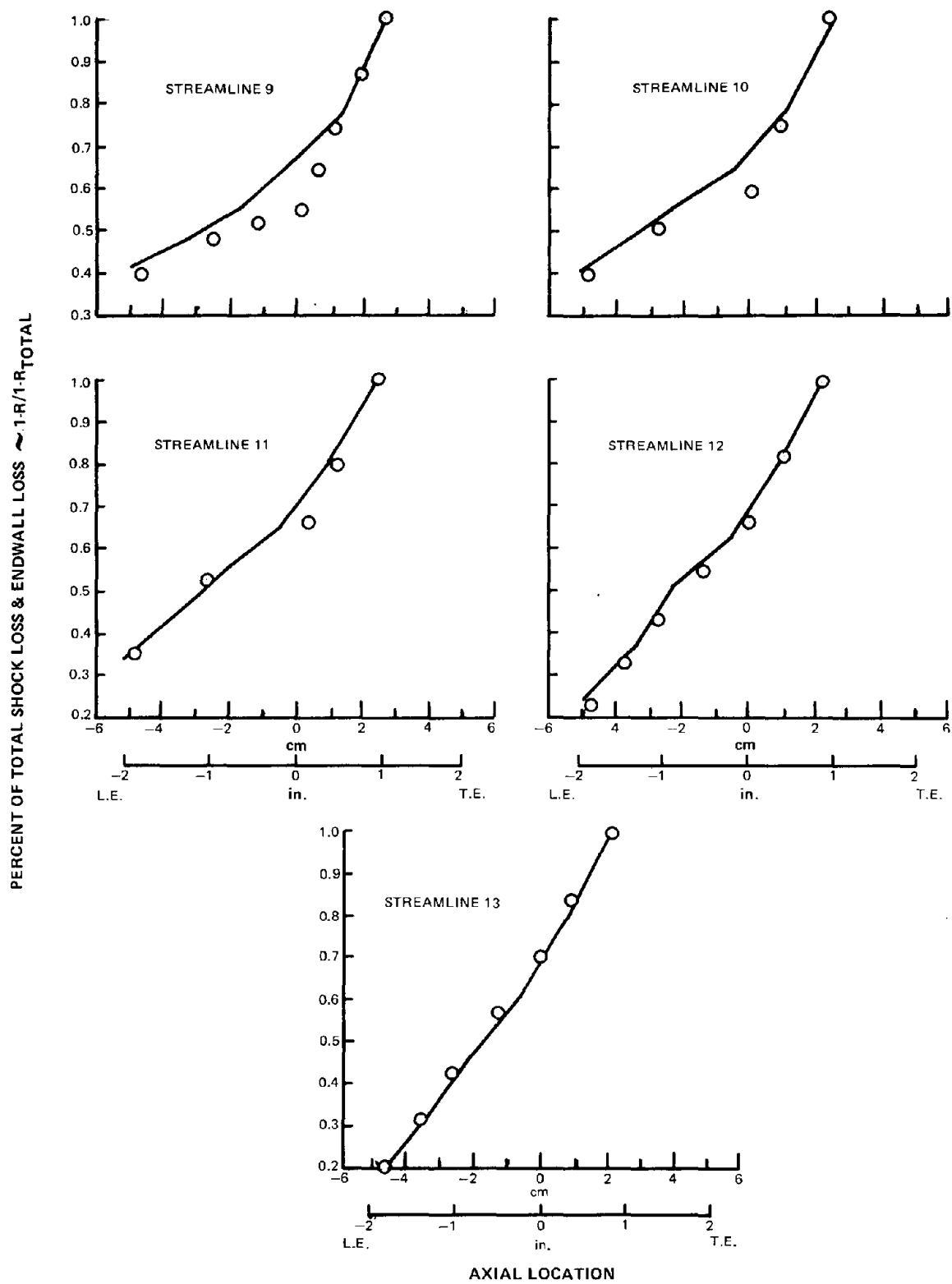


Figure 19 (Cont'd) Axial Loss Distributions for Design Streamlines

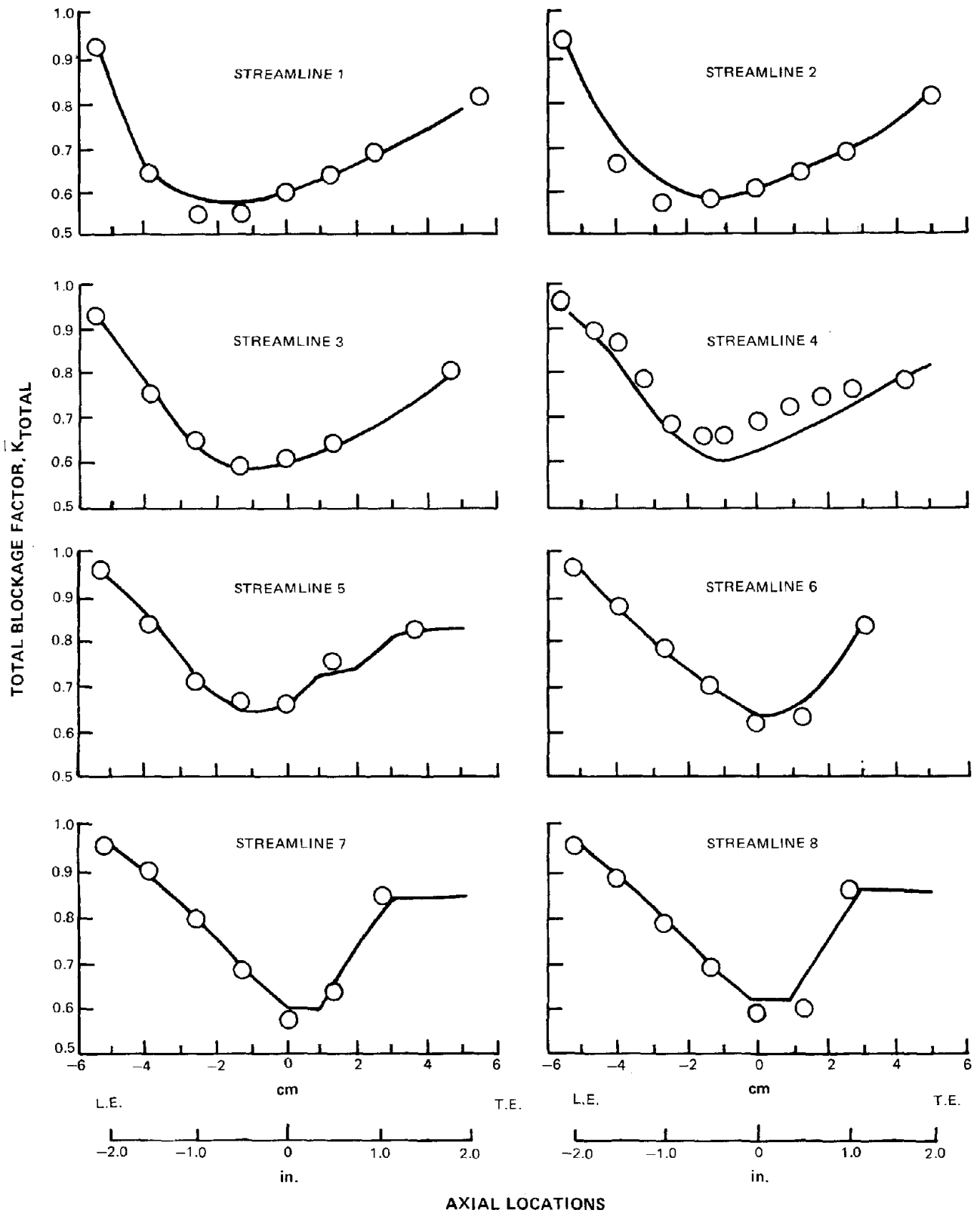


Figure 20 Axial Blockage Distributions for Design Streamlines. Curve shows Wu-Marsh, and circles indicate blade program values (metal + blade boundary + endwall blockage).

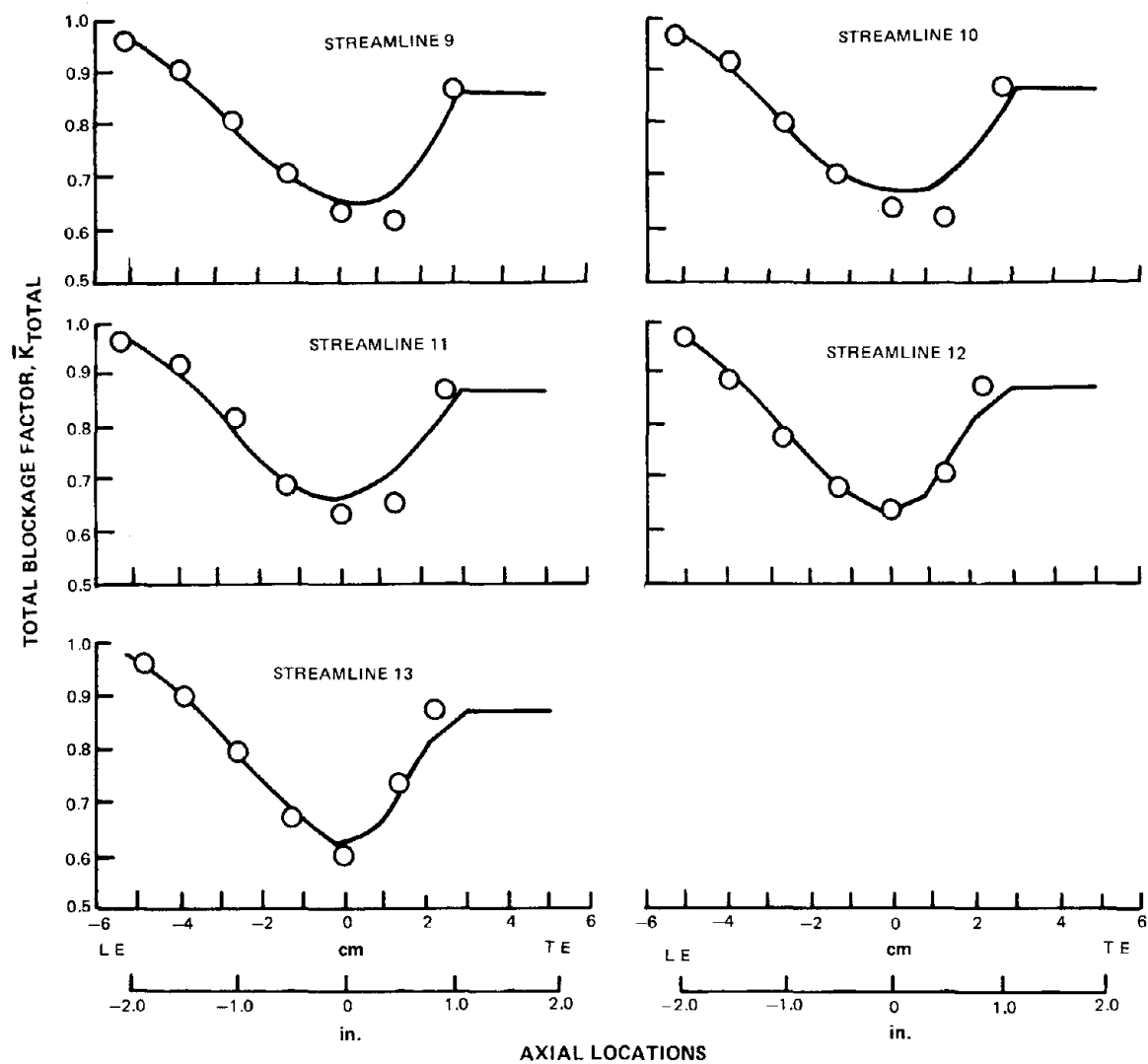


Figure 20 (Cont'd) Axial Blockage Distributions for Design Streamlines. Curve shows Wu-Marsh, and circles indicate blade program values (metal + blade boundary + endwall blockage).

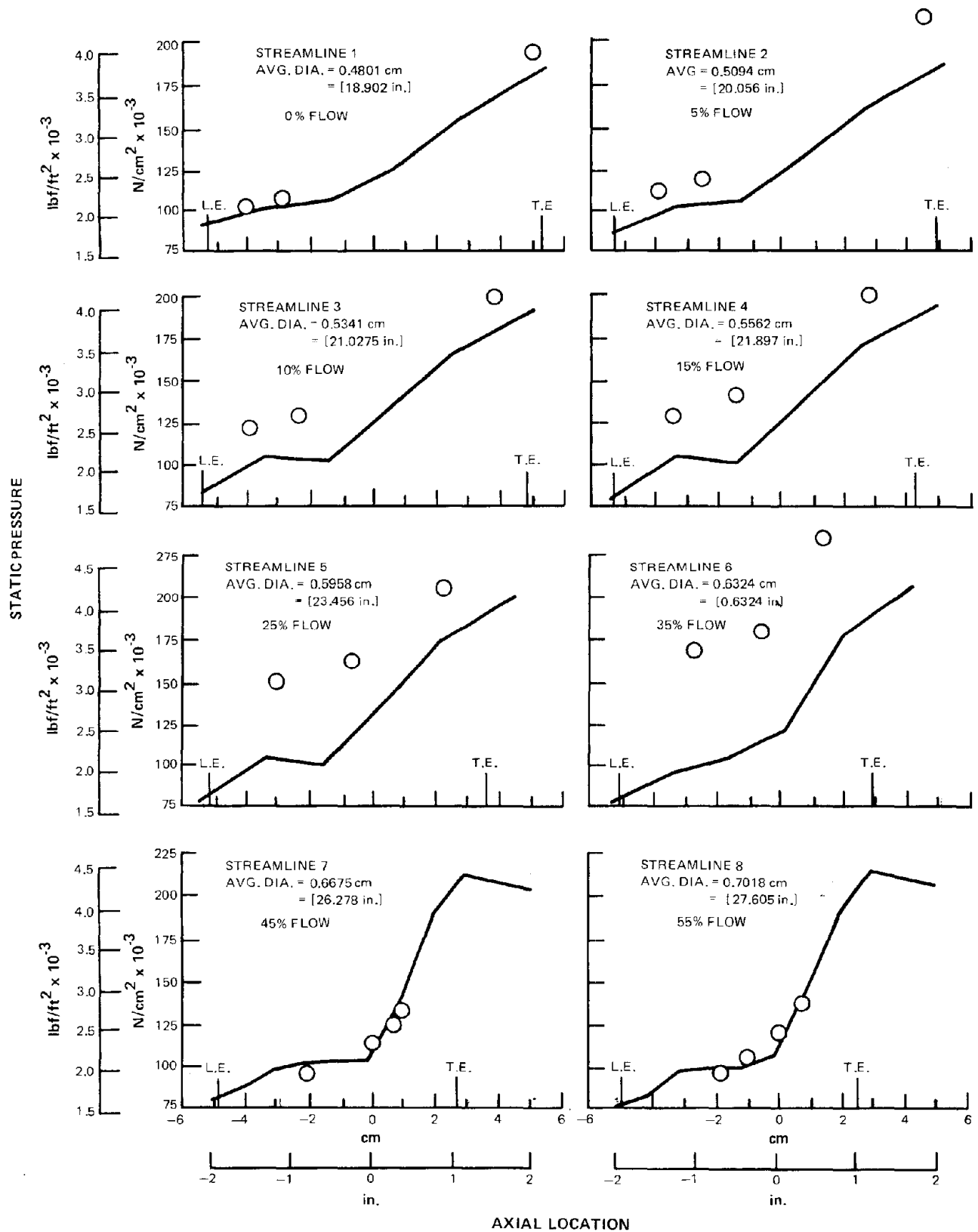


Figure 21 Axial Static Pressure Distributions for Design Streamlines. Curve shows Wu-Marsh, and circles indicate blade program values.

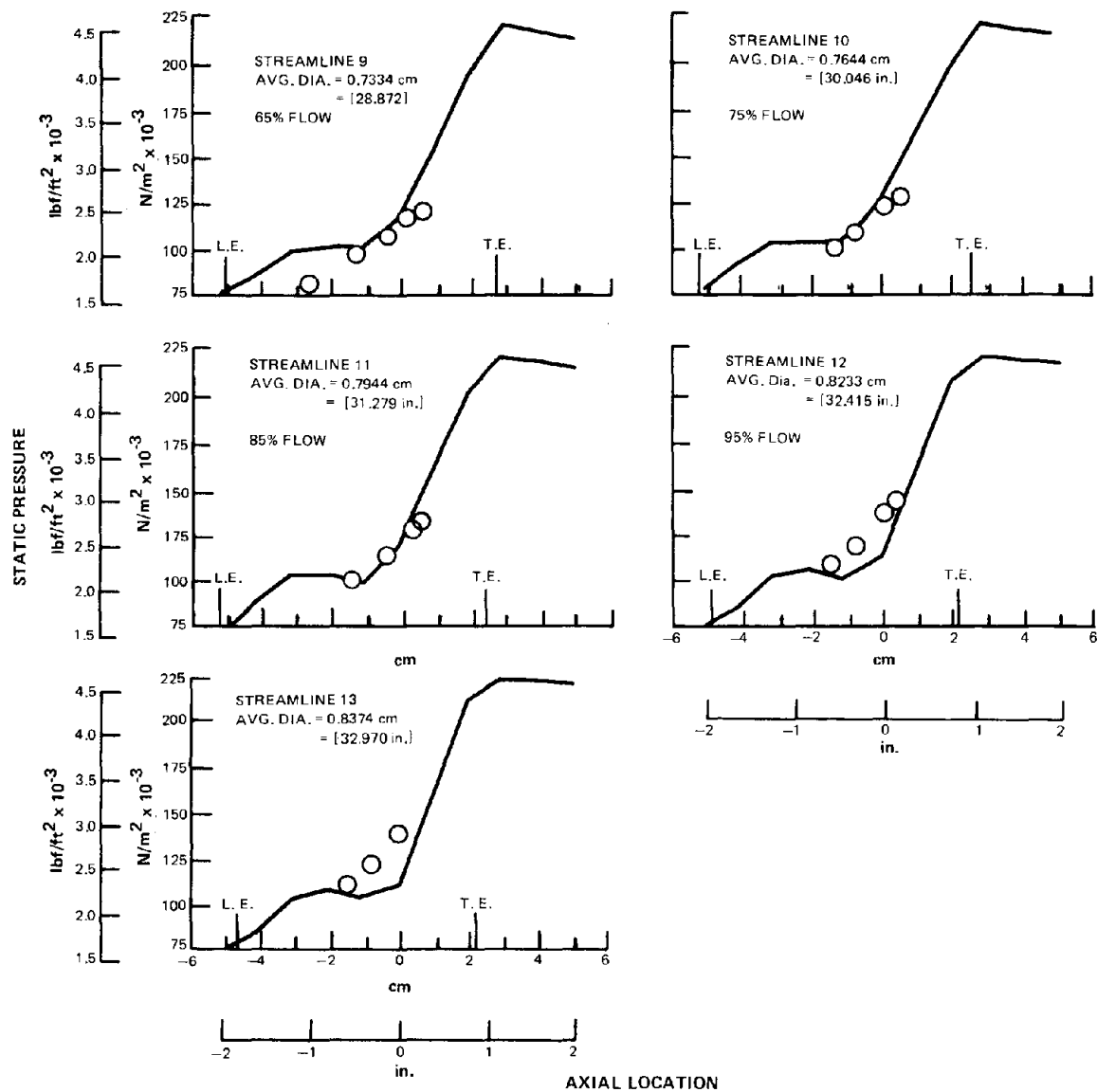


Figure 21 (Cont'd) Axial Static Pressure Distributions for Design Streamlines. Curve shows Wu-Marsh, and circles indicate blade program values.

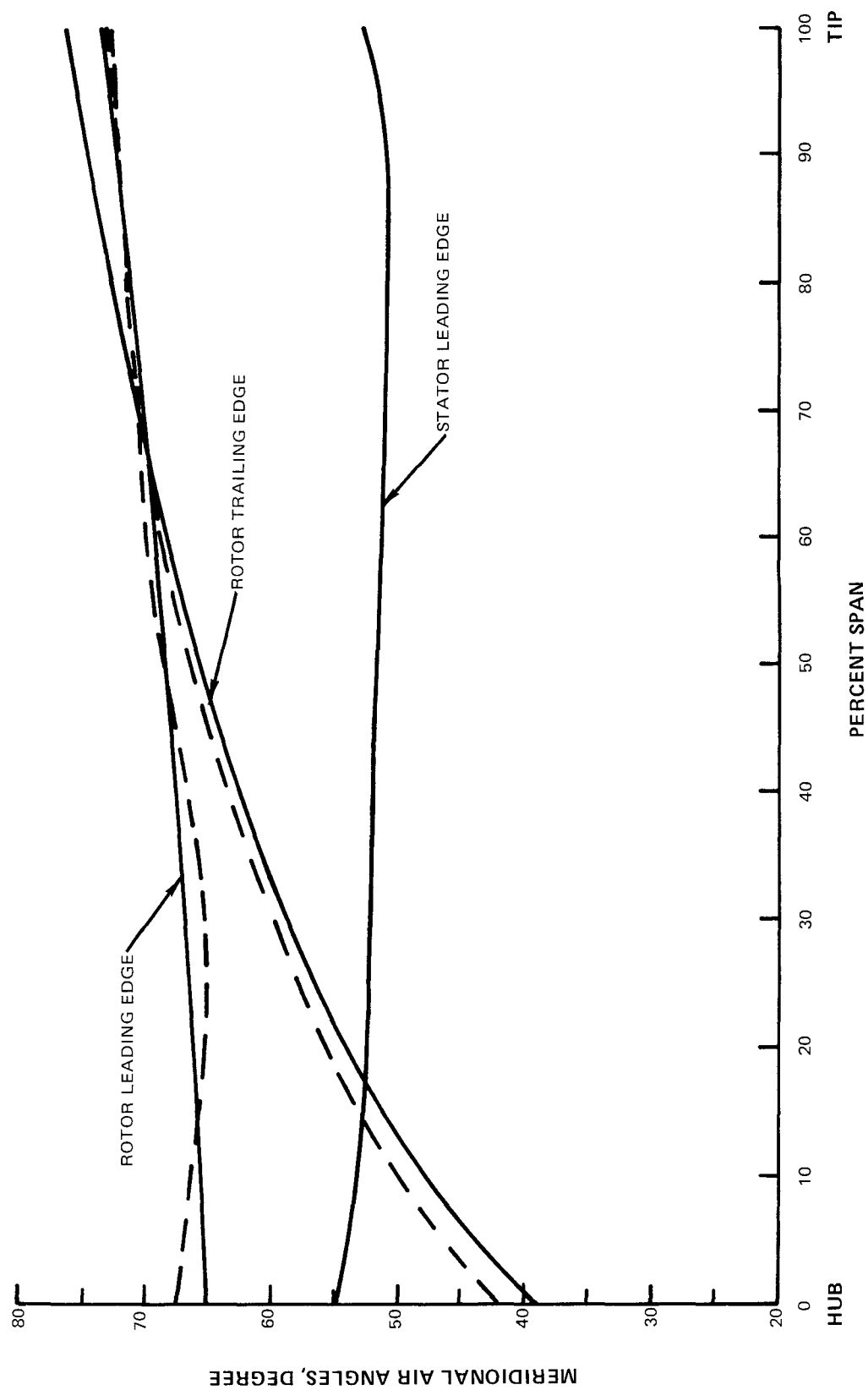


Figure 22 Rotor Inlet and Exit and Stator Inlet Meridional Air Angles. Rotor air angles relative; stator air angle absolute. Continuous line curves from streamline program, and broken line curves from Wu-Marsh

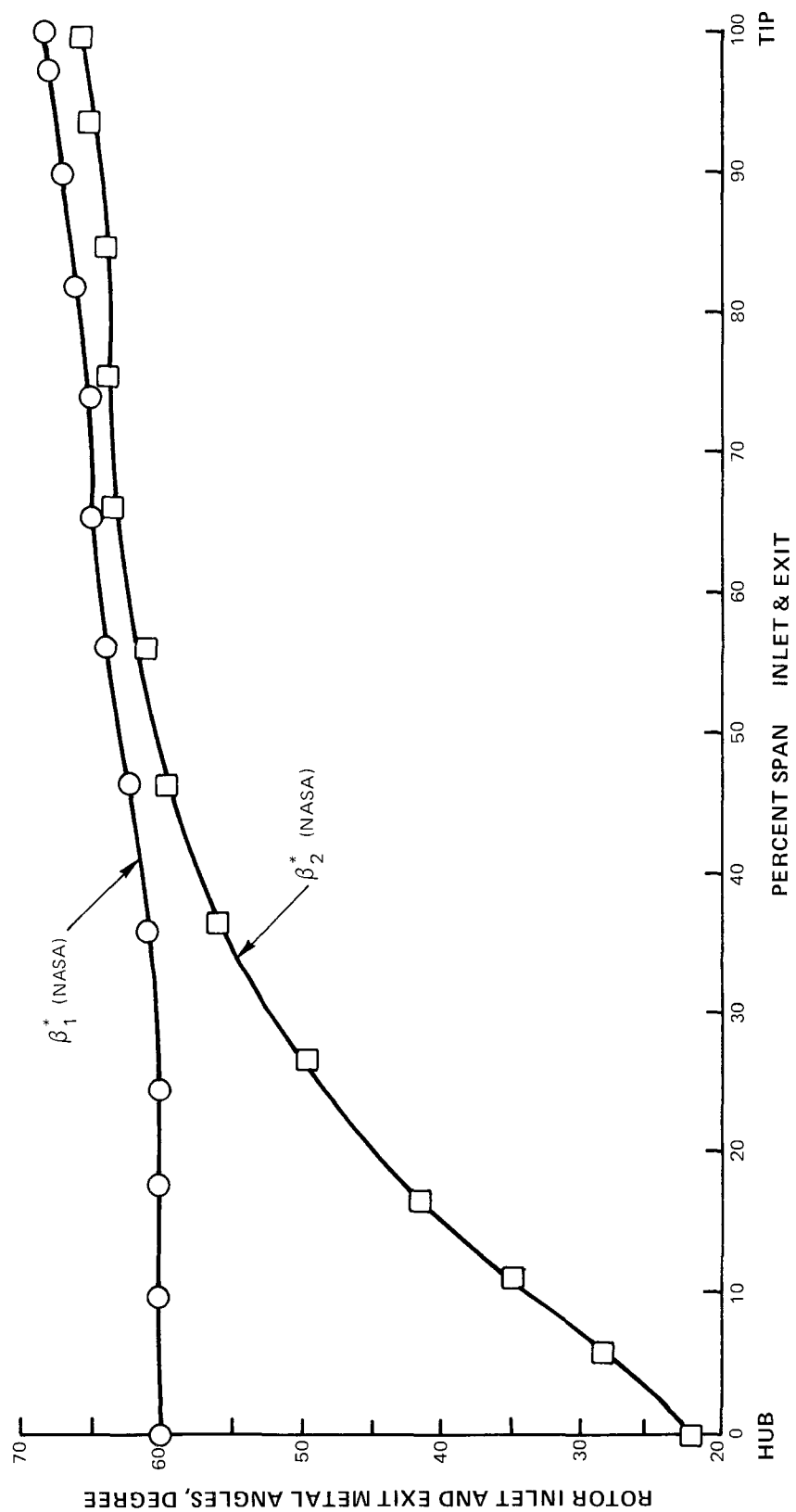


Figure 23 Rotor Inlet and Exit Meanline Angles as a Function of Span

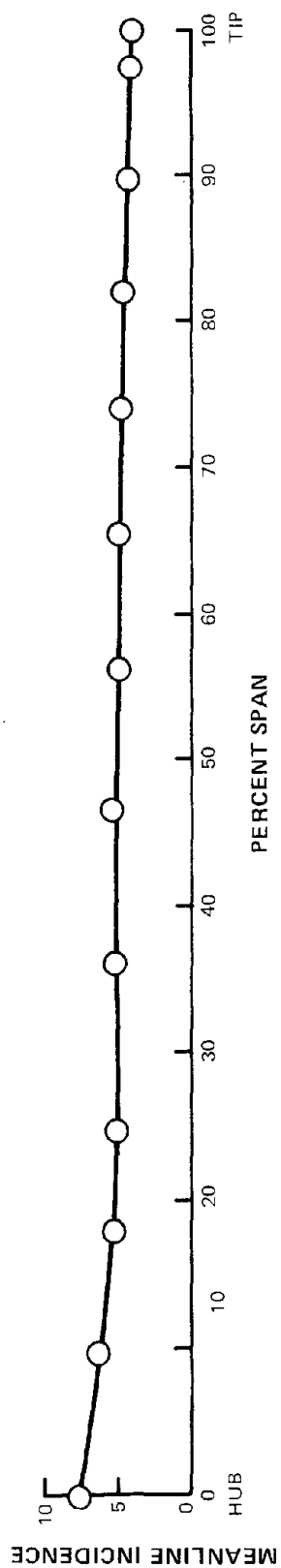


Figure 24 Rotor Deviation as a Function of Span

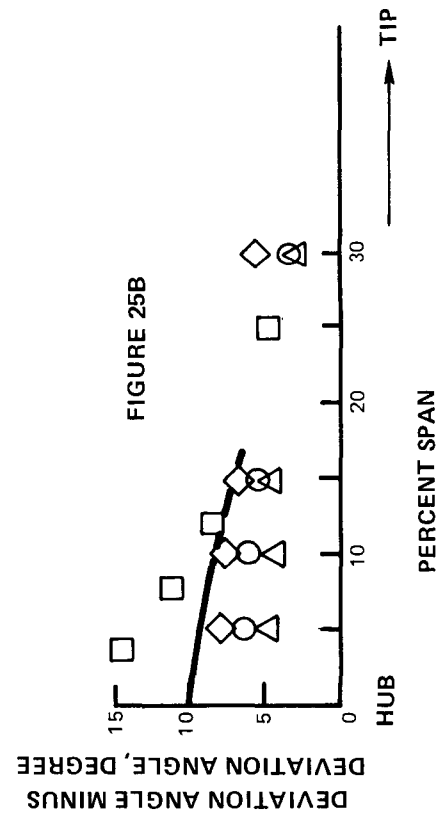
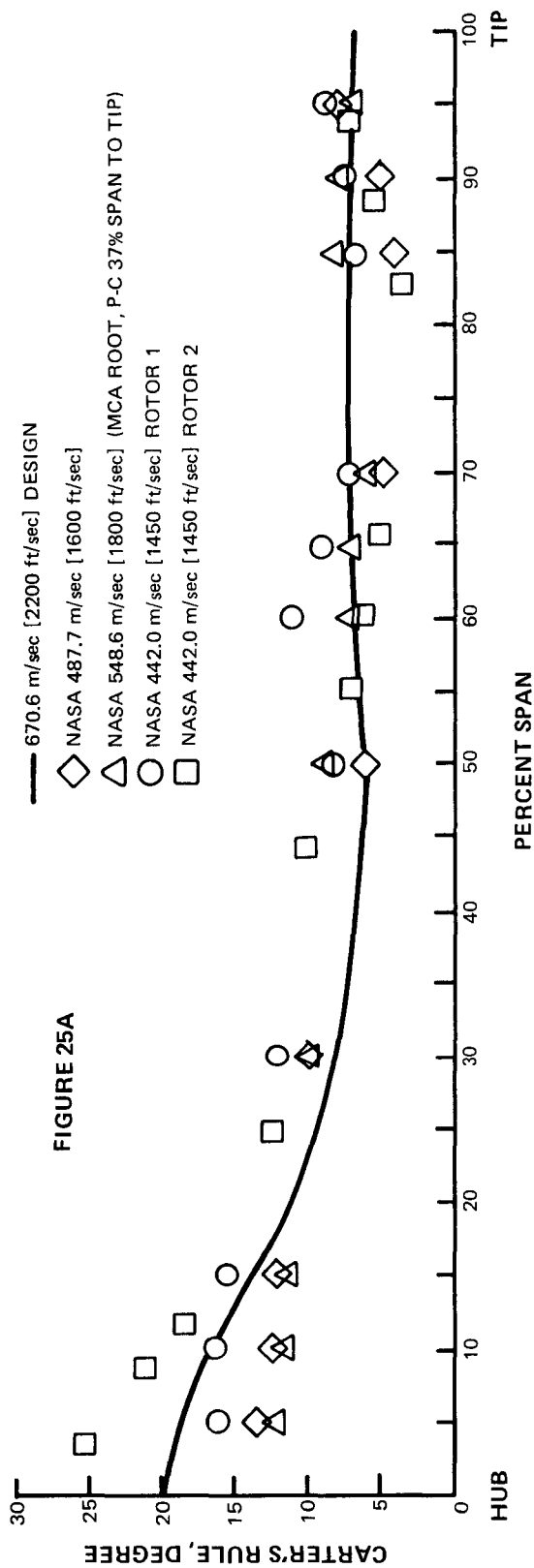


Figure 25 Rotor Design Deviation Angles (Figure 25A) and Rotor Design Deviation Angles Minus Carter's Rule (Figure 25B) as Functions of Percent Span, Comparing 670.6 m/sec [2200 ft/sec] Values With Data From Other NASA Fan Programs

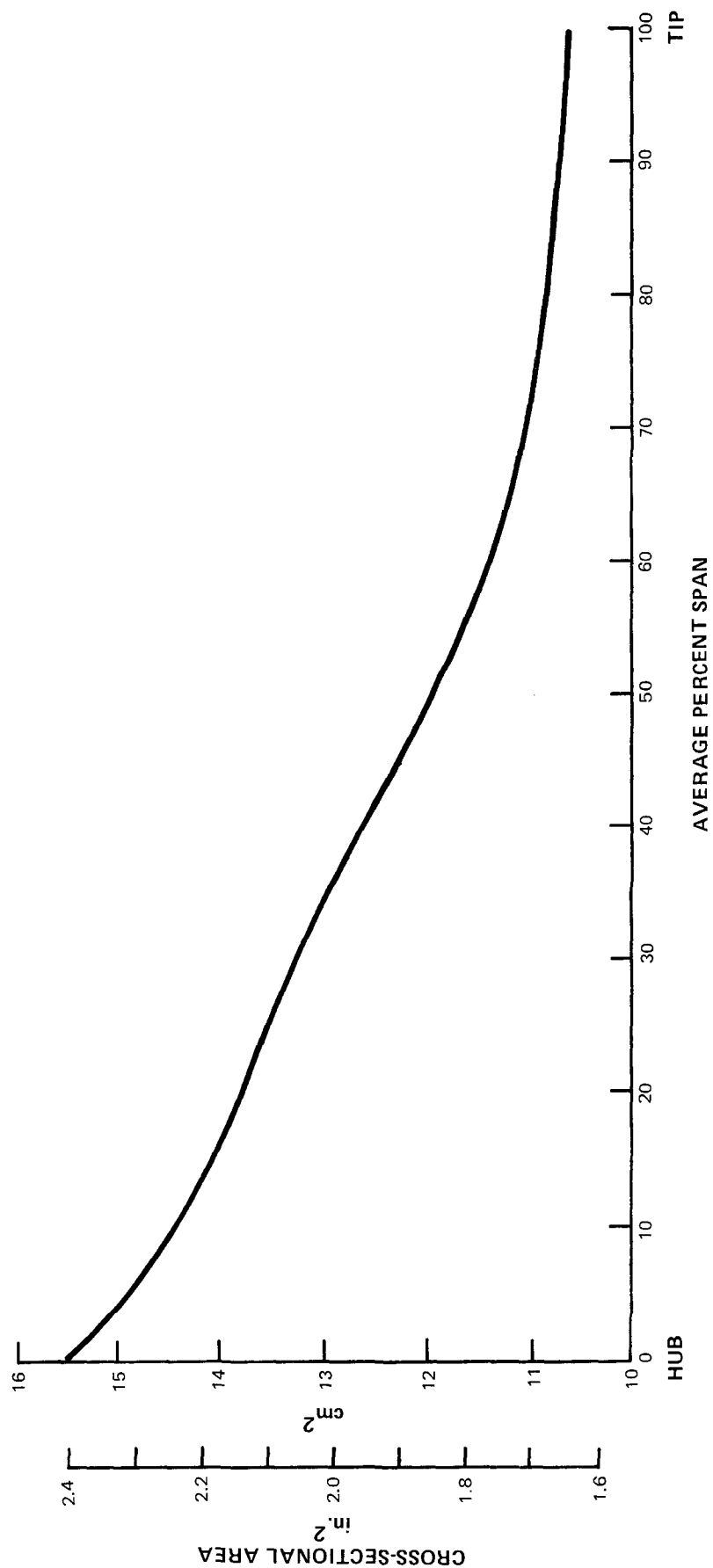


Figure 26 Rotor Cross-Sectional Area as a Function of Span

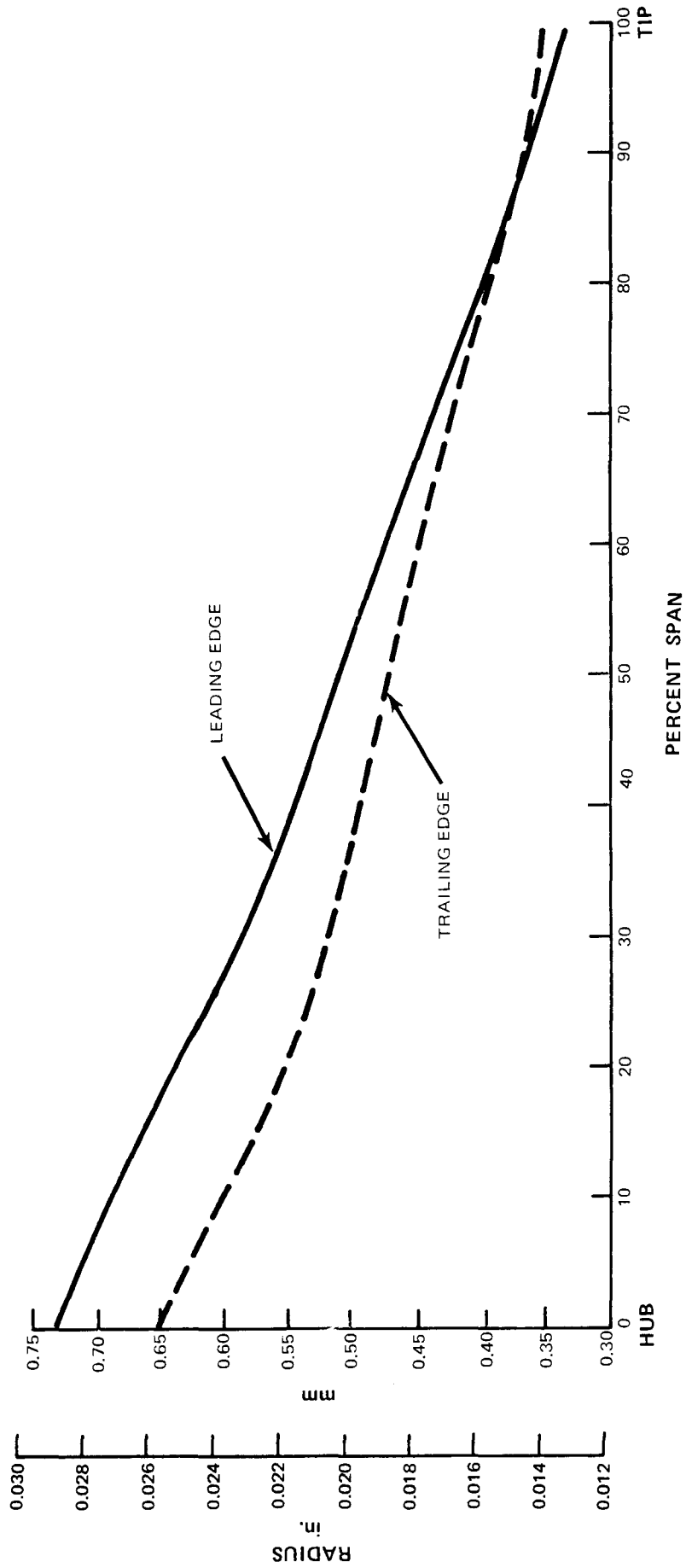


Figure 27 Rotor Leading and Trailing Edge Radii as a Function of Span

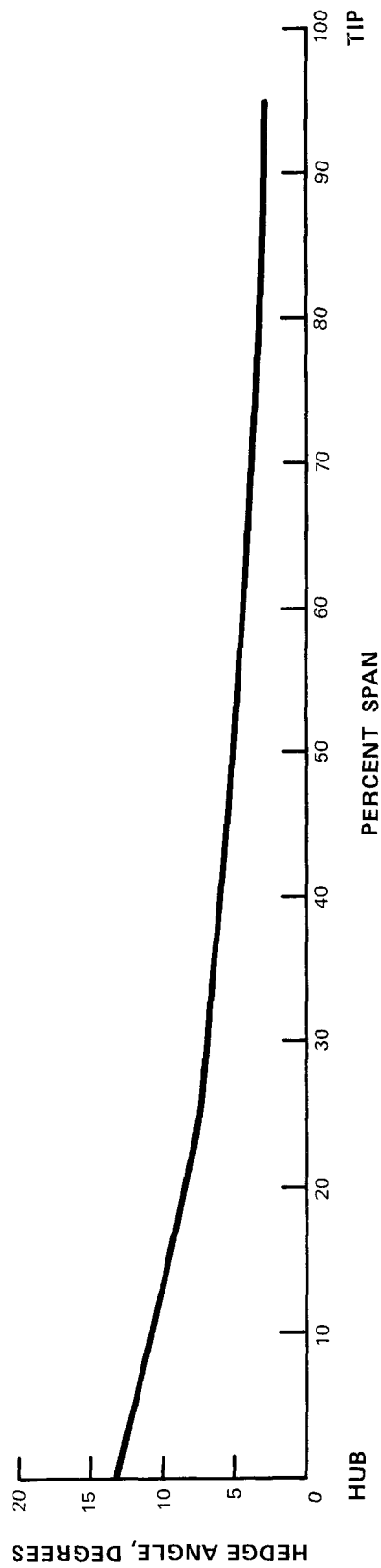


Figure 28 Rotor Leading Edge Wedge Angle as a Function of Span

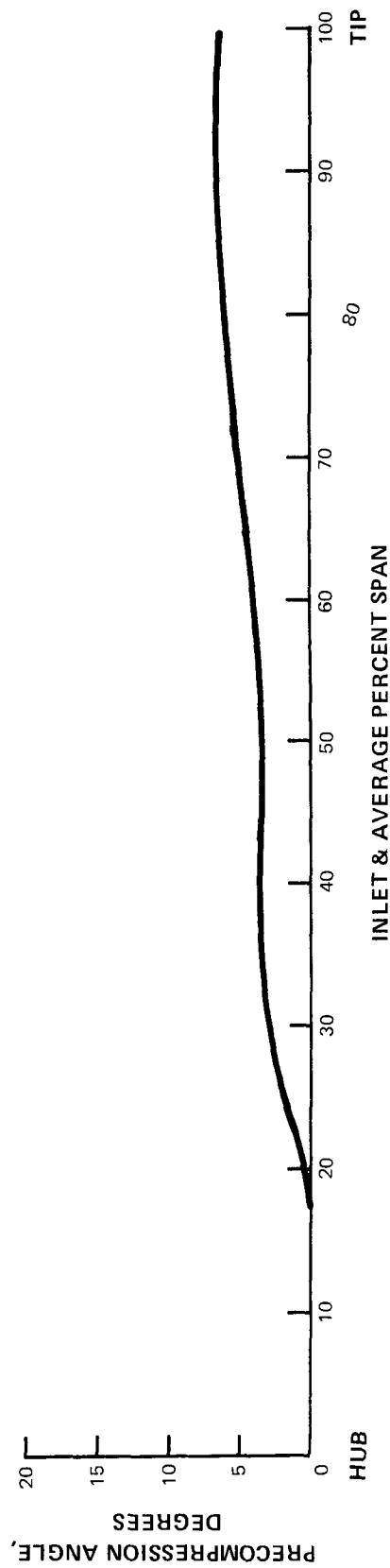


Figure 29 Rotor Precompression Ramp Angle as a Function of Span

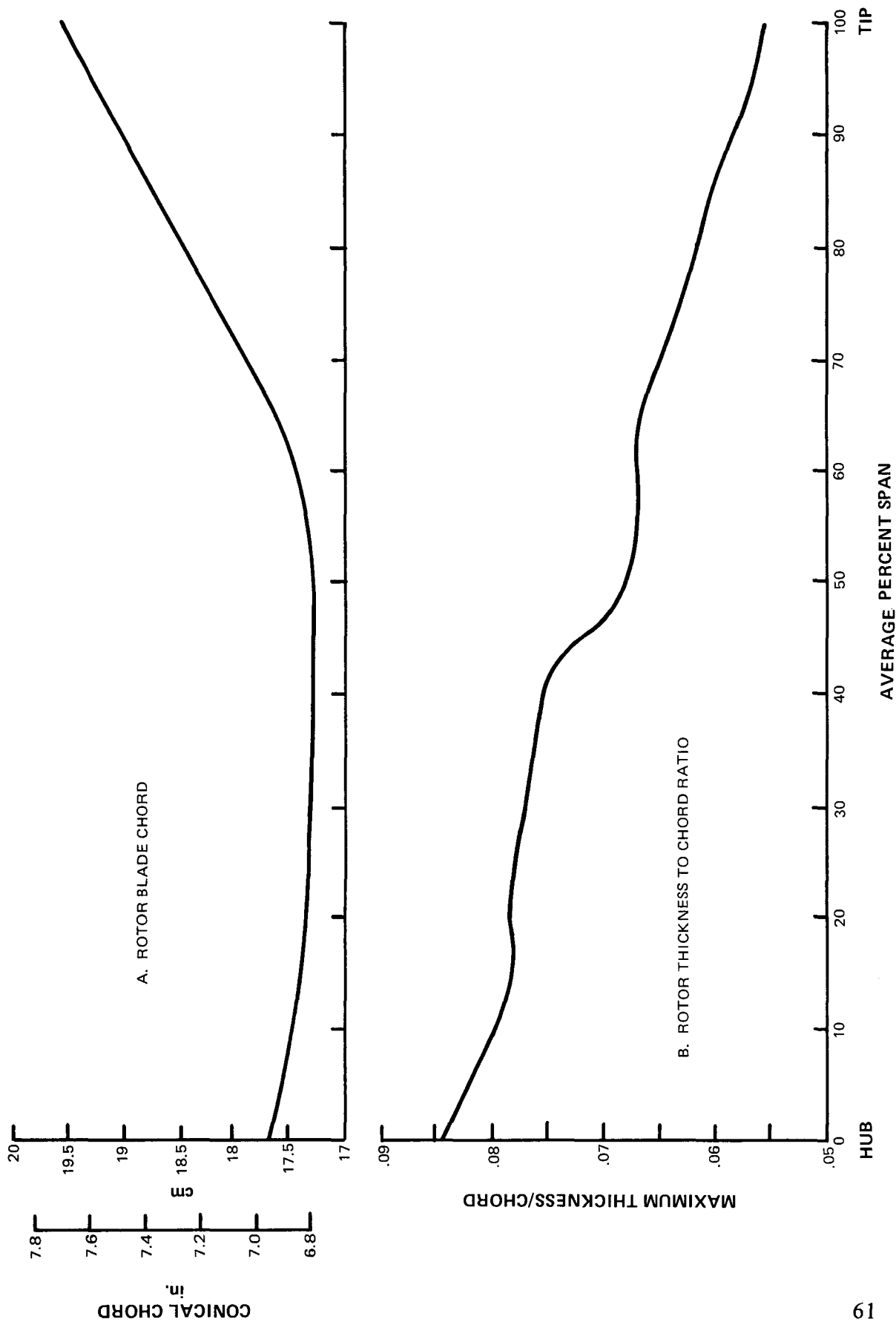


Figure 30 Rotor Thickness-to-Chord Ratio and Blade Chord as a Function of Span

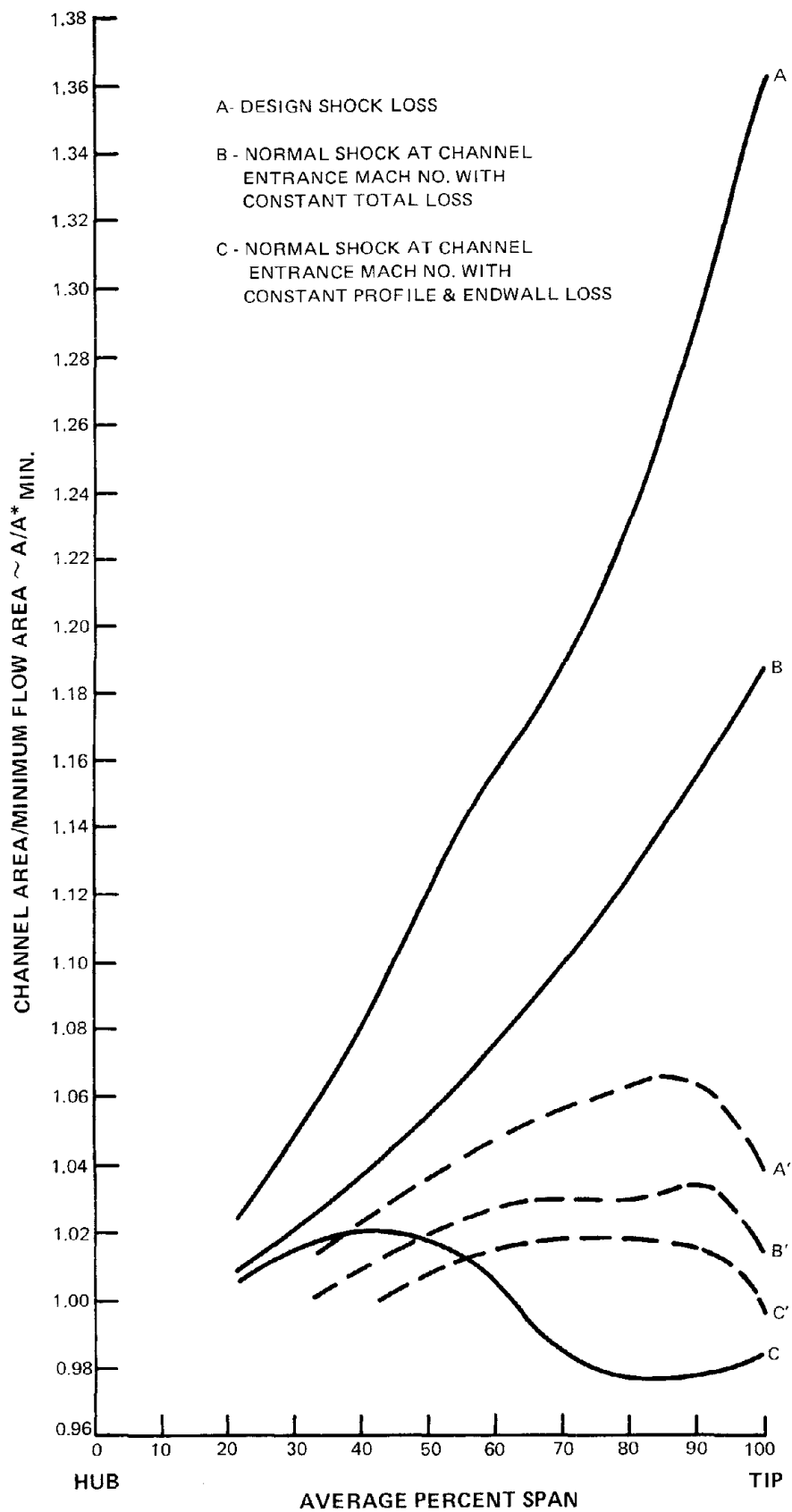


Figure 31 Critical Area Ratios as Functions of Span for Precompression Sections. Solid line curves indicate 670.6 m/sec [2200 ft/sec] tip speed fan, and broken line curves indicate 548.6 m/sec [1800 ft/sec] fan.

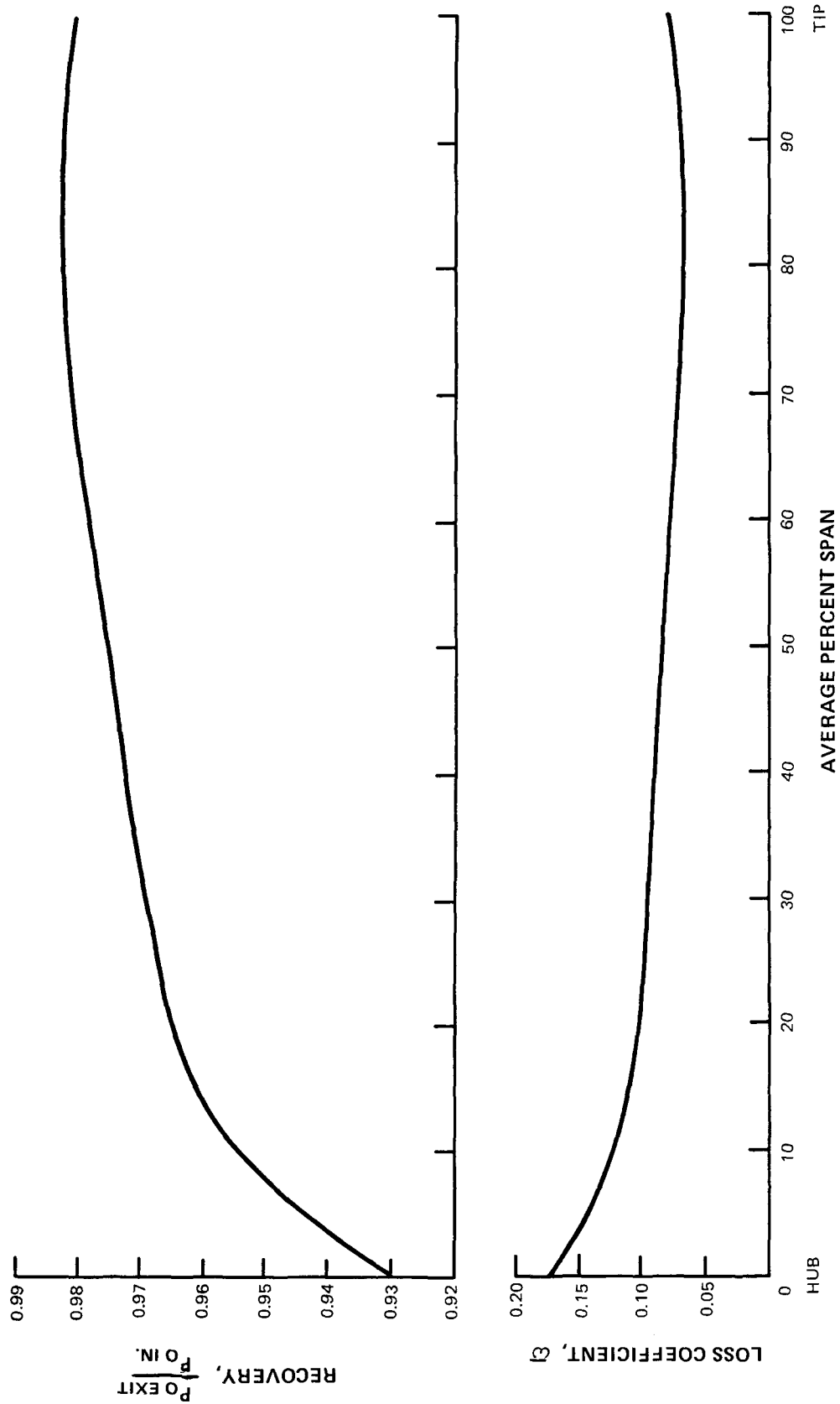


Figure 32 Stator Recovery and Loss Coefficient as a Function of Span

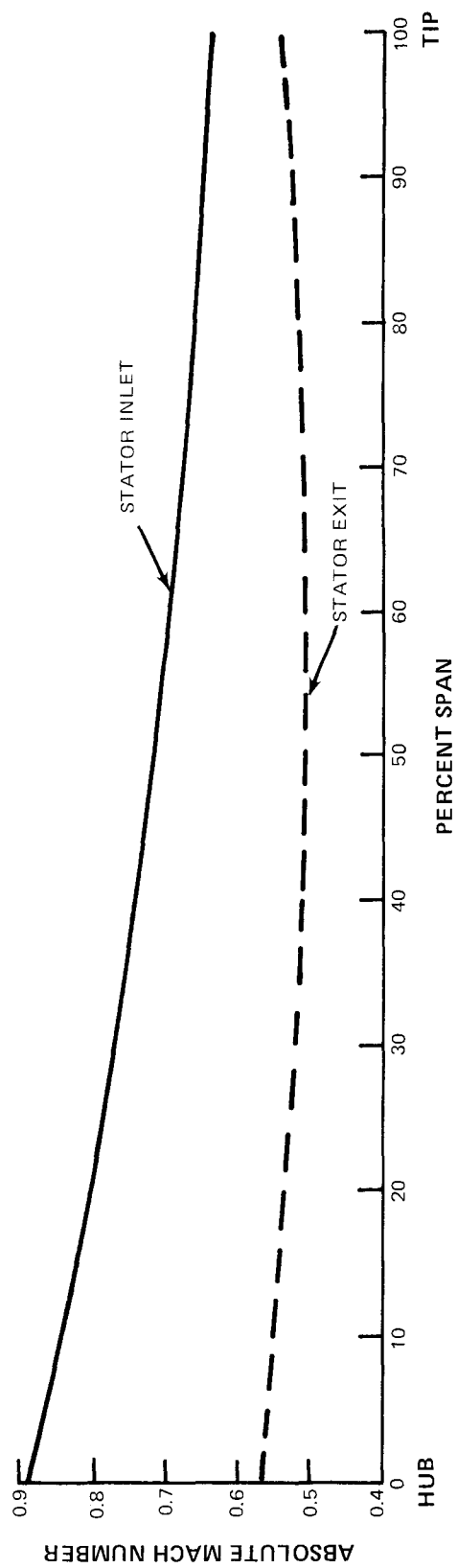


Figure 33 Stator Inlet and Exit Absolute Mach Numbers as Functions of Span

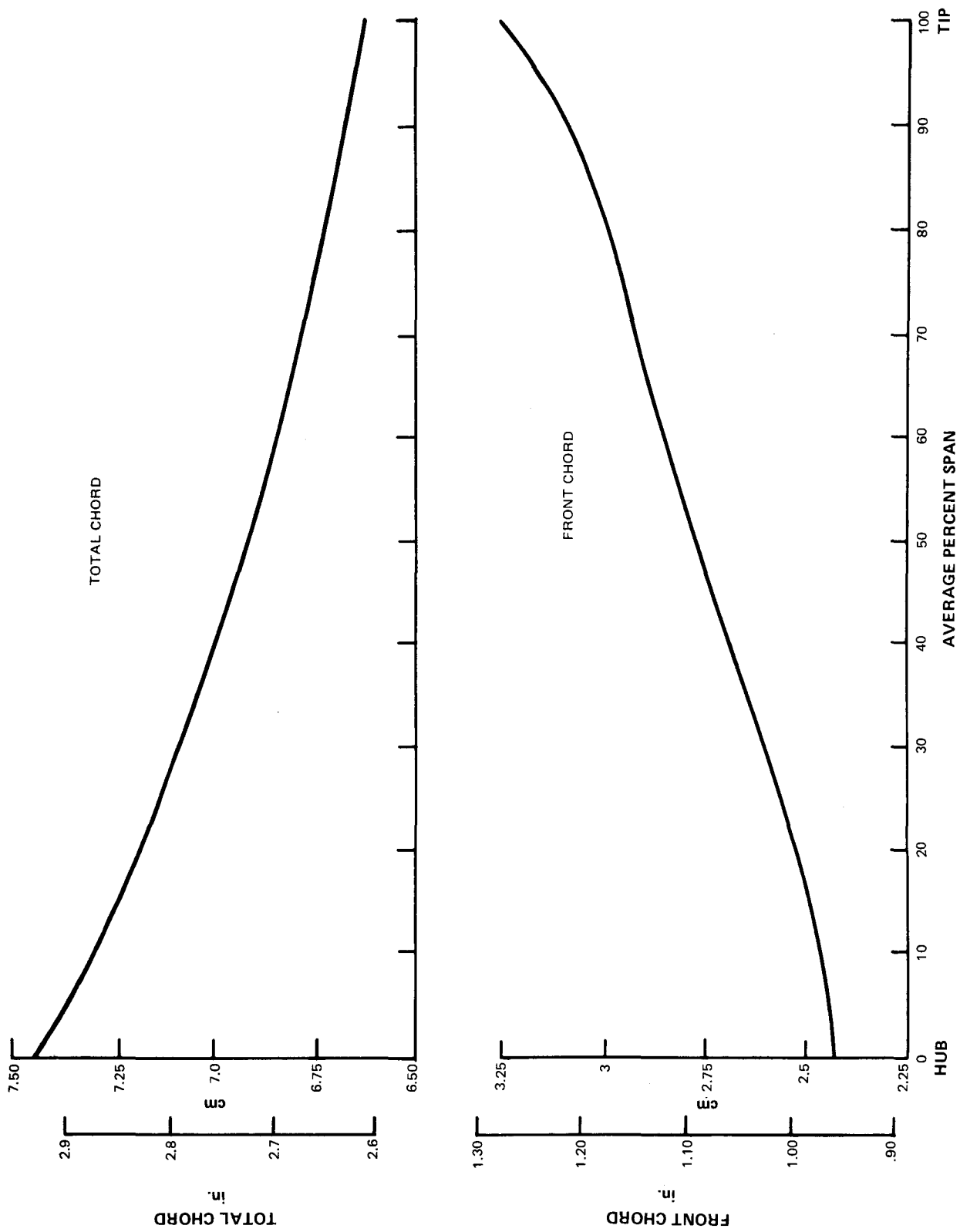


Figure 34 Stator Vane Front and Total Chords as Functions of Span

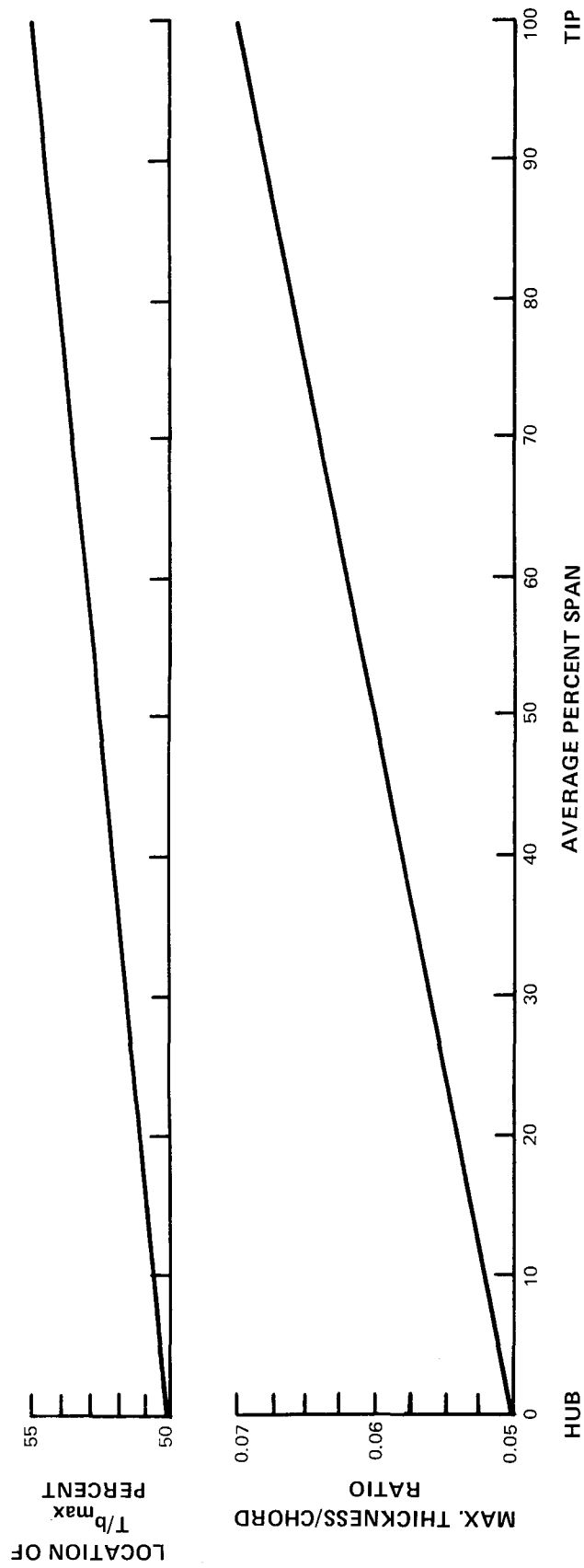


Figure 35 Stator Maximum Thickness-to-Chord Ratio and Chordwise Location as a Function of Span

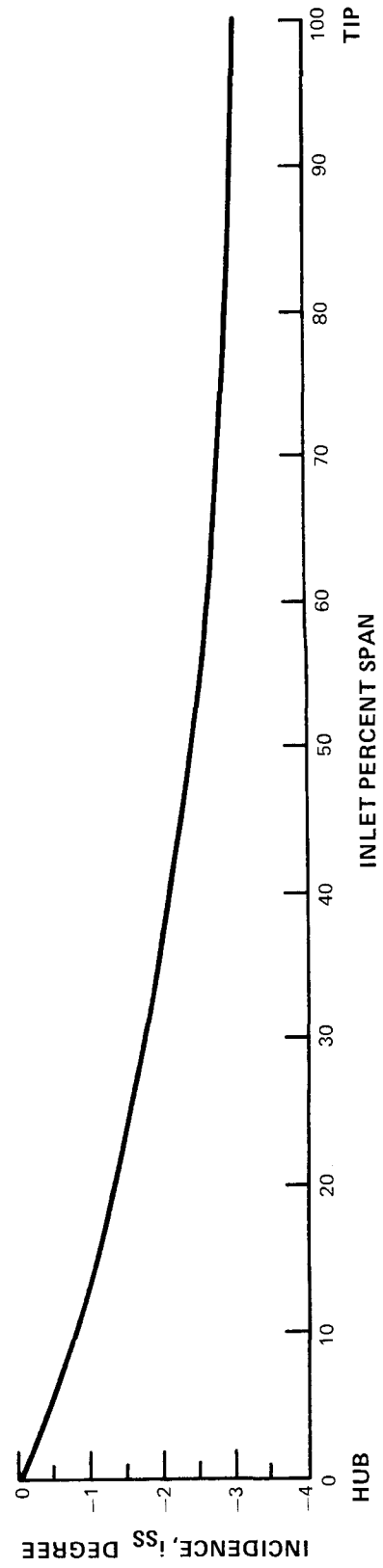


Figure 36 Stator Vane Suction Surface Incidence as a Function of Span

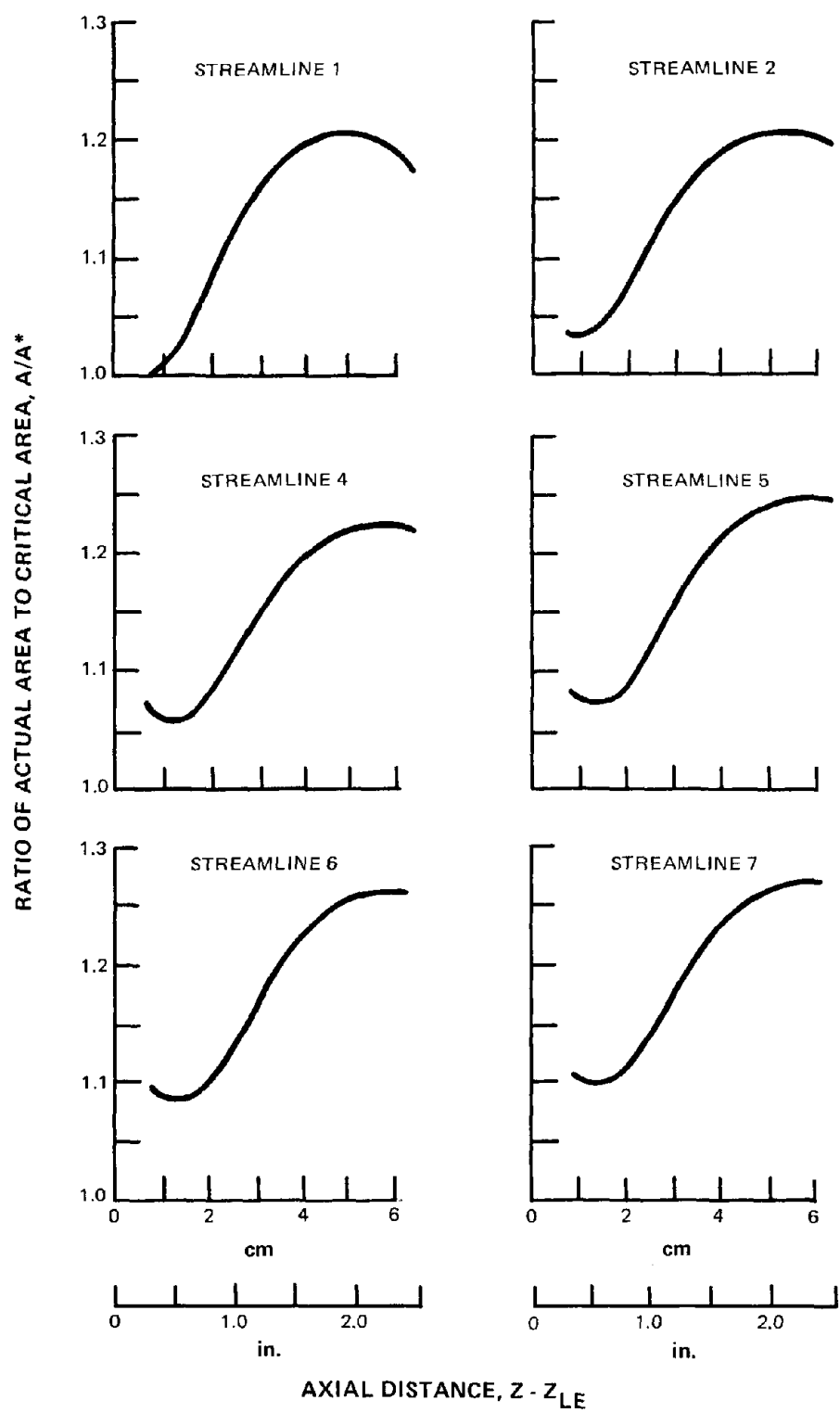


Figure 37 Stator Channel Area Ratios as a Function of Axial Distance

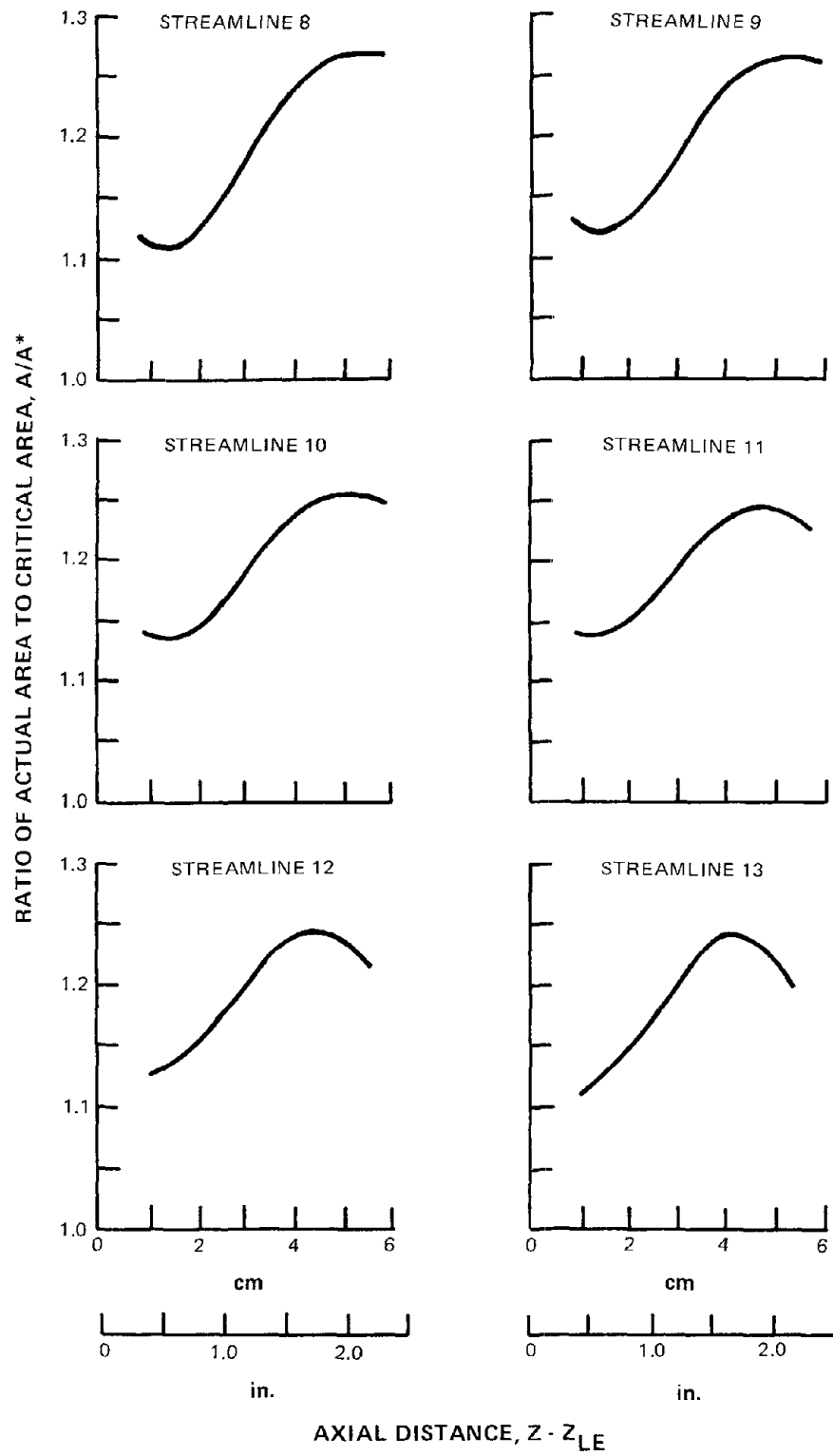


Figure 37 (Cont'd) Stator Channel Area Ratios as a Function of Axial Distance

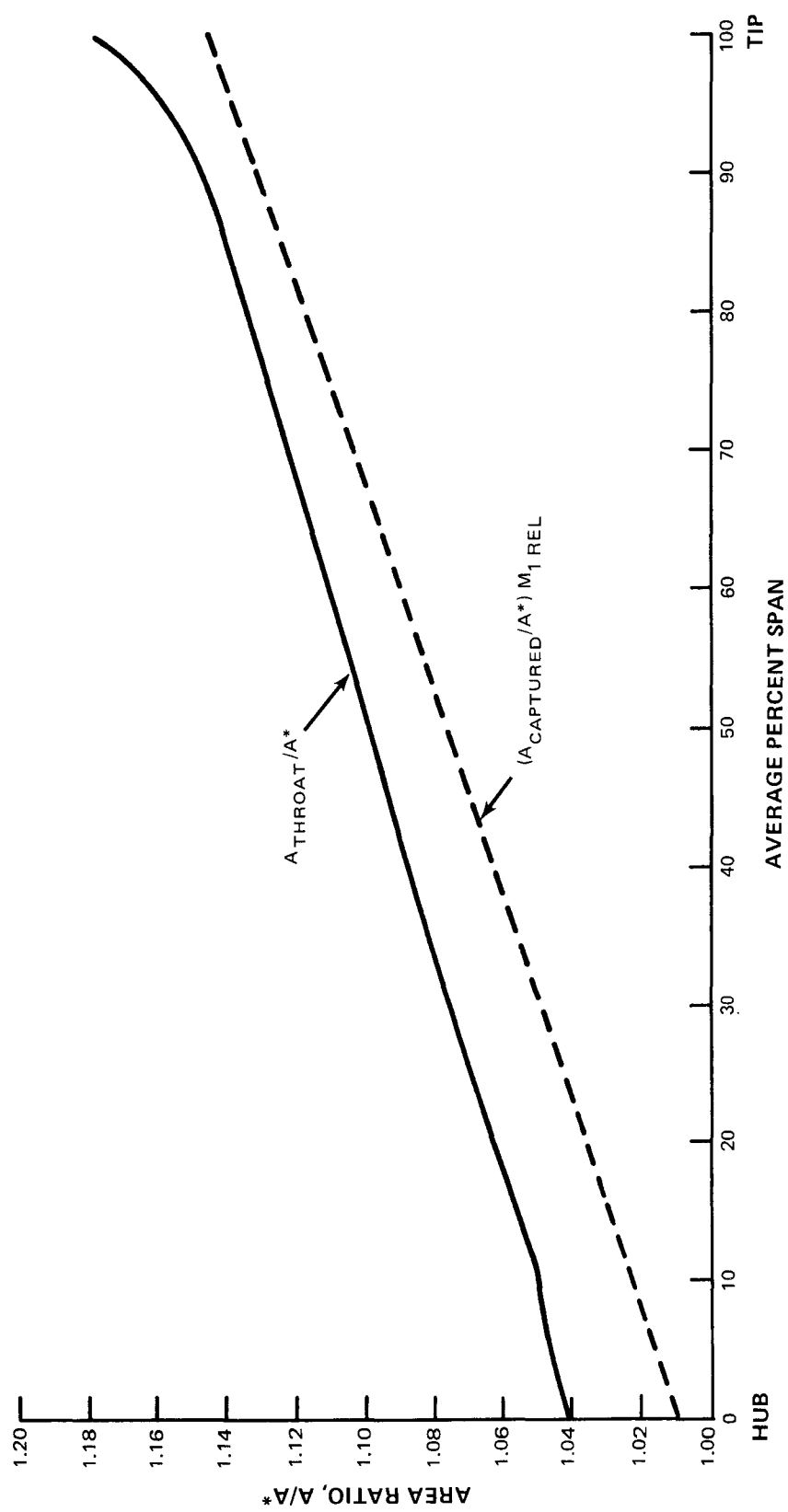


Figure 38 Stator Minimum A/A^* as a Function of Span

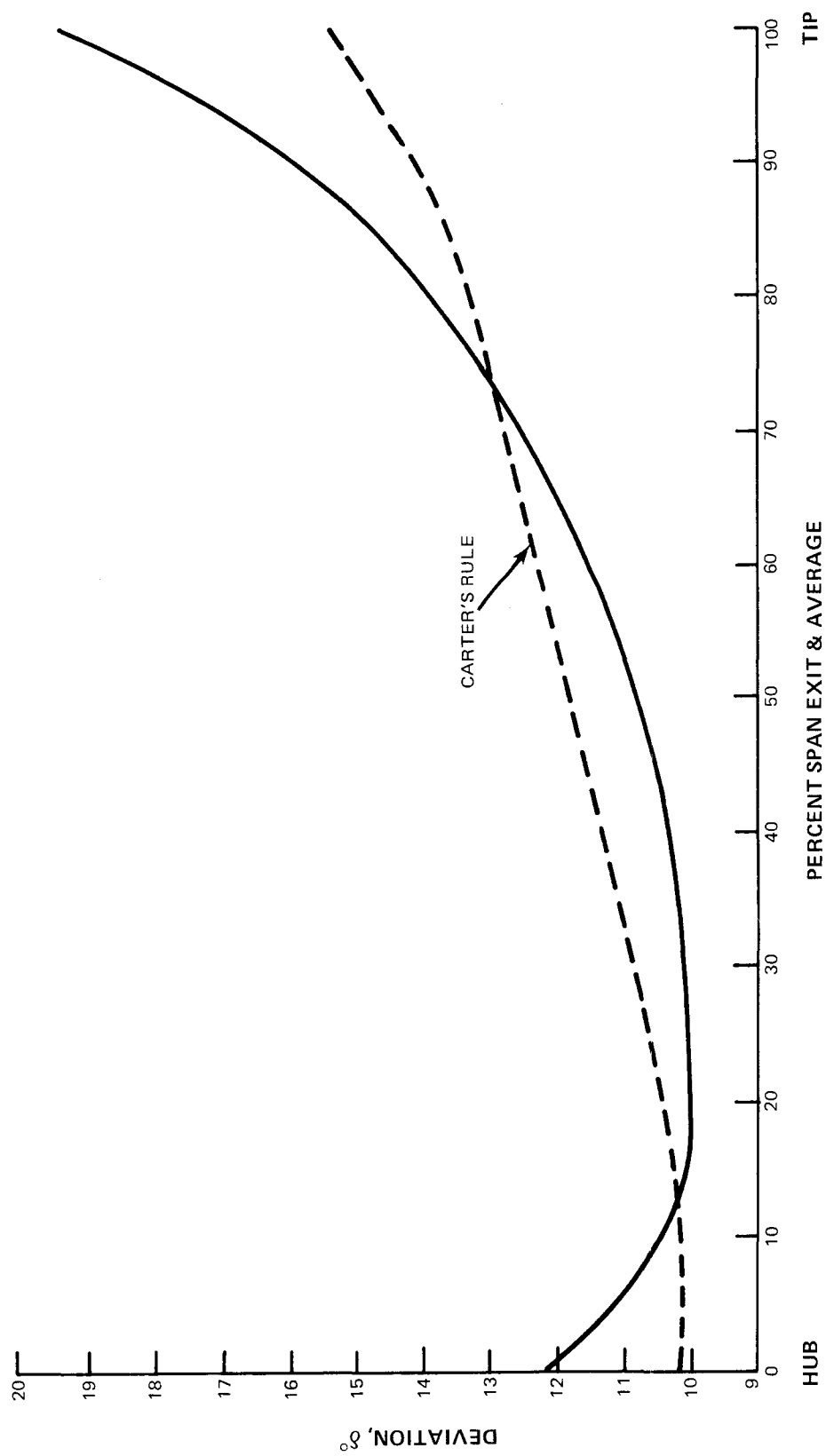


Figure 39 Stator Vane Deviation and Comparison With Carter's Rule

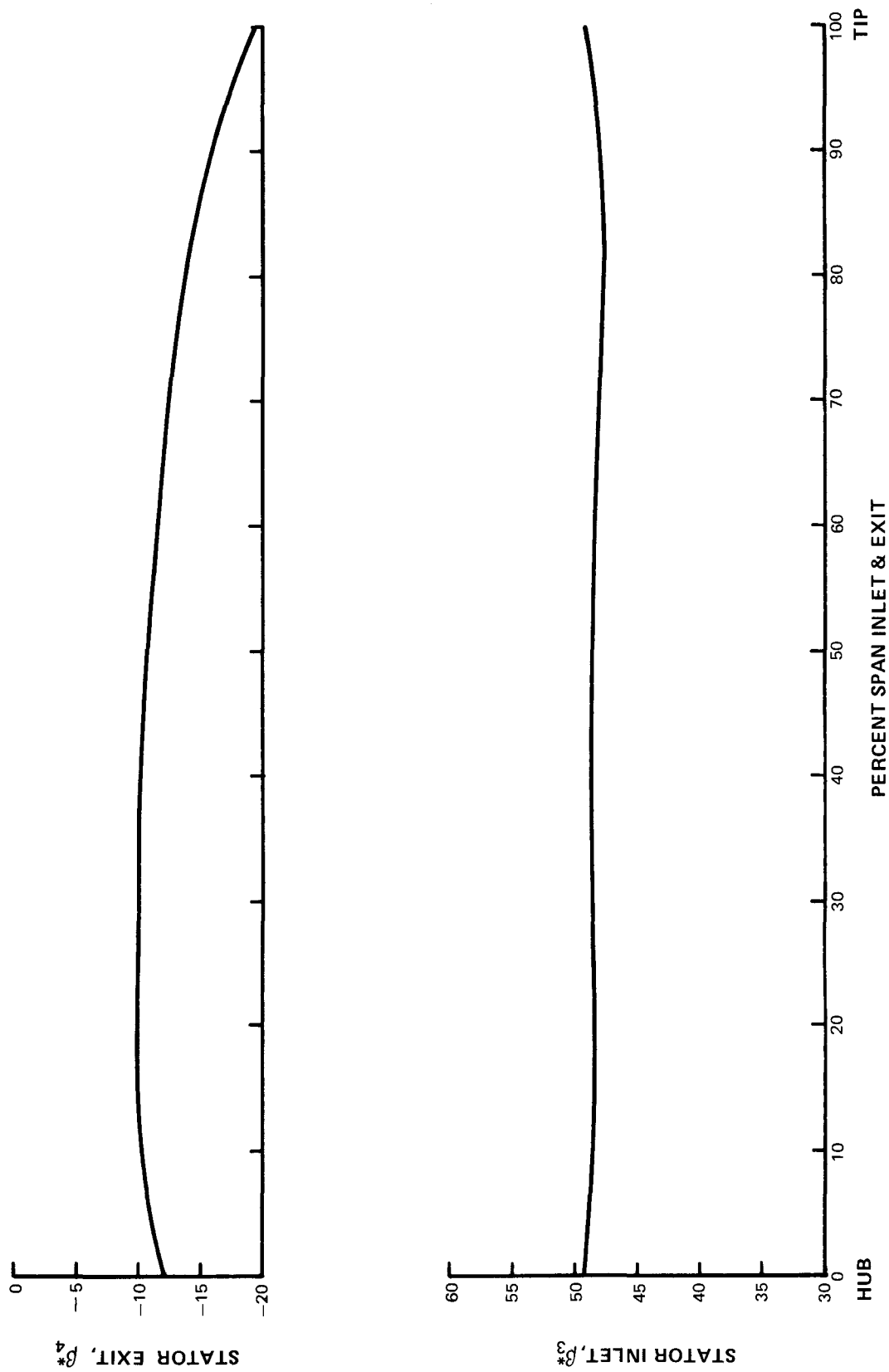


Figure 40 Stator Vane Inlet and Exit Mean Camber Line

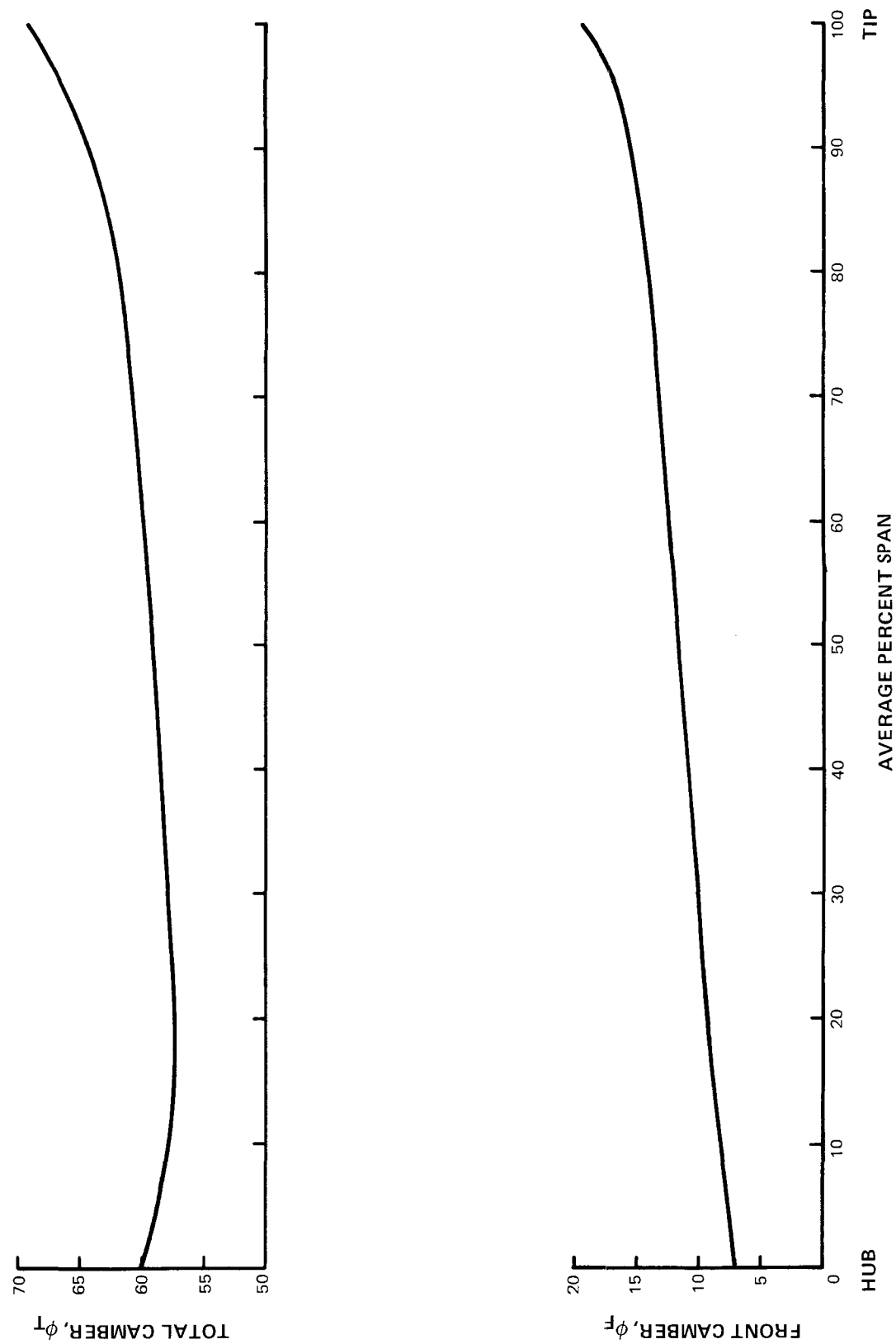


Figure 41 Stator Vane Front and Total Cambers

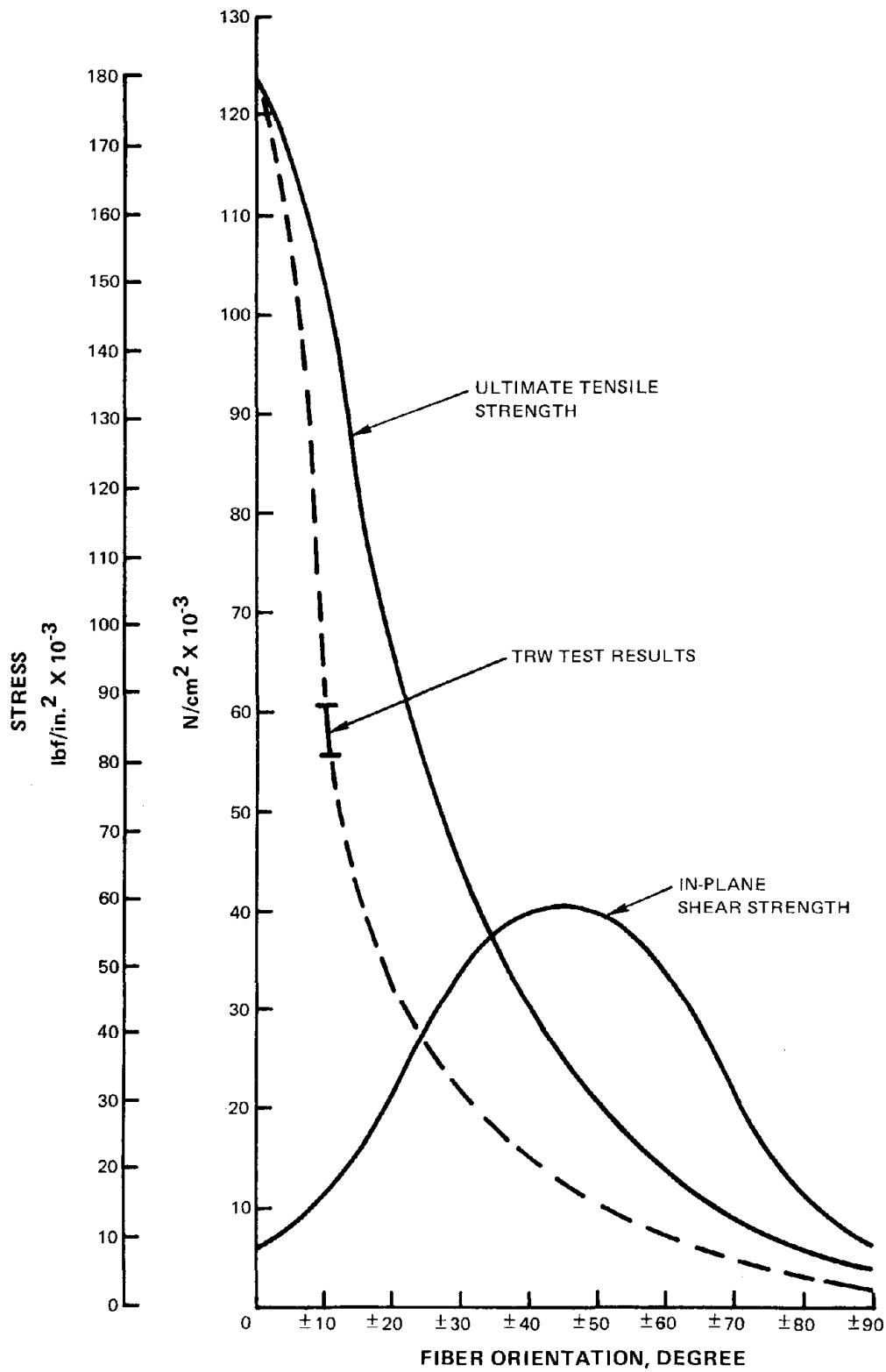


Figure 42 Strength as a Function of Ply Orientation

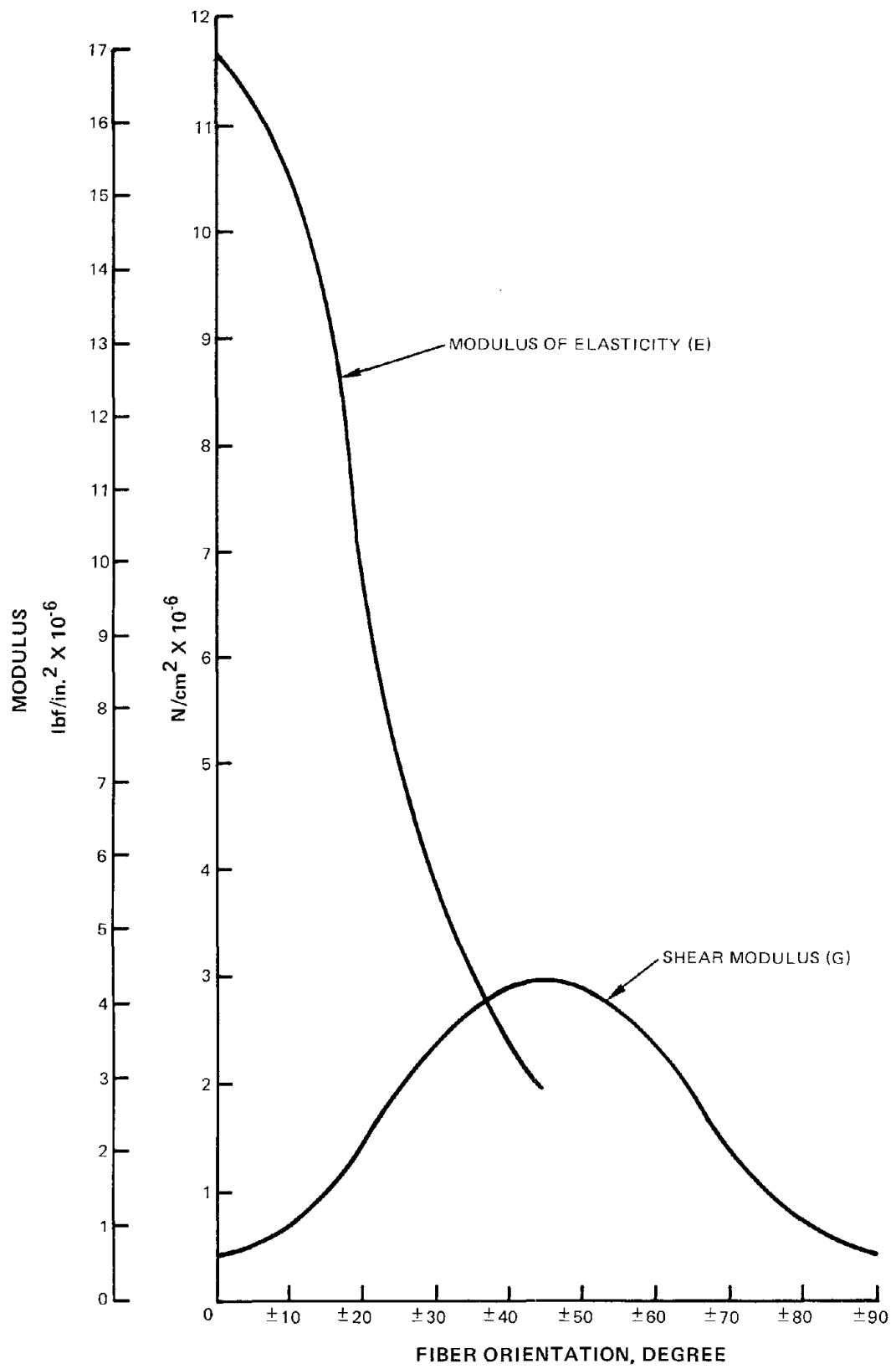


Figure 43 Tensile and Shear Moduli of Elasticity as a Function of Ply Orientation

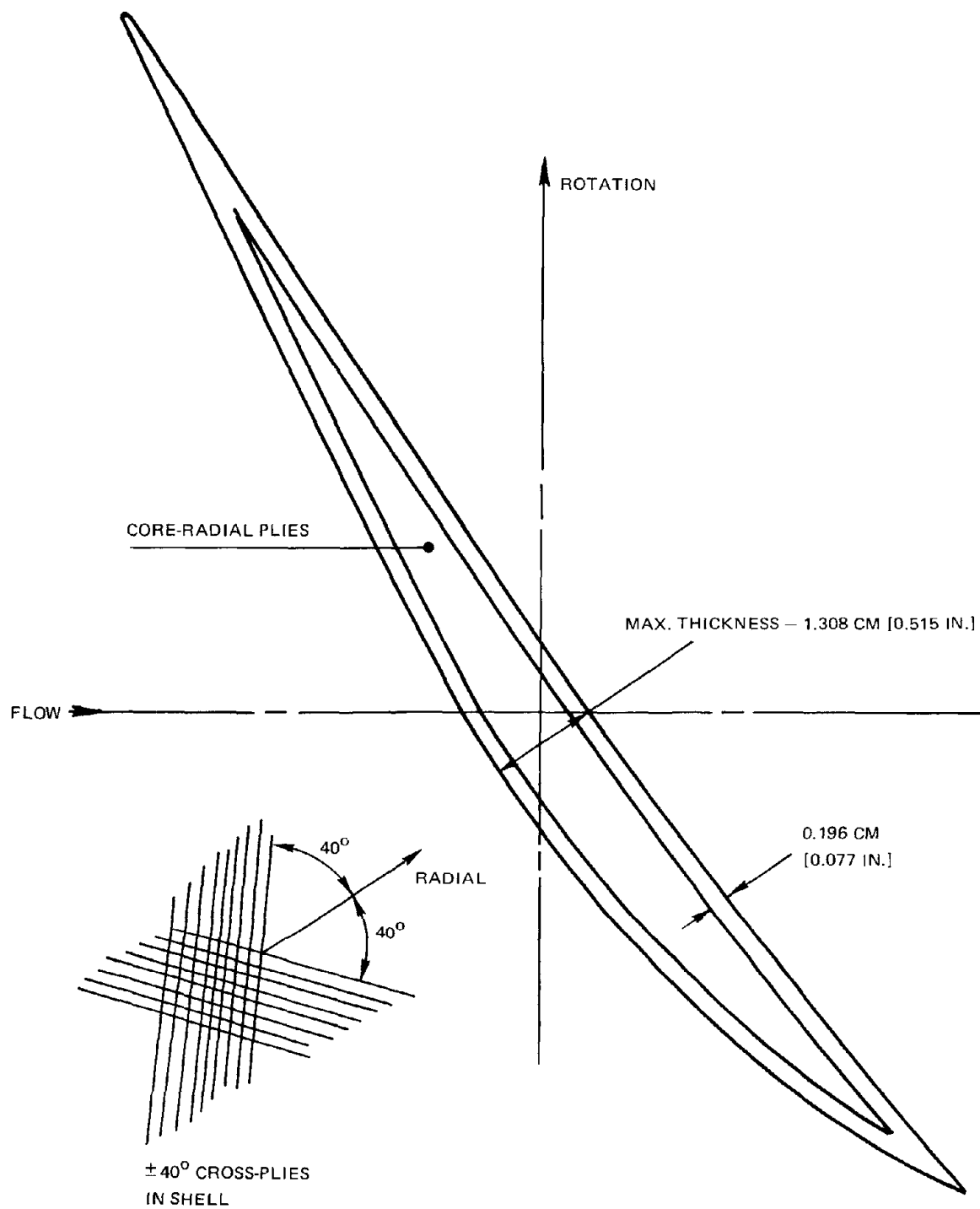


Figure 44 Typical Blade Section (0.2774 m [10.92 in.] radius)

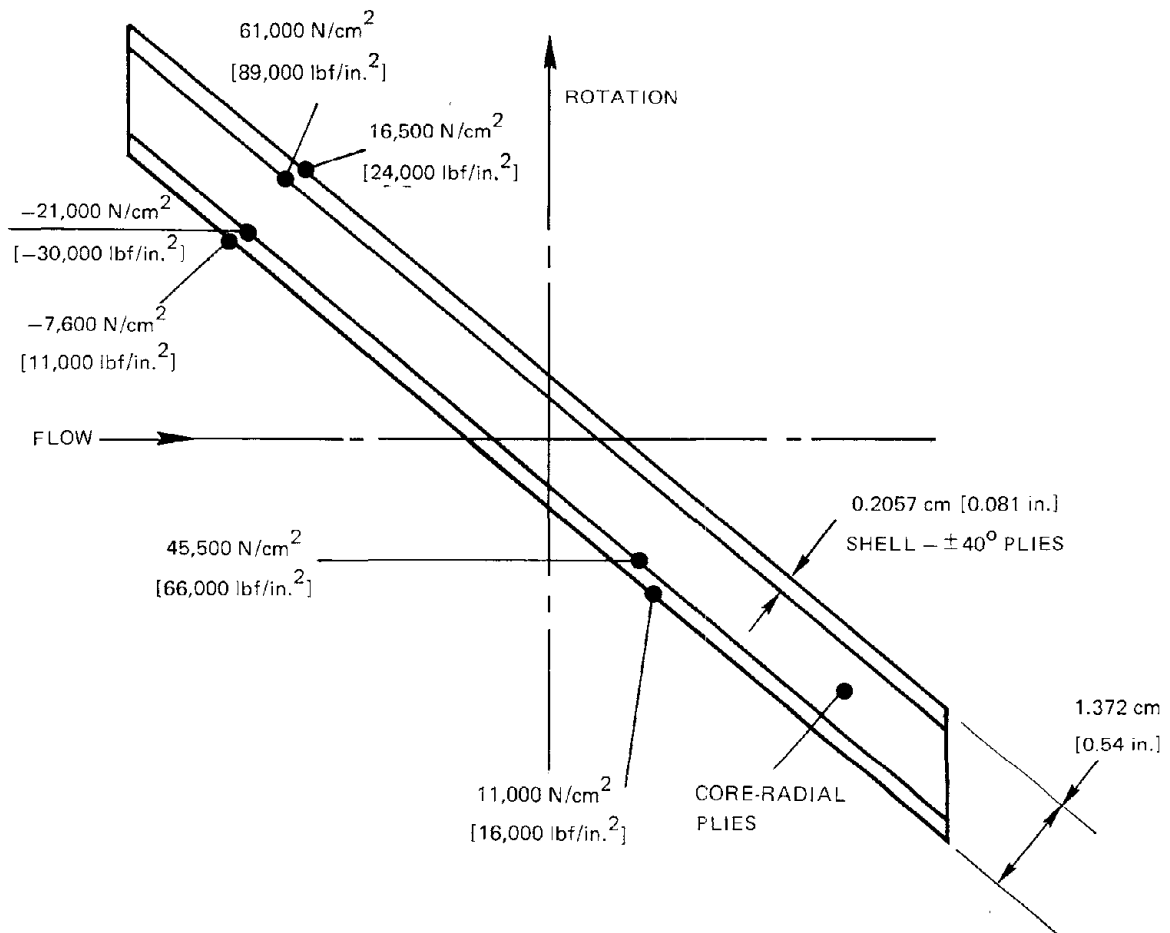


Figure 45 Blade Section in Root Area (0.1829 m [7.2 in.] radius)

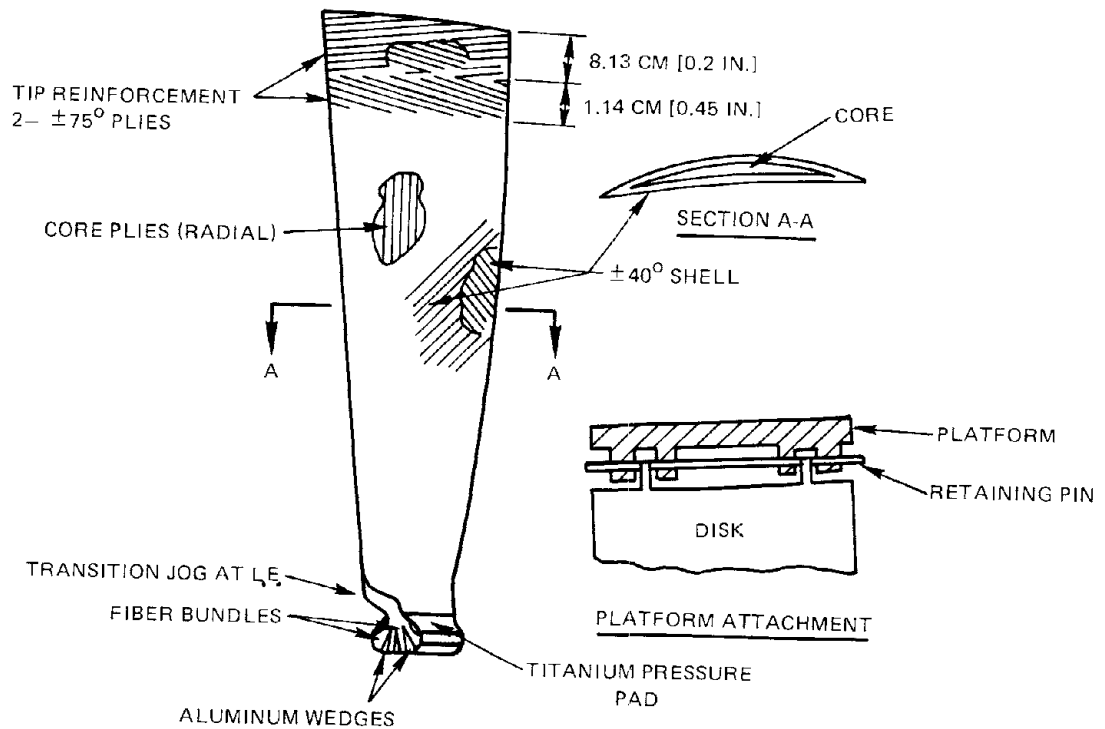


Figure 46 Blade Construction Details

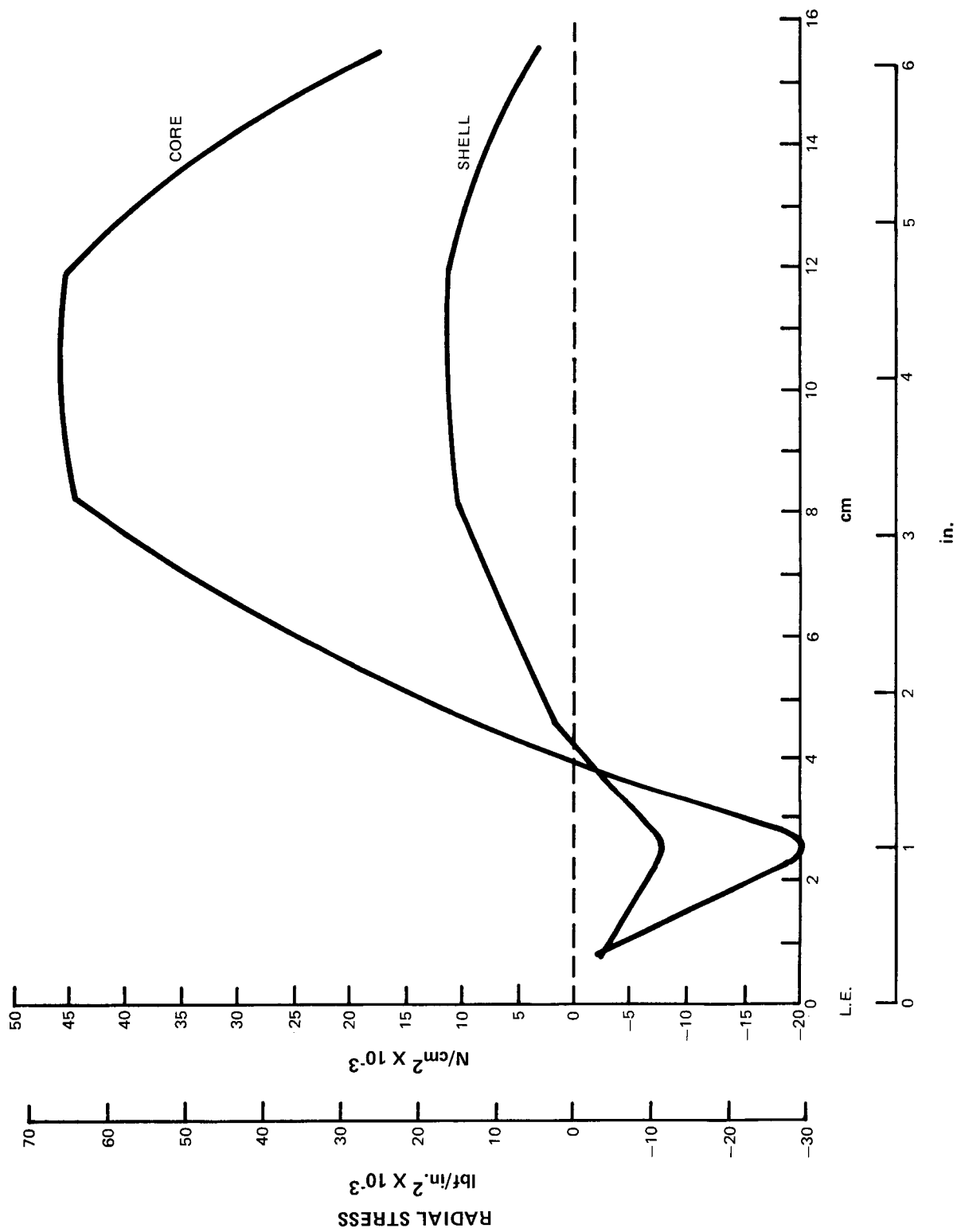


Figure 47 Centrifugal Stress, Suction Surface (0.1829 m [7.2 in.] radius)

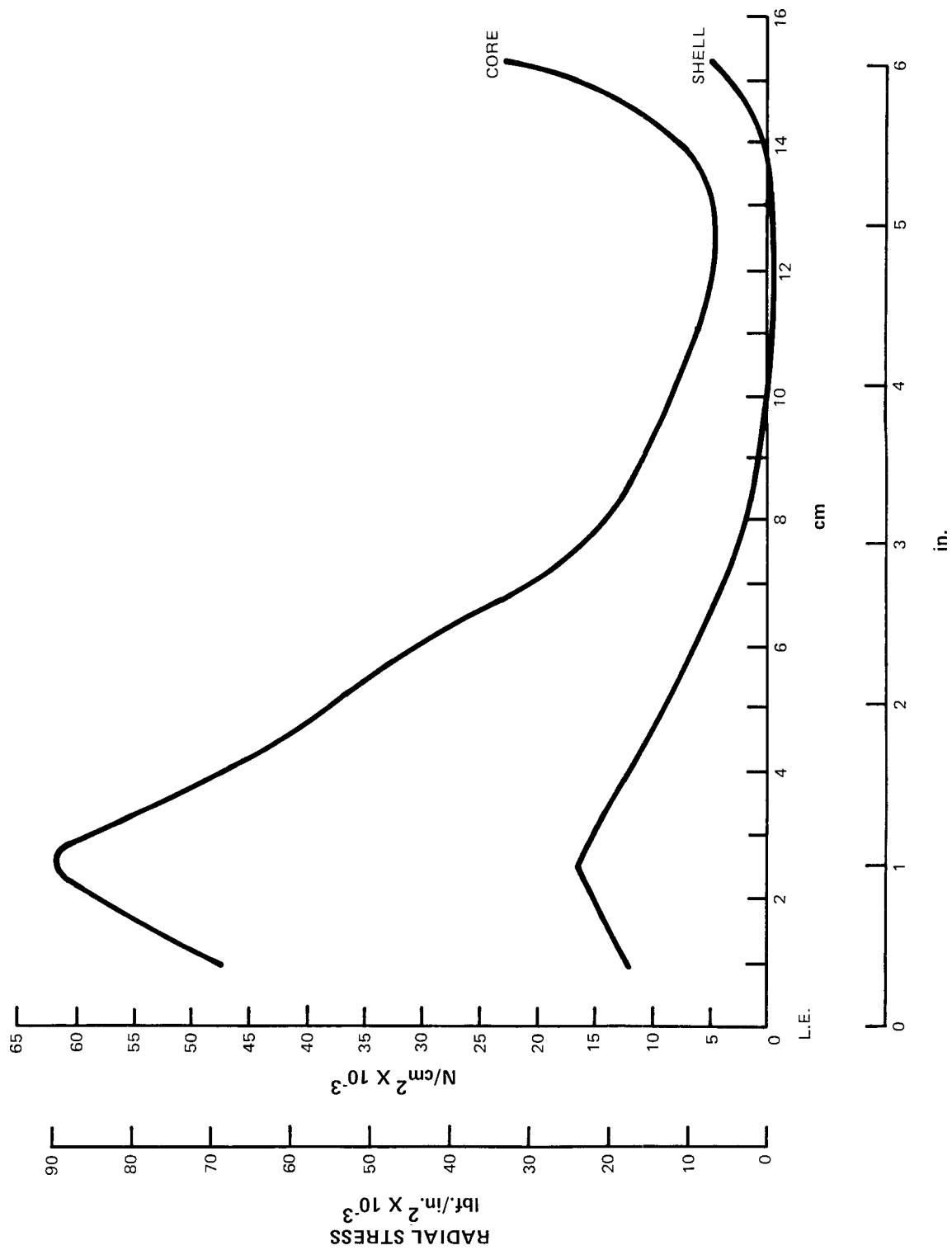


Figure 48 Centrifugal Stress, Pressure Surface (0.1829 m [7.2 in.] radius)

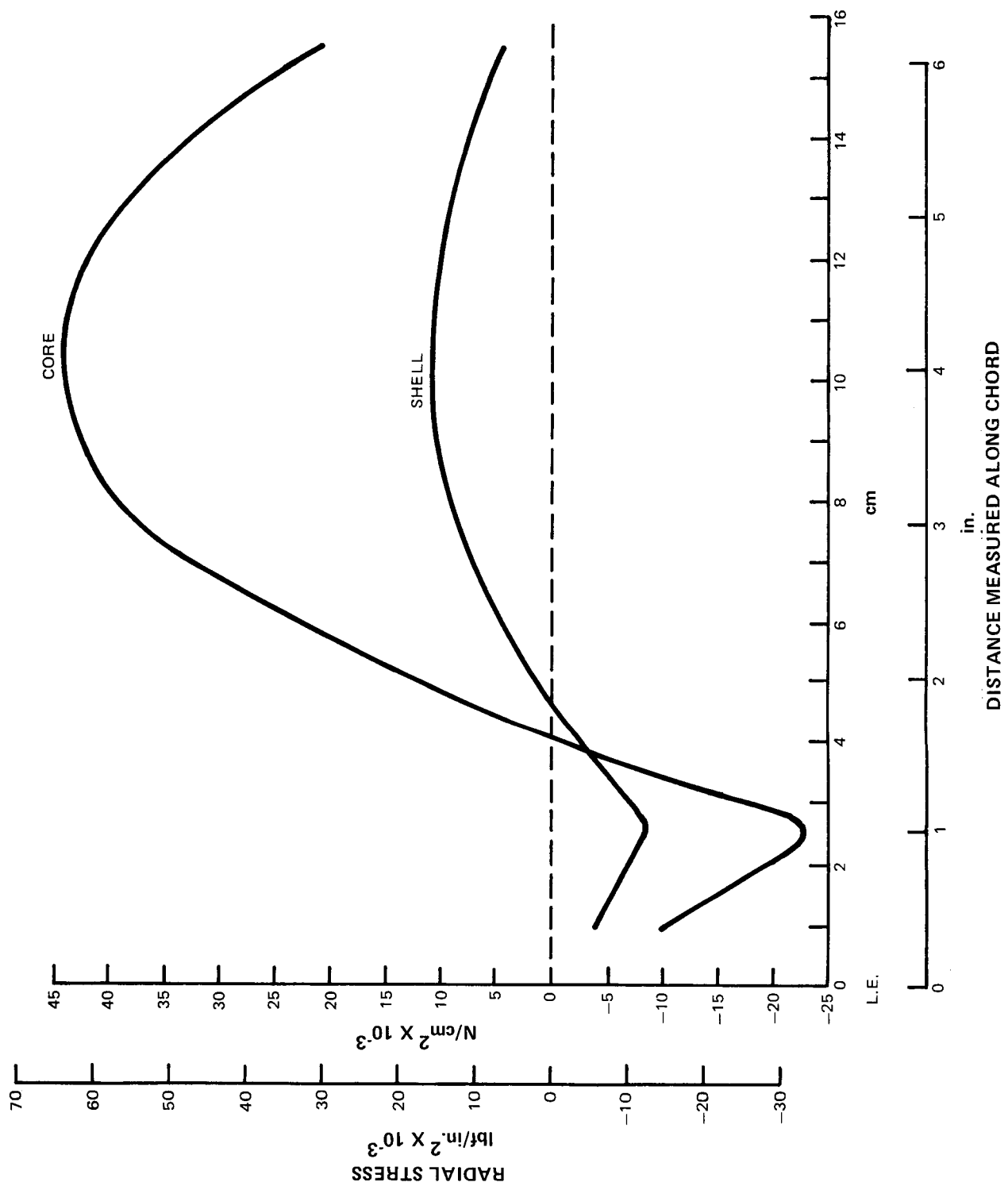


Figure 49 Centrifugal Stress, Suction Surface (0.1857 m [7.31 in.] radius)

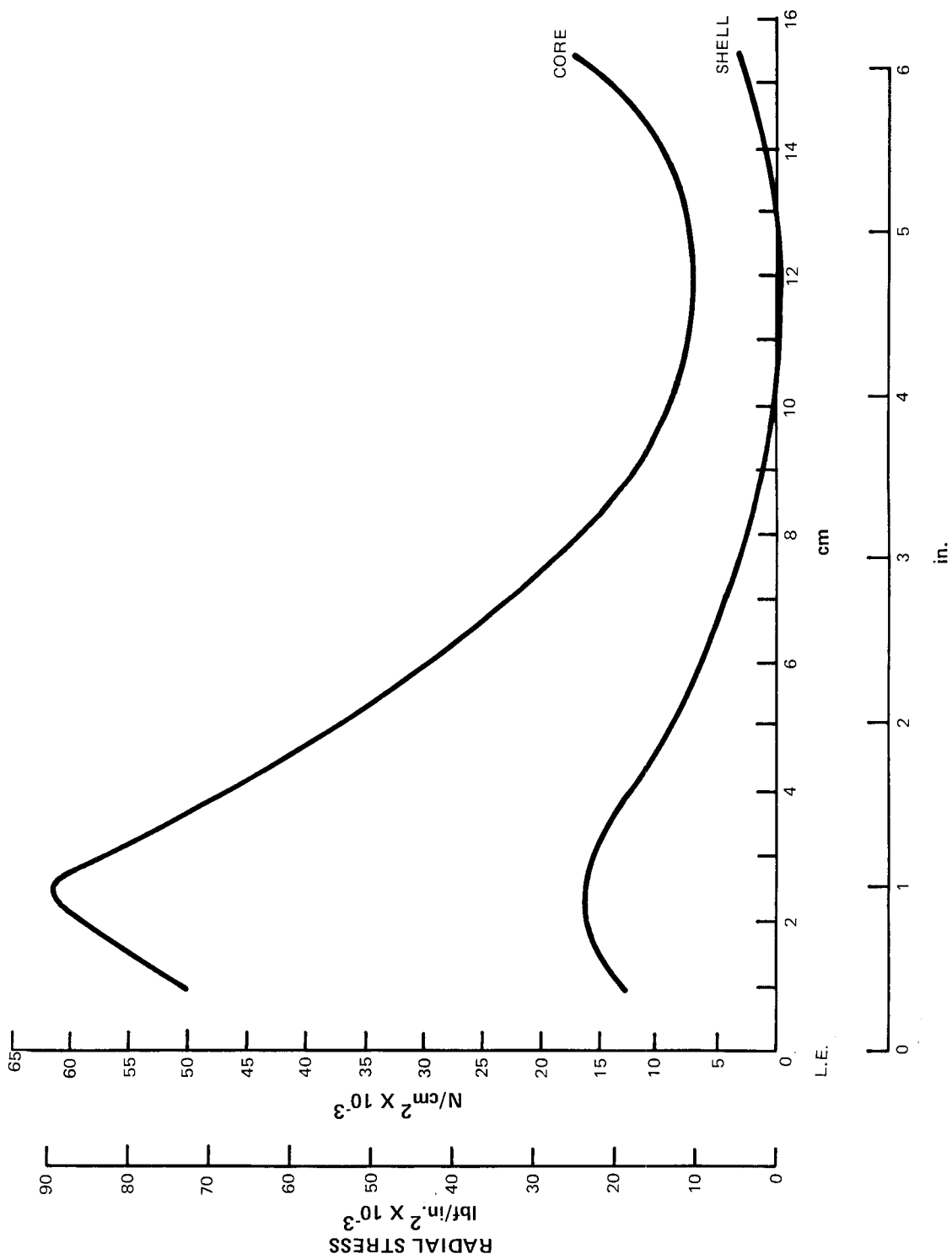


Figure 50 Centrifugal Stress, Pressure Surface (0.1857 m [7.32 in.] radius)

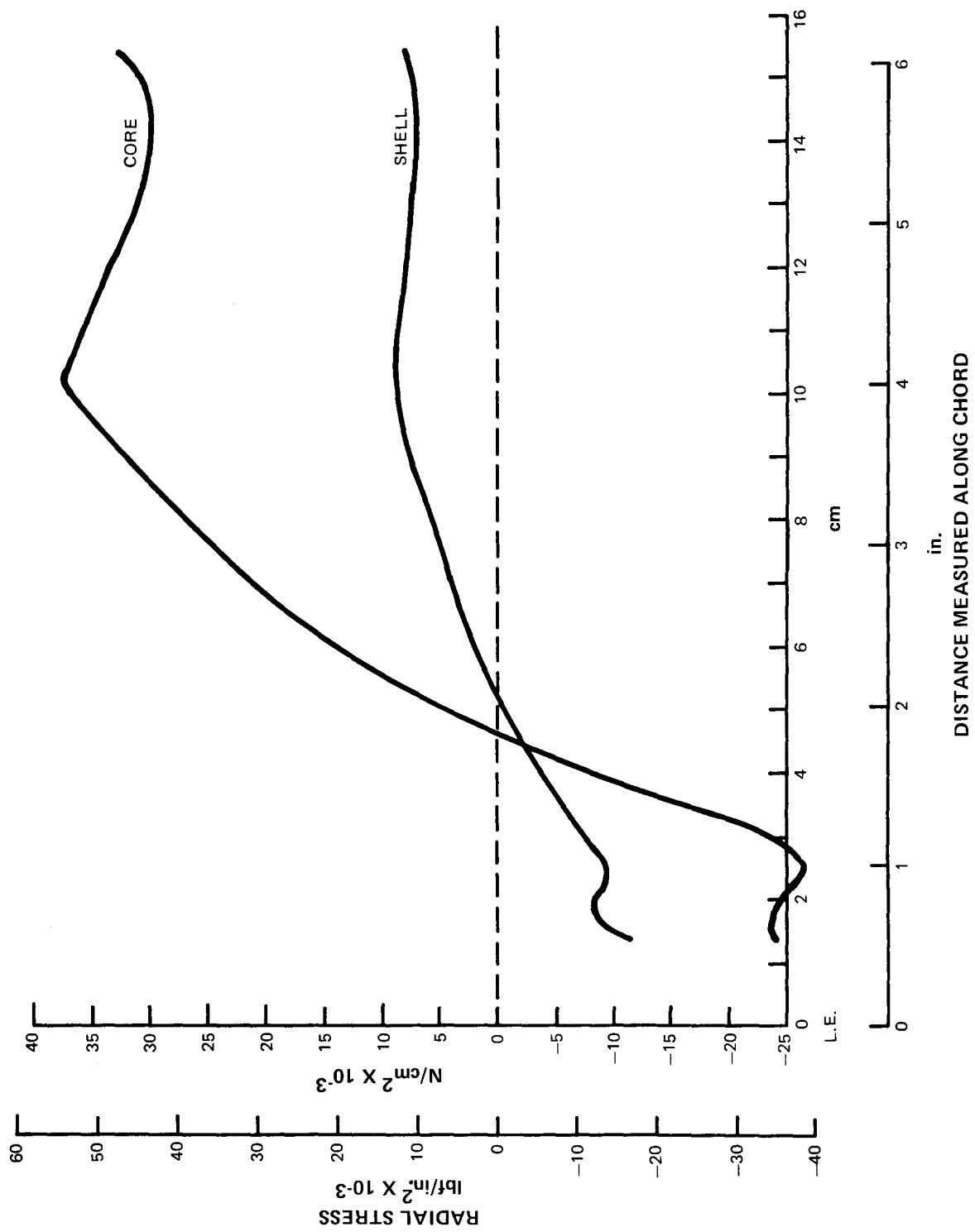


Figure 51 Centrifugal Stress, Suction Surface (0.1923 m [7.57 in.] radius)

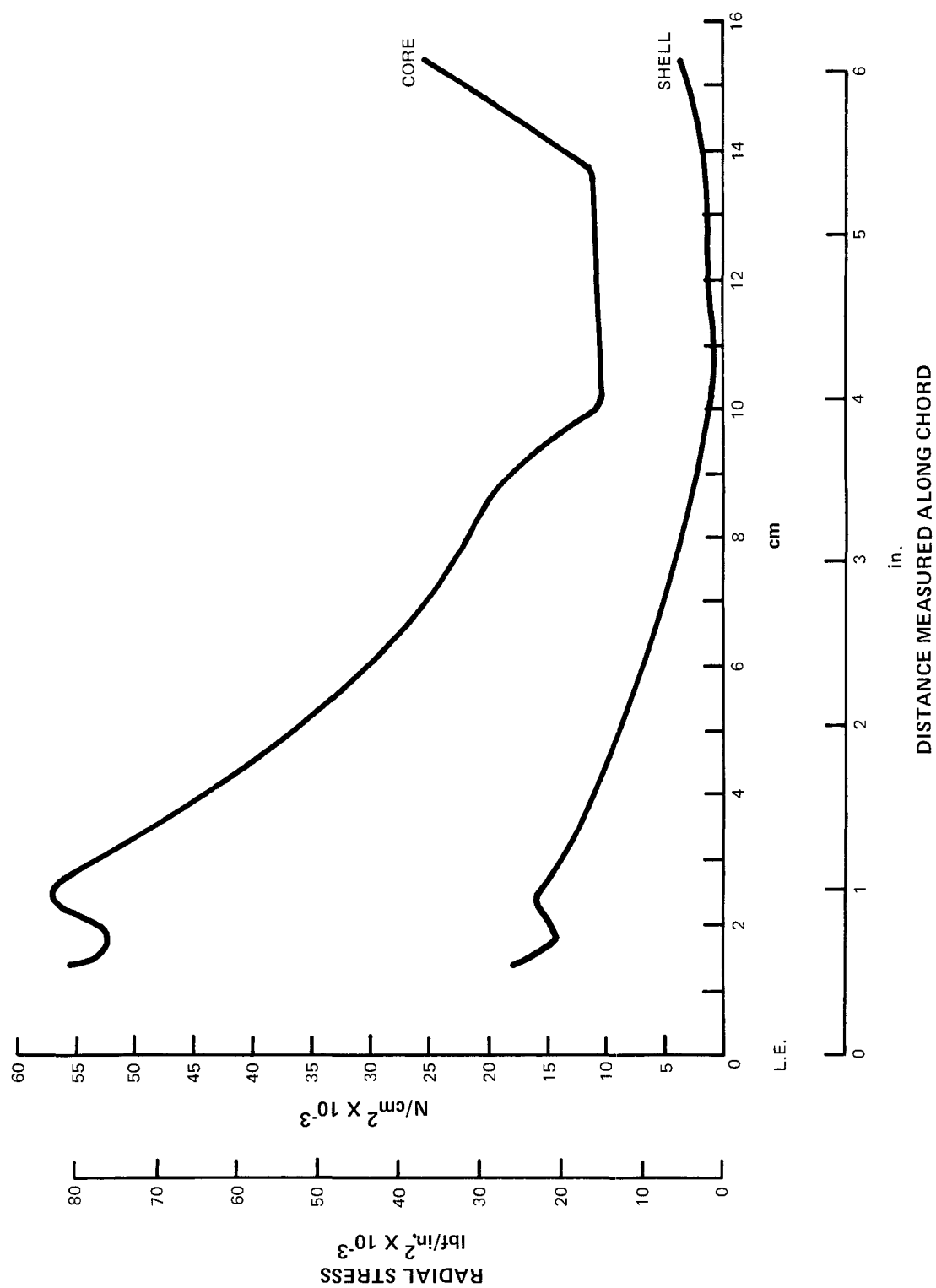


Figure 52 Centrifugal Stress, Pressure Surface (0.1923 m [7.57 in.] radius)

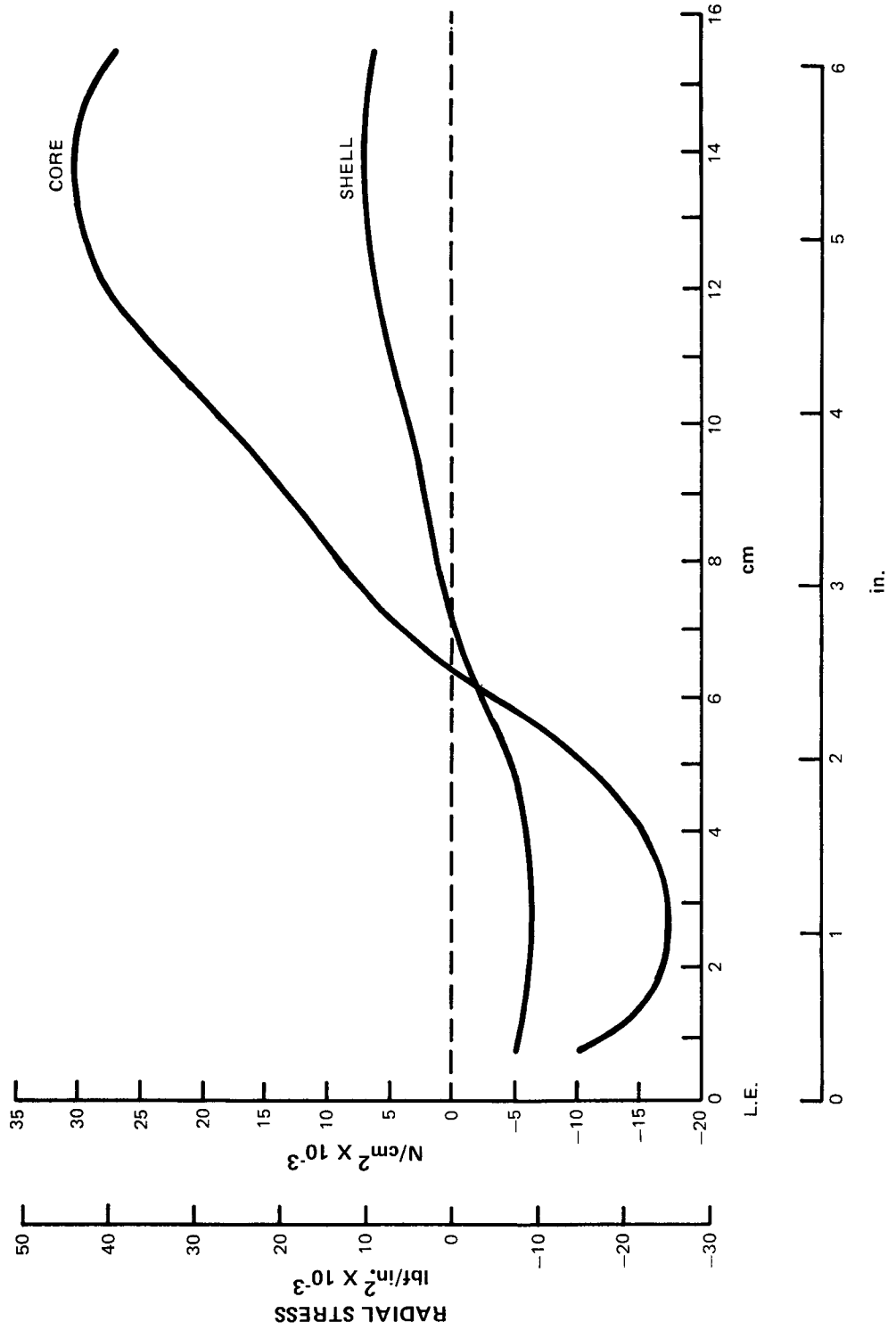


Figure 53 Centrifugal Stress, Suction Surface (0.2017 m [7.94 in.] radius)

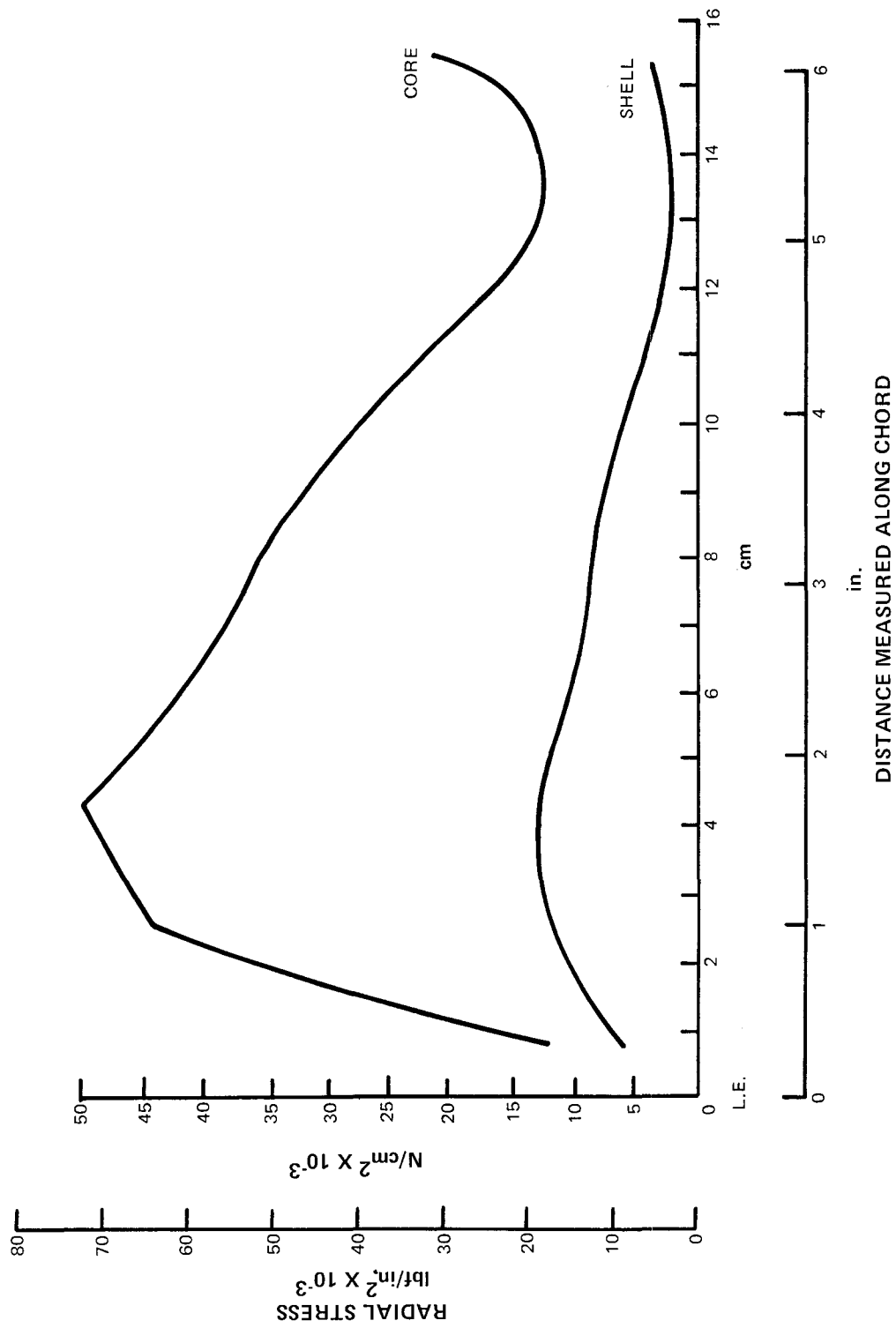


Figure 54 Centrifugal Stress, Pressure Surface (0.2017 m [7.94 in.] radius)

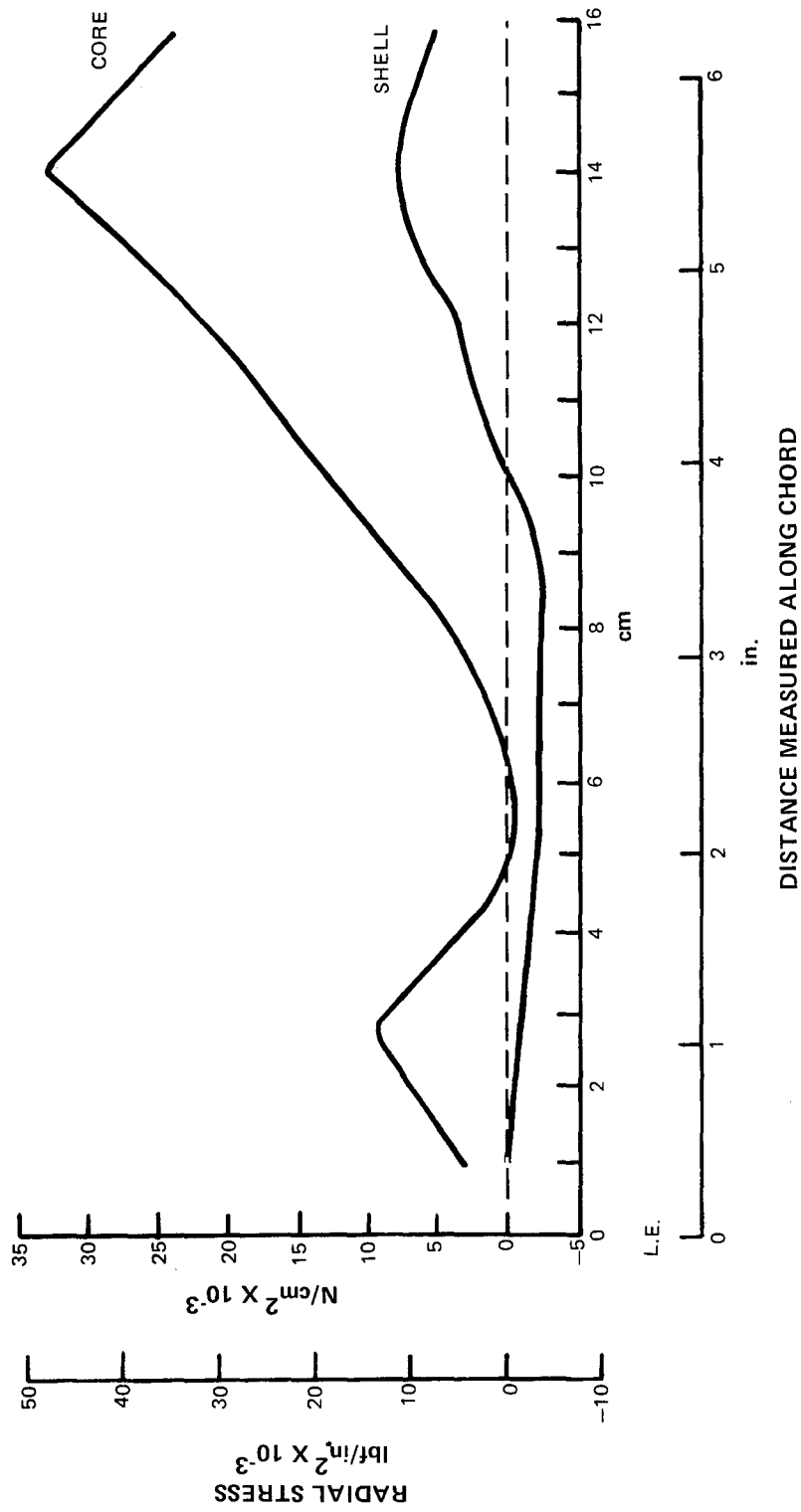


Figure 55 Centrifugal Stress, Suction Surface (0.2182 m [8.59 in.] radius)

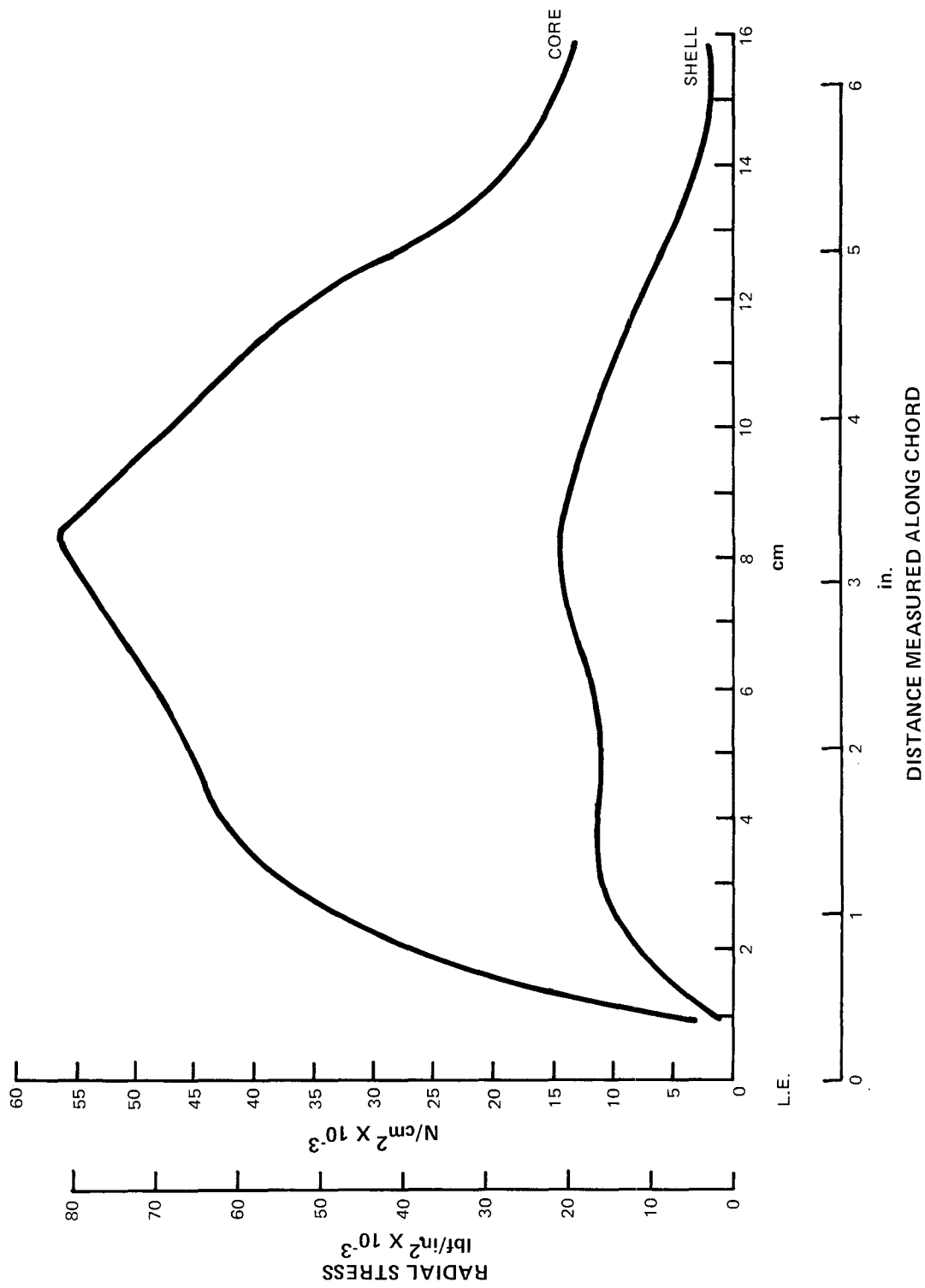


Figure 56 Centrifugal Stress, Pressure Surface (0.2182 m [8.59 in.] radius)

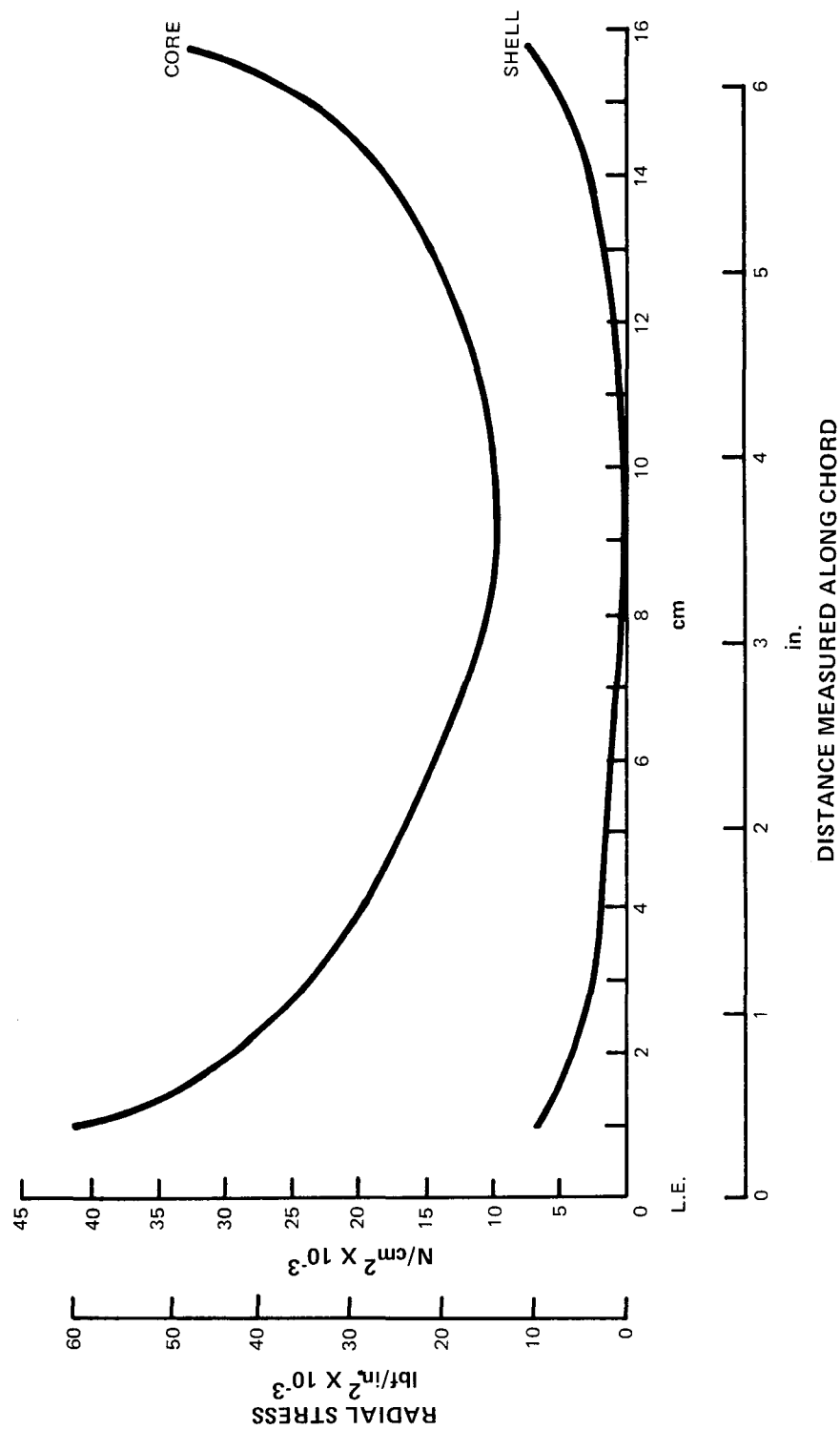


Figure 57 Centrifugal Stress, Suction Surface (0.2393 m [9.42 in.] radius)

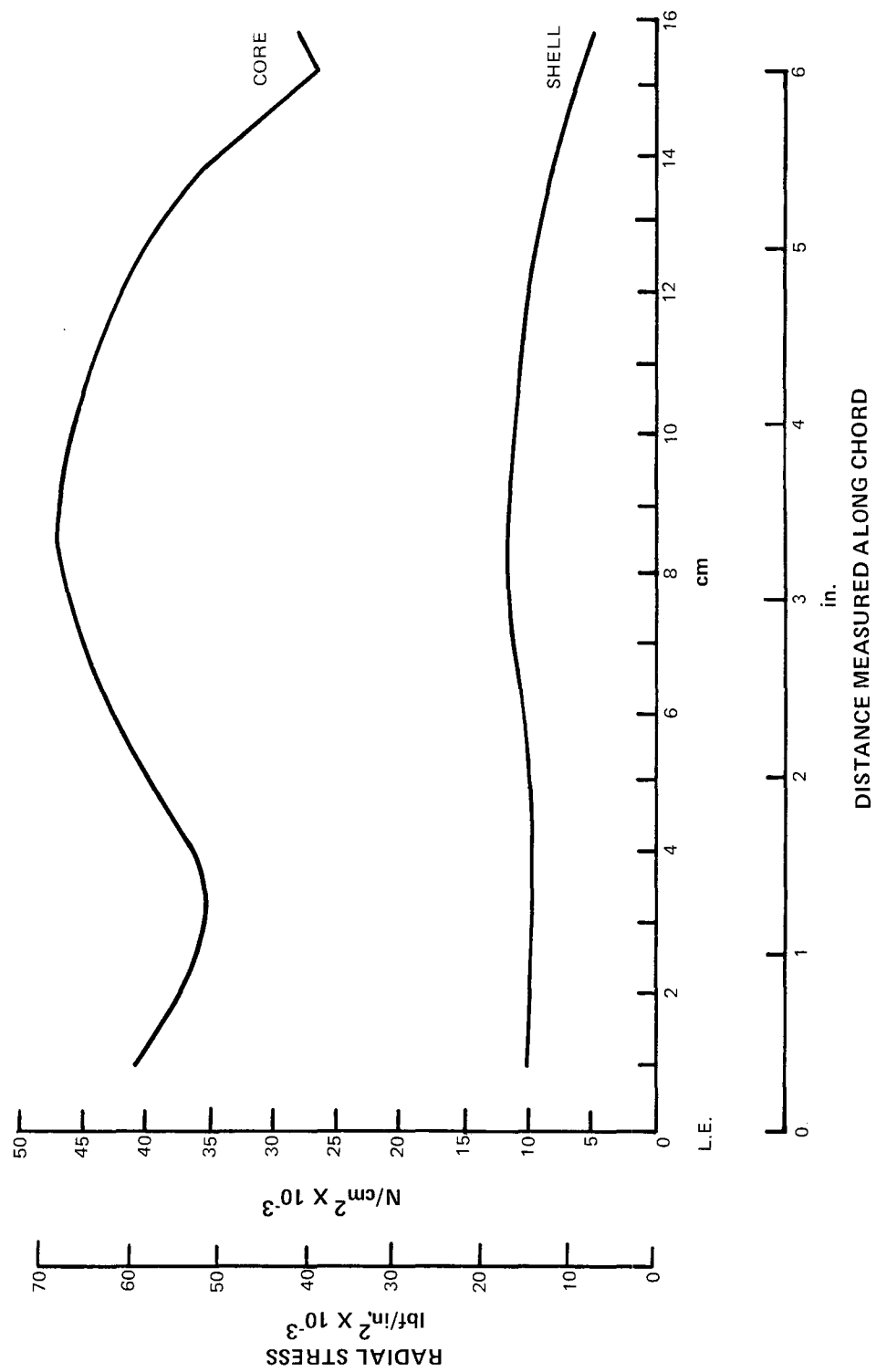


Figure 58 Centrifugal Stress, Pressure Surface (0.2393 m [9.42 in.] radius)

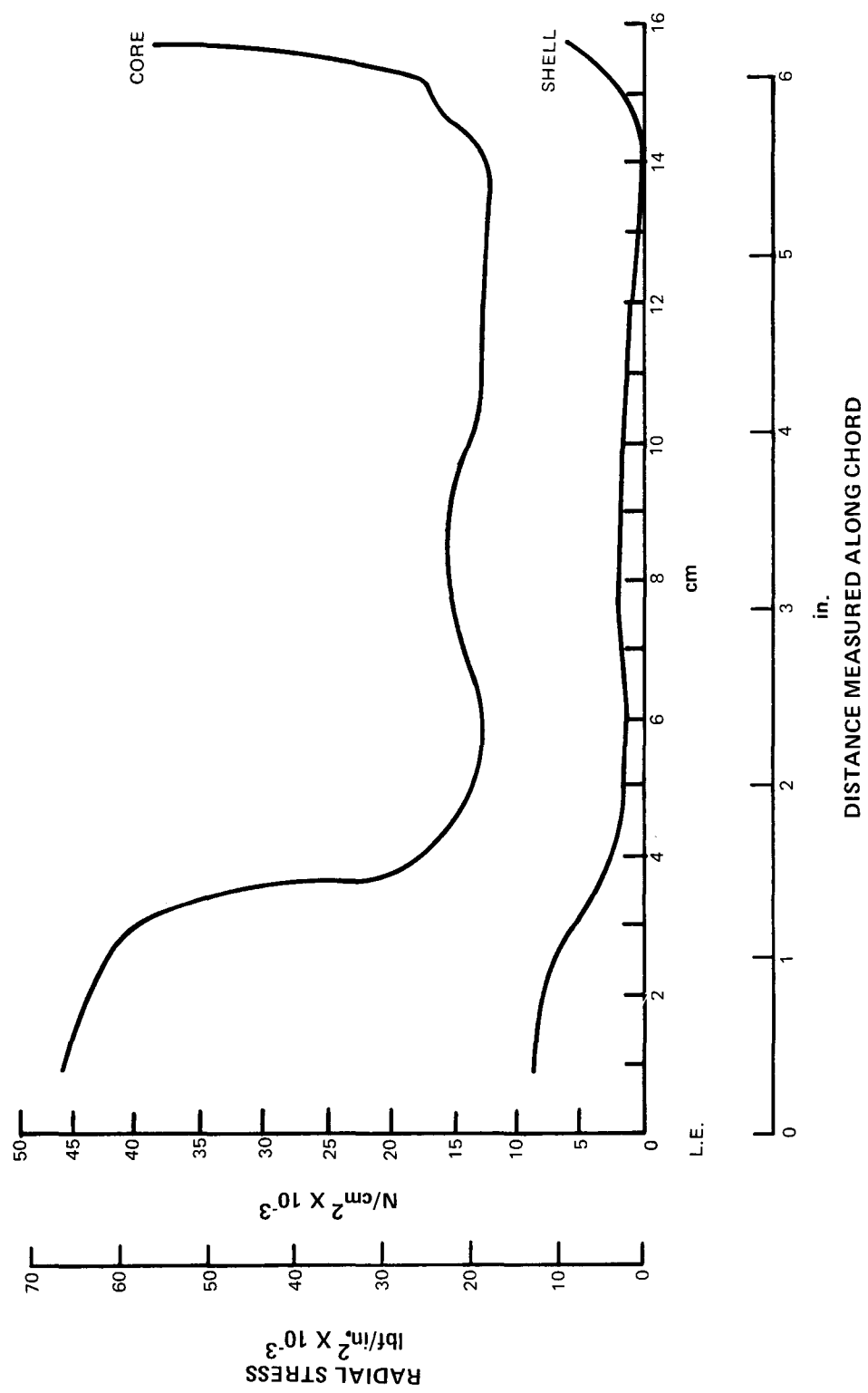


Figure 59 Centrifugal Stress, Suction Surface (0.2769 m [10.9 in.] radius)

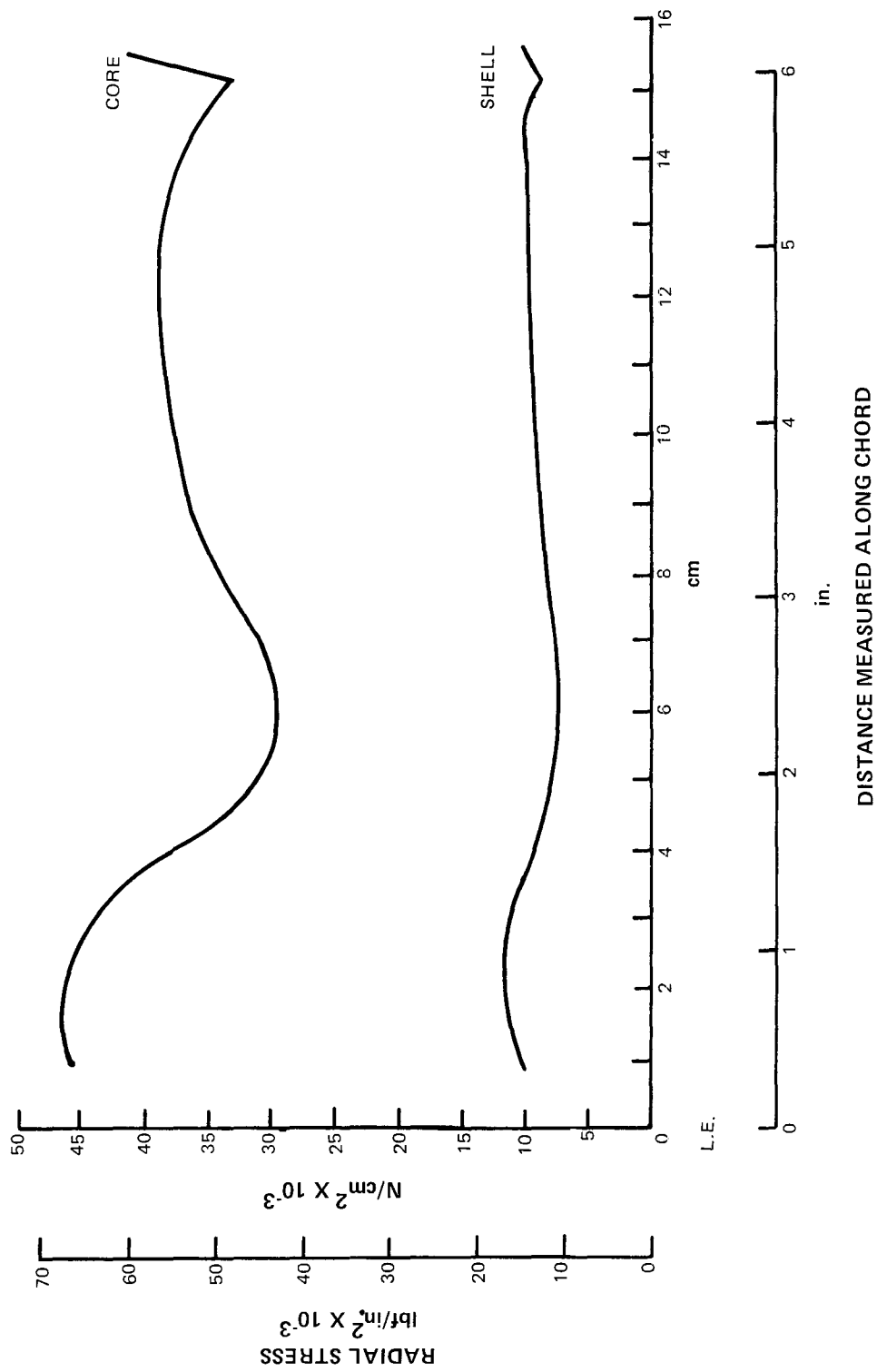


Figure 60 Centrifugal Stress, Pressure Surface (0.2769 m [10.9 in.] radius)

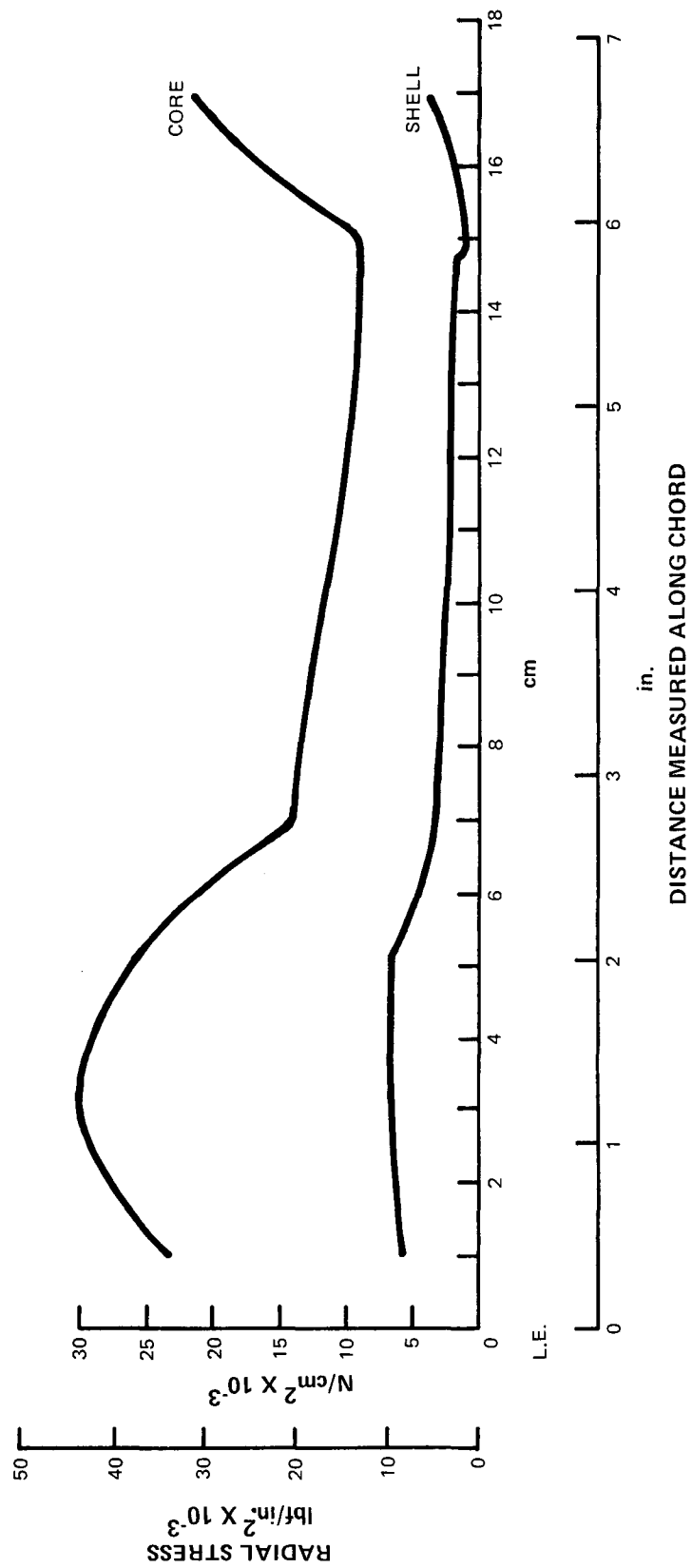


Figure 61 Centrifugal Stress, Suction Surface (0.3713 m [14.62] radius)

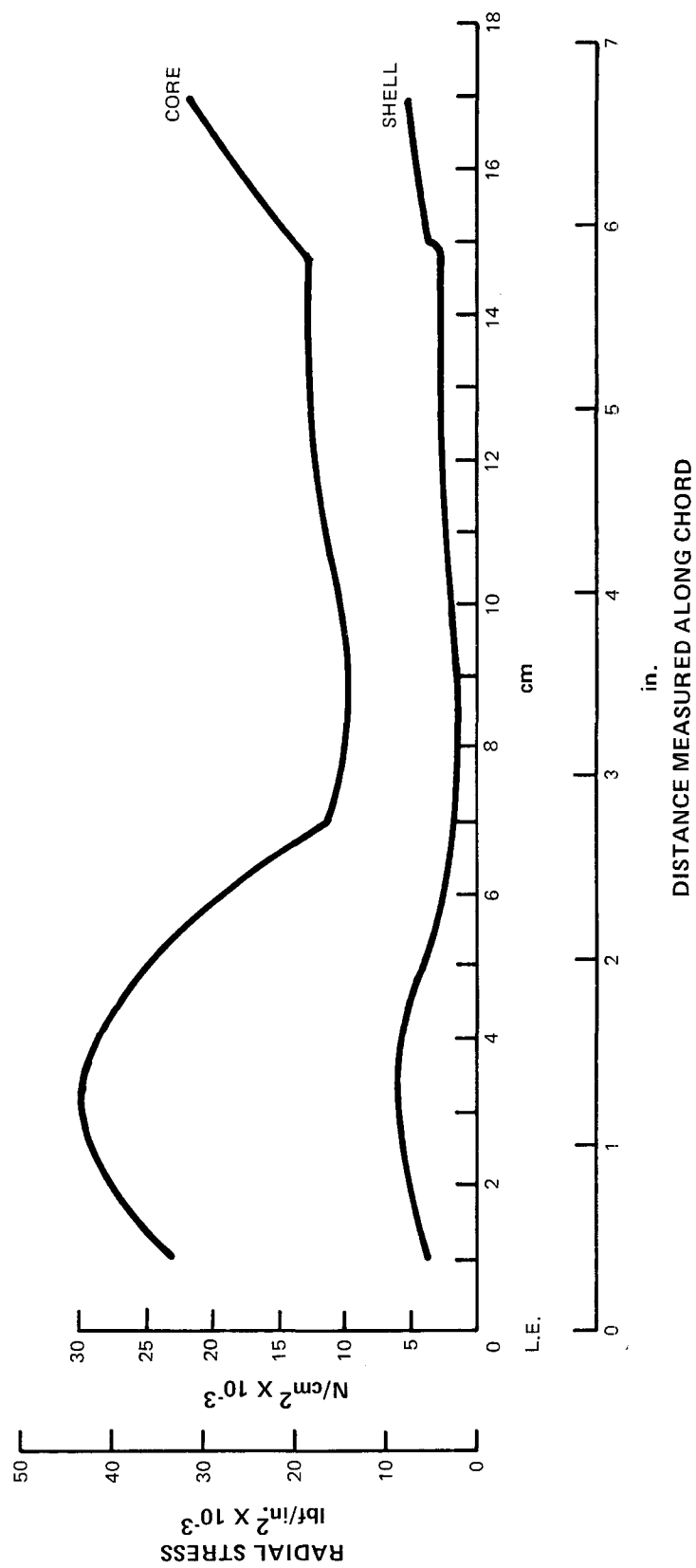
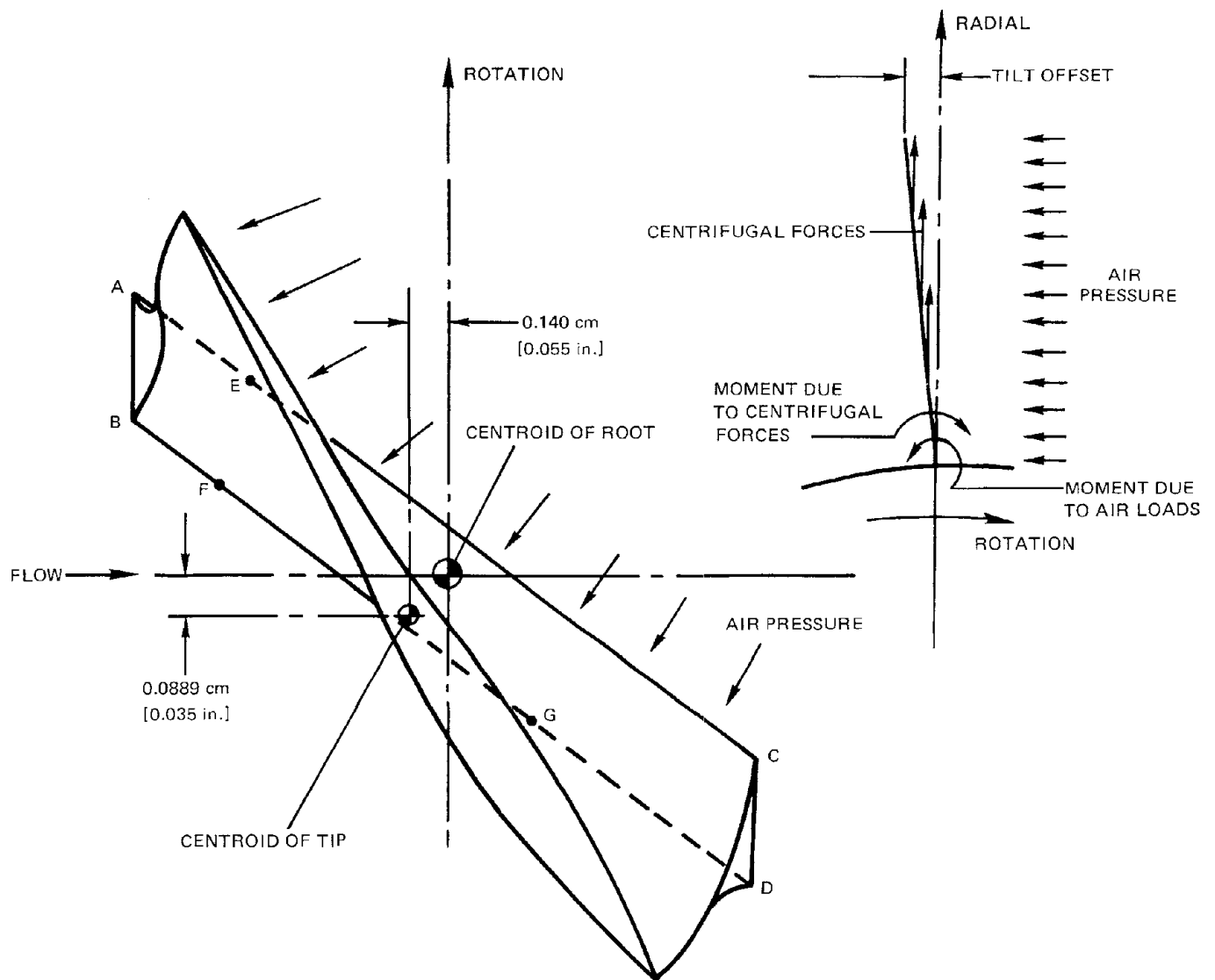


Figure 62 Centrifugal Stress, Pressure Surface (0.3713 m [14.62 in.] radius)



CORE STRESSES, N/cm [lbf/in.²] $\times 10^{-3}$

POINT	A	B	C	D	E	F	G
CENTRIFUGAL	11.7 [17]	-6.89 [-10]	-22.8 [-33]	17.2 [25]	61.4 [89]	-20.7 [-30]	45.5 [66]
AIR LOAD (50.8 cm Hg)	2.8 [4]	-10.3 [-15]	+10.3 [+15]	-2.1 [-3]	2.8 [+4]	-7.58 [-11]	-8.96 [-13]
AIR LOAD + TILT	0.34 [0.5]	-1.4 [-2]	+1.4 [+2]	-0.34 [-0.5]	+0.34 [+0.5]	-1.4 [-2]	-1.4 [-2]
NORMAL OPERATING	12.07 [17.5]	-8.27 [-12]	-21.4 [-31]	+16.89 [+24.5]	+61.71 [+89.5]	-22.8 [-33]	+44.1 [+64]
SURGE (LESS AIR LOAD)	9.31 [13.5]	+2.1 [+3]	-31.7 [-46]	+18.96 [+27.5]	58.95 [+85.5]	-15.2 [-22]	+53.1 [+77]

Figure 64 Blade Tilt to Offset Air Loads

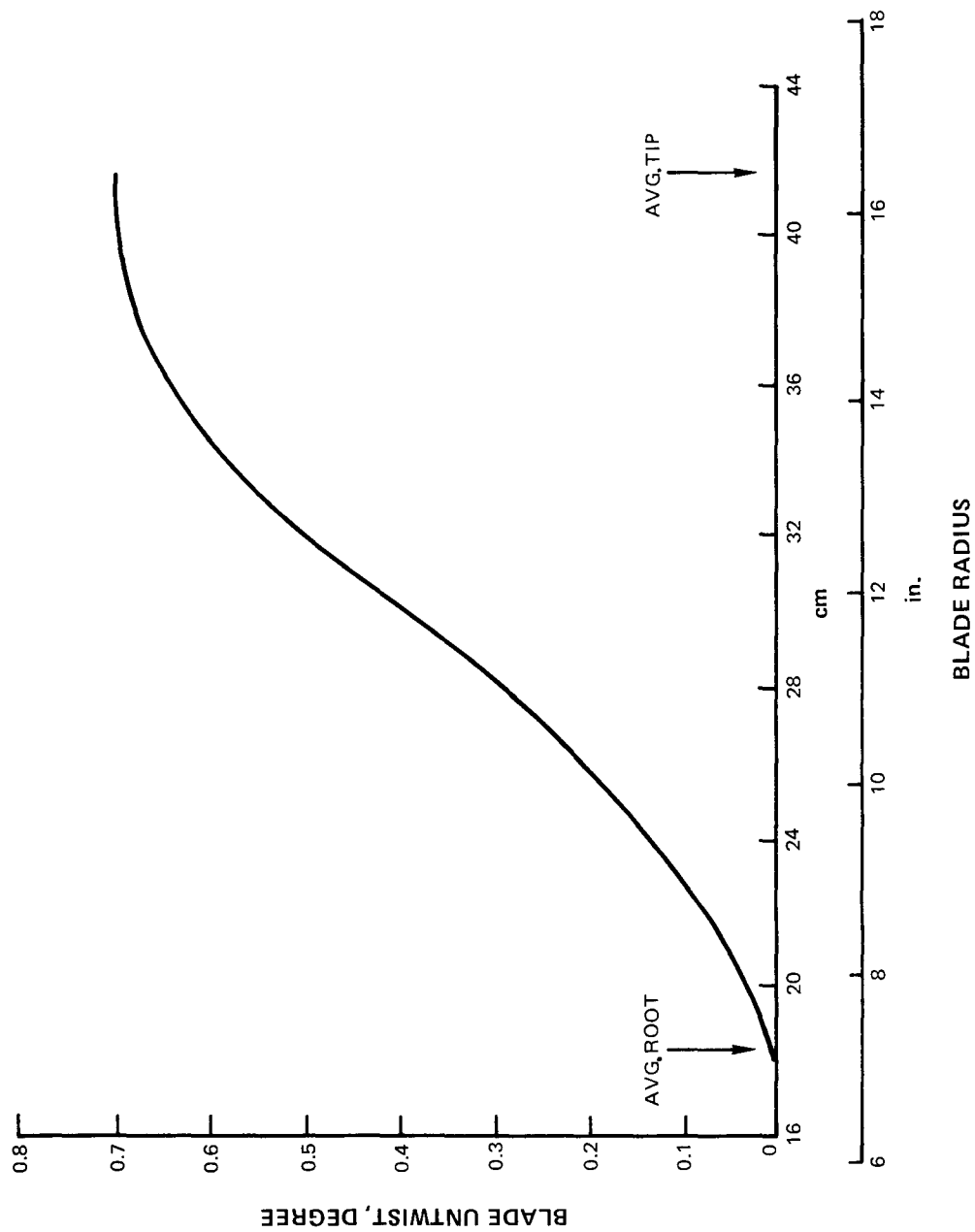


Figure 65 Blade Untwist as a Function of Blade Radius

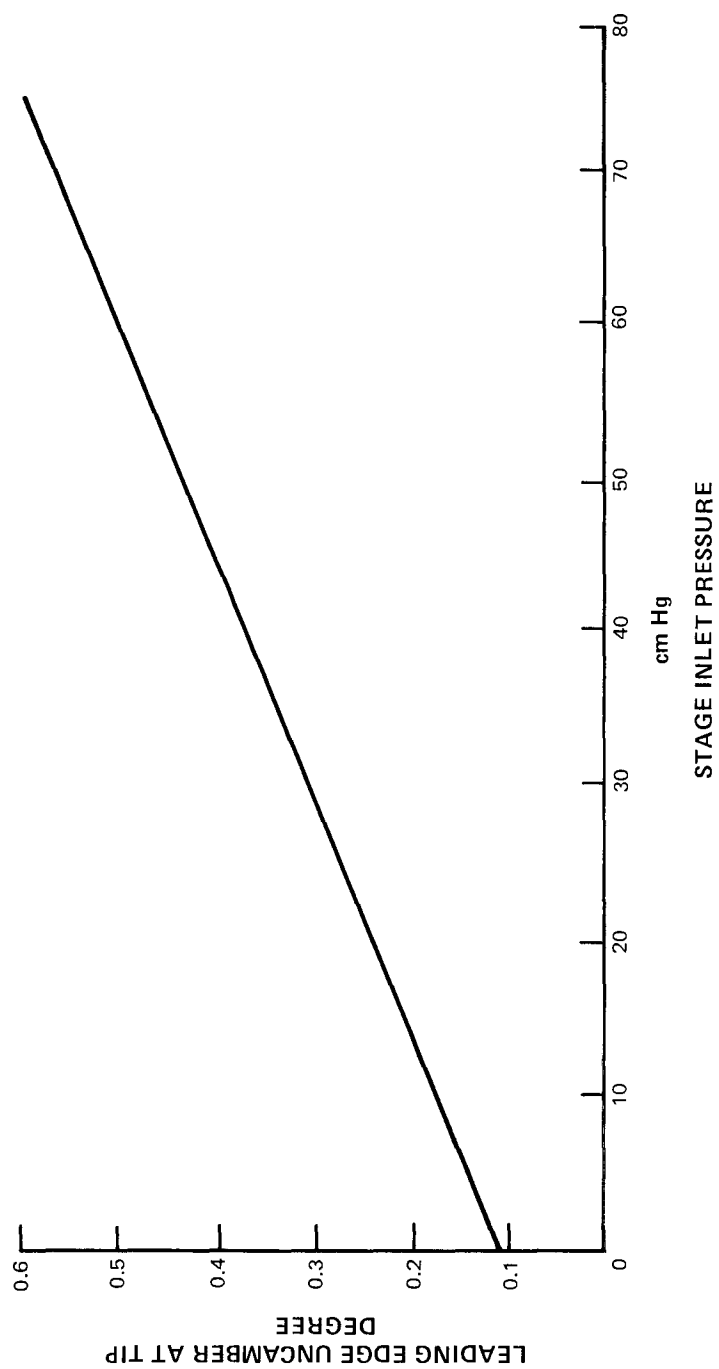


Figure 66 Leading Edge Uncamber as a Function of Inlet Pressure

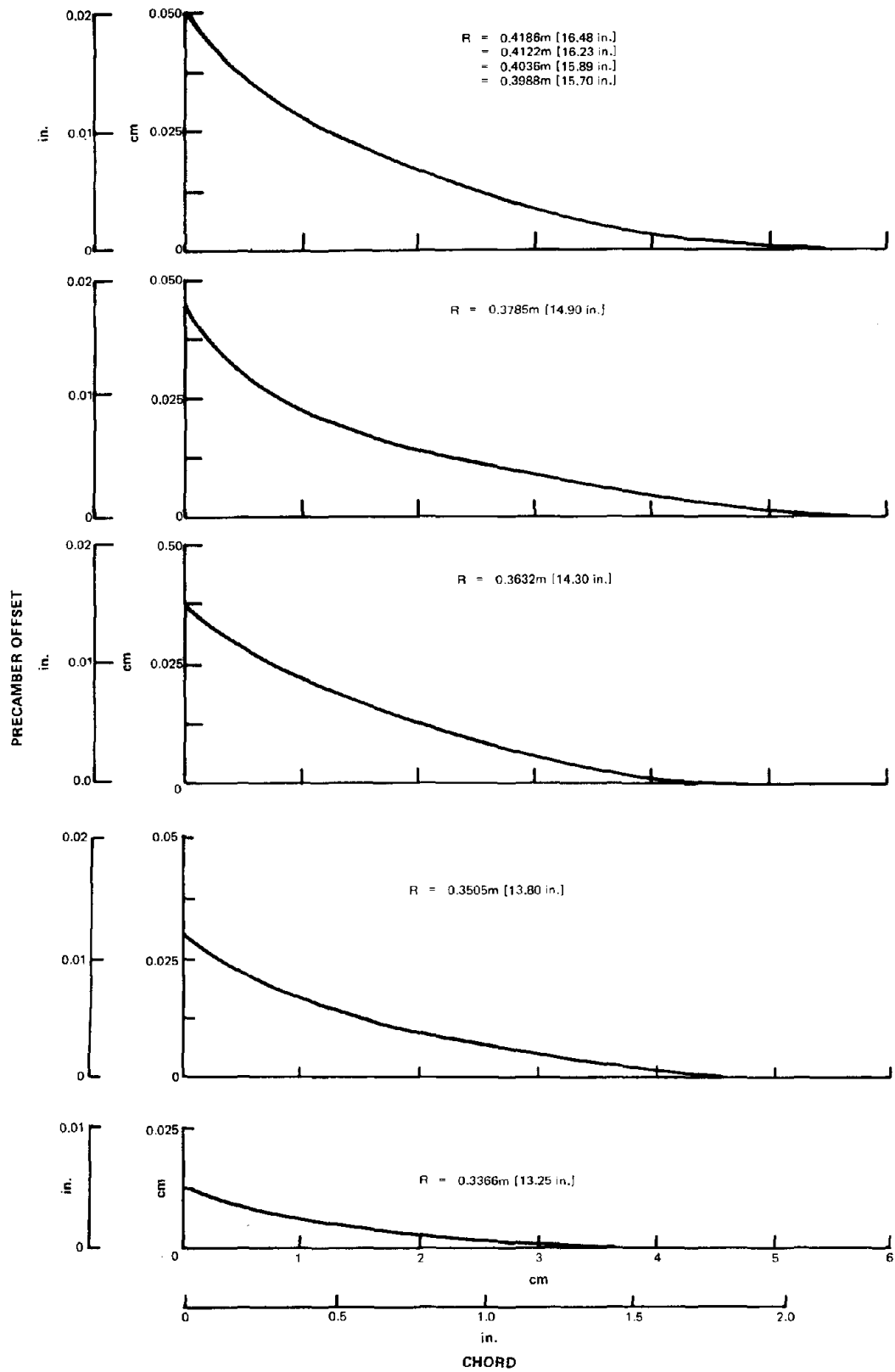
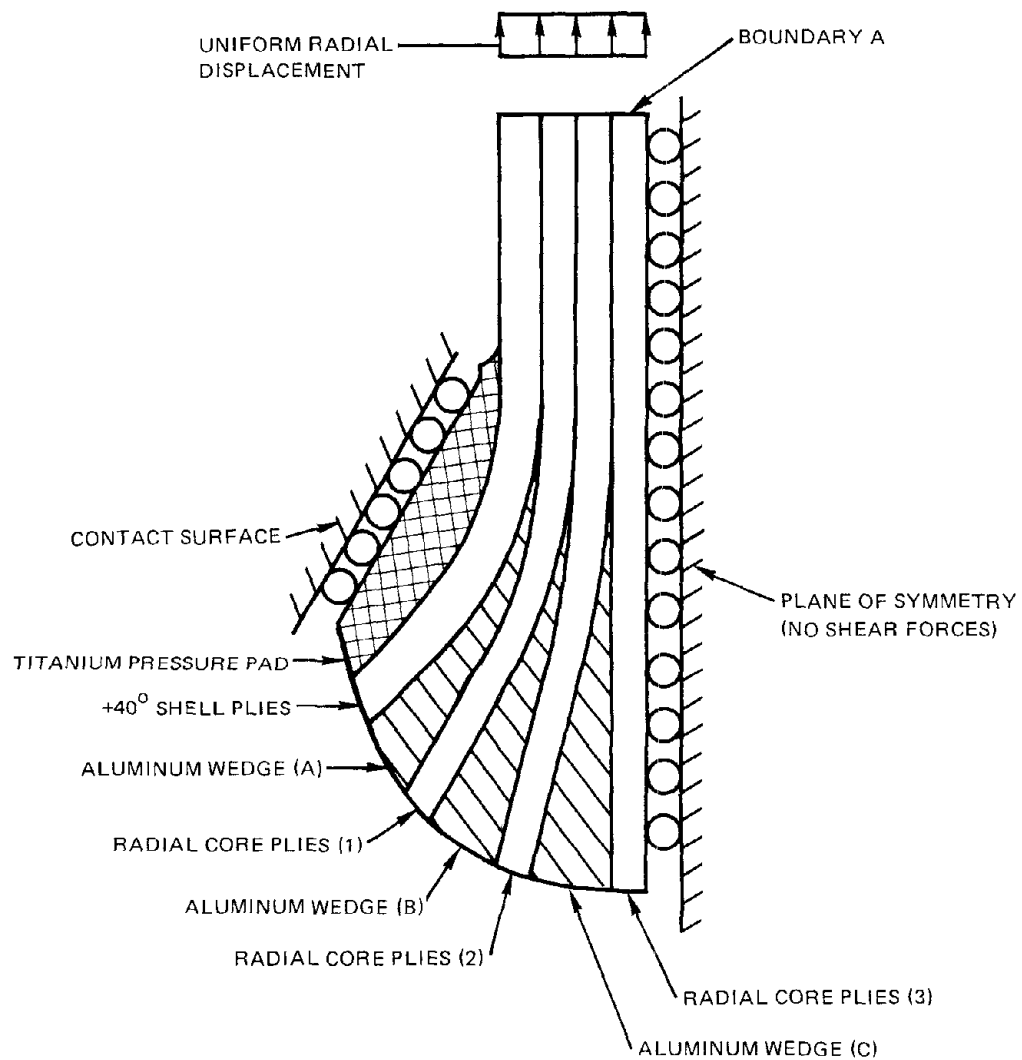


Figure 67 Precamber Offset Curves for Tip Leading Edge



BOND SHEAR STRESS, N/cm^2 [lbf/in.^2] $\times 10^{-3}$

INTERFACE	PEAK SHEAR	AVERAGE SHEAR
PRESSURE PAD/SHELL PLIES	2.84 [7.7]	0.793 [2.15]
SHELL PLIES/WEDGE (A)	1.92 [5.2]	
WEDGE (A)/CORE PLIES (1)	0.640 [4.7]	0.800 [2.17]
CORE PLIES (1)/WEDGE (B)	1.14 [3.1]	
WEDGE (B)/CORE PLIES (2)	1.51 [4.1]	0.491 [1.33]
CORE PLIES (2)/WEDGE (C)	0.516 [1.4]	
WEDGE (C)/CORE PLIES (3)	0.959 [2.6]	0.616 [1.67]

Figure 68 Six-Wedge Dovetail Configuration Analysis

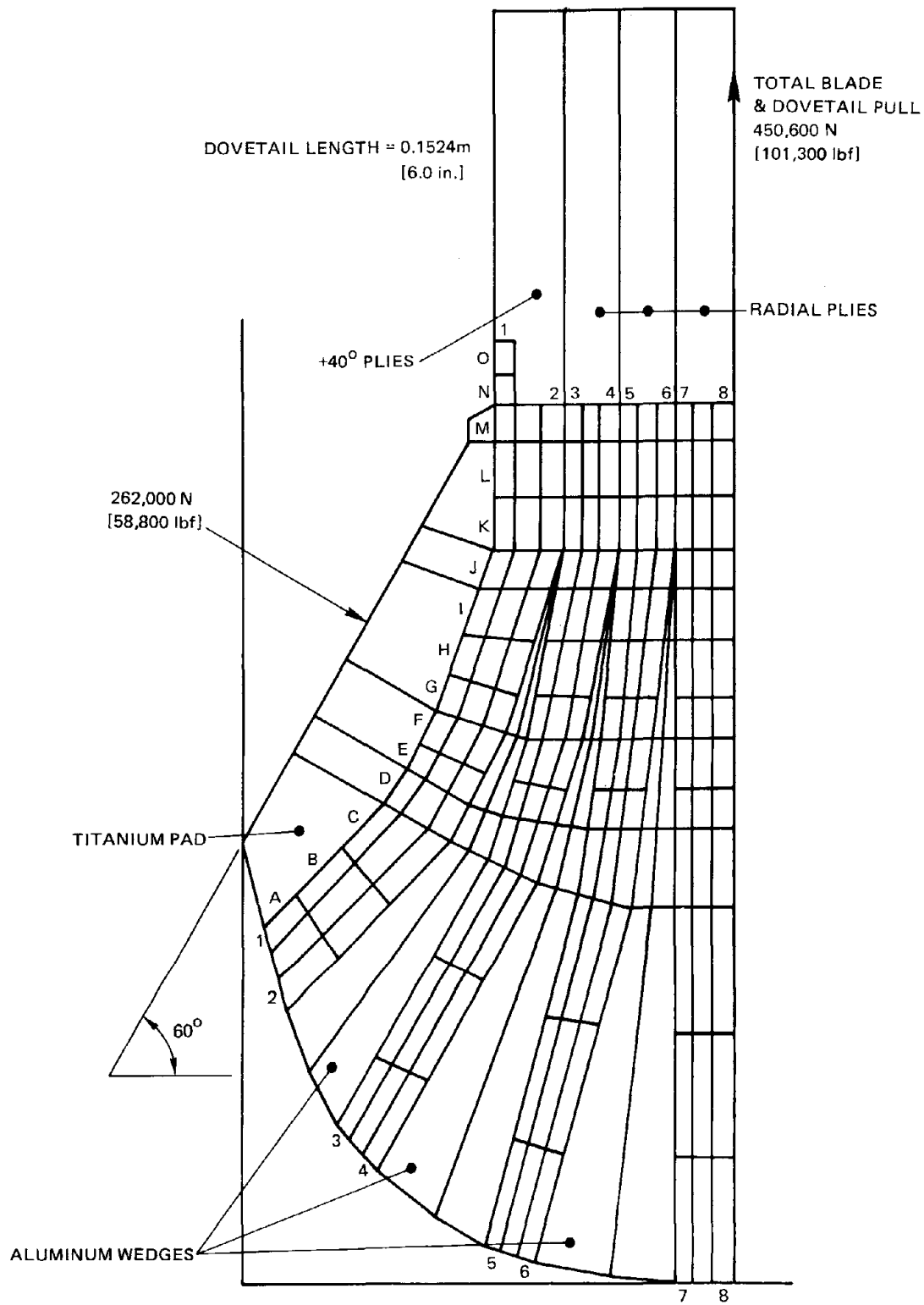


Figure 69 Identification of Stress Location Areas

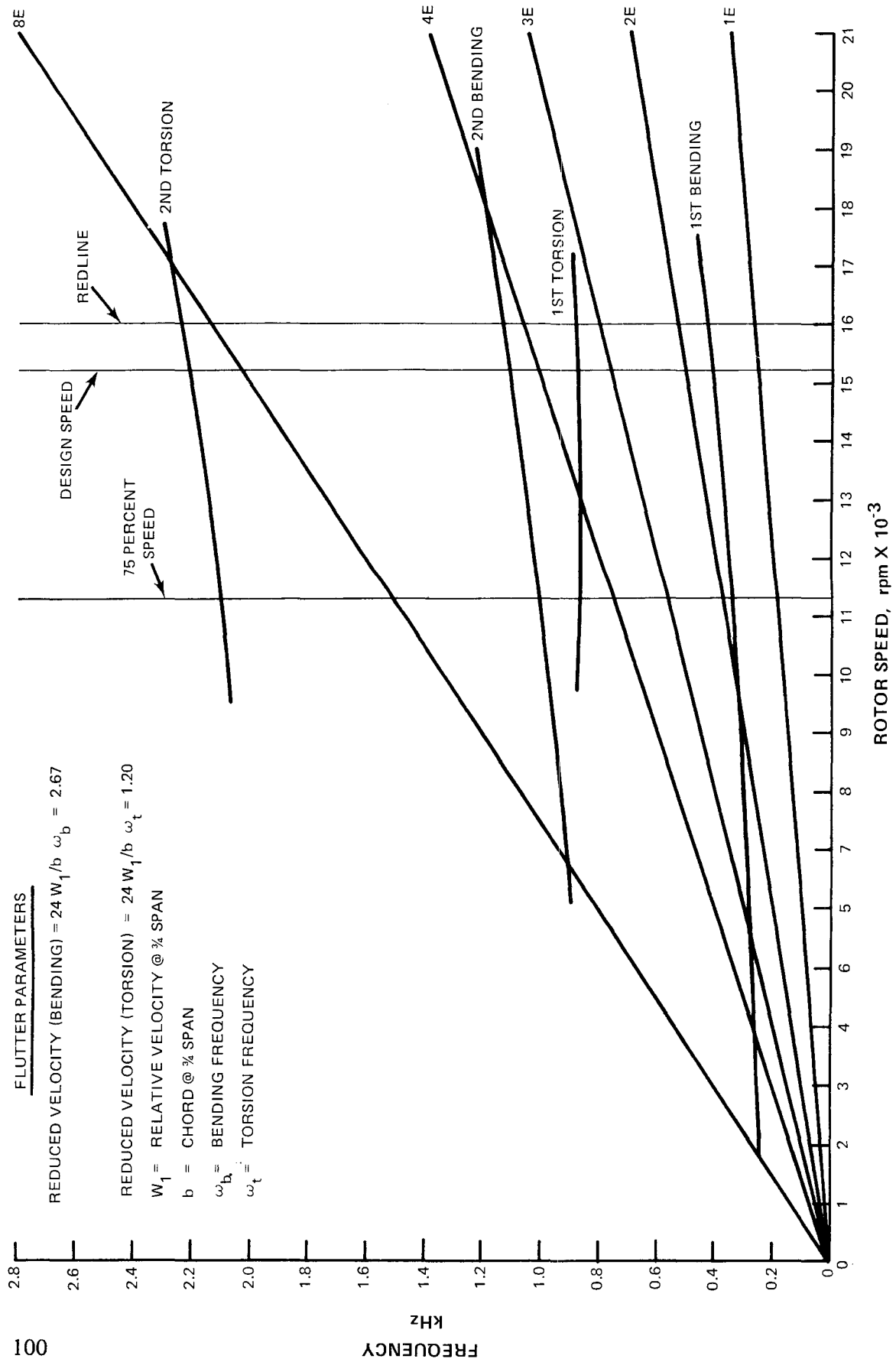


Figure 70 Campbell Diagram

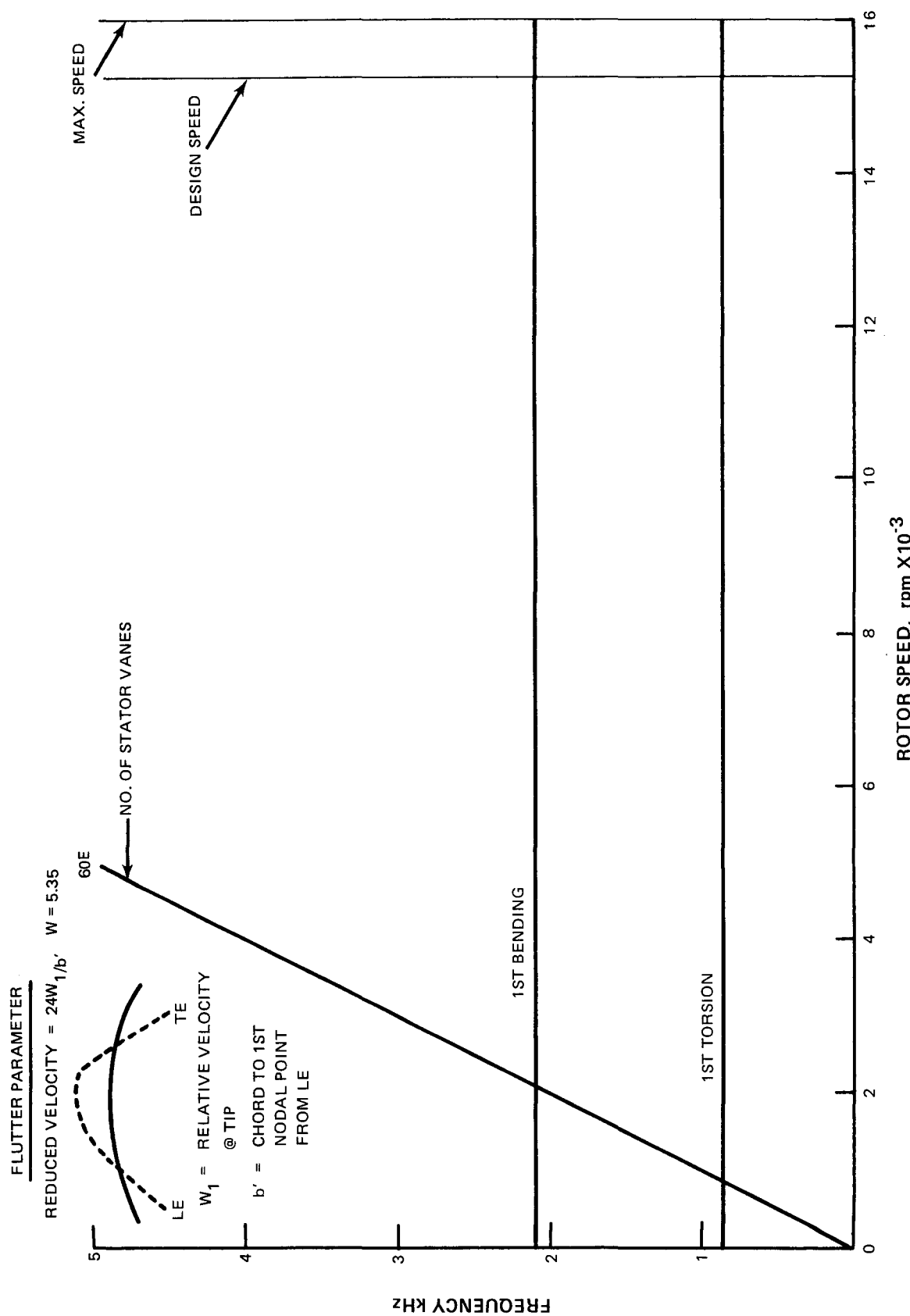


Figure 71 Campbell Diagram, Tip Modes (With $2 - \pm 75^\circ$ Plies)

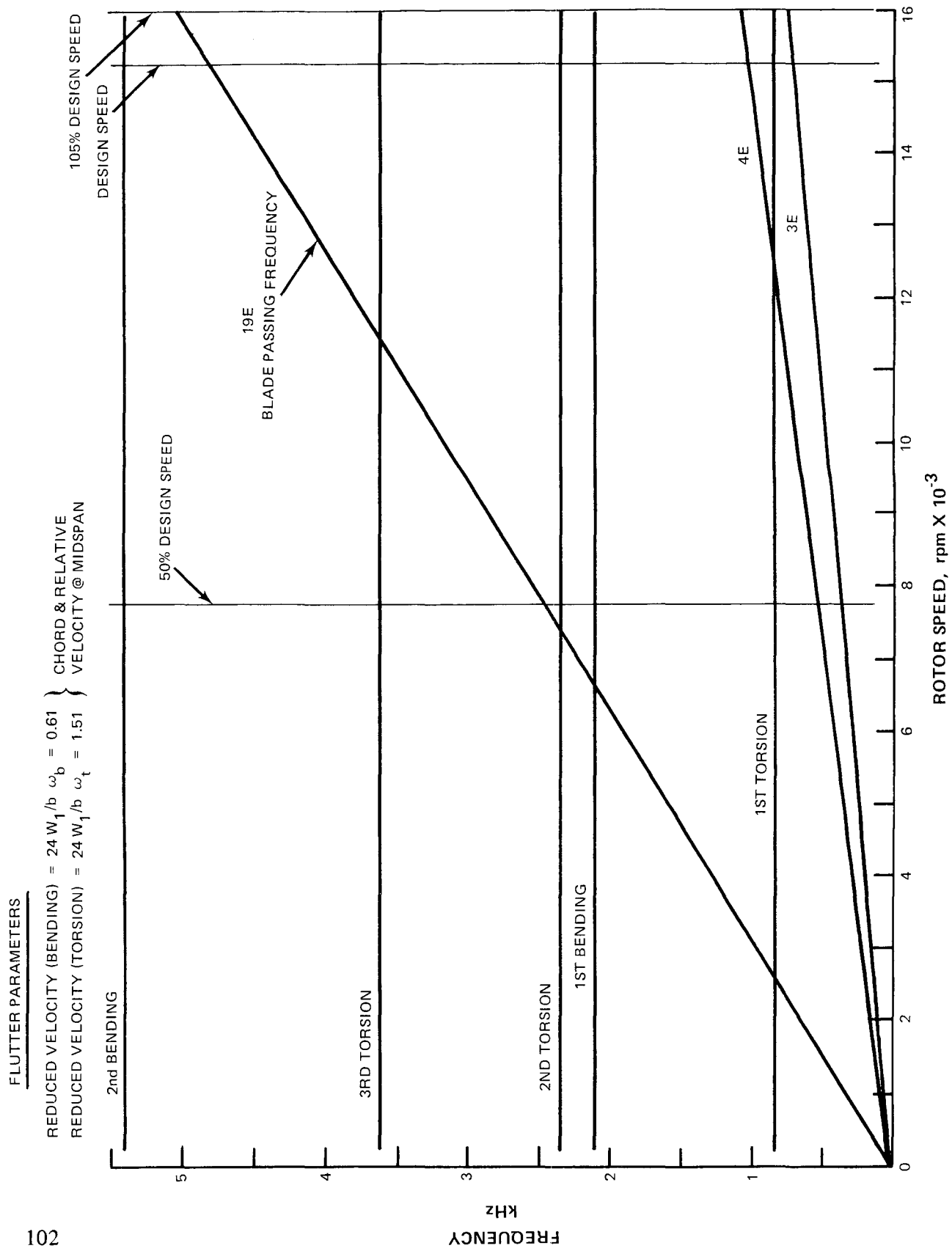


Figure 72 Campbell Diagram

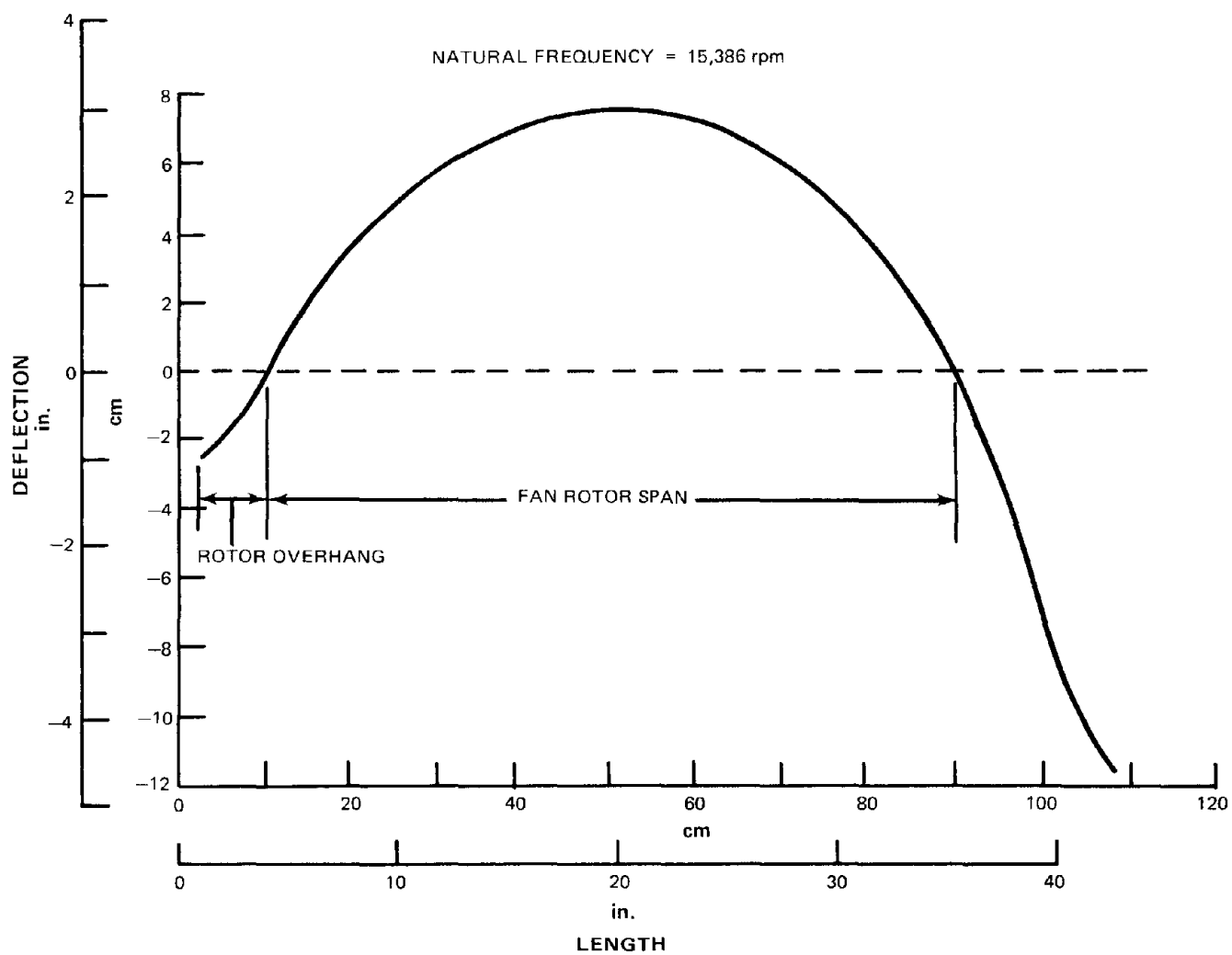


Figure 73 Stiff Bearing Critical Speed

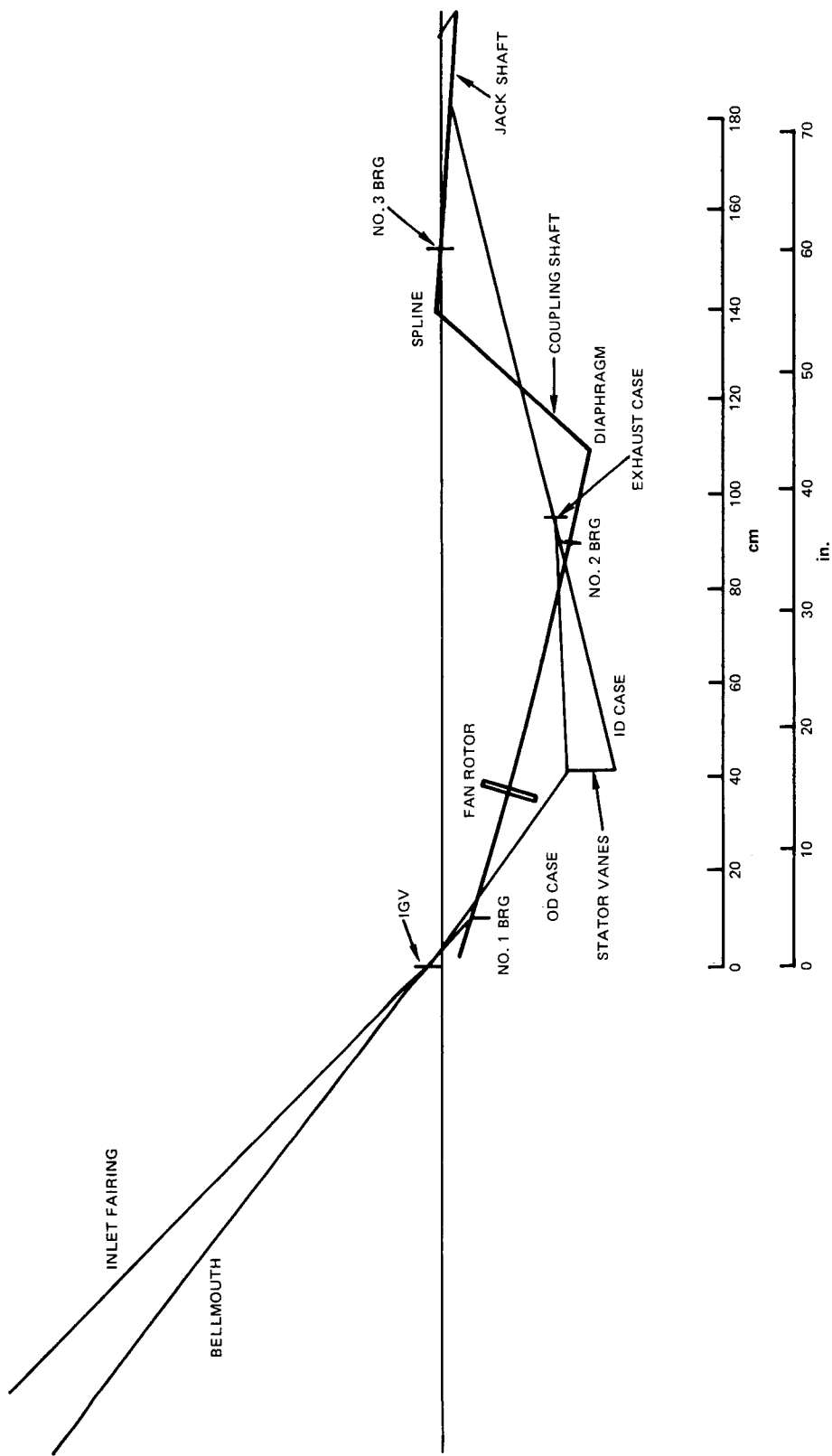


Figure 75 Mode Shapes of Criticals Having Significant Fan Rotor Motion (Natural Frequency = 5540 rpm)

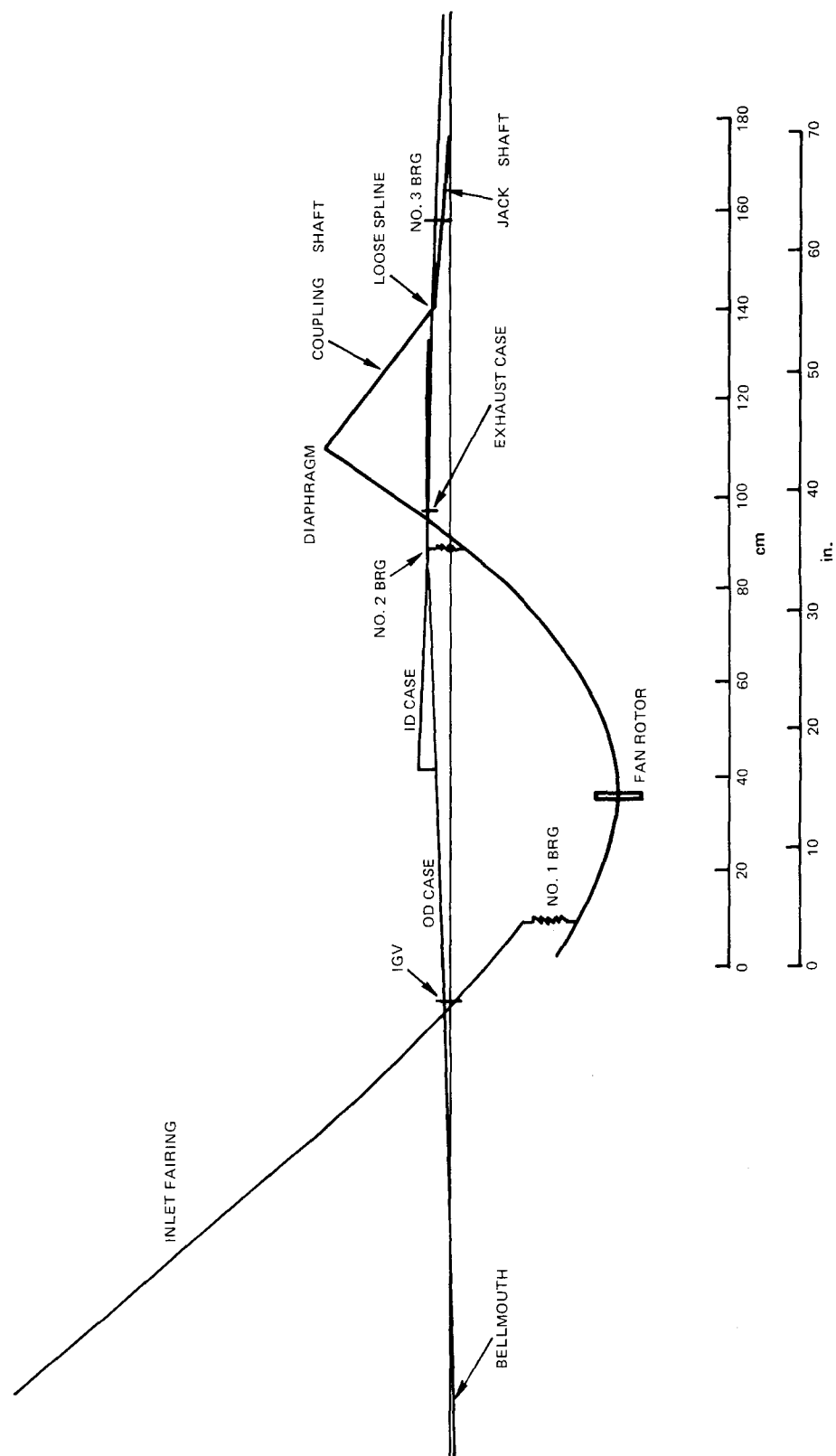


Figure 76 Mode Shapes of Criticals Having Significant Fan Rotor Motion (Natural Frequency = 11481 rpm)

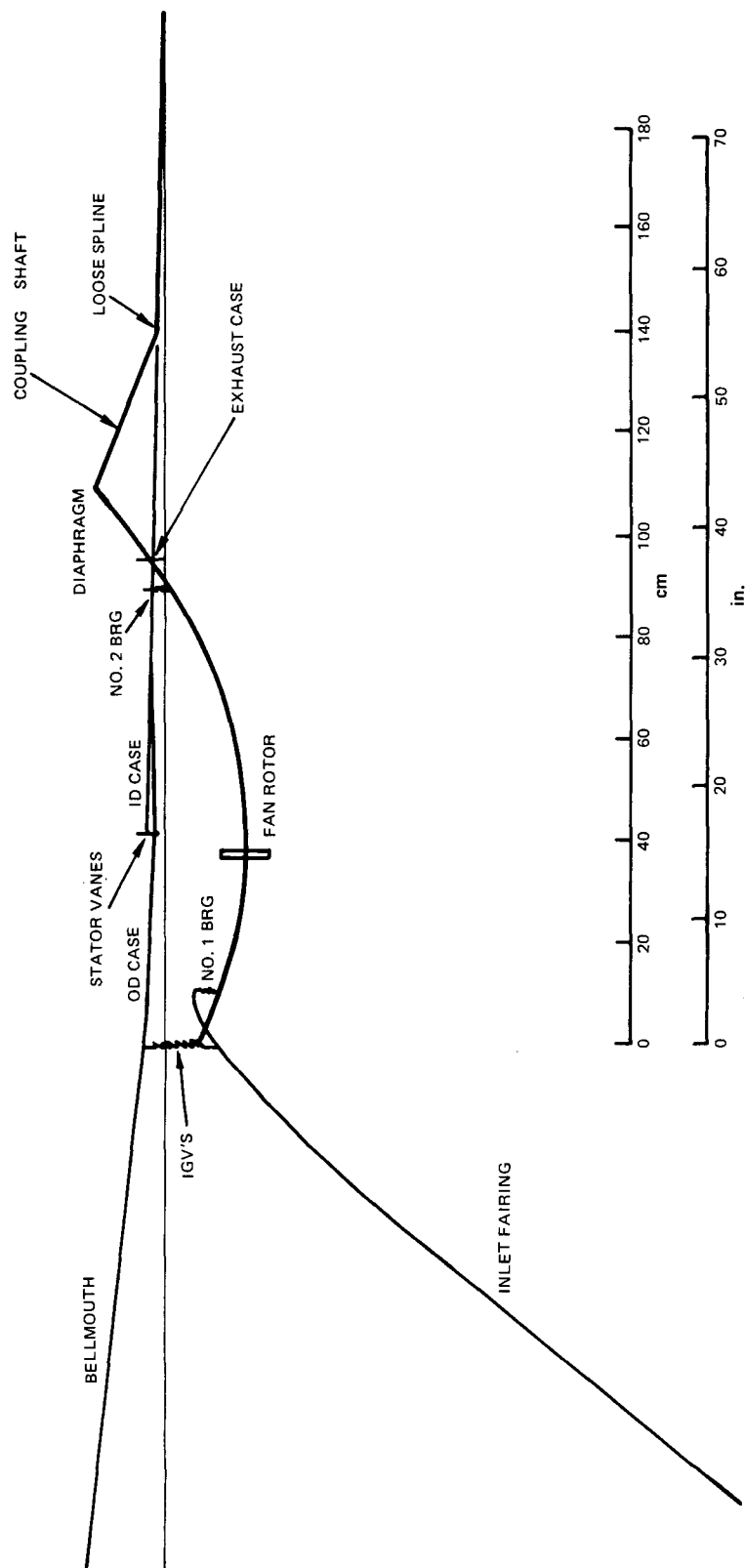


Figure 77 Mode Shapes of Criticals Having Significant Fan Rotor Motion (Natural Frequency = 12280 rpm)

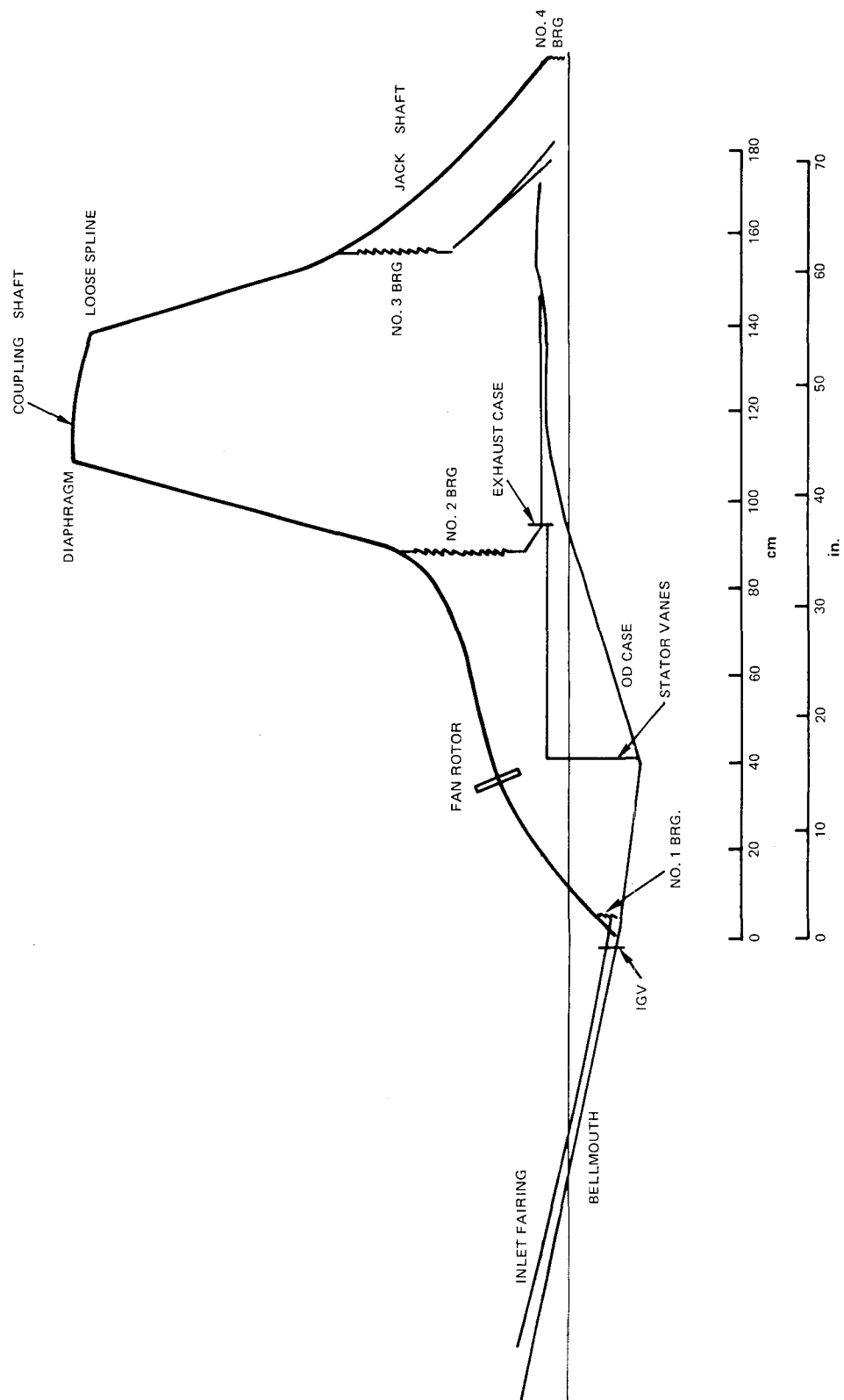


Figure 78 Mode Shapes of Critical Having Significant Fan Rotor Motion (Natural Frequency = 17686 rpm)

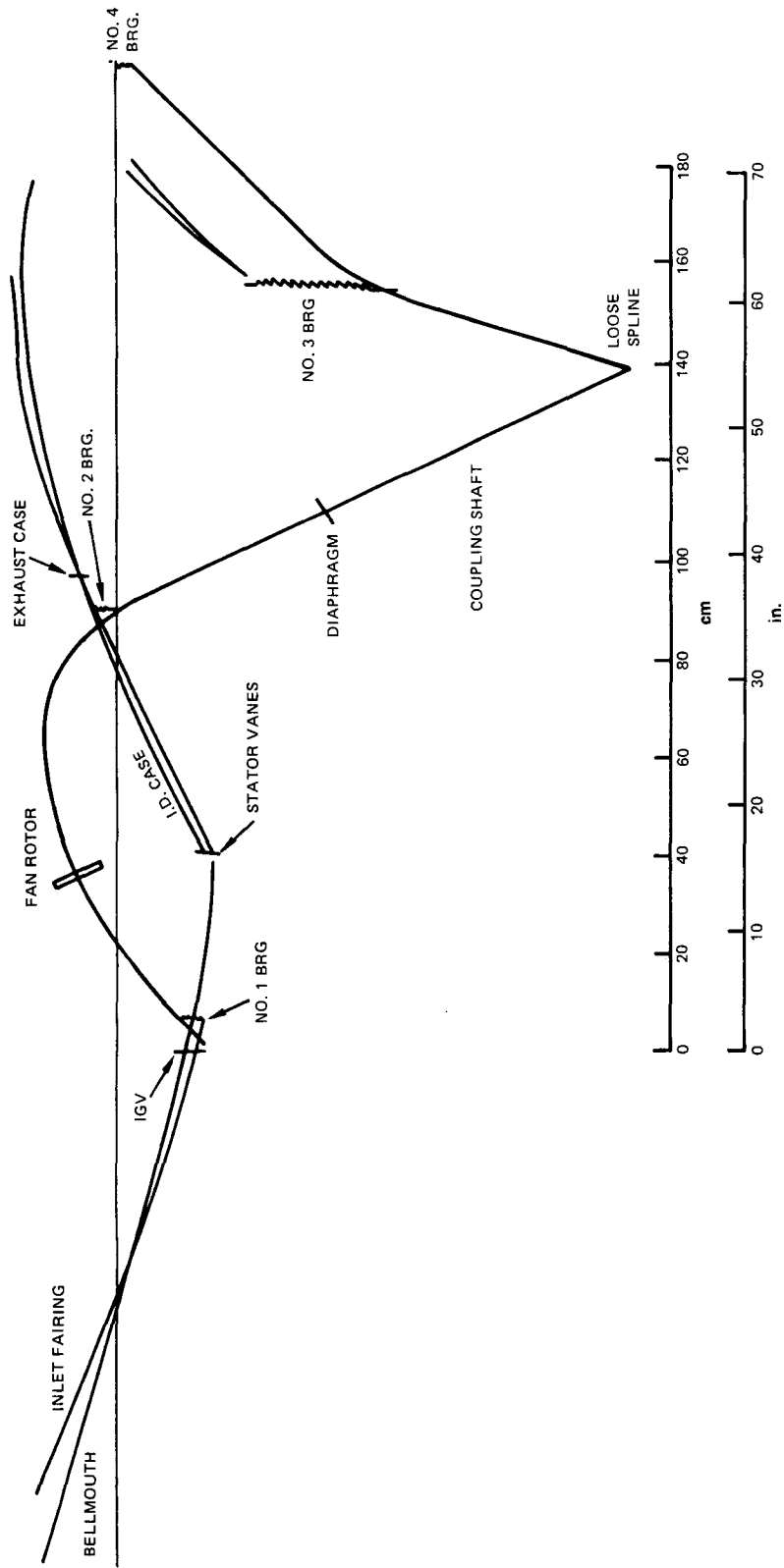


Figure 79 Mode Shape of Criticals Having Significant Fan Rotor Motion (Natural Frequency = 18400 rpm)

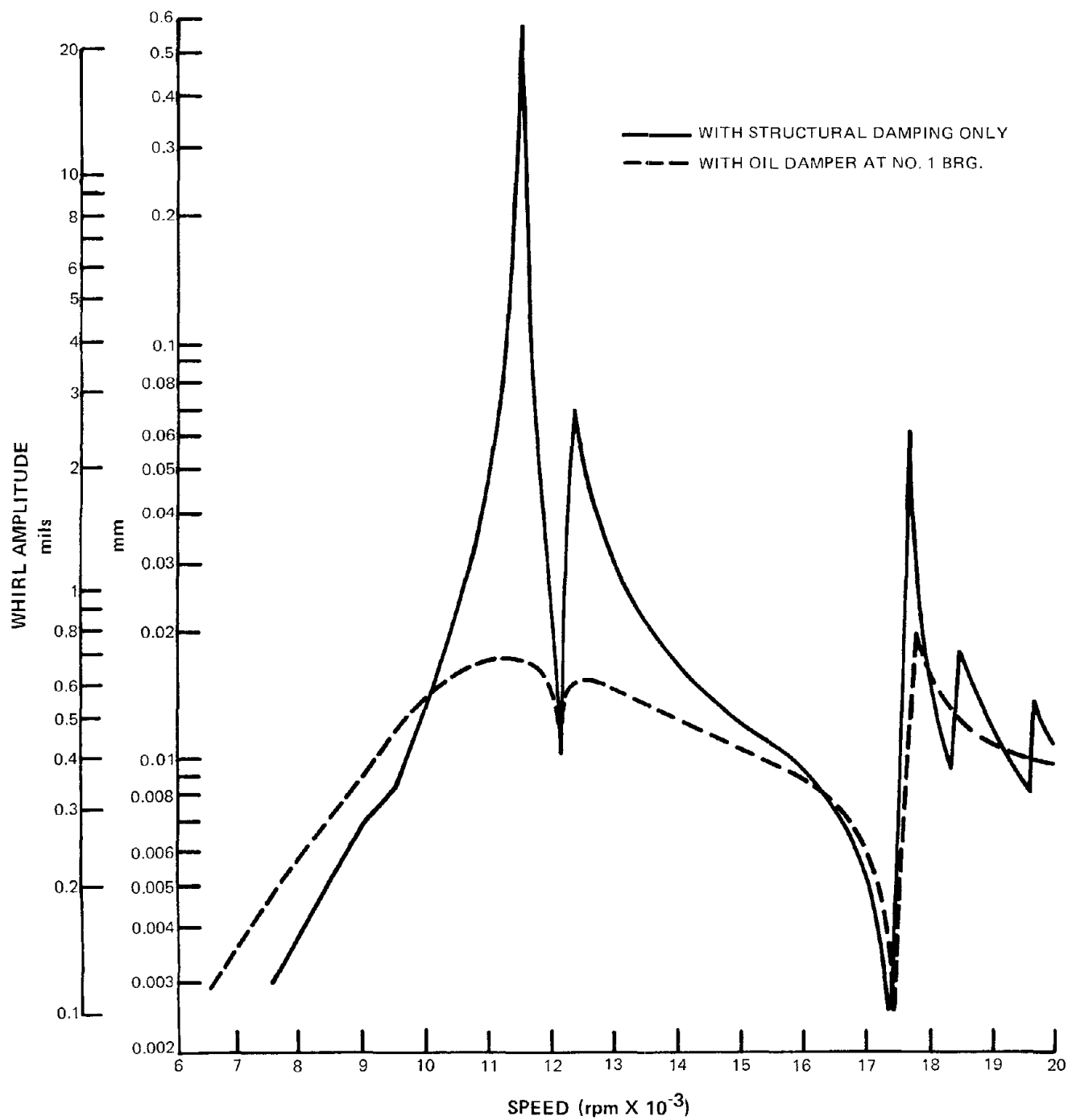


Figure 80 Response of Rotor to 0.706 N-cm [1 oz-in.] Unbalance in the Plane of the Rotor

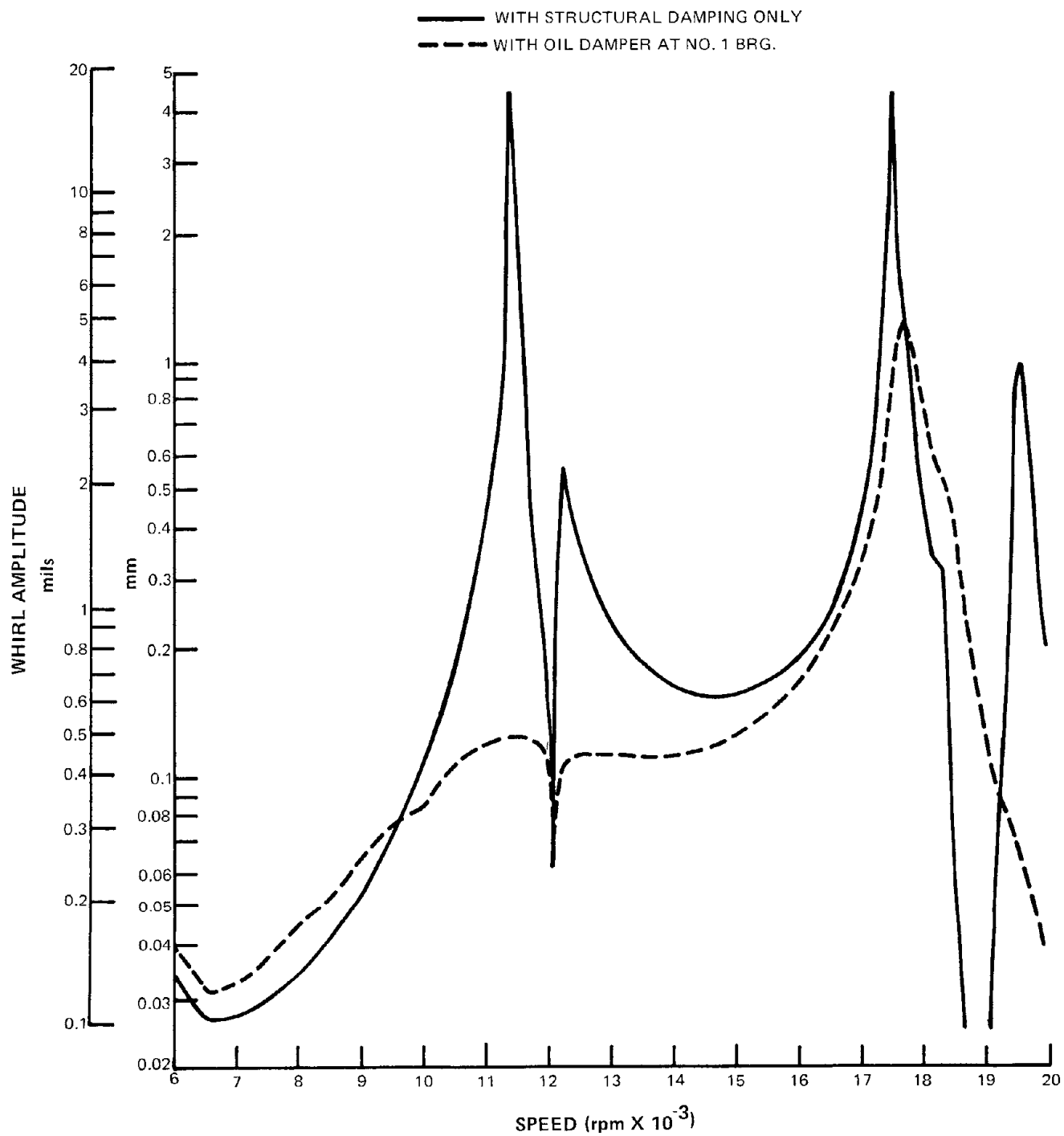


Figure 81 Response of Rotor to 0.706 N-cm [1 oz-in.] Unbalance in the Plane of the Coupling Diaphragm

Page Intentionally Left Blank

APPENDIX A

NOMENCLATURE

<u>Symbol</u>	<u>Definition</u>
A	area
A/A*	(area)/(sonic flow area)
a	distance along chord line to maximum camber point from leading edge
b	rotor semichord at 75 percent of span from root
c	aerodynamic chord, i.e., along the flow surface
D	diffusion factor for rotor = $1 - \frac{V'_2}{V'_1} + \frac{r_2 V_{\theta 2} - r_1 V_{\theta 1}}{(r_1 + r_2) \sigma V'_1}$ for stator = $1 - \frac{V_4}{V_3} + \frac{r_3 V_{\theta 3} - r_4 V_{\theta 4}}{(r_3 + r_4) \sigma V_3}$
E	excitations per rotor revolution
H	stagnation enthalpy
H	boundary layer shape factor
i _m	incidence angle between inlet air direction and line tangent to blade mean camber line at leading edge, degrees
i _{ss}	incidence angle between inlet air direction and line tangent to blade suction surface at leading edge, degrees
\overline{K}	blockage factor, effective/actual flow area
K ₁₋₈	radial spring rates
K _t	stress concentration factor
LE	leading edge
M	Mach number
MCA	multiple-circular-arc blade
N	rotor speed, rpm
p	pressure

NOMENCLATURE (Continued)

<u>Symbol</u>	<u>Definition</u>
P/A	centrifugal pull stress
PC	precompression blade
r	radius
\bar{R}	total pressure recovery defined as $p_{\text{actual}}/p_{\text{ideal}}$
R	distance along conical surface from apex to blade
R_c	streamline radius of curvature
s	blade spacing
T	temperature
t	blade maximum thickness
TE	trailing edge
T_{1-4}	torsional spring rates
U	rotor tangential speed
V	air velocity
W	weight flow
WA	leading edge wedge angle
x conical	distance in unwrapped conical plane
Y_p	airfoil coordinate of pressure surface normal to chord line
Y_s	airfoil coordinate of suction surface normal to chord line
Y_{ccg}	vertical distance to airfoil center of gravity from chord line
y	length along calculation station
y conical	distance normal to x conical

NOMENCLATURE (Continued)

<u>Symbol</u>	<u>Definition</u>
Z	axial distance
Z^* ratio	shroud modulus/airfoil modulus
Z_c	airfoil coordinate parallel to chord line
Z_{cgg}	horizontal distance to airfoil center of gravity from leading edge along chord line
β	absolute air angle = $\text{COT}^{-1} (V_m/V_\theta)$
β'	relative air angle = $\text{COT}^{-1} \frac{(V_m)}{(V'_\theta)}$
β^*	metal angle, angle between tangent to mean camber line and meridional direction
γ	blade chord angle, angle between chord and axial direction
δ°	deviation angle, exit air angle minus metal angle at trailing edge
δ^*	boundary layer displacement thickness
ϵ	angle between tangent to streamline projected on meridional plane and axial direction
$\bar{\epsilon}$	cone angle = $\text{TAN}^{-1} \frac{(r_{te} - r_{le})}{(Z_{te} - Z_{le})}$
η_{ad}	adiabatic efficiency
θ	circumferential direction
λ	angle of calculation station measured from axial direction
ρ	density
Σ	angle on conical surface of revolution
σ	solidity or stress
ϕ	camber angle, difference between blade angles at leading and trailing edges on conical surface
$\phi\Sigma$	camber angle, difference between blade angles at leading and trailing edges on the unwrapped conical surface

NOMENCLATURE (Continued)

<u>Symbol</u>	<u>Definition</u>
$\phi_{f\Sigma}$	front camber angle, difference between blade angles at leading edge and MCA transition point on the unwrapped conical surface
ω	angular velocity
ω_t	torsional frequency
$\bar{\omega}$	total pressure loss coefficient, mass average defect in relative total pressure divided by difference between inlet stagnation and static pressures
<u>Subscripts:</u>	
av	average
ew	end wall
f	front
le	leading edge
m	meridional direction (r - z plane)
p	profile
r	radial direction
ss	suction surface
t	total or stagnation
te	trailing edge
z	axial direction
θ	circumferential
1	station into rotor along leading edge
2	station out of rotor along trailing edge
3	station into stator along leading edge
4	station out of stator along trailing edge

NOMENCLATURE (Continued)

<u>Symbol</u>	<u>Definition</u>
	<u>Superscripts:</u>
'	relative to rotor
*	designates blade metal angle
°	degrees of arc or temperature

Page Intentionally Left Blank

APPENDIX B

STREAMLINE FLOW FIELD CALCULATION PROCEDURES

The aerodynamic flow field calculation used in the flow-path design assumes axisymmetric flow and uses solutions of continuity, energy, and radial equilibrium equations. These equations account for streamline curvature and radial gradients of enthalpy and entropy, but viscous terms are neglected. Calculations were performed on stations oriented at an angle λ with respect to the axial direction.

The equation of motion is in the form of:

$$\frac{1}{2} \frac{\partial V_m^2}{\partial m} \cos(\lambda - \epsilon) + \frac{V_m^2}{R_c} \sin(\lambda - \epsilon) - \frac{V_\theta^2}{r} + \frac{1}{\rho} \frac{\partial p}{\partial r} = 0$$

$$R_c = \frac{\partial \epsilon}{\partial m} = \text{streamline radius of curvature}$$

Enthalpy rise across a rotor for a streamline ψ is given by the Euler relationship

$$\Delta H_{\text{Rotor}} = (U_2 V_{\theta_2}) \psi - (U_1 V_{\theta_1}) \psi$$

Weight flow is calculated by the continuity equation

$$W = 2\pi \int_{y \text{ root}}^{y \text{ tip}} \bar{K} \rho V_m \frac{\sin(\lambda - \epsilon)}{\sin \lambda} y dy$$

where \bar{K} is the local blockage factor and y is the length along the calculation station from the centerline to the point of interest.

Page Intentionally Left Blank

APPENDIX C
AERODYNAMIC SUMMARY

ROTOR AERODYNAMIC SUMMARY, WU-MARSH SOLUTION

ROTOR INLET

Percent Flow	Diameter Inches	M	M'	V ft/sec	V' ft/sec	V _m ft/sec	English Units			
							V _θ ft/sec	V _θ ' ft/sec	U ft/sec	β Degrees
0	16.705	.4173	1.086	458.1	1192.	458.1	0.0	-1100.5	1100.5	0.0
5	18.354	.4842	1.210	528.1	1321.	528.1	0.0	-1209.3	1209.3	0.0
10	19.670	.5484	1.315	594.8	1427.	594.8	0.0	-1296.0	1296.0	0.0
15	20.799	.5897	1.400	636.7	1527.	636.7	0.0	-1370.4	1370.4	0.0
25	22.750	.6165	1.523	663.7	1638.	663.7	0.0	-1498.9	1498.9	0.0
35	24.485	.6138	1.619	681.0	1743.	661.0	0.0	-1613.2	1613.2	0.0
45	26.119	.6028	1.706	690.0	1840.	650.0	0.0	-1720.9	1720.9	0.0
55	27.650	.6113	1.799	698.5	1938.	658.5	0.0	-1821.8	1821.8	0.0
65	29.072	.6334	1.892	680.6	2032.	680.6	0.0	-1915.5	1915.5	0.0
75	30.423	.6289	1.968	676.1	2117.	676.1	0.0	-2004.4	2004.4	0.0
85	31.729	.6268	2.043	673.9	2200.	673.9	0.0	-2090.5	2090.5	0.0
95	32.982	.6361	2.121	683.2	2279.	683.2	0.0	-2173.1	2173.1	0.0
100	33.595	.6268	2.153	676.0	2314.	676.0	0.0	-2213.2	2213.2	0.0

β	β'	ε
0.0	67.41	26.38
0.0	66.40	26.41
0.0	65.35	22.10
0.0	65.09	17.52
0.0	66.12	10.08
0.0	67.72	4.80
0.0	69.31	2.34
0.0	70.13	.43
0.0	71.36	-1.99
0.0	72.14	-5.00
0.0	72.55	-8.06
0.0	73.02	-11.20
0.0		-12.39

SI Units

Percent Flow	Diameter Meters	M	M'	V m/sec	V' m/sec	V _m m/sec	SI Units			
							V _θ m/sec	V _θ ' m/sec	U m/sec	β Radians
0	.4243	.4173	1.086	139.6	363.3	139.6	0.0	-335.4	335.4	0.0
5	.4662	.4842	1.210	161.1	402.6	161.1	0.0	-368.6	368.6	0.0
10	.4996	.5484	1.315	181.3	434.9	181.3	0.0	-395.0	395.0	0.0
15	.5283	.5897	1.400	194.1	464.4	194.1	0.0	-417.7	417.7	0.0
25	.5779	.6165	1.523	202.3	499.3	202.3	0.0	-456.9	456.9	0.0
35	.6219	.6138	1.619	201.5	531.3	201.5	0.0	-491.7	491.7	0.0
45	.6634	.6028	1.706	198.1	560.8	198.1	0.0	-524.5	524.5	0.0
55	.7023	.6113	1.799	200.7	590.7	200.7	0.0	-555.3	555.3	0.0
65	.7384	.6334	1.892	207.4	619.4	207.4	0.0	-583.8	583.8	0.0
75	.7727	.6289	1.968	206.1	645.3	206.1	0.0	-610.9	610.9	0.0
85	.8059	.6268	2.043	205.4	670.6	205.4	0.0	-637.2	637.2	0.0
95	.8377	.6361	2.121	208.2	694.5	208.2	0.0	-662.4	662.4	0.0
100	.8533	.6288	2.153	206.0	705.3	206.0	0.0	-674.6	674.6	0.0

β	β'	ε
0.0	1.1763	.4603
0.0	1.1587	.4609
0.0	1.1404	.3856
0.0	1.1358	.3057
0.0	1.1538	.1759
0.0	1.1817	.0838
0.0	1.2095	.0408
0.0	1.2238	.0075
0.0	1.2290	-.0347
0.0	1.2452	-.0873
0.0	1.2588	-.1406
0.0	1.2660	-.1954
0.0	1.2742	-.2162

ROTOR AERODYNAMIC SUMMARY, WU-MARSH SOLUTION (MIXED)

Percent Flow	Diameter Inches	English Units									
		ROTOR EXIT									
		V	V _r	V _h	V _q	V _θ	U	β	β'	ε	D
		ft/sec	ft/sec	ft/sec	ft/sec	ft/sec	ft/sec	Degrees	Degrees	Degrees	
0	21.099	1058.	708.2	527.4	917.5	472.5	1390.1	60.11	41.87	26.04	.5988
5	21.758	1019.	767.4	523.3	872.3	561.0	1433.6	59.04	47.01	21.91	.5912
10	22.365	985.	820.3	516.6	837.7	636.5	1470.9	58.34	50.97	18.06	.5834
15	22.995	959.	869.3	509.9	811.0	704.5	1515.0	57.84	51.09	17.70	.5784
20	24.163	921.	961.2	501.8	772.2	820.0	1592.0	56.99	56.54	10.39	.5518
25	25.306	886.	1043.4	482.0	714.9	925.0	1667.3	56.99	62.48	5.87	.5283
30	26.437	852.	1127.0	463.9	714.9	1027.0	1741.9	57.01	66.69	1.61	.5123
35	27.560	825.	1212.0	450.1	690.4	1127.0	1815.8	56.90	69.91	-3.17	.4923
40	28.672	802.	1301.5	446.9	666.7	1222.0	1899.1	56.16	71.28	-7.59	.4701
45	29.769	786.	1388.1	445.4	646.7	1314.0	1961.4	55.44	71.87	-12.02	.4477
50	30.829	781.	1473.3	458.3	631.0	1400.0	2031.2	54.01	71.87	-13.08	.4278
55	31.848	783.	1563.0	467.2	627.8	1472.0	2098.4	53.35	72.38	-13.22	.4178
60	32.844	785.	1573.7	470.9	629.4	1502.0	2131.0	53.20	72.59	-13.78	.4144
		V	V _r	V _h	V _q	V _θ	U	β	β'	ε	D
		m/sec	m/sec	m/sec	m/sec	m/sec	m/sec	Radians	Radians	Radians	
0	.5359	322.5	215.9	160.8	279.7	144.0	423.7	1.0489	.7306	.4544	.5988
5	.5527	310.6	233.9	159.5	265.9	171.0	436.9	1.0302	.8203	.3823	.5912
10	.5686	300.2	250.0	157.5	255.3	194.0	449.5	1.0180	.8894	.3151	.5834
15	.5841	292.3	264.9	155.4	247.2	214.7	463.8	1.0093	.9439	.2565	.5741
20	.6137	280.7	292.9	152.9	235.4	249.9	485.2	.9945	1.0215	.1813	.5513
25	.6428	270.1	318.0	146.9	226.9	281.9	508.2	.9945	1.0903	.1024	.5323
30	.6715	259.7	343.5	144.4	217.8	313.0	530.9	.9945	1.1463	.0281	.5123
35	.7000	251.5	369.4	141.4	210.4	343.5	553.5	.9929	1.1901	-.0553	.4923
40	.7293	244.4	396.7	137.2	204.2	372.5	575.8	.9800	1.2199	-.1321	.4701
45	.7581	239.6	423.1	135.8	197.4	400.5	597.8	.9674	1.2438	-.2087	.4477
50	.7831	238.0	449.1	139.7	192.3	428.7	619.1	.9425	1.2544	-.2282	.4278
55	.8089	238.7	470.3	142.4	191.4	448.7	639.6	.9309	1.2630	-.2307	.4178
60	.8215	239.3	479.7	143.5	191.8	457.8	649.5	.9283	1.2667	-.2405	.4144

Percent Flow	Diameter Meters	SI Units									
		V	V _r	V _h	V _q	V _θ	U	β	β'	ε	D
		m/sec	m/sec	m/sec	m/sec	m/sec	m/sec	Radians	Radians	Radians	
0	.5359	322.5	215.9	160.8	279.7	144.0	423.7	1.0489	.7306	.4544	.5988
5	.5527	310.6	233.9	159.5	265.9	171.0	436.9	1.0302	.8203	.3823	.5912
10	.5686	300.2	250.0	157.5	255.3	194.0	449.5	1.0180	.8894	.3151	.5834
15	.5841	292.3	264.9	155.4	247.2	214.7	463.8	1.0093	.9439	.2565	.5741
20	.6137	280.7	292.9	152.9	235.4	249.9	485.2	.9945	1.0215	.1813	.5513
25	.6428	270.1	318.0	146.9	226.9	281.9	508.2	.9945	1.0903	.1024	.5323
30	.6715	259.7	343.5	144.4	217.8	313.0	530.9	.9945	1.1463	.0281	.5123
35	.7000	251.5	369.4	141.4	210.4	343.5	553.5	.9929	1.1901	-.0553	.4923
40	.7293	244.4	396.7	137.2	204.2	372.5	575.8	.9800	1.2199	-.1321	.4701
45	.7581	239.6	423.1	135.8	197.4	400.5	597.8	.9674	1.2438	-.2087	.4477
50	.7831	238.0	449.1	139.7	192.3	428.7	619.1	.9425	1.2544	-.2282	.4278
55	.8089	238.7	470.3	142.4	191.4	448.7	639.6	.9309	1.2630	-.2307	.4178
60	.8215	239.3	479.7	143.5	191.8	457.8	649.5	.9283	1.2667	-.2405	.4144

ROTOR AERODYNAMIC SUMMARY, STREAMLINE SOLUTION

ROTOR INLET

Percent Flow	Diameter Inches	\bar{M}	\bar{M}'	English Units				β Degrees	β' Degrees	ϵ Degrees
				V ft./sec	V' ft./sec	V_m ft./sec	V_q ft./sec			
0	16.705	.166	1.109	509.4	1212.7	509.4	0.0	0.0	65.16	28.06
5	18.142	.199	1.205	543.5	1313.0	543.5	0.0	0.0	65.55	22.74
10	19.102	.526	1.288	571.6	1400.2	571.6	0.0	0.0	65.90	18.52
15	20.540	.549	1.363	595.1	1478.2	595.1	0.0	0.0	66.26	14.99
25	22.555	.584	1.494	630.6	1614.8	630.6	0.0	0.0	67.01	9.27
35	24.362	.607	1.608	653.9	1733.1	653.9	0.0	0.0	67.83	4.73
45	26.005	.621	1.709	668.1	1838.9	668.1	0.0	0.0	68.69	.96
55	27.535	.628	1.801	675.3	1935.7	675.3	0.0	0.0	69.68	-2.26
65	28.981	.630	1.885	677.4	2025.9	677.4	0.0	0.0	70.47	-5.05
75	30.360	.629	1.964	675.7	2111.1	675.7	0.0	0.0	71.33	-7.54
85	31.685	.624	2.039	671.1	2192.7	671.1	0.0	0.0	72.18	-9.78
95	32.968	.618	2.110	665.0	2271.4	665.0	0.0	0.0	72.98	-11.79
100	33.595	.615	2.145	661.9	2310.1	661.9	0.0	0.0	73.35	-12.68

SI Units

Percent Flow	Diameter Meters	\bar{M}	\bar{M}'	SI Units				β Radians	β' Radians	ϵ Radians
				V m/sec	V' m/sec	V_m m/sec	V_q m/sec			
0	.4243	.166	1.109	155.3	369.6	155.3	0.0	0.0	1.1370	.4896
5	.4608	.199	1.205	155.7	400.2	155.7	0.0	0.0	1.1438	.3968
10	.4928	.526	1.288	174.2	426.8	174.2	0.0	0.0	1.1500	.3232
15	.5217	.549	1.363	181.4	450.6	181.4	0.0	0.0	1.1562	.2616
25	.5732	.584	1.494	192.2	492.2	192.2	0.0	0.0	1.1693	.1618
35	.6188	.607	1.608	199.3	528.2	199.3	0.0	0.0	1.1836	.0825
45	.6605	.621	1.709	203.6	560.5	203.6	0.0	0.0	1.1986	.0168
55	.6994	.628	1.801	205.8	590.0	205.8	0.0	0.0	1.2159	-.0394
65	.7361	.630	1.885	206.5	617.5	206.5	0.0	0.0	1.2297	-.0881
75	.7711	.629	1.964	205.9	643.5	205.9	0.0	0.0	1.2447	-.1316
85	.8048	.624	2.039	204.6	668.3	204.6	0.0	0.0	1.2595	-.1707
95	.8374	.618	2.110	202.7	692.3	202.7	0.0	0.0	1.2735	-.2057
100	.8533	.615	2.145	201.7	704.1	201.7	0.0	0.0	1.2800	-.2213

ROTOR AERODYNAMIC SUMMARY, STREAMLINE SOLUTION

ROTOR EXIT

ENGLISH UNITS

Percent Flow	Diameter Inches	M	M'	V ft/sec	V' ft/sec	V _m ft/sec	V _p ft/sec	V' _p ft/sec	U ft/sec	β Degrees	β' Degrees	ε Degrees	Ω	D	P/P _{Inlet}	T/T _{Inlet}
0	21.099	.881	.602	1085.4	761.7	576.5	920.9	-469.1	1390.0	58.04	39.23	25.96	.2512	.5787	3.01140	1.14097
5	21.725	.815	.611	1044.6	792.2	566.7	877.6	-553.7	1331.2	57.15	40.33	22.43	.2059	.5707	2.9734	1.14020
10	22.328	.816	.677	1010.5	838.2	556.1	813.8	-627.2	1171.0	56.61	48.41	19.26	.1804	.5635	2.9434	1.13973
15	22.917	.791	.709	982.2	881.2	544.9	817.2	-692.5	1509.7	56.31	51.80	16.37	.1569	.5572	2.9230	1.13919
20	24.063	.749	.768	935.6	959.9	519.6	778.1	-807.1	1585.2	56.27	57.23	11.88	.1561	.5453	2.8858	1.13918
25	25.183	.715	.827	888.2	1038.3	497.6	747.7	-911.3	1659.1	56.36	61.37	6.85	.1533	.5330	2.8810	1.13971
30	26.287	.685	.866	844.8	1118.4	477.9	720.8	-1011.1	1731.9	56.45	64.70	2.88	.1518	.5171	2.8703	1.13996
35	27.368	.659	.896	834.6	1199.7	459.7	696.8	-1107.6	1804.2	56.58	67.46	-0.71	.1518	.5002	2.8523	1.14022
40	28.478	.634	.916	805.9	1281.9	443.0	673.2	-1202.9	1878.1	56.65	69.78	-3.99	.1511	.4816	2.8353	1.14042
45	29.568	.612	1.069	780.5	1364.1	427.9	652.7	-1295.2	1947.9	56.75	71.72	-6.99	.1511	.4608	2.8524	1.14069
50	30.659	.591	1.127	757.2	1443.7	411.2	635.9	-1383.9	2019.8	57.11	73.45	-9.71	.1509	.4408	2.8515	1.14110
55	31.770	.573	1.173	738.5	1512.1	384.4	630.5	-1468.4	2092.9	58.63	75.27	-12.13	.1730	.4302	2.8549	1.14223
60	32.344	.561	1.193	730.2	1542.7	365.7	632.0	-1498.8	2130.8	59.95	76.29	-13.21	.1877	.4272	2.8576	1.14309

SI UNITS

Percent Flow	Diameter Meters	M	M'	V m/sec	V' m/sec	V _m m/sec	V _p m/sec	V' _p m/sec	U m/sec	β Radians	β' Radians	ε Radians	Ω	D	P/P _{Inlet}	T/T _{Inlet}
0	.5359	.881	.602	330.8	226.1	175.1	208.7	-142.9	423.7	1.0128	.6816	.4530	.2512	.5787	3.01140	1.14097
5	.5518	.815	.611	318.4	241.5	172.7	267.5	-168.6	436.2	.9973	.7736	.3914	.2059	.5707	2.9734	1.14020
10	.5571	.816	.677	308.0	255.5	169.5	257.2	-191.2	448.4	.9878	.8453	.3361	.1804	.5635	2.9434	1.13973
15	.5621	.791	.709	299.4	268.6	166.1	249.1	-211.1	460.2	.9826	.9039	.2857	.1569	.5572	2.9230	1.13919
20	.6112	.749	.768	285.2	292.6	158.4	237.2	-246.0	481.2	.9819	.9987	.1963	.1561	.5453	2.8858	1.13918
25	.6396	.715	.827	273.8	316.5	151.7	227.9	-277.8	505.7	.9835	1.0709	.1195	.1533	.5330	2.8810	1.13971
30	.6677	.685	.866	263.6	340.9	145.7	219.7	-308.2	527.9	.9851	1.1290	.0503	.1518	.5171	2.8703	1.13996
35	.6956	.659	.896	254.4	365.5	140.1	212.3	-337.6	549.9	.9873	1.1772	.0000	.1518	.5002	2.8523	1.14022
40	.7233	.634	1.008	245.6	390.7	135.0	205.2	-368.6	571.8	.9885	1.2177	-.0696	.1511	.4816	2.8353	1.14042
45	.7510	.612	1.069	237.9	415.8	130.4	198.9	-394.8	593.7	.9903	1.2515	-.1220	.1511	.4608	2.8524	1.14069
50	.7787	.591	1.127	230.8	440.0	125.3	193.8	-421.8	615.6	.9966	1.2817	-.1694	.1509	.4408	2.8515	1.14110
55	.8070	.573	1.173	225.1	460.9	117.2	192.2	-445.7	637.9	1.0231	1.3133	-.2117	.1730	.4302	2.8549	1.14223
60	.8215	.561	1.193	222.6	470.2	111.5	192.6	-456.8	649.5	1.0461	1.3313	-.2305	.1877	.4272	2.8576	1.14309

STATOR AERODYNAMIC SUMMARY, STREAMLINE SOLUTION

STATOR INLET

ENGLISH UNITS

Percent Flow	Diameter Inches	M	M'	V ft/sec	V'	V _m ft/sec	V _q ft/sec	V' _q ft/sec	U ft/sec	β Degrees	β' Degrees	ε Degrees
0	21.68	.892	.673	1097.8	827.6	634.0	896.2	-532.1	1428.3	54.73	10.01	23.58
5	22.273	.862	.712	1062.3	877.2	629.1	856.0	-611.3	1467.3	53.69	14.18	20.18
10	22.838	.836	.746	1032.9	921.0	621.6	825.0	-679.6	1504.6	53.00	17.55	17.22
15	23.383	.815	.776	1009.0	961.0	613.7	800.9	-739.5	1540.4	52.54	50.31	14.57
25	24.129	.780	.830	970.5	1032.1	595.4	766.4	-843.0	1609.4	52.16	54.76	10.03
35	25.135	.753	.881	940.8	1100.8	580.5	740.3	-935.3	1675.7	51.90	58.18	6.13
45	26.108	.729	.932	915.1	1169.4	568.0	717.5	-1022.2	1739.8	51.64	60.94	2.62
55	27.353	.709	.982	892.6	1237.2	557.2	697.4	-1104.7	1802.0	51.38	63.23	- .64
65	28.275	.690	1.033	871.7	1305.3	547.9	678.0	-1184.7	1862.8	51.06	65.18	- 3.74
75	29.176	.674	1.082	853.8	1371.4	539.9	661.4	-1260.7	1922.1	50.78	66.81	- 6.74
85	30.060	.659	1.128	837.8	1433.5	530.3	648.6	-1331.8	1980.3	50.73	68.29	- 9.67
95	30.938	.646	1.159	825.5	1481.9	512.0	647.5	-1390.7	2038.2	51.66	69.79	-12.69
100	31.380	.639	1.170	820.1	1501.0	498.2	651.4	-1415.9	2067.3	52.59	70.61	-14.34

SI UNITS

Percent Flow	Diameter Meters	M	M'	V m/sec	V'	V _m m/sec	V _q m/sec	V' _q m/sec	U m/sec	β Radians	β' Radians	ε Radians
0	.5507	.892	.673	334.6	252.3	193.2	273.2	-162.2	435.3	.9550	.6982	.4115
5	.5637	.862	.712	323.8	267.4	191.7	260.9	-186.3	447.2	.9369	.7709	.3521
10	.5801	.836	.746	314.8	280.7	189.5	251.5	-207.1	458.6	.9249	.8297	.3005
15	.5939	.815	.776	307.5	292.9	187.1	244.1	-225.4	469.5	.9168	.8779	.2542
25	.6205	.780	.830	295.8	314.6	181.5	233.6	-256.9	490.5	.9102	.9556	.1750
35	.6460	.753	.881	286.8	335.5	176.9	225.6	-285.1	510.8	.9057	1.0152	.1070
45	.6708	.729	.932	278.9	356.4	173.1	218.7	-311.6	530.3	.9011	1.0634	.0457
55	.6948	.709	.982	272.1	377.1	169.8	212.6	-336.7	549.2	.8966	1.1034	-.0112
65	.7182	.690	1.033	265.7	397.9	167.0	206.7	-361.1	567.8	.8909	1.1374	-.0653
75	.7411	.674	1.082	260.2	418.0	164.6	201.6	-384.3	585.9	.8861	1.1658	-.1176
85	.7659	.659	1.128	255.4	436.9	161.6	197.7	-405.9	603.6	.8852	1.1917	-.1687
95	.7838	.646	1.159	251.6	451.7	156.1	197.4	-423.9	621.2	.9015	1.2178	-.2214
100	.7971	.639	1.170	250.0	457.5	151.9	198.5	-431.6	630.1	.9177	1.2321	-.2502

STATOR AERODYNAMIC SUMMARY, STREAMLINE SOLUTION

STATOR EXIT

ENGLISH UNITS

Percent Flow	Diameter Inches	M	M'	V ft/sec	V'	V _m ft/sec	V _g ft/sec	V' _g ft/sec	U ft/sec	β Degrees	β' Degrees	ε Degrees	ω	D	P/P _{inlet}	T/T _{inlet}
0	23.060	.568	1.313	729.3	1685.2	729.3	0.0	-1519.2	1519.2	0.0	64.36	6.39	.1751	.1930	2.8012	1.1097
5	23.465	.559	1.330	715.9	1703.6	715.9	0.0	-1515.9	1515.9	0.0	65.15	5.76	.1166	.1874	2.8052	1.1020
10	23.865	.554	1.348	708.4	1721.4	708.4	0.0	-1512.2	1512.2	0.0	65.74	5.12	.1180	.1795	2.8158	1.0973
15	24.259	.544	1.362	695.8	1743.1	695.8	0.0	-1598.2	1598.2	0.0	66.47	4.47	.1073	.1801	2.8122	1.0919
20	25.011	.527	1.391	675.5	1782.6	675.5	0.0	-1619.7	1619.7	0.0	67.73	3.17	.0967	.1832	2.8031	1.0918
25	25.809	.517	1.421	663.8	1825.3	663.8	0.0	-1700.3	1700.3	0.0	68.67	1.86	.0909	.1828	2.7991	1.0971
30	26.562	.512	1.454	658.2	1869.6	658.2	0.0	-1709.9	1709.9	0.0	69.39	.54	.0818	.1782	2.7978	1.0996
35	27.297	.511	1.487	657.4	1914.7	657.4	0.0	-1798.3	1798.3	0.0	69.92	-.77	.0782	.1695	2.7885	1.1022
40	28.014	.512	1.521	659.3	1959.8	659.3	0.0	-1815.5	1815.5	0.0	70.34	-2.10	.0728	.1678	2.7987	1.1042
45	28.710	.517	1.556	666.0	2005.3	666.0	0.0	-1891.4	1891.4	0.0	70.60	-3.43	.0687	.1421	2.8010	1.1069
50	29.388	.524	1.590	675.4	2050.5	675.4	0.0	-1936.1	1936.1	0.0	70.77	-4.79	.0689	.1245	2.8019	1.1110
55	30.047	.533	1.620	689.6	2096.2	689.6	0.0	-1979.5	1979.5	0.0	70.79	-6.21	.0753	.1070	2.8023	1.1123
60	30.370	.536	1.634	698.3	2119.1	698.3	0.0	-2000.8	2000.8	0.0	70.76	-6.95	.0517	.0984	2.8016	1.11309

SI UNITS

Percent Flow	Diameter Meters	M	M'	V m/sec	V'	V _m m/sec	V _g m/sec	V' _g m/sec	U m/sec	β Radians	β' Radians	ε Radians	ω	D	P/P _{inlet}	T/T _{inlet}
0	.587	.568	1.313	222.3	513.6	222.3	0.0	-463.1	463.1	0.0	1.1231	.1115	.1751	.1939	2.8012	1.1097
5	.5960	.559	1.330	218.2	515.3	218.2	0.0	-471.2	471.2	0.0	1.1369	.1005	.1166	.1874	2.8062	1.1020
10	.6062	.554	1.348	215.9	525.6	215.9	0.0	-479.2	479.2	0.0	1.1472	.0893	.1180	.1795	2.8158	1.0973
15	.6162	.544	1.362	212.1	531.3	212.1	0.0	-487.1	487.1	0.0	1.1599	.0780	.1073	.1801	2.8122	1.0919
20	.6260	.527	1.391	205.9	543.3	205.9	0.0	-502.8	502.8	0.0	1.1819	.0553	.0967	.1832	2.8031	1.0918
25	.6355	.517	1.421	202.3	556.4	202.3	0.0	-518.3	518.3	0.0	1.1983	.0325	.0909	.1828	2.7991	1.0971
30	.6493	.512	1.454	200.6	569.9	200.6	0.0	-533.4	533.4	0.0	1.2109	.0094	.0818	.1782	2.7978	1.0996
35	.6633	.511	1.487	200.4	583.6	200.4	0.0	-548.1	548.1	0.0	1.2201	-.0134	.0782	.1695	2.7885	1.1022
40	.6716	.512	1.521	201.0	597.3	201.0	0.0	-562.5	562.5	0.0	1.2274	-.0366	.0728	.1678	2.7987	1.1042
45	.7292	.517	1.556	203.0	611.2	203.0	0.0	-576.5	576.5	0.0	1.2320	-.0599	.0687	.1421	2.8010	1.1069
50	.7465	.524	1.590	205.9	625.0	205.9	0.0	-590.1	590.1	0.0	1.2369	-.0836	.0689	.1245	2.8019	1.1110
55	.7632	.533	1.620	210.2	638.9	210.2	0.0	-603.4	603.4	0.0	1.2353	-.1084	.0753	.1070	2.8023	1.1123
60	.7714	.536	1.634	212.8	645.9	212.8	0.0	-609.8	609.8	0.0	1.2348	-.1213	.0517	.0984	2.8016	1.11309

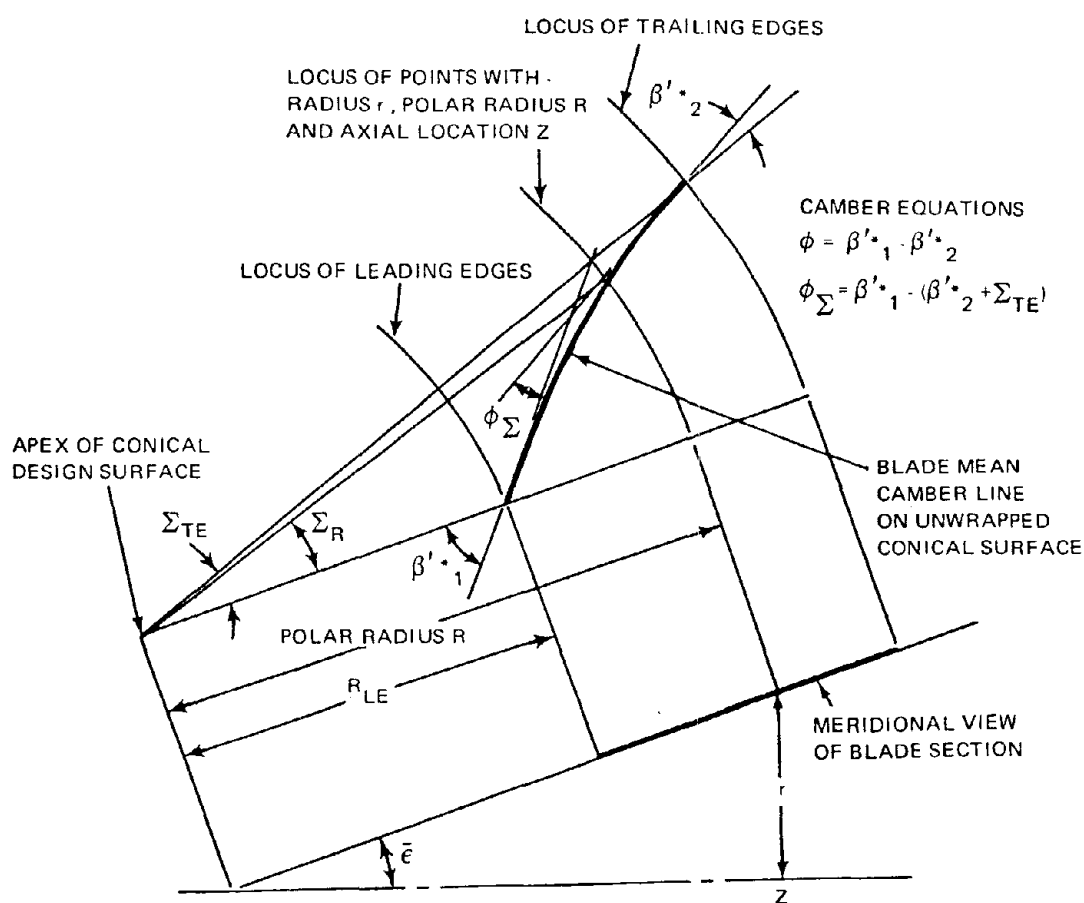
Reproduced from
best available copy

Page Intentionally Left Blank

APPENDIX D

AIRFOIL GEOMETRY ON CONICAL SURFACES

The tables on the following pages present detailed data on the airfoil geometry on conical surfaces for the rotor blades and the stator vanes. These data are based on the geometrical definitions presented in the sketch of an unwrapped conical surface shown below.



ROTOR BLADE GEOMETRY ON CONICAL SURFACES

19 BLADES

Inlet Hub Diameter 16.7 Inches (.424m) Inlet Tip Diameter 33.6 Inches (.853m)

Exit Hub Diameter 21.1 Inches (.536m) Exit Tip Diameter 32.3 Inches (.820m)

Percent Flow	Diameter LE Inches	Diameter TE Inches	C Inches	C _f Inches	LER Inches	TER Inches	β_1^* Degrees	β_2^* Degrees	W.A. Degrees	ϕ_k Degrees	γ_f Degrees	Precompression Ramp Angle Degrees	ϵ Degrees	ξ Degrees	E/C	P/C	t/C _{max}	Location t/C _{max}	σ
0	16.705	21.099	6.960	2.55	.0288	.0258	60.03	22.00	13.33	23.61	-4.81		26.04	14.42			.02450	54.12	2.2270
5	18.354	21.758	6.890	2.76	.0271	.0246	60.14	28.40	12.40	20.29	-3.46		21.94	11.44			.02106	56.34	2.2820
10	19.670	22.385	6.853	2.95	.0256	.0234	60.01	34.80	9.12	15.92	-2.63		18.66	9.28			.01864	58.42	1.2710
15	20.799	22.995	6.831		.0242	.0224	59.75	40.88	7.40				14.70	7.57	.111	.578	.01823	58.96	1.2627
25	22.750	24.163	6.848		.0220	.0208	60.37	49.83	6.37				10.39	4.97	.110	.586	.01668	60.22	1.7394
35	24.485	25.306	6.860		.0205	.0189	62.25	57.11	5.47				5.83	2.99	.105	.547	.01484	64.23	1.6319
45	26.119	26.437	6.880		.0192	.0179	65.11	58.60	4.63				3.00	1.61	.108	.553	.01353	66.00	1.5636
55	27.650	27.560	6.860		.0178	.0165	65.32	59.65	3.93				3.00	1.16	.105	.547	.01268	67.79	1.5773
65	29.072	28.672	7.050		.0165	.0159	66.34	63.37	3.56				3.00	1.16	.108	.553	.01153	69.46	1.4767
75	30.423	29.769	7.240		.0152	.0149	67.28	64.64	2.95				3.00	1.16	.105	.547	.01065	71.45	1.4549
85	31.729	30.829	7.435		.0142	.0141	67.82	64.64	2.95				3.00	1.16	.105	.547	.00993	73.18	1.4376
95	32.982	31.848	7.613		.0133	.0141	67.82	63.79	2.81				3.00	1.16	.105	.547	.00957	75.18	1.4203
100	33.595	32.344	7.700		.0130	.0137	68.53	63.98	2.75				3.00	1.16	.102	.559	.00955	77.32	1.4125

SI UNITS

Percent Flow	Diameter LE Meters	Diameter TE Meters	C Meters	C _f Meters	LER Meters	TER Meters	β_1^* Radians	β_2^* Radians	W.A. Radians	ϕ_k Radians	γ_f Radians	Precompression Ramp Angle Radians	ϵ Radians	ξ Radians	E/C	P/C	t/C _{max}	Location t/C _{max}	σ
0	.4243	.5359	.1768	.0648	.00073	.0065	1.0475	.3872	.2326	.4120	-.0839		.4544	.2516					
5	.4662	.5527	.1750	.0701	.0068	.0062	1.0494	.4056	.1913	.3541	-.0604		.3822	.1966					
10	.4986	.5686	.1741	.0749	.0065	.0059	1.0472	.6073	.1591	.2778	-.0459		.3151	.1619					
15	.5283	.5841	.1735		.0061	.0056	1.0426	.7834	.1291			.0698	.265	.1221					
25	.5779	.6137	.1729		.0055	.0052	1.0639	.8695	.1112			.0963	.1813	.0867					
35	.6219	.6428	.1727		.0052	.0050	1.0863	.9965	.0995			.0922	.1024	.0522					
45	.6634	.6715	.1727		.0048	.0048	1.1201	1.0260	.0808			.0576	.0281	.0206					
55	.7023	.7000	.1748		.0045	.0045	1.1362	1.0409	.0686			.0730	.0553	-.0059					
65	.7384	.7283	.1791		.0041	.0042	1.1398	1.0756	.0625			.0968	-.1324	-.0267					
75	.7727	.7561	.1839		.0038	.0040	1.1576	1.1058	.0567			.1037	-.2097	-.0448					
85	.8059	.7831	.1888		.0036	.0037	1.1740	1.1280	.0515			.1082	-.2282	-.0633					
95	.8377	.8089	.1934		.0033	.0035	1.1835	1.1131	.0490			.1139	-.2307	-.0827					
100	.8533	.8215	.1956		.0033	.0034	1.1958	1.1165	.0480			.1091	-.2405	-.0927					

STATOR VANE GEOMETRY ON CONICAL SURFACES

60 VANES

Inlet Hub Diameter 21.68 Inches (.551m) Inlet Tip Diameter 31.38 Inches (.797m)

Exit Hub Diameter 23.06 Inches (.586m) Exit Tip Diameter 30.37 Inches (.771m)

Percent Flow	Diameter IE Inches	Diameter TE Inches	C Inches	C _f Inches	LER Inches	TER Inches	β ³ Degrees	β ⁴ Degrees	W.A. Degrees	φ _s Degrees	φ _f Degrees	Ē Degrees	ξ Degrees	T/Cmax	Location T/Cmax	a/c	σ
0	21.733	23.097	2.928	.956	.00669	.00688	49.37	-12.27	9.944	60.663	7.220	14.868	1.577	.0500	50.0	.5370	2.425
5	22.314	23.493	2.895	.964	.00676	.00695	48.73	-11.06	10.681	58.463	7.92	12.901	1.327	.0512	50.2	.5367	2.414
10	22.874	23.887	2.867	.976	.00684	.00703	48.45	-10.38	10.423	57.713	8.55	11.172	1.117	.0523	50.5	.5370	2.342
15	23.442	24.277	2.843	.989	.00693	.00711	48.32	-10.00	10.160	57.385	9.09	9.603	.9354	.0534	50.8	.5376	2.277
25	24.453	25.051	2.802	1.022	.00715	.00726	48.41	-10.02	10.214	57.864	9.99	6.718	.6257	.0555	51.4	.5405	2.162
35	25.451	25.807	2.763	1.056	.00735	.00741	48.50	-10.25	10.380	58.388	10.80	4.062	.3625	.0577	51.9	.5441	2.059
45	26.416	26.551	2.731	1.086	.00754	.00756	48.46	-10.67	10.473	58.998	11.53	1.555	.1326	.0598	52.5	.5476	1.969
55	27.352	27.276	2.701	1.118	.00772	.00771	48.33	-11.37	10.617	59.771	12.35	-.881	-.0714	.0617	53.0	.5514	1.889
65	28.263	27.982	2.679	1.147	.00793	.00786	48.06	-12.30	10.817	60.614	13.14	-3.290	-.2527	.0636	53.4	.5547	1.820
75	29.153	28.667	2.657	1.173	.00812	.00801	47.70	-13.50	11.018	61.612	14.03	-5.710	-.4120	.0655	53.8	.5577	1.755
85	30.023	29.330	2.639	1.203	.00831	.00816	47.57	-15.10	11.172	63.224	15.15	-8.166	-.5535	.0674	54.3	.5609	1.698
95	30.885	29.976	2.622	1.251	.00850	.00830	48.40	-17.65	11.355	66.741	17.20	-10.780	-.6915	.0691	54.8	.5656	1.646
100	31.315	30.278	2.614	1.283	.00860	.00836	49.18	-19.46	11.488	69.390	19.69	-12.294	-.7502	.0700	55.0	.5649	1.621

Percent Flow	Diameter IE Meters	Diameter TE Meters	C Meters	C _f Meters	LER Meters	TER Meters	β ³ Radians	β ⁴ Radians	W.A. Radians	φ _s Radians	φ _f Radians	Ē Radians	ξ Radians
0	.5520	.5867	.0744	.0243	.000169	.000174	.8615	-.2141	.1735	1.0481	.1260	.2584	.0275
5	.5628	.5967	.0735	.0245	.000171	.000176	.8503	-.1930	.1739	1.0202	.1382	.2251	.0232
10	.5610	.6067	.0728	.0248	.000173	.000178	.8455	-.1811	.1766	1.0071	.1492	.1950	.0195
15	.5947	.6166	.0722	.0251	.000176	.000180	.8432	-.1745	.1773	1.0014	.1586	.1676	.0163
25	.6211	.6363	.0712	.0260	.000181	.000184	.8448	-.1748	.1782	1.0087	.1743	.1172	.0109
35	.6465	.6555	.0702	.0268	.000186	.000188	.8463	-.1789	.1811	1.0189	.1895	.0709	.0063
45	.6709	.6744	.0694	.0276	.000191	.000192	.8456	-.1862	.1828	1.0295	.2012	.0271	.0023
55	.6947	.6928	.0686	.0284	.000196	.000195	.8434	-.1984	.1853	1.0430	.2155	-.0154	-.0012
65	.7179	.7107	.0680	.0291	.000201	.000199	.8386	-.2146	.1888	1.0577	.2293	-.0574	-.0044
75	.7405	.7281	.0675	.0298	.000206	.000203	.8324	-.2356	.1923	1.0751	.2448	-.0956	-.0072
85	.7626	.7450	.0670	.0306	.000211	.000207	.8301	-.2635	.1950	1.1033	.2644	-.1425	-.0097
95	.7845	.7614	.0666	.0318	.000215	.000210	.8446	-.3080	.1981	1.1466	.3001	-.1881	-.0121
100	.7954	.7691	.0664	.0326	.000218	.000212	.8582	-.3396	.2005	1.2109	.3436	-.2145	-.0131

APPENDIX E

COSINE VARIATION OF BLADE CHANNEL AREA

The suction surface D-G of Figure 12 is obtained by knowing the pressure surface shape and the local channel areas determined by the equation

$$A = A_D + (A_G - A_D) \left[1 - \cos \left(\frac{\pi}{2} \frac{Z - Z_D}{Z_G - Z_D} \right) \right]$$

where $A_D = A_D(Z)$ This function is calculated assuming constant corrected specific flow from core-flow conditions downstream of the oblique shock at D.

and $A_G = A_G(Z)$ This function is calculated assuming constant corrected specific flow from exit core-flow conditions.

Page Intentionally Left Blank

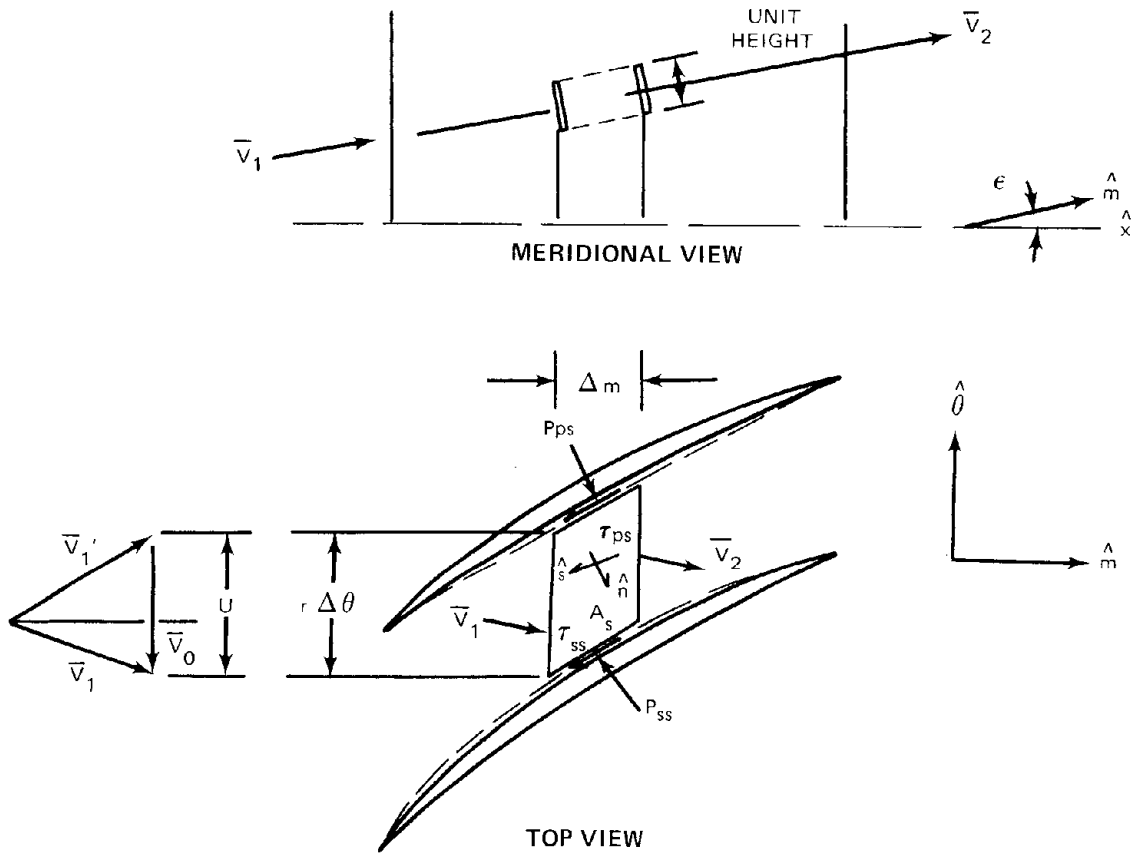
APPENDIX F

CALCULATION OF INTRABLADE WORK DISTRIBUTION BASED ON BLADE CHANNEL STATIC PRESSURE DISTRIBUTIONS

The precompression airfoil-design programs calculate static pressure distributions along the pressure and suction surfaces. From these pressure distributions it is possible to calculate a tangential velocity distribution by dividing the aerodynamic channel between boundary layers into tangential slices and applying the momentum equation to each control volume as shown in the figure below. Momentum in the tangential direction is given by

$$(p A_s) \hat{n} \cdot \hat{u} + (\tau A_s) \hat{s} \cdot \hat{u} = \oint V_\theta (\rho V \cdot dA)$$

where $dA = r d\theta$ for a unit increment normal to the meridional
 $A_s \hat{n} \cdot \hat{u} = \Delta m$ direction (see meridional view)



If the friction term is ignored, the equation can be integrated to give:

$$(p_{ps} - p_{ss}) \Delta m = \rho_2 V_{m2} \Delta \theta r_2 V_{\theta 2} - \rho_1 V_{m1} \Delta \theta r_1 V_{\theta 1}$$

If an average ρV_m term is assumed across the element, the equation can be solved for $\Delta r V_\theta$ as follows:

$$r V_\theta = \frac{p_{ps} - p_{ss}}{\rho V_m \text{ average}} \times \frac{\Delta m}{\Delta \theta}$$

where p_{ps} = average static pressure on the pressure surface
 p_{ss} = average static pressure on the suction surface
 Δm = control volume increment in meridional direction (length units)
 $r \Delta \theta$ = average control volume increment in tangential direction (length units)

The ρV_m distribution in the blade channel is obtained by correcting the input annulus ρV_m distribution (from Wu-Marsh calculation) by area ratios.

$$\rho V_m \text{ channel} = \rho V_m \text{ annulus} \times \frac{\theta_\tau}{\Delta \theta} \quad \text{where } \theta_\tau = \text{blade gap in radians.}$$

The meridional distribution of $r V_\theta$ is obtained by summing the increments from leading to trailing edges. The trailing edge value did not always agree well with the known blade element work calculated by the flow field program due to inaccuracies in the static pressure distribution and the assumption of negligible friction along the blade surfaces. As a result, the ratio of the local calculated $r V_\theta$ to the trailing edge $r V_\theta$ was used for the intrablade distribution input to the Wu-Marsh flowfield program rather than absolute values. The axial (meridional) distributions of $r V_\theta / r V_\theta \text{ total}$ are shown in the previous figure.

APPENDIX G

BLOCKAGE CALCULATIONS

Total blockage factor \bar{K} is defined as follows:

$$\text{Flowrate, } W = \int \rho V_m \bar{K} dA_{\text{annulus}}$$

where $\bar{K} = A_{\text{effective}}/A_{\text{annulus}}$ for an annular stream tube.

1. Normal flow field streamline calculations have end-wall and part-span shroud blockages included as one factor defined by:

$$\bar{K}_{EW} = \frac{A_{\text{effective annulus}}}{A_{\text{annulus}}} = \bar{K}_1$$

where $A_{\text{effective annulus}}$ refers to the flow field annulus area minus the boundary layer blockage of the end walls and part-span shroud(s) in the radial direction.

2. To run a flow field solution for the core (nonboundary layer) flow, the blade metal and blade boundary layer blockages must be accounted for in the tangential direction at a given spanwise location. This blockage is defined by:

$$\bar{K}_{\text{blade}} = \frac{s - t - \delta^*_{\text{tot}}}{S} \quad \text{where } s = \begin{array}{l} \text{blade gap at any axial loca-} \\ \text{tion along a streamline} \\ \text{(diameter changes according} \\ \text{to streamline angle.)} \end{array}$$

$$\bar{K}_2 = \frac{A_{\text{effective channel}}}{A_{\text{effective annulus segment}}} \quad \begin{array}{l} t = \text{blade thickness at the cor-} \\ \text{responding axial locationn.} \\ \delta^*_{\text{tot}} = \text{combined suction and pres-} \\ \text{sure surface boundary layer} \\ \text{displacement thickness} \end{array}$$

3. Two additional tangential blockages due to shock-boundary layer growth and non-axisymmetric flow contribute to reducing the effective channel area. These are described separately below:

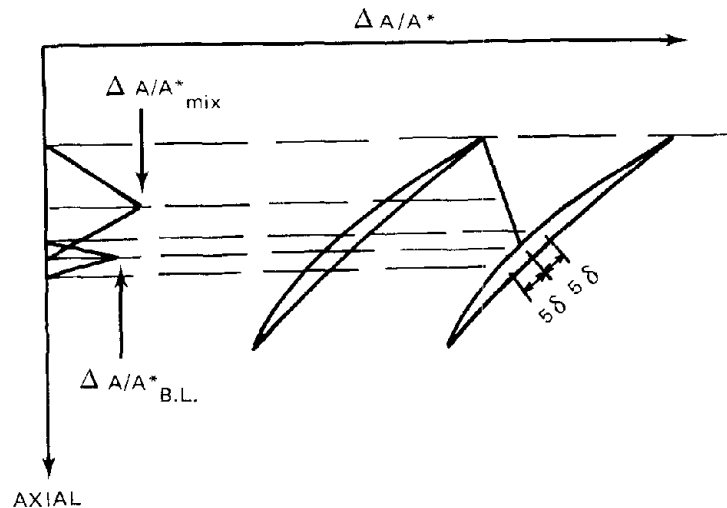
a. Shock-Boundary Layer Interaction Blockage

Data published in reference 10 indicates that shocks interact with the blade boundary layer in a manner which prevents the full theoretical static pressure rise from occurring across the shock. For the range of supersonic approach Mach numbers used for this design, the data show that the shock static pressure rise corresponds to downstream subsonic flow with an A/A^* ratio between 1.001 and 1.002. In this design, an A/A^* value of 1.0015 at the shock-suction surface intersection was assumed. The difference between 1.0015 and the theoretical A/A^* downstream of the shock was used to calculate a blockage as follows:

$$\bar{K} = \frac{A_{\text{flow}}}{A_{\text{eff chan}}} = \frac{A_{\text{eff chan}} - \Delta A_{\text{B.L.}}}{A_{\text{eff chan}}} = 1 - \frac{\Delta A/A^*)_{\text{B.L.}}}{A_{\text{eff chan}}/A^*}$$

where $\Delta A/A^*)_{\text{B.L.}} = A/A^*)_{\text{My}} - 1.0015$

The A/A^* value was distributed in a triangular pattern with the peak at the shock-suction surface intersection and zero at distances of five boundary layers on both sides of the peak (see the following figure).



b. Blockage Due to Non-Axisymmetric Flow

The flow field calculation is made assuming axisymmetric flow. In general, gradients of velocity and static pressure occur across gaps between blades. Gapwise total pressure gradients also exist in axial planes intersected by shocks in the blade passages. Real flow, with these gapwise gradients, requires more flow area than the theoretical axisymmetric flow at the average total and static pressures of the non-axisymmetric flow. The effect was significant only where total pressure gradients exist, i.e., where shocks were present. The average A/A^* at the midshock axial location for the nonaxisymmetric flow condition was assumed to be the average of the axisymmetric values upstream and downstream of the shock. The axisymmetric A/A^* was assumed to be the value corresponding to the average of static to total pressure ratios upstream and downstream of the shock. The differences in the flow areas was used to calculate a blockage as shown below:

$$\bar{K} = \frac{A_{\text{flow}}}{A_{\text{eff channel}}} = \frac{A_{\text{eff chan}} - \Delta A_{\text{mix}}}{A_{\text{eff chan}}} = 1 - \frac{\Delta A/A^*_{\text{mix}}}{A_{\text{eff chan}}/A^*}$$

where $\Delta A/A^*_{\text{mix}} = A/A^*_{\text{non-axi}} - A/A^*_{\text{axi}}$,

$$A/A^*_{\text{non-axi}} = 1/2 (A/A^*)_{M_x} + A/A^*_{M_y} \text{ at mid shock location}$$

$$A/A^*_{\text{axi}} \text{ corresponds to } p/P_{\text{axi}} = \frac{p_x + p_y}{P_x + P_y}$$

The $\Delta A/A^*$ value was also distributed triangularly with the peak at the shock center and zero at the shock ends (see previous figure).

Since the blockages due to the boundary layer and nonaxisymmetric flow were calculated similarly by reducing the channel effective area, they were combined into one blockage term. At any axial location, the blade effective channel area will be reduced by the total ΔA shown in the previous figure.

$$\begin{aligned} \bar{K}_3 &= \frac{A_{\text{flow}}}{A_{\text{eff channel}}} = \frac{A_{\text{eff chan}} - \Delta A_{\text{mix}} - \Delta A_{\text{B.L.}}}{A_{\text{eff chan}}} \\ &= 1 - \frac{\Delta A/A^*_{\text{mix}} + \Delta A/A^*_{\text{B.L.}}}{A_{\text{eff chan}}/A^*} \end{aligned}$$

4. Total Blockage

The product of the three major blockage terms described previously determines a total blockage as shown below:

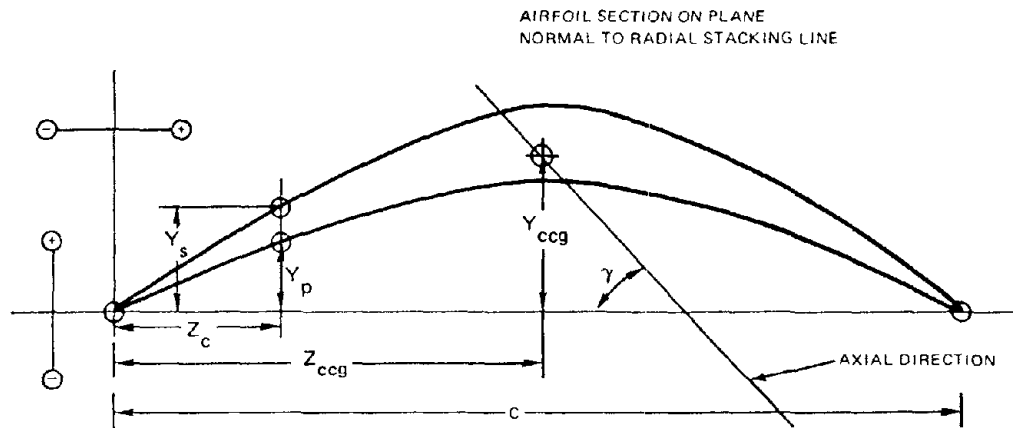
$$\bar{K}_{\text{total}} = \bar{K}_1 \times \bar{K}_2 \times \bar{K}_3$$

$$\frac{A_{\text{flow}}}{A_{\text{annulus}}} = \frac{A_{\text{eff annulus}}}{A_{\text{annulus}}} \times \frac{A_{\text{eff channel}}}{A_{\text{eff annulus}}} \times \frac{A_{\text{flow}}}{A_{\text{eff channel}}}$$

APPENDIX H

MANUFACTURING COORDINATES FOR
SECTIONS NORMAL TO THE STACKING LINE

The tabulations on the following pages present manufacturing coordinates for both the rotor and stator at several sections, as defined by the radius dimension, in both English and SI units. The sketch below defines the airfoil coordinate system corresponding to the tabulations.



Rotor, Section 1

METERS			INCHES		
ZC	YP	YS	ZC	YP	YS
0.0	0.0	0.0	0.0	0.0	0.0
0.0004		0.0008	0.0160		0.0320
0.0006	-0.0005		0.0230	-0.0200	
0.0022	-0.0004	0.0014	0.0861	-0.0150	0.0540
0.0044	-0.0001	0.0021	0.1722	-0.0050	0.0840
0.0087	0.0005	0.0037	0.3444	0.0180	0.1440
0.0131	0.0011	0.0051	0.5166	0.0420	0.2020
0.0175	0.0016	0.0067	0.6888	0.0620	0.2620
0.0262	0.0029	0.0098	1.0332	0.1140	0.3840
0.0350	0.0049	0.0133	1.3776	0.1920	0.5220
0.0437	0.0065	0.0163	1.7220	0.2560	0.6400
0.0525	0.0077	0.0187	2.0664	0.3040	0.7380
0.0700	0.0092	0.0217	2.7552	0.3610	0.8550
0.0875	0.0096	0.0228	3.4440	0.3760	0.8960
0.1050	0.0090	0.0222	4.1328	0.3530	0.8740
0.1225	0.0071	0.0201	4.8216	0.2800	0.7910
0.1400	0.0040	0.0168	5.5104	0.1590	0.6620
0.1575	-0.0000	0.0121	6.1992	-0.0010	0.4770
0.1745	-0.0040		6.8690	-0.1590	
0.1750	0.0	0.0	6.8880	0.0	0.0
0.1755		0.0044	6.9090		0.1720
RADIUS (METERS) = 0.2144			RADIUS (INCHES) = 8.4400		
CHORD (METERS) = 0.1551			CHORD (INCHES) = 6.1064		
ZCSL (METERS) = 0.0890			ZCSL (INCHES) = 3.5037		
YCSL (METERS) = 0.0124			YCSL (INCHES) = 0.4868		
RLE (METERS) = 0.000660			RLE (INCHES) = 0.0260		
RTE (METERS) = 0.0			RTE (INCHES) = 0.0		
X-AREA (SQ. METERS) = 0.0			X-AREA (SQ. IN.) = 0.0		
GAMMA-CHORD (DEG.) = 39.62			GAMMA-CHORD (RAD.) = 0.6915		

This section is partially buried in the blade root attachment.

Rotor, Section 2

METERS			INCHES		
ZC	YP	YS	ZC	YP	YS
0.0	0.0	0.0	0.0	0.0	0.0
0.0004		0.0007	0.0160		0.0280
0.0007	-0.0005		0.0260	-0.0190	
0.0022	-0.0003	0.0012	0.0852	-0.0120	0.0490
0.0043	-0.0002	0.0018	0.1704	-0.0060	0.0720
0.0087	0.0003	0.0030	0.3408	0.0100	0.1200
0.0130	0.0007	0.0042	0.5112	0.0260	0.1670
0.0173	0.0011	0.0055	0.6816	0.0420	0.2180
0.0260	0.0021	0.0082	1.0224	0.0830	0.3220
0.0346	0.0033	0.0109	1.3632	0.1290	0.4300
0.0433	0.0046	0.0137	1.7040	0.1820	0.5380
0.0519	0.0061	0.0164	2.0448	0.2400	0.6460
0.0693	0.0092	0.0216	2.7264	0.3620	0.8500
0.0866	0.0111	0.0244	3.4080	0.4360	0.9600
0.1039	0.0114	0.0243	4.0896	0.4470	0.9580
0.1212	0.0100	0.0225	4.7712	0.3920	0.8870
0.1385	0.0069	0.0185	5.4528	0.2710	0.7280
0.1558	0.0019	0.0120	6.1344	0.0740	0.4740
0.1727	-0.0028		6.8000	-0.1100	
0.1731	0.0	0.0	6.8160	0.0	0.0
0.1734		0.0028	6.8280		0.1100
RADIUS (METERS) = 0.2296			RADIUS (INCHES) = 9.0400		
CHORD (METERS) = 0.1656			CHORD (INCHES) = 6.5177		
ZCSL (METERS) = 0.0910			ZCSL (INCHES) = 3.5842		
YCSL (METERS) = 0.0118			YCSL (INCHES) = 0.4665		
RLE (METERS) = 0.000635			RLE (INCHES) = 0.0250		
RTE (METERS) = 0.0			RTE (INCHES) = 0.0		
X-AREA (SQ. METERS) = 0.0			X-AREA (SQ. IN.) = 0.0		
GAMMA-CHORD (DEG.) = 41.78			GAMMA-CHORD (RAD.) = 0.7292		

This section is partially buried in the blade root attachment.

Rotor, Section 3

METERS			INCHES		
ZC	YP	YS	ZC	YP	YS
0.0	0.0	0.0	0.0	0.0	0.0
0.0005		0.0007	0.0180		0.0280
0.0006	-0.0005		0.0240	-0.0200	
0.0022	-0.0004	0.0012	0.0848	-0.0140	0.0460
0.0043	-0.0002	0.0017	0.1696	-0.0060	0.0660
0.0086	0.0003	0.0027	0.3392	0.0100	0.1070
0.0129	0.0007	0.0038	0.5088	0.0260	0.1490
0.0172	0.0010	0.0049	0.6784	0.0400	0.1930
0.0258	0.0016	0.0070	1.0176	0.0640	0.2740
0.0345	0.0022	0.0090	1.3568	0.0880	0.3560
0.0431	0.0030	0.0112	1.6960	0.1180	0.4400
0.0517	0.0039	0.0133	2.0352	0.1520	0.5230
0.0689	0.0061	0.0177	2.7136	0.2390	0.6980
0.0862	0.0082	0.0212	3.3920	0.3240	0.8340
0.1034	0.0096	0.0225	4.0704	0.3760	0.8860
0.1206	0.0096	0.0215	4.7488	0.3760	0.8480
0.1379	0.0075	0.0181	5.4272	0.2950	0.7120
0.1551	0.0037	0.0113	6.1056	0.1460	0.4460
0.1721	-0.0014		6.7750	-0.0560	
0.1723	0.0	0.0	6.7840	0.0	0.0
0.1726		0.0015	6.7950		0.0590
RADIUS (METERS) = 0.2446			RADIUS (INCHES) = 9.6300		
CHORD (METERS) = 0.1722			CHORD (INCHES) = 6.7807		
ZCSL (METERS) = 0.0935			ZCSL (INCHES) = 3.6805		
YCSL (METERS) = 0.0106			YCSL (INCHES) = 0.4192		
RLE (METERS) = 0.000610			RLE (INCHES) = 0.0240		
RTE (METERS) = 0.0			RTE (INCHES) = 0.0		
X-AREA (SQ. METERS) = 0.0			X-AREA (SQ. IN.) = 0.0		
GAMMA-CHORD (DEG.) = 46.84			GAMMA-CHORD (RAD.) = 0.8174		

This section is partially buried in the blade root attachment.

Rotor, Section 4

METERS			INCHES		
ZC	YP	YS	ZC	YP	YS
0.0	-0.0006	0.0006	0.0	-0.0237	0.0237
0.0006	-0.0005	0.0007	0.0249	-0.0217	0.0293
0.0055	-0.0001	0.0018	0.2173	-0.0054	0.0723
0.0110	0.0003	0.0030	0.4346	0.0119	0.1198
0.0166	0.0007	0.0042	0.6518	0.0279	0.1660
0.0221	0.0011	0.0053	0.8691	0.0425	0.2104
0.0276	0.0014	0.0064	1.0864	0.0556	0.2533
0.0331	0.0017	0.0075	1.3037	0.0679	0.2957
0.0386	0.0020	0.0086	1.5209	0.0796	0.3391
0.0442	0.0023	0.0097	1.7382	0.0913	0.3836
0.0497	0.0026	0.0109	1.9555	0.1033	0.4287
0.0552	0.0030	0.0120	2.1728	0.1164	0.4743
0.0607	0.0033	0.0132	2.3900	0.1305	0.5203
0.0662	0.0037	0.0144	2.6073	0.1465	0.5663
0.0717	0.0042	0.0155	2.8246	0.1641	0.6115
0.0773	0.0046	0.0166	3.0419	0.1815	0.6545
0.0828	0.0050	0.0175	3.2592	0.1967	0.6884
0.0883	0.0053	0.0182	3.4764	0.2101	0.7147
0.0938	0.0056	0.0187	3.6937	0.2209	0.7351
0.0993	0.0058	0.0189	3.9110	0.2294	0.7438
0.1049	0.0060	0.0190	4.1283	0.2347	0.7470
0.1104	0.0060	0.0188	4.3455	0.2377	0.7410
0.1159	0.0060	0.0185	4.5628	0.2358	0.7270
0.1214	0.0059	0.0179	4.7801	0.2321	0.7056
0.1269	0.0057	0.0171	4.9974	0.2259	0.6732
0.1325	0.0055	0.0160	5.2147	0.2160	0.6318
0.1380	0.0051	0.0148	5.4319	0.2024	0.5810
0.1435	0.0046	0.0133	5.6492	0.1826	0.5223
0.1490	0.0040	0.0115	5.8665	0.1580	0.4539
0.1545	0.0033	0.0095	6.0838	0.1282	0.3741
0.1600	0.0022	0.0071	6.3011	0.0885	0.2787
0.1656	0.0011	0.0042	6.5183	0.0415	0.1665
0.1705	-0.0003	0.0012	6.7134	-0.0128	0.0466
0.1711	-0.0005	0.0008	6.7356	-0.0190	0.0330
RADIUS (METERS) = 0.2598			RADIUS (INCHES) = 10.2300		
CHORD (METERS) = 0.1711			CHORD (INCHES) = 6.7356		
ZCSL (METERS) = 0.0946			ZCSL (INCHES) = 3.7244		
YCSL (METERS) = 0.0084			YCSL (INCHES) = 0.3320		
RLE (METERS) = 0.000638			RLE (INCHES) = 0.0251		
RTE (METERS) = 0.000683			RTE (INCHES) = 0.0269		
X-AREA (SQ. METERS) = 0.001456			X-AREA (SQ. IN.) = 2.2575		
GAMMA-CHORD (DEG.) = 51.87			GAMMA-CHORD (RAD.) = 0.9052		

Rotor, Section 5

METERS			INCHES		
ZC	YP	YS	ZC	YP	YS
0.0	-0.0006	0.0006	0.0	-0.0223	0.0223
0.0006	-0.0005	0.0007	0.0234	-0.0209	0.0267
0.0055	-0.0002	0.0016	0.2163	-0.0090	0.0629
0.0110	0.0001	0.0026	0.4326	0.0029	0.1025
0.0165	0.0003	0.0036	0.6489	0.0133	0.1402
0.0220	0.0006	0.0045	0.8652	0.0224	0.1757
0.0275	0.0008	0.0053	1.0815	0.0302	0.2094
0.0330	0.0009	0.0062	1.2978	0.0370	0.2424
0.0385	0.0011	0.0070	1.5141	0.0436	0.2774
0.0440	0.0013	0.0080	1.7303	0.0508	0.3149
0.0494	0.0015	0.0090	1.9466	0.0586	0.3537
0.0549	0.0017	0.0100	2.1629	0.0671	0.3931
0.0604	0.0019	0.0110	2.3792	0.0764	0.4334
0.0659	0.0022	0.0120	2.5955	0.0865	0.4741
0.0714	0.0025	0.0131	2.8118	0.0969	0.5144
0.0769	0.0027	0.0141	3.0281	0.1064	0.5533
0.0824	0.0029	0.0150	3.2444	0.1138	0.5898
0.0879	0.0030	0.0156	3.4607	0.1195	0.6160
0.0934	0.0031	0.0160	3.6770	0.1229	0.6310
0.0989	0.0032	0.0161	3.8933	0.1246	0.6340
0.1044	0.0032	0.0161	4.1096	0.1252	0.6330
0.1099	0.0032	0.0160	4.3259	0.1252	0.6301
0.1154	0.0031	0.0155	4.5422	0.1235	0.6109
0.1209	0.0031	0.0148	4.7585	0.1206	0.5834
0.1264	0.0029	0.0140	4.9748	0.1157	0.5524
0.1319	0.0028	0.0131	5.1910	0.1090	0.5170
0.1373	0.0025	0.0121	5.4073	0.1000	0.4768
0.1428	0.0023	0.0109	5.6236	0.0888	0.4282
0.1483	0.0019	0.0094	5.8399	0.0740	0.3707
0.1538	0.0014	0.0077	6.0562	0.0566	0.3018
0.1593	0.0009	0.0056	6.2725	0.0353	0.2213
0.1648	0.0003	0.0033	6.4888	0.0113	0.1289
0.1698	-0.0003	0.0009	6.6847	-0.0127	0.0356
0.1703	-0.0004	0.0007	6.7051	-0.0152	0.0259
RADIUS (METERS) = 0.2751			RADIUS (INCHES) = 10.8300		
CHORD (METERS) = 0.1703			CHORD (INCHES) = 6.7051		
ZCSL (METERS) = 0.0945			ZCSL (INCHES) = 3.7198		
YCSL (METERS) = 0.0062			YCSL (INCHES) = 0.2445		
RLE (METERS) = 0.000597			RLE (INCHES) = 0.0235		
RTE (METERS) = 0.000579			RTE (INCHES) = 0.0228		
X-AREA (SQ. METERS) = 0.001397			X-AREA (SQ. IN.) = 2.1657		
GAMMA-CHORD (DEG.) = 54.05			GAMMA-CHORD (RAD.) = 0.9433		

Rotor, Section 6

METERS			INCHES		
ZC	YP	YS	ZC	YP	YS
0.0	-0.0006	0.0004	0.0	-0.0251	0.0170
0.0006	-0.0006	0.0005	0.0221	-0.0241	0.0206
0.0055	-0.0004	0.0013	0.2161	-0.0158	0.0518
0.0110	-0.0002	0.0022	0.4323	-0.0060	0.0864
0.0165	0.0000	0.0031	0.6484	0.0019	0.1205
0.0220	0.0003	0.0039	0.8646	0.0125	0.1543
0.0275	0.0005	0.0046	1.0807	0.0189	0.1822
0.0329	0.0004	0.0053	1.2969	0.0174	0.2093
0.0384	0.0006	0.0062	1.5130	0.0236	0.2431
0.0439	0.0006	0.0071	1.7292	0.0237	0.2777
0.0494	0.0007	0.0078	1.9453	0.0268	0.3072
0.0549	0.0008	0.0087	2.1615	0.0318	0.3410
0.0604	0.0008	0.0096	2.3776	0.0315	0.3769
0.0659	0.0008	0.0105	2.5938	0.0321	0.4121
0.0714	0.0008	0.0113	2.8096	0.0332	0.4465
0.0769	0.0009	0.0120	3.0261	0.0338	0.4742
0.0824	0.0010	0.0127	3.2422	0.0379	0.4988
0.0878	0.0011	0.0132	3.4584	0.0433	0.5194
0.0933	0.0012	0.0137	3.6745	0.0475	0.5382
0.0988	0.0013	0.0141	3.8906	0.0519	0.5534
0.1043	0.0014	0.0142	4.1068	0.0533	0.5604
0.1098	0.0014	0.0141	4.3229	0.0561	0.5557
0.1153	0.0014	0.0136	4.5391	0.0543	0.5335
0.1208	0.0013	0.0128	4.7552	0.0527	0.5042
0.1263	0.0012	0.0118	4.9714	0.0459	0.4663
0.1318	0.0009	0.0109	5.1875	0.0370	0.4276
0.1373	0.0007	0.0098	5.4037	0.0292	0.3849
0.1427	0.0005	0.0087	5.6198	0.0202	0.3417
0.1482	0.0004	0.0074	5.8360	0.0143	0.2915
0.1537	0.0002	0.0060	6.0521	0.0061	0.2364
0.1592	-0.0001	0.0045	6.2683	-0.0037	0.1761
0.1647	-0.0003	0.0026	6.4844	-0.0102	0.1039
0.1697	-0.0004	0.0006	6.6808	-0.0176	0.0238
0.1702	-0.0005	0.0004	6.7006	-0.0184	0.0157
RADIUS (METERS) = 0.2878			RADIUS (INCHES) = 11.3300		
CHORD (METERS) = 0.1702			CHORD (INCHES) = 6.7006		
ZCSL (METERS) = 0.0946			ZCSL (INCHES) = 3.7237		
YCSL (METERS) = 0.0042			YCSL (INCHES) = 0.1638		
RLE (METERS) = 0.000564			RLE (INCHES) = 0.0222		
RTE (METERS) = 0.000505			RTE (INCHES) = 0.0199		
X-AREA (SQ. METERS) = 0.001348			X-AREA (SQ. IN.) = 2.0887		
GAMMA-CHORD (DEG.) = 56.89			GAMMA-CHORD (RAD.) = 0.9929		

Rotor, Section 7

METERS			INCHES		
ZC	YP	YS	ZC	YP	YS
0.0	-0.0006	0.0005	0.0	-0.0231	0.0196
0.0006	-0.0006	0.0005	0.0221	-0.0230	0.0214
0.0055	-0.0006	0.0009	0.2163	-0.0225	0.0370
0.0110	-0.0006	0.0014	0.4325	-0.0236	0.0561
0.0165	-0.0007	0.0020	0.6488	-0.0263	0.0776
0.0220	-0.0007	0.0024	0.8651	-0.0279	0.0947
0.0275	-0.0008	0.0028	1.0813	-0.0311	0.1120
0.0330	-0.0009	0.0034	1.2976	-0.0337	0.1340
0.0385	-0.0010	0.0040	1.5139	-0.0387	0.1580
0.0439	-0.0011	0.0046	1.7301	-0.0440	0.1826
0.0494	-0.0012	0.0053	1.9464	-0.0468	0.2104
0.0549	-0.0014	0.0060	2.1627	-0.0556	0.2353
0.0604	-0.0016	0.0066	2.3790	-0.0637	0.2590
0.0659	-0.0018	0.0072	2.5952	-0.0728	0.2828
0.0714	-0.0021	0.0078	2.8115	-0.0818	0.3062
0.0769	-0.0023	0.0084	3.0278	-0.0921	0.3291
0.0824	-0.0025	0.0089	3.2440	-0.0981	0.3520
0.0879	-0.0025	0.0094	3.4603	-0.0992	0.3701
0.0934	-0.0024	0.0098	3.6765	-0.0950	0.3864
0.0989	-0.0023	0.0102	3.8928	-0.0902	0.3996
0.1044	-0.0021	0.0103	4.1091	-0.0830	0.4072
0.1099	-0.0020	0.0104	4.3254	-0.0778	0.4075
0.1154	-0.0019	0.0101	4.5416	-0.0753	0.3983
0.1209	-0.0017	0.0096	4.7579	-0.0682	0.3789
0.1263	-0.0016	0.0090	4.9742	-0.0631	0.3536
0.1318	-0.0015	0.0082	5.1904	-0.0583	0.3228
0.1373	-0.0013	0.0074	5.4067	-0.0510	0.2900
0.1428	-0.0012	0.0063	5.6230	-0.0465	0.2497
0.1483	-0.0010	0.0052	5.8392	-0.0389	0.2065
0.1538	-0.0009	0.0042	6.0555	-0.0339	0.1648
0.1593	-0.0007	0.0029	6.2718	-0.0270	0.1159
0.1648	-0.0006	0.0018	6.4880	-0.0252	0.0721
0.1697	-0.0006	0.0007	6.6796	-0.0237	0.0265
0.1703	-0.0006	0.0005	6.7043	-0.0235	0.0206
RADIUS (METERS) = 0.3056			RADIUS (INCHES) = 12.0300		
CHORD (METERS) = 0.1703			CHORD (INCHES) = 6.7043		
ZCSL (METERS) = 0.0950			ZCSL (INCHES) = 3.7406		
YCSL (METERS) = 0.0011			YCSL (INCHES) = 0.0452		
RLE (METERS) = 0.000561			RLE (INCHES) = 0.0221		
RTE (METERS) = 0.000627			RTE (INCHES) = 0.0247		
X-AREA (SQ. METERS) = 0.001277			X-AREA (SQ. IN.) = 1.9796		
GAMMA-CHORD (DEG.) = 60.88			GAMMA-CHORD (RAD.) = 1.0625		

Rotor, Section 8

METERS			INCHES		
ZC	YP	YS	ZC	YP	YS
0.0	-0.0005	0.0005	0.0	-0.0190	0.0189
0.0005	-0.0005	0.0005	0.0197	-0.0194	0.0201
0.0056	-0.0006	0.0008	0.2191	-0.0228	0.0326
0.0111	-0.0007	0.0012	0.4382	-0.0276	0.0454
0.0167	-0.0009	0.0014	0.6573	-0.0346	0.0570
0.0223	-0.0011	0.0017	0.8764	-0.0437	0.0664
0.0278	-0.0014	0.0019	1.0955	-0.0544	0.0745
0.0334	-0.0017	0.0021	1.3146	-0.0666	0.0815
0.0390	-0.0020	0.0022	1.5337	-0.0803	0.0884
0.0445	-0.0024	0.0024	1.7528	-0.0957	0.0964
0.0501	-0.0029	0.0028	1.9719	-0.1125	0.1119
0.0557	-0.0033	0.0033	2.1910	-0.1306	0.1293
0.0612	-0.0038	0.0038	2.4101	-0.1497	0.1479
0.0668	-0.0043	0.0042	2.6292	-0.1692	0.1665
0.0723	-0.0047	0.0047	2.8483	-0.1870	0.1847
0.0779	-0.0051	0.0051	3.0674	-0.1996	0.2026
0.0835	-0.0052	0.0056	3.2865	-0.2058	0.2202
0.0890	-0.0053	0.0060	3.5056	-0.2071	0.2373
0.0946	-0.0052	0.0064	3.7247	-0.2030	0.2532
0.1002	-0.0050	0.0068	3.9438	-0.1956	0.2675
0.1057	-0.0047	0.0071	4.1629	-0.1860	0.2785
0.1113	-0.0045	0.0072	4.3820	-0.1754	0.2854
0.1169	-0.0042	0.0073	4.6011	-0.1645	0.2855
0.1224	-0.0039	0.0071	4.8202	-0.1538	0.2792
0.1280	-0.0036	0.0068	5.0393	-0.1429	0.2690
0.1336	-0.0033	0.0065	5.2584	-0.1315	0.2555
0.1391	-0.0030	0.0060	5.4775	-0.1195	0.2376
0.1447	-0.0027	0.0054	5.6966	-0.1058	0.2109
0.1503	-0.0023	0.0045	5.9157	-0.0896	0.1767
0.1558	-0.0018	0.0035	6.1348	-0.0707	0.1374
0.1614	-0.0012	0.0024	6.3539	-0.0474	0.0960
0.1670	-0.0008	0.0014	6.5730	-0.0300	0.0534
0.1704	-0.0004	0.0006	6.7095	-0.0170	0.0240
0.1709	-0.0004	0.0005	6.7300	-0.0150	0.0210
RADIUS (METERS) = 0.3233			RADIUS (INCHES) = 12.7300		
CHORD (METERS) = 0.1709			CHORD (INCHES) = 6.7300		
ZCSL (METERS) = 0.0969			ZCSL (INCHES) = 3.8137		
YCSL (METERS) = -0.0012			YCSL (INCHES) = -0.0489		
RLE (METERS) = 0.000500			RLE (INCHES) = 0.0197		
RTE (METERS) = 0.000521			RTE (INCHES) = 0.0205		
X-AREA (SQ. METERS) = 0.001224			X-AREA (SQ. IN.) = 1.8978		
GAMMA-CHORD (DEG.) = 64.25			GAMMA-CHORD (RAD.) = 1.1213		

Rotor, Section 9

METERS			INCHES		
ZC	YP	YS	ZC	YP	YS
0.0	-0.0004	0.0005	0.0	-0.0174	0.0194
0.0005	-0.0005	0.0005	0.0189	-0.0177	0.0202
0.0056	-0.0005	0.0007	0.2201	-0.0211	0.0286
0.0112	-0.0007	0.0010	0.4403	-0.0269	0.0406
0.0168	-0.0009	0.0013	0.6604	-0.0347	0.0499
0.0224	-0.0011	0.0015	0.8806	-0.0438	0.0588
0.0280	-0.0014	0.0017	1.1007	-0.0539	0.0670
0.0336	-0.0017	0.0019	1.3209	-0.0652	0.0737
0.0391	-0.0020	0.0020	1.5410	-0.0777	0.0791
0.0447	-0.0023	0.0023	1.7612	-0.0912	0.0889
0.0503	-0.0027	0.0025	1.9813	-0.1046	0.0999
0.0559	-0.0031	0.0029	2.2015	-0.1202	0.1128
0.0615	-0.0035	0.0033	2.4216	-0.1396	0.1289
0.0671	-0.0041	0.0037	2.6418	-0.1599	0.1475
0.0727	-0.0046	0.0041	2.8619	-0.1801	0.1624
0.0783	-0.0052	0.0045	3.0821	-0.2031	0.1772
0.0839	-0.0056	0.0049	3.3022	-0.2212	0.1919
0.0895	-0.0059	0.0052	3.5224	-0.2341	0.2044
0.0951	-0.0060	0.0054	3.7425	-0.2364	0.2115
0.1007	-0.0058	0.0056	3.9627	-0.2302	0.2186
0.1062	-0.0056	0.0058	4.1828	-0.2199	0.2264
0.1118	-0.0052	0.0059	4.4030	-0.2051	0.2304
0.1174	-0.0048	0.0059	4.6231	-0.1904	0.2321
0.1230	-0.0045	0.0060	4.8433	-0.1770	0.2353
0.1286	-0.0041	0.0060	5.0634	-0.1600	0.2379
0.1342	-0.0036	0.0059	5.2836	-0.1421	0.2339
0.1398	-0.0032	0.0057	5.5037	-0.1269	0.2257
0.1454	-0.0029	0.0053	5.7239	-0.1134	0.2094
0.1510	-0.0025	0.0046	5.9440	-0.0979	0.1803
0.1566	-0.0020	0.0037	6.1642	-0.0781	0.1467
0.1622	-0.0015	0.0028	6.3843	-0.0608	0.1092
0.1678	-0.0010	0.0016	6.6045	-0.0396	0.0638
0.1729	-0.0004	0.0006	6.8061	-0.0158	0.0223
0.1733	-0.0003	0.0005	6.8246	-0.0136	0.0185
RADIUS (METERS) = 0.3360			RADIUS (INCHES) = 13.2300		
CHORD (METERS) = 0.1733			CHORD (INCHES) = 6.8246		
ZCSL (METERS) = 0.0987			ZCSL (INCHES) = 3.8846		
YCSL (METERS) = -0.0018			YCSL (INCHES) = -0.0702		
RLE (METERS) = 0.000480			RLE (INCHES) = 0.0189		
RTE (METERS) = 0.000478			RTE (INCHES) = 0.0188		
X-AREA (SQ. METERS) = 0.001178			X-AREA (SQ. IN.) = 1.8256		
GAMMA-CHORD (DEG.) = 65.64			GAMMA-CHORD (RAD.) = 1.1456		

Rotor, Section 10

METERS			INCHES		
ZC	YP	YS	ZC	YP	YS
0.0	-0.0007	0.0001	0.0	-0.0288	0.0046
0.0004	-0.0007	0.0001	0.0173	-0.0292	0.0053
0.0057	-0.0009	0.0003	0.2235	-0.0344	0.0137
0.0114	-0.0011	0.0005	0.4469	-0.0422	0.0207
0.0170	-0.0013	0.0007	0.6704	-0.0517	0.0262
0.0227	-0.0016	0.0008	0.8939	-0.0624	0.0303
0.0284	-0.0019	0.0008	1.1174	-0.0743	0.0333
0.0341	-0.0022	0.0009	1.3408	-0.0872	0.0361
0.0397	-0.0026	0.0010	1.5643	-0.1017	0.0394
0.0454	-0.0030	0.0011	1.7878	-0.1180	0.0448
0.0511	-0.0034	0.0014	2.0112	-0.1358	0.0546
0.0568	-0.0039	0.0018	2.2347	-0.1550	0.0698
0.0624	-0.0045	0.0022	2.4582	-0.1756	0.0856
0.0681	-0.0050	0.0026	2.6817	-0.1974	0.1014
0.0738	-0.0056	0.0029	2.9051	-0.2204	0.1154
0.0795	-0.0062	0.0033	3.1286	-0.2445	0.1283
0.0851	-0.0068	0.0036	3.3521	-0.2679	0.1403
0.0908	-0.0073	0.0038	3.5755	-0.2860	0.1503
0.0965	-0.0075	0.0040	3.7990	-0.2948	0.1591
0.1022	-0.0072	0.0042	4.0225	-0.2824	0.1666
0.1078	-0.0068	0.0044	4.2460	-0.2660	0.1727
0.1135	-0.0063	0.0045	4.4694	-0.2475	0.1769
0.1192	-0.0058	0.0046	4.6929	-0.2276	0.1798
0.1249	-0.0053	0.0046	4.9164	-0.2075	0.1814
0.1306	-0.0048	0.0046	5.1398	-0.1873	0.1814
0.1362	-0.0042	0.0045	5.3633	-0.1669	0.1779
0.1419	-0.0037	0.0043	5.5868	-0.1464	0.1702
0.1476	-0.0032	0.0040	5.8103	-0.1257	0.1586
0.1533	-0.0027	0.0037	6.0337	-0.1043	0.1444
0.1589	-0.0021	0.0031	6.2572	-0.0825	0.1233
0.1646	-0.0015	0.0024	6.4807	-0.0596	0.0925
0.1703	-0.0010	0.0014	6.7041	-0.0379	0.0565
0.1755	-0.0005	0.0005	6.9084	-0.0184	0.0204
0.1760	-0.0004	0.0004	6.9276	-0.0165	0.0171
RADIUS (METERS) = 0.3500			RADIUS (INCHES) = 13.7800		
CHORD (METERS) = 0.1760			CHORD (INCHES) = 6.9276		
ZCSL (METERS) = 0.1006			ZCSL (INCHES) = 3.9624		
YCSL (METERS) = -0.0024			YCSL (INCHES) = -0.0930		
RLE (METERS) = 0.000439			RLE (INCHES) = 0.0173		
RTE (METERS) = 0.000488			RTE (INCHES) = 0.0192		
X-AREA (SQ. METERS) = 0.001149			X-AREA (SQ. IN.) = 1.7805		
GAMMA-CHORD (DEG.) = 66.37			GAMMA-CHORD (RAD.) = 1.1584		

Rotor, Section 11

METERS			INCHES		
ZC	YP	YS	ZC	YP	YS
0.0	-0.0008	0.0000	0.0	-0.0307	0.0010
0.0004	-0.0008	0.0000	0.0163	-0.0309	0.0016
0.0058	-0.0009	0.0003	0.2280	-0.0347	0.0106
0.0116	-0.0011	0.0005	0.4560	-0.0414	0.0178
0.0174	-0.0013	0.0006	0.6840	-0.0507	0.0229
0.0232	-0.0015	0.0007	0.9120	-0.0606	0.0258
0.0290	-0.0018	0.0007	1.1400	-0.0709	0.0265
0.0347	-0.0021	0.0007	1.3680	-0.0828	0.0266
0.0405	-0.0025	0.0007	1.5960	-0.0970	0.0277
0.0463	-0.0029	0.0008	1.8239	-0.1139	0.0312
0.0521	-0.0034	0.0010	2.0520	-0.1329	0.0392
0.0579	-0.0039	0.0014	2.2799	-0.1538	0.0537
0.0637	-0.0045	0.0018	2.5079	-0.1768	0.0696
0.0695	-0.0051	0.0022	2.7359	-0.2007	0.0864
0.0753	-0.0057	0.0026	2.9639	-0.2250	0.1011
0.0811	-0.0063	0.0029	3.1919	-0.2494	0.1144
0.0869	-0.0069	0.0032	3.4199	-0.2731	0.1263
0.0927	-0.0074	0.0034	3.6479	-0.2928	0.1351
0.0984	-0.0077	0.0036	3.8759	-0.3048	0.1424
0.1042	-0.0075	0.0038	4.1039	-0.2947	0.1481
0.1100	-0.0071	0.0039	4.3319	-0.2790	0.1525
0.1158	-0.0066	0.0039	4.5599	-0.2599	0.1552
0.1216	-0.0061	0.0040	4.7879	-0.2389	0.1565
0.1274	-0.0055	0.0040	5.0159	-0.2177	0.1566
0.1332	-0.0050	0.0039	5.2439	-0.1962	0.1552
0.1390	-0.0044	0.0039	5.4719	-0.1745	0.1522
0.1448	-0.0039	0.0037	5.6999	-0.1526	0.1445
0.1506	-0.0033	0.0034	5.9278	-0.1305	0.1337
0.1564	-0.0027	0.0031	6.1558	-0.1079	0.1205
0.1621	-0.0022	0.0026	6.3838	-0.0851	0.1038
0.1679	-0.0016	0.0020	6.6118	-0.0615	0.0802
0.1737	-0.0010	0.0013	6.8398	-0.0386	0.0505
0.1790	-0.0005	0.0005	7.0678	-0.0184	0.0202
0.1795	-0.0004	0.0004	7.0678	-0.0165	0.0174
RADIUS (METERS) = 0.3627			RADIUS (INCHES) = 14.2800		
CHORD (METERS) = 0.1795			CHORD (INCHES) = 7.0678		
ZCSL (METERS) = 0.1030			ZCSL (INCHES) = 4.0544		
YCSL (METERS) = -0.0027			YCSL (INCHES) = -0.1080		
RLE (METERS) = 0.000414			RLE (INCHES) = 0.0163		
RTE (METERS) = 0.000485			RTE (INCHES) = 0.0191		
X-AREA (SQ. METERS) = 0.001119			X-AREA (SQ. IN.) = 1.7344		
GAMMA-CHORD (DEG.) = 67.03			GAMMA-CHORD (RAD.) = 1.1700		

Rotor, Section 12

METERS			INCHES		
ZC	YP	YS	ZC	YP	YS
0.0	-0.0008	-0.0001	0.0	-0.0324	-0.0036
0.0004	-0.0008	-0.0001	0.0148	-0.0324	-0.0028
0.0059	-0.0008	0.0002	0.2339	-0.0327	0.0090
0.0119	-0.0010	0.0004	0.4679	-0.0384	0.0166
0.0178	-0.0012	0.0005	0.7018	-0.0473	0.0213
0.0238	-0.0015	0.0006	0.9357	-0.0571	0.0229
0.0297	-0.0017	0.0006	1.1697	-0.0675	0.0224
0.0357	-0.0020	0.0005	1.4036	-0.0787	0.0214
0.0416	-0.0023	0.0005	1.6375	-0.0920	0.0216
0.0475	-0.0027	0.0006	1.8715	-0.1076	0.0248
0.0535	-0.0032	0.0008	2.1054	-0.1258	0.0327
0.0594	-0.0037	0.0012	2.3393	-0.1467	0.0472
0.0654	-0.0043	0.0016	2.5733	-0.1690	0.0644
0.0713	-0.0049	0.0021	2.8072	-0.1916	0.0835
0.0772	-0.0054	0.0026	3.0411	-0.2144	0.1005
0.0832	-0.0060	0.0029	3.2751	-0.2373	0.1158
0.0891	-0.0066	0.0033	3.5090	-0.2599	0.1283
0.0951	-0.0071	0.0035	3.7429	-0.2794	0.1379
0.1010	-0.0074	0.0037	3.9769	-0.2916	0.1458
0.1070	-0.0072	0.0039	4.2108	-0.2843	0.1523
0.1129	-0.0068	0.0040	4.4447	-0.2687	0.1568
0.1188	-0.0063	0.0041	4.6787	-0.2475	0.1597
0.1248	-0.0057	0.0041	4.9126	-0.2244	0.1611
0.1307	-0.0051	0.0041	5.1465	-0.2008	0.1610
0.1367	-0.0045	0.0040	5.3805	-0.1766	0.1593
0.1426	-0.0039	0.0040	5.6144	-0.1533	0.1559
0.1485	-0.0033	0.0038	5.8483	-0.1305	0.1495
0.1545	-0.0028	0.0035	6.0823	-0.1092	0.1389
0.1604	-0.0022	0.0031	6.3162	-0.0883	0.1234
0.1664	-0.0017	0.0026	6.5501	-0.0679	0.1032
0.1723	-0.0012	0.0020	6.7841	-0.0484	0.0786
0.1783	-0.0008	0.0013	7.0180	-0.0302	0.0502
0.1838	-0.0004	0.0005	7.2346	-0.0160	0.0191
0.1842	-0.0004	0.0004	7.2519	-0.0148	0.0166
RADIUS (METERS) = 0.3780			RADIUS (INCHES) = 14.8800		
CHORD (METERS) = 0.1842			CHORD (INCHES) = 7.2519		
ZCSL (METERS) = 0.1065			ZCSL (INCHES) = 4.1932		
YCSL (METERS) = -0.0027			YCSL (INCHES) = -0.1061		
RLE (METERS) = 0.000376			RLE (INCHES) = 0.0148		
RTE (METERS) = 0.000442			RTE (INCHES) = 0.0174		
X-AREA (SQ. METERS) = 0.001098			X-AREA (SQ. IN.) = 1.7018		
GAMMA-CHORD (DEG.) = 67.52			GAMMA-CHORD (RAD.) = 1.1784		

Rotor, Section 13

METERS			INCHES		
ZC	YP	YS	ZC	YP	YS
0.0	-0.0009	-0.0002	0.0	-0.0340	-0.0061
0.0004	-0.0009	-0.0001	0.0143	-0.0336	-0.0050
0.0062	-0.0007	0.0003	0.2423	-0.0267	0.0131
0.0123	-0.0006	0.0007	0.4847	-0.0249	0.0277
0.0185	-0.0007	0.0010	0.7270	-0.0268	0.0388
0.0246	-0.0008	0.0011	0.9693	-0.0307	0.0450
0.0308	-0.0009	0.0012	1.2117	-0.0364	0.0467
0.0369	-0.0012	0.0011	1.4540	-0.0456	0.0452
0.0431	-0.0015	0.0011	1.6964	-0.0587	0.0415
0.0492	-0.0019	0.0009	1.9387	-0.0756	0.0371
0.0554	-0.0024	0.0009	2.1810	-0.0958	0.0344
0.0616	-0.0030	0.0011	2.4234	-0.1179	0.0438
0.0677	-0.0036	0.0015	2.6657	-0.1411	0.0582
0.0739	-0.0042	0.0020	2.9080	-0.1650	0.0768
0.0800	-0.0048	0.0023	3.1504	-0.1893	0.0916
0.0862	-0.0054	0.0026	3.3927	-0.2139	0.1042
0.0923	-0.0061	0.0029	3.6350	-0.2386	0.1137
0.0985	-0.0067	0.0031	3.8774	-0.2621	0.1209
0.1046	-0.0071	0.0032	4.1197	-0.2812	0.1266
0.1108	-0.0073	0.0033	4.3620	-0.2881	0.1308
0.1170	-0.0072	0.0034	4.6044	-0.2829	0.1334
0.1231	-0.0068	0.0034	4.8467	-0.2668	0.1346
0.1293	-0.0063	0.0034	5.0890	-0.2470	0.1348
0.1354	-0.0057	0.0034	5.3314	-0.2261	0.1337
0.1416	-0.0052	0.0033	5.5737	-0.2037	0.1314
0.1477	-0.0046	0.0032	5.8160	-0.1810	0.1271
0.1539	-0.0040	0.0031	6.0584	-0.1580	0.1214
0.1600	-0.0034	0.0029	6.3007	-0.1345	0.1132
0.1662	-0.0028	0.0026	6.5430	-0.1107	0.1013
0.1723	-0.0022	0.0021	6.7854	-0.0863	0.0846
0.1785	-0.0016	0.0016	7.0277	-0.0615	0.0635
0.1847	-0.0009	0.0011	7.2701	-0.0365	0.0414
0.1904	-0.0004	0.0004	7.4964	-0.0152	0.0170
0.1908	-0.0003	0.0004	7.5124	-0.0136	0.0153
RADIUS (METERS) = 0.3983			RADIUS (INCHES) = 15.6800		
CHORD (METERS) = 0.1908			CHORD (INCHES) = 7.5124		
ZCSL (METERS) = 0.1109			ZCSL (INCHES) = 4.3662		
YCSL (METERS) = -0.0030			YCSL (INCHES) = -0.1195		
RLE (METERS) = 0.000363			RLE (INCHES) = 0.0143		
RTE (METERS) = 0.000406			RTE (INCHES) = 0.0160		
X-AREA (SQ. METERS) = 0.001074			X-AREA (SQ. IN.) = 1.6645		
GAMMA-CHORD (DEG.) = 69.09			GAMMA-CHORD (RAD.) = 1.2059		

Rotor, Section 14

METERS			INCHES		
ZC	YP	YS	ZC	YP	YS
0.0	-0.0008	-0.0002	0.0	-0.0329	-0.0073
0.0003	-0.0008	-0.0002	0.0131	-0.0327	-0.0064
0.0063	-0.0007	0.0002	0.2477	-0.0291	0.0083
0.0126	-0.0008	0.0005	0.4953	-0.0298	0.0198
0.0189	-0.0008	0.0007	0.7430	-0.0331	0.0270
0.0252	-0.0010	0.0008	0.9906	-0.0378	0.0307
0.0315	-0.0011	0.0008	1.2383	-0.0434	0.0320
0.0377	-0.0013	0.0008	1.4859	-0.0520	0.0306
0.0440	-0.0016	0.0007	1.7336	-0.0637	0.0283
0.0503	-0.0020	0.0007	1.9812	-0.0783	0.0287
0.0566	-0.0024	0.0008	2.2289	-0.0961	0.0323
0.0629	-0.0030	0.0010	2.4765	-0.1168	0.0394
0.0692	-0.0036	0.0014	2.7242	-0.1399	0.0555
0.0755	-0.0042	0.0018	2.9718	-0.1639	0.0725
0.0818	-0.0048	0.0023	3.2195	-0.1882	0.0900
0.0881	-0.0054	0.0027	3.4671	-0.2126	0.1051
0.0944	-0.0060	0.0030	3.7148	-0.2366	0.1186
0.1006	-0.0065	0.0032	3.9625	-0.2572	0.1280
0.1069	-0.0069	0.0034	4.2101	-0.2712	0.1353
0.1132	-0.0068	0.0036	4.4578	-0.2668	0.1407
0.1195	-0.0064	0.0037	4.7054	-0.2525	0.1443
0.1258	-0.0059	0.0037	4.9531	-0.2340	0.1466
0.1321	-0.0055	0.0038	5.2007	-0.2149	0.1478
0.1384	-0.0049	0.0038	5.4484	-0.1946	0.1478
0.1447	-0.0044	0.0037	5.6960	-0.1742	0.1455
0.1510	-0.0039	0.0036	5.9437	-0.1539	0.1414
0.1573	-0.0034	0.0034	6.1913	-0.1336	0.1354
0.1636	-0.0029	0.0032	6.4390	-0.1133	0.1269
0.1698	-0.0024	0.0029	6.6866	-0.0932	0.1144
0.1761	-0.0019	0.0024	6.9343	-0.0730	0.0943
0.1824	-0.0013	0.0018	7.1819	-0.0529	0.0726
0.1887	-0.0008	0.0013	7.4296	-0.0317	0.0512
0.1947	-0.0003	0.0004	7.6639	-0.0113	0.0159
0.1950	-0.0003	0.0004	7.6772	-0.0101	0.0139
RADIUS (METERS) = 0.4117			RADIUS (INCHES) = 16.2100		
CHORD (METERS) = 0.1950			CHORD (INCHES) = 7.6772		
ZCSL (METERS) = 0.1135			ZCSL (INCHES) = 4.4673		
YCSL (METERS) = -0.0029			YCSL (INCHES) = -0.1130		
RLE (METERS) = 0.000333			RLE (INCHES) = 0.0131		
RTE (METERS) = 0.000343			RTE (INCHES) = 0.0135		
X-AREA (SQ. METERS) = 0.001065			X-AREA (SQ. IN.) = 1.6504		
GAMMA-CHORD (DEG.) = 70.63			GAMMA-CHORD (RAD.) = 1.2327		

Rotor, Section 15

METERS			INCHES		
ZC	YP	YS	ZC	YP	YS
0.0	-0.0008	-0.0002	0.0	-0.0328	-0.0073
0.0003	-0.0008	-0.0002	0.0131	-0.0326	-0.0064
0.0064	-0.0007	0.0002	0.2526	-0.0288	0.0085
0.0128	-0.0007	0.0005	0.5051	-0.0288	0.0191
0.0192	-0.0008	0.0007	0.7577	-0.0322	0.0270
0.0257	-0.0009	0.0008	1.0103	-0.0362	0.0328
0.0321	-0.0011	0.0009	1.2628	-0.0415	0.0349
0.0385	-0.0012	0.0009	1.5154	-0.0492	0.0337
0.0449	-0.0015	0.0008	1.7680	-0.0597	0.0311
0.0513	-0.0019	0.0007	2.0205	-0.0737	0.0291
0.0577	-0.0023	0.0009	2.2731	-0.0903	0.0341
0.0642	-0.0028	0.0011	2.5256	-0.1097	0.0425
0.0706	-0.0034	0.0014	2.7782	-0.1320	0.0551
0.0770	-0.0040	0.0018	3.0308	-0.1560	0.0713
0.0834	-0.0046	0.0023	3.2833	-0.1801	0.0886
0.0898	-0.0052	0.0026	3.5359	-0.2043	0.1041
0.0962	-0.0058	0.0030	3.7885	-0.2280	0.1187
0.1026	-0.0063	0.0033	4.0410	-0.2476	0.1309
0.1091	-0.0068	0.0036	4.2936	-0.2678	0.1401
0.1155	-0.0066	0.0037	4.5462	-0.2589	0.1471
0.1219	-0.0061	0.0038	4.7987	-0.2386	0.1500
0.1283	-0.0056	0.0038	5.0513	-0.2197	0.1514
0.1347	-0.0051	0.0038	5.3038	-0.2011	0.1514
0.1411	-0.0046	0.0038	5.5564	-0.1810	0.1499
0.1475	-0.0041	0.0037	5.8090	-0.1611	0.1465
0.1540	-0.0036	0.0036	6.0615	-0.1416	0.1416
0.1604	-0.0031	0.0034	6.3141	-0.1224	0.1347
0.1668	-0.0026	0.0032	6.5667	-0.1036	0.1248
0.1732	-0.0022	0.0028	6.8192	-0.0852	0.1119
0.1796	-0.0017	0.0023	7.0718	-0.0672	0.0925
0.1860	-0.0013	0.0018	7.3244	-0.0497	0.0717
0.1925	-0.0008	0.0013	7.5769	-0.0323	0.0530
0.1984	-0.0004	0.0007	7.8100	-0.0143	0.0267
0.1989	-0.0003	0.0006	7.8295	-0.0128	0.0246
RADIUS (METERS) = 0.4262			RADIUS (INCHES) = 16.7800		
CHORD (METERS) = 0.1989			CHORD (INCHES) = 7.8295		
ZCSL (METERS) = 0.1156			ZCSL (INCHES) = 4.5531		
YCSL (METERS) = -0.0029			YCSL (INCHES) = -0.1147		
RLE (METERS) = 0.000333			RLE (INCHES) = 0.0131		
RTE (METERS) = 0.000518			RTE (INCHES) = 0.0204		
X-AREA (SQ. METERS) = 0.001059			X-AREA (SQ. IN.) = 1.6414		
GAMMA-CHORD (DEG.) = 72.05			GAMMA-CHORD (RAD.) = 1.2576		

Stator, Section 1

METERS			INCHES		
ZC	YP	YS	ZC	YP	YS
0.0	-0.0002	0.0002	0.0	-0.0064	0.0071
0.0002	-0.0001	0.0003	0.0060	-0.0042	0.0105
0.0024	0.0007	0.0015	0.0926	0.0277	0.0596
0.0047	0.0016	0.0028	0.1853	0.0621	0.1116
0.0071	0.0024	0.0041	0.2780	0.0956	0.1611
0.0094	0.0033	0.0053	0.3706	0.1290	0.2096
0.0118	0.0041	0.0065	0.4633	0.1616	0.2541
0.0141	0.0049	0.0076	0.5559	0.1941	0.2979
0.0165	0.0057	0.0086	0.6486	0.2262	0.3393
0.0188	0.0066	0.0096	0.7412	0.2579	0.3795
0.0212	0.0074	0.0106	0.8339	0.2897	0.4169
0.0235	0.0081	0.0115	0.9265	0.3181	0.4524
0.0259	0.0088	0.0122	1.0192	0.3449	0.4806
0.0282	0.0093	0.0128	1.1118	0.3671	0.5057
0.0306	0.0098	0.0133	1.2045	0.3862	0.5254
0.0329	0.0102	0.0137	1.2972	0.4019	0.5408
0.0353	0.0105	0.0141	1.3898	0.4118	0.5533
0.0377	0.0107	0.0142	1.4825	0.4194	0.5584
0.0400	0.0107	0.0142	1.5751	0.4231	0.5609
0.0424	0.0107	0.0142	1.6678	0.4230	0.5591
0.0447	0.0107	0.0140	1.7604	0.4201	0.5520
0.0471	0.0104	0.0137	1.8531	0.4112	0.5405
0.0494	0.0101	0.0133	1.9457	0.3992	0.5245
0.0518	0.0097	0.0128	2.0384	0.3838	0.5036
0.0541	0.0092	0.0121	2.1311	0.3636	0.4771
0.0565	0.0086	0.0113	2.2237	0.3368	0.4459
0.0588	0.0078	0.0104	2.3164	0.3067	0.4077
0.0612	0.0069	0.0092	2.4090	0.2717	0.3631
0.0635	0.0059	0.0079	2.5017	0.2309	0.3118
0.0659	0.0046	0.0064	2.5943	0.1823	0.2516
0.0682	0.0032	0.0046	2.6870	0.1265	0.1829
0.0706	0.0016	0.0026	2.7796	0.0631	0.1028
0.0728	-0.0001	0.0004	2.8672	-0.0041	0.0144
0.0730	-0.0002	0.0002	2.8723	-0.0080	0.0093
RADIUS (METERS) = 0.2667			RADIUS (INCHES) = 10.5000		
CHORD (METERS) = 0.0730			CHORD (INCHES) = 2.8723		
ZCSL (METERS) = 0.0365			ZCSL (INCHES) = 1.4376		
YCSL (METERS) = 0.0095			YCSL (INCHES) = 0.3726		
RLE (METERS) = 0.000168			RLE (INCHES) = 0.0066		
RTE (METERS) = 0.000175			RTE (INCHES) = 0.0069		
X-AREA (SQ. METERS) = 0.000193			X-AREA (SQ. IN.) = 0.2986		
GAMMA-CHORD (DEG.) = 23.98			GAMMA-CHORD (RAD.) = 0.4184		

Stator, Section 2

METERS			INCHES		
ZC	YP	YS	ZC	YP	YS
0.0	-0.0002	0.0002	0.0	-0.0044	0.0071
0.0002	-0.0001	0.0003	0.0061	-0.0043	0.0104
0.0023	0.0007	0.0015	0.0921	0.0259	0.0577
0.0047	0.0015	0.0027	0.1843	0.0582	0.1077
0.0070	0.0023	0.0039	0.2764	0.0897	0.1551
0.0094	0.0031	0.0051	0.3686	0.1209	0.2012
0.0117	0.0038	0.0062	0.4607	0.1513	0.2437
0.0140	0.0046	0.0072	0.5529	0.1812	0.2853
0.0164	0.0054	0.0082	0.6450	0.2108	0.3243
0.0187	0.0061	0.0092	0.7371	0.2398	0.3620
0.0211	0.0068	0.0101	0.8293	0.2688	0.3971
0.0234	0.0075	0.0109	0.9214	0.2950	0.4300
0.0257	0.0081	0.0116	1.0136	0.3196	0.4572
0.0281	0.0086	0.0122	1.1057	0.3402	0.4806
0.0304	0.0091	0.0127	1.1978	0.3575	0.4993
0.0328	0.0094	0.0130	1.2900	0.3719	0.5136
0.0351	0.0097	0.0133	1.3821	0.3810	0.5249
0.0374	0.0098	0.0135	1.4743	0.3878	0.5300
0.0398	0.0099	0.0135	1.5664	0.3909	0.5317
0.0421	0.0099	0.0134	1.6586	0.3903	0.5294
0.0445	0.0098	0.0133	1.7507	0.3869	0.5223
0.0468	0.0096	0.0130	1.8428	0.3787	0.5109
0.0491	0.0093	0.0126	1.9350	0.3670	0.4952
0.0515	0.0089	0.0121	2.0271	0.3520	0.4747
0.0538	0.0085	0.0114	2.1193	0.3328	0.4490
0.0562	0.0078	0.0106	2.2114	0.3080	0.4187
0.0585	0.0071	0.0097	2.3035	0.2797	0.3821
0.0609	0.0063	0.0086	2.3957	0.2471	0.3395
0.0632	0.0053	0.0074	2.4878	0.2089	0.2905
0.0655	0.0042	0.0059	2.5800	0.1644	0.2339
0.0679	0.0029	0.0043	2.6721	0.1137	0.1694
0.0702	0.0014	0.0024	2.7642	0.0565	0.0950
0.0724	-0.0001	0.0003	2.8512	-0.0039	0.0137
0.0726	-0.0002	0.0002	2.8564	-0.0076	0.0088
RADIUS (METERS) = 0.2760			RADIUS (INCHES) = 10.8660		
CHORD (METERS) = 0.0726			CHORD (INCHES) = 2.8564		
ZCSL (METERS) = 0.0363			ZCSL (INCHES) = 1.4307		
YCSL (METERS) = 0.0089			YCSL (INCHES) = 0.3501		
RLE (METERS) = 0.000170			RLE (INCHES) = 0.0067		
RTE (METERS) = 0.000173			RTE (INCHES) = 0.0068		
X-AREA (SQ. METERS) = 0.000194			X-AREA (SQ. IN.) = 0.3005		
GAMMA-CHORD (DEG.) = 23.90			GAMMA-CHORD (RAD.) = 0.4171		

Stator, Section 3

METERS			INCHES		
ZC	YP	YS	ZC	YP	YS
0.0	-0.0002	0.0002	0.0	-0.0064	0.0072
0.0002	-0.0001	0.0003	0.0061	-0.0043	0.0105
0.0023	0.0006	0.0014	0.0917	0.0248	0.0566
0.0047	0.0014	0.0027	0.1833	0.0559	0.1054
0.0070	0.0022	0.0038	0.2750	0.0860	0.1513
0.0093	0.0029	0.0050	0.3666	0.1154	0.1955
0.0116	0.0037	0.0060	0.4583	0.1438	0.2361
0.0140	0.0044	0.0070	0.5499	0.1713	0.2757
0.0163	0.0050	0.0079	0.6416	0.1984	0.3122
0.0186	0.0057	0.0088	0.7333	0.2248	0.3475
0.0210	0.0064	0.0097	0.8249	0.2510	0.3804
0.0233	0.0070	0.0104	0.9166	0.2752	0.4109
0.0256	0.0076	0.0111	1.0082	0.2977	0.4372
0.0279	0.0080	0.0117	1.0999	0.3169	0.4589
0.0303	0.0084	0.0121	1.1915	0.3325	0.4767
0.0326	0.0088	0.0124	1.2832	0.3456	0.4901
0.0349	0.0090	0.0127	1.3748	0.3540	0.5002
0.0372	0.0091	0.0128	1.4665	0.3599	0.5052
0.0396	0.0092	0.0129	1.5582	0.3625	0.5062
0.0419	0.0092	0.0128	1.6498	0.3616	0.5035
0.0442	0.0091	0.0126	1.7415	0.3578	0.4964
0.0466	0.0089	0.0123	1.8331	0.3502	0.4850
0.0489	0.0086	0.0119	1.9248	0.3386	0.4696
0.0512	0.0082	0.0114	2.0164	0.3241	0.4495
0.0535	0.0078	0.0108	2.1081	0.3058	0.4245
0.0559	0.0072	0.0100	2.1997	0.2828	0.3950
0.0582	0.0065	0.0091	2.2914	0.2561	0.3600
0.0605	0.0057	0.0081	2.3830	0.2254	0.3192
0.0629	0.0048	0.0069	2.4747	0.1898	0.2723
0.0652	0.0038	0.0056	2.5664	0.1490	0.2187
0.0675	0.0026	0.0040	2.6580	0.1026	0.1577
0.0698	0.0013	0.0022	2.7497	0.0506	0.0882
0.0720	-0.0001	0.0003	2.8359	-0.0039	0.0132
0.0722	-0.0002	0.0002	2.8413	-0.0073	0.0085
RADIUS (METERS) = 0.2847			RADIUS (INCHES) = 11.2070		
CHORD (METERS) = 0.0722			CHORD (INCHES) = 2.8413		
ZCSL (METERS) = 0.0362			ZCSL (INCHES) = 1.4246		
YCSL (METERS) = 0.0084			YCSL (INCHES) = 0.3307		
RLE (METERS) = 0.000172			RLE (INCHES) = 0.0068		
RTE (METERS) = 0.000173			RTE (INCHES) = 0.0068		
X-AREA (SQ. METERS) = 0.000195			X-AREA (SQ. IN.) = 0.3022		
GAMMA-CHORD (DEG.) = 23.85			GAMMA-CHORD (RAD.) = 0.4162		

Stator, Section 4

METERS			INCHES		
ZC	YP	YS	ZC	YP	YS
0.0	-0.0002	0.0002	0.0	-0.0065	0.0073
0.0002	-0.0001	0.0003	0.0063	-0.0044	0.0106
0.0023	0.0006	0.0014	0.0912	0.0240	0.0558
0.0046	0.0014	0.0026	0.1824	0.0542	0.1034
0.0069	0.0021	0.0038	0.2736	0.0832	0.1481
0.0093	0.0028	0.0049	0.3648	0.1115	0.1911
0.0116	0.0035	0.0059	0.4560	0.1387	0.2306
0.0139	0.0042	0.0068	0.5472	0.1649	0.2690
0.0162	0.0048	0.0077	0.6384	0.1904	0.3041
0.0185	0.0055	0.0086	0.7296	0.2150	0.3376
0.0208	0.0061	0.0094	0.8207	0.2390	0.3689
0.0232	0.0066	0.0101	0.9119	0.2614	0.3976
0.0255	0.0072	0.0107	1.0031	0.2820	0.4230
0.0278	0.0076	0.0113	1.0943	0.2999	0.4436
0.0301	0.0080	0.0117	1.1855	0.3141	0.4605
0.0324	0.0083	0.0120	1.2767	0.3258	0.4730
0.0347	0.0085	0.0122	1.3679	0.3334	0.4820
0.0371	0.0086	0.0124	1.4591	0.3383	0.4867
0.0394	0.0086	0.0124	1.5503	0.3401	0.4867
0.0417	0.0086	0.0123	1.6415	0.3384	0.4834
0.0440	0.0085	0.0121	1.7327	0.3340	0.4759
0.0463	0.0083	0.0118	1.8239	0.3264	0.4642
0.0486	0.0080	0.0114	1.9151	0.3147	0.4487
0.0510	0.0076	0.0109	2.0063	0.3003	0.4287
0.0533	0.0072	0.0103	2.0975	0.2826	0.4040
0.0556	0.0066	0.0095	2.1886	0.2610	0.3751
0.0579	0.0060	0.0087	2.2798	0.2357	0.3415
0.0602	0.0052	0.0077	2.3710	0.2067	0.3023
0.0625	0.0044	0.0065	2.4622	0.1734	0.2571
0.0649	0.0034	0.0052	2.5534	0.1356	0.2059
0.0672	0.0024	0.0038	2.6446	0.0929	0.1479
0.0695	0.0012	0.0021	2.7358	0.0453	0.0821
0.0717	-0.0001	0.0003	2.8214	-0.0039	0.0129
0.0718	-0.0002	0.0002	2.8270	-0.0071	0.0083
RADIUS (METERS) = 0.2933			RADIUS (INCHES) = 11.5480		
CHORD (METERS) = 0.0718			CHORD (INCHES) = 2.8270		
ZCSL (METERS) = 0.0361			ZCSL (INCHES) = 1.4207		
YCSL (METERS) = 0.0080			YCSL (INCHES) = 0.3158		
RLE (METERS) = 0.000174			RLE (INCHES) = 0.0069		
RTE (METERS) = 0.000175			RTE (INCHES) = 0.0069		
X-AREA (SQ. METERS) = 0.000196			X-AREA (SQ. IN.) = 0.3041		
GAMMA-CHORD (DEG.) = 23.97			GAMMA-CHORD (RAD.) = 0.4183		

Stator, Section 5

METERS			INCHES		
ZC	YP	YS	ZC	YP	YS
0.0	-0.0002	0.0002	0.0	-0.0069	0.0077
0.0002	-0.0001	0.0003	0.0067	-0.0047	0.0112
0.0023	0.0006	0.0014	0.0896	0.0225	0.0549
0.0046	0.0013	0.0026	0.1792	0.0516	0.1011
0.0068	0.0020	0.0037	0.2688	0.0791	0.1444
0.0091	0.0027	0.0047	0.3584	0.1058	0.1860
0.0114	0.0033	0.0057	0.4480	0.1313	0.2238
0.0137	0.0040	0.0066	0.5376	0.1556	0.2604
0.0159	0.0045	0.0075	0.6272	0.1789	0.2938
0.0182	0.0051	0.0083	0.7168	0.2011	0.3255
0.0205	0.0057	0.0090	0.8064	0.2225	0.3549
0.0228	0.0062	0.0097	0.8960	0.2424	0.3822
0.0250	0.0066	0.0103	0.9856	0.2611	0.4070
0.0273	0.0071	0.0109	1.0752	0.2782	0.4275
0.0296	0.0074	0.0113	1.1648	0.2915	0.4449
0.0319	0.0077	0.0116	1.2544	0.3024	0.4572
0.0341	0.0079	0.0118	1.3440	0.3097	0.4663
0.0364	0.0080	0.0120	1.4336	0.3142	0.4705
0.0387	0.0080	0.0120	1.5232	0.3159	0.4709
0.0410	0.0080	0.0119	1.6128	0.3136	0.4678
0.0432	0.0078	0.0117	1.7024	0.3088	0.4603
0.0455	0.0076	0.0114	1.7920	0.3009	0.4483
0.0478	0.0074	0.0110	1.8816	0.2897	0.4330
0.0501	0.0070	0.0105	1.9712	0.2754	0.4131
0.0523	0.0066	0.0099	2.0608	0.2581	0.3883
0.0546	0.0060	0.0091	2.1504	0.2374	0.3595
0.0569	0.0054	0.0083	2.2400	0.2131	0.3261
0.0592	0.0047	0.0073	2.3295	0.1858	0.2877
0.0614	0.0039	0.0062	2.4192	0.1551	0.2438
0.0637	0.0030	0.0049	2.5087	0.1199	0.1944
0.0660	0.0021	0.0035	2.5983	0.0811	0.1392
0.0683	0.0010	0.0020	2.6880	0.0386	0.0774
0.0704	-0.0001	0.0003	2.7715	-0.0041	0.0131
0.0705	-0.0002	0.0002	2.7775	-0.0072	0.0085
RADIUS (METERS) = 0.3175			RADIUS (INCHES) = 12.5000		
CHORD (METERS) = 0.0705			CHORD (INCHES) = 2.7775		
ZCSL (METERS) = 0.0358			ZCSL (INCHES) = 1.4095		
YCSL (METERS) = 0.0076			YCSL (INCHES) = 0.3003		
RLE (METERS) = 0.000185			RLE (INCHES) = 0.0073		
RTE (METERS) = 0.000184			RTE (INCHES) = 0.0072		
X-AREA (SQ. METERS) = 0.000202			X-AREA (SQ. IN.) = 0.3129		
GAMMA-CHORD (DEG.) = 24.35			GAMMA-CHORD (RAD.) = 0.4250		

Stator, Section 6

METERS			INCHES		
ZC	YP	YS	ZC	YP	YS
0.0	-0.0002	0.0002	0.0	-0.0072	0.0080
0.0002	-0.0001	0.0003	0.0070	-0.0049	0.0117
0.0022	0.0005	0.0014	0.0875	0.0212	0.0543
0.0044	0.0013	0.0025	0.1749	0.0494	0.0999
0.0067	0.0019	0.0036	0.2624	0.0758	0.1419
0.0089	0.0026	0.0046	0.3498	0.1013	0.1829
0.0111	0.0032	0.0056	0.4372	0.1257	0.2195
0.0133	0.0038	0.0065	0.5247	0.1488	0.2549
0.0155	0.0043	0.0073	0.6121	0.1708	0.2877
0.0178	0.0049	0.0081	0.6996	0.1917	0.3186
0.0200	0.0054	0.0088	0.7870	0.2118	0.3471
0.0222	0.0058	0.0095	0.8745	0.2302	0.3738
0.0244	0.0063	0.0101	0.9619	0.2478	0.3980
0.0267	0.0067	0.0107	1.0494	0.2643	0.4195
0.0289	0.0071	0.0111	1.1368	0.2782	0.4388
0.0311	0.0074	0.0115	1.2243	0.2898	0.4523
0.0333	0.0076	0.0118	1.3117	0.2983	0.4627
0.0355	0.0077	0.0119	1.3992	0.3036	0.4687
0.0378	0.0078	0.0120	1.4866	0.3062	0.4705
0.0400	0.0077	0.0119	1.5741	0.3047	0.4690
0.0422	0.0076	0.0117	1.6615	0.3008	0.4621
0.0444	0.0075	0.0115	1.7490	0.2938	0.4514
0.0466	0.0072	0.0111	1.8364	0.2834	0.4367
0.0489	0.0069	0.0106	1.9239	0.2700	0.4176
0.0511	0.0064	0.0100	2.0113	0.2536	0.3938
0.0533	0.0059	0.0093	2.0988	0.2333	0.3657
0.0555	0.0053	0.0085	2.1862	0.2098	0.3330
0.0578	0.0046	0.0075	2.2737	0.1831	0.2945
0.0600	0.0039	0.0064	2.3611	0.1526	0.2502
0.0622	0.0030	0.0051	2.4486	0.1185	0.2002
0.0644	0.0020	0.0037	2.5360	0.0802	0.1439
0.0666	0.0010	0.0020	2.6235	0.0381	0.0804
0.0687	-0.0001	0.0004	2.7047	-0.0042	0.0142
0.0689	-0.0002	0.0002	2.7109	-0.0074	0.0091
RADIUS (METERS) = 0.3429			RADIUS (INCHES) = 13.5000		
CHORD (METERS) = 0.0689			CHORD (INCHES) = 2.7109		
ZCSL (METERS) = 0.0353			ZCSL (INCHES) = 1.3905		
YCSL (METERS) = 0.0075			YCSL (INCHES) = 0.2964		
RLE (METERS) = 0.000194			RLE (INCHES) = 0.0076		
RTE (METERS) = 0.000193			RTE (INCHES) = 0.0076		
X-AREA (SQ. METERS) = 0.000207			X-AREA (SQ. IN.) = 0.3211		
GAMMA-CHORD (DEG.) = 24.27			GAMMA-CHORD (RAD.) = 0.4237		

Stator, Section 7

METERS			INCHES		
ZC	YP	YS	ZC	YP	YS
0.0	-0.0002	0.0002	0.0	-0.0075	0.0086
0.0002	-0.0001	0.0003	0.0073	-0.0051	0.0125
0.0022	0.0005	0.0014	0.0851	0.0210	0.0551
0.0043	0.0012	0.0026	0.1702	0.0491	0.1014
0.0065	0.0019	0.0036	0.2552	0.0756	0.1434
0.0086	0.0026	0.0047	0.3403	0.1011	0.1844
0.0108	0.0032	0.0056	0.4254	0.1253	0.2214
0.0130	0.0038	0.0065	0.5105	0.1482	0.2570
0.0151	0.0043	0.0074	0.5956	0.1699	0.2899
0.0173	0.0048	0.0081	0.6806	0.1905	0.3207
0.0194	0.0053	0.0089	0.7657	0.2101	0.3492
0.0216	0.0058	0.0095	0.8508	0.2280	0.3757
0.0238	0.0062	0.0102	0.9359	0.2451	0.3998
0.0259	0.0066	0.0107	1.0209	0.2609	0.4218
0.0281	0.0070	0.0112	1.1060	0.2752	0.4423
0.0303	0.0073	0.0116	1.1911	0.2878	0.4575
0.0324	0.0076	0.0119	1.2762	0.2975	0.4699
0.0346	0.0077	0.0121	1.3613	0.3042	0.4782
0.0367	0.0078	0.0122	1.4463	0.3076	0.4815
0.0389	0.0078	0.0122	1.5314	0.3077	0.4810
0.0411	0.0077	0.0121	1.6165	0.3049	0.4760
0.0432	0.0076	0.0119	1.7016	0.2990	0.4667
0.0454	0.0073	0.0115	1.7866	0.2890	0.4536
0.0475	0.0070	0.0110	1.8717	0.2762	0.4350
0.0497	0.0066	0.0105	1.9568	0.2600	0.4116
0.0519	0.0061	0.0097	2.0419	0.2404	0.3837
0.0540	0.0055	0.0089	2.1270	0.2169	0.3504
0.0562	0.0048	0.0079	2.2121	0.1901	0.3115
0.0583	0.0040	0.0068	2.2971	0.1591	0.2663
0.0605	0.0031	0.0054	2.3822	0.1237	0.2144
0.0627	0.0021	0.0039	2.4673	0.0841	0.1551
0.0648	0.0010	0.0022	2.5524	0.0400	0.0869
0.0668	-0.0001	0.0004	2.6311	-0.0043	0.0157
0.0670	-0.0002	0.0003	2.6374	-0.0078	0.0100
RADIUS (METERS) = 0.3683			RADIUS (INCHES) = 14.5000		
CHORD (METERS) = 0.0670			CHORD (INCHES) = 2.6374		
ZCSL (METERS) = 0.0347			ZCSL (INCHES) = 1.3679		
YCSL (METERS) = 0.0077			YCSL (INCHES) = 0.3017		
RLE (METERS) = 0.000204			RLE (INCHES) = 0.0080		
RTE (METERS) = 0.000204			RTE (INCHES) = 0.0080		
X-AREA (SQ. METERS) = 0.000213			X-AREA (SQ. IN.) = 0.3299		
GAMMA-CHORD (DEG.) = 23.20			GAMMA-CHORD (RAD.) = 0.4049		

Stator, Section 8

METERS			INCHES		
ZC	YP	YS	ZC	YP	YS
0.0	-0.0002	0.0002	0.0	-0.0078	0.0089
0.0002	-0.0001	0.0003	0.0074	-0.0051	0.0132
0.0021	0.0006	0.0015	0.0831	0.0222	0.0574
0.0042	0.0013	0.0027	0.1662	0.0518	0.1058
0.0063	0.0020	0.0038	0.2493	0.0798	0.1493
0.0084	0.0027	0.0049	0.3324	0.1067	0.1917
0.0106	0.0034	0.0059	0.4155	0.1323	0.2305
0.0127	0.0040	0.0068	0.4985	0.1565	0.2675
0.0148	0.0046	0.0077	0.5816	0.1794	0.3018
0.0169	0.0051	0.0085	0.6647	0.2011	0.3340
0.0190	0.0056	0.0092	0.7478	0.2217	0.3637
0.0211	0.0061	0.0099	0.8309	0.2406	0.3914
0.0232	0.0066	0.0106	0.9140	0.2586	0.4164
0.0253	0.0070	0.0112	0.9971	0.2751	0.4394
0.0274	0.0074	0.0117	1.0802	0.2903	0.4607
0.0295	0.0077	0.0121	1.1633	0.3041	0.4782
0.0317	0.0080	0.0125	1.2464	0.3157	0.4933
0.0338	0.0082	0.0128	1.3295	0.3246	0.5037
0.0359	0.0084	0.0129	1.4126	0.3300	0.5097
0.0380	0.0084	0.0130	1.4957	0.3320	0.5113
0.0401	0.0084	0.0129	1.5787	0.3311	0.5085
0.0422	0.0083	0.0127	1.6618	0.3262	0.5012
0.0443	0.0081	0.0124	1.7449	0.3178	0.4895
0.0464	0.0078	0.0120	1.8280	0.3063	0.4724
0.0485	0.0074	0.0114	1.9111	0.2907	0.4503
0.0507	0.0069	0.0107	1.9942	0.2701	0.4229
0.0528	0.0062	0.0099	2.0773	0.2457	0.3894
0.0549	0.0055	0.0089	2.1604	0.2168	0.3484
0.0570	0.0047	0.0076	2.2435	0.1831	0.3006
0.0591	0.0037	0.0062	2.3266	0.1441	0.2448
0.0612	0.0025	0.0046	2.4097	0.0993	0.1797
0.0633	0.0012	0.0026	2.4928	0.0484	0.1025
0.0653	-0.0001	0.0005	2.5699	-0.0043	0.0179
0.0654	-0.0002	0.0003	2.5758	-0.0083	0.0113
RADIUS (METERS) = 0.3845			RADIUS (INCHES) = 15.1390		
CHORD (METERS) = 0.0654			CHORD (INCHES) = 2.5758		
ZCSL (METERS) = 0.0343			ZCSL (INCHES) = 1.3493		
YCSL (METERS) = 0.0082			YCSL (INCHES) = 0.3225		
RLE (METERS) = 0.000210			RLE (INCHES) = 0.0083		
RTE (METERS) = 0.000209			RTE (INCHES) = 0.0082		
X-AREA (SQ. METERS) = 0.000216			X-AREA (SQ. IN.) = 0.3354		
GAMMA-CHORD (DEG.) = 22.01			GAMMA-CHORD (RAD.) = 0.3841		

Stator, Section 9

METERS			INCHES		
ZC	YP	YS	ZC	YP	YS
0.0	-0.0002	0.0002	0.0	-0.0081	0.0094
0.0002	-0.0001	0.0004	0.0073	-0.0050	0.0142
0.0021	0.0007	0.0016	0.0811	0.0268	0.0634
0.0041	0.0016	0.0030	0.1622	0.0611	0.1173
0.0062	0.0024	0.0042	0.2433	0.0936	0.1657
0.0082	0.0032	0.0054	0.3243	0.1246	0.2126
0.0103	0.0039	0.0065	0.4054	0.1540	0.2556
0.0124	0.0046	0.0075	0.4865	0.1819	0.2962
0.0144	0.0053	0.0085	0.5676	0.2080	0.3337
0.0165	0.0059	0.0094	0.6487	0.2325	0.3687
0.0185	0.0065	0.0102	0.7298	0.2555	0.4007
0.0206	0.0070	0.0109	0.8109	0.2764	0.4305
0.0227	0.0075	0.0116	0.8919	0.2961	0.4567
0.0247	0.0080	0.0122	0.9730	0.3136	0.4808
0.0268	0.0084	0.0128	1.0541	0.3294	0.5023
0.0288	0.0087	0.0132	1.1352	0.3438	0.5206
0.0309	0.0090	0.0136	1.2163	0.3557	0.5368
0.0330	0.0093	0.0139	1.2974	0.3652	0.5482
0.0350	0.0094	0.0141	1.3784	0.3716	0.5553
0.0371	0.0095	0.0142	1.4595	0.3738	0.5582
0.0391	0.0095	0.0141	1.5406	0.3726	0.5557
0.0412	0.0093	0.0139	1.6217	0.3673	0.5487
0.0433	0.0091	0.0136	1.7028	0.3580	0.5363
0.0453	0.0088	0.0132	1.7839	0.3452	0.5188
0.0474	0.0083	0.0126	1.8650	0.3276	0.4955
0.0494	0.0078	0.0119	1.9460	0.3052	0.4677
0.0515	0.0071	0.0110	2.0271	0.2785	0.4314
0.0535	0.0063	0.0098	2.1082	0.2468	0.3878
0.0556	0.0053	0.0085	2.1893	0.2089	0.3364
0.0577	0.0042	0.0070	2.2704	0.1648	0.2757
0.0597	0.0029	0.0052	2.3515	0.1145	0.2035
0.0618	0.0014	0.0030	2.4325	0.0563	0.1172
0.0637	-0.0001	0.0005	2.5081	-0.0044	0.0206
0.0638	-0.0002	0.0003	2.5136	-0.0089	0.0135
RADIUS (METERS) = 0.3977			RADIUS (INCHES) = 15.6570		
CHORD (METERS) = 0.0638			CHORD (INCHES) = 2.5136		
ZCSL (METERS) = 0.0337			ZCSL (INCHES) = 1.3277		
YCSL (METERS) = 0.0091			YCSL (INCHES) = 0.3573		
RLE (METERS) = 0.000213			RLE (INCHES) = 0.0084		
RTE (METERS) = 0.000219			RTE (INCHES) = 0.0086		
X-AREA (SQ. METERS) = 0.000219			X-AREA (SQ. IN.) = 0.3402		
GAMMA-CHORD (DEG.) = 20.32			GAMMA-CHORD (RAD.) = 0.3546		

Stator, Section 10

METERS			INCHES		
ZC	YP	YS	ZC	YP	YS
0.0	-0.0002	0.0002	0.0	-0.0083	0.0098
0.0002	-0.0001	0.0004	0.0072	-0.0049	0.0151
0.0020	0.0008	0.0017	0.0799	0.0302	0.0682
0.0041	0.0017	0.0032	0.1597	0.0681	0.1266
0.0061	0.0026	0.0045	0.2396	0.1037	0.1784
0.0081	0.0035	0.0058	0.3195	0.1375	0.2286
0.0101	0.0043	0.0070	0.3993	0.1693	0.2741
0.0122	0.0051	0.0081	0.4792	0.1995	0.3170
0.0142	0.0058	0.0091	0.5591	0.2274	0.3564
0.0162	0.0064	0.0100	0.6389	0.2534	0.3929
0.0183	0.0070	0.0108	0.7188	0.2775	0.4259
0.0203	0.0076	0.0116	0.7987	0.2993	0.4565
0.0223	0.0081	0.0123	0.8785	0.3199	0.4829
0.0243	0.0086	0.0129	0.9584	0.3374	0.5069
0.0264	0.0090	0.0134	1.0383	0.3532	0.5279
0.0284	0.0093	0.0139	1.1181	0.3673	0.5460
0.0304	0.0096	0.0143	1.1980	0.3788	0.5622
0.0325	0.0099	0.0146	1.2779	0.3883	0.5738
0.0345	0.0100	0.0148	1.3577	0.3949	0.5814
0.0365	0.0101	0.0149	1.4376	0.3971	0.5849
0.0385	0.0101	0.0148	1.5175	0.3957	0.5823
0.0406	0.0099	0.0146	1.5973	0.3904	0.5753
0.0426	0.0097	0.0143	1.6772	0.3804	0.5629
0.0446	0.0093	0.0138	1.7570	0.3668	0.5450
0.0467	0.0089	0.0132	1.8369	0.3486	0.5212
0.0487	0.0083	0.0125	1.9168	0.3252	0.4927
0.0507	0.0076	0.0116	1.9966	0.2976	0.4553
0.0527	0.0067	0.0104	2.0765	0.2641	0.4103
0.0548	0.0057	0.0091	2.1564	0.2232	0.3570
0.0568	0.0045	0.0075	2.2362	0.1765	0.2939
0.0588	0.0031	0.0055	2.3161	0.1230	0.2183
0.0609	0.0015	0.0032	2.3960	0.0606	0.1273
0.0627	-0.0001	0.0006	2.4704	-0.0048	0.0233
0.0629	-0.0002	0.0004	2.4758	-0.0096	0.0157
RADIUS (METERS) = 0.4064			RADIUS (INCHES) = 16.0000		
CHORD (METERS) = 0.0629			CHORD (INCHES) = 2.4758		
ZCSL (METERS) = 0.0333			ZCSL (INCHES) = 1.3117		
YCSL (METERS) = 0.0096			YCSL (INCHES) = 0.3777		
RLE (METERS) = 0.000216			RLE (INCHES) = 0.0085		
RTE (METERS) = 0.000234			RTE (INCHES) = 0.0092		
X-AREA (SQ. METERS) = 0.000222			X-AREA (SQ. IN.) = 0.3440		
GAMMA-CHORD (DEG.) = 19.05			GAMMA-CHORD (RAD.) = 0.3325		

Page Intentionally Left Blank

APPENDIX I

**EVALUATION OF KERIMID 601 POLYIMIDE
ULTRA-HIGH TIP SPEED FAN BLADES**

Contract NAS3-15335

**Prepared by
J. A. Arnold**

**Pratt & Whitney Aircraft
East Hartford, Connecticut**

INTRODUCTION

This appendix describes the materials and construction of four ultra-high tip speed fan blades and their spin test evaluation. The blades were constructed of HT-S graphite fiber in polyimide Kerimid 601. Twenty blades were fabricated, but sixteen (blades S/N 1 through S/N 15 and S/N 19) were used to develop processes and tooling. This appendix summarizes the results of spin tests, bench frequency tests, and strain-gage measurements made on the four evaluation blades, S/N 16, S/N 17, S/N 18, and S/N 20.

BLADE CONSTRUCTION

The materials and the composite ply orientation and thicknesses of each test blade are defined in Table I-I. The reinforcement was HT-S graphite fiber, and the composite construction was a shell-core design. Blades S/N 16, S/N 17, and S/N 18 had $\pm 40^\circ$ shell plies separated from the 0° core plies by a simple pair of $\pm 20^\circ$ transition plies. Blade S/N 20 was modified to incorporate $\pm 10^\circ$ core plies.

TABLE I-I
BLADE CONSTRUCTION

Blade S/N	Fiber	Resin	Ply Orientation (degrees)				Ply Thickness (mm)		Leading Edge
			Tip	Shell	Trans.	Core	Shell	Core	
16	HT-S	Kerimid 601	± 75	± 40	± 20	0	0.127 (5 mils)	0.254 (10 mils)	Yes
17	HT-S	Kerimid 601	± 75	± 40	± 20	0	0.127	0.254	Yes
18	HT-S	Kerimid 601	± 75	± 40	± 20	0	0.127	0.254	Yes
20	HT-S	Kerimid 601	± 75	± 40	± 20	± 10	0.127	0.254	Yes

BLADE EVALUATION METHODS

All blades were radiographed, ultrasonically inspected, and bench frequency checked upon receipt at P&WA. The blades were then spin tested, and those blades that did not fail catastrophically were frequency tested a second time. A summary of bench frequencies, including predicted frequencies, is shown in Table I-II.

Initial evaluation in the spin pit consisted of acceleration from 60 to 100 percent speed in 10 percent increments – 100 percent speed is at 15,200 rpm. After each incremental change, the blade was ultrasonically inspected.

Blades S/N 16 and S/N 18 were low-cycle-fatigue (LCF) tested after the initial spin evaluation. These two blades were also strain gaged.

TABLE I-II
FREQUENCY TESTING SUMMARY

Mode	Prediction	Frequency (Hz)							
		Blade S/N 16		Blade S/N 17		Blade S/N 18		Blade S/N 19	
		Before Spin	After Spin	Before Spin	After Spin	Before Spin	After Spin	Before Spin	After Spin
1st Bending	250	249	224	251	— — —	256	256	249	— — —
1st Torsion	760	249	707	813	— — —	864	851	814	— — —
2nd Bending	840	932	856	908	— — —	960	906	932	— — —
Tip	850	1165	991	1268	— — —	1388	1410	1311	— — —

TEST RESULTS

Blade S/N 18 was the only blade to survive the entire testing procedure although significant delamination and change in natural frequency were observed.

The results of the blade natural-frequency tests are shown in Table I-II. Blades S/N 16 and S/N 18 were frequency tested before and after the initial spin. First bending frequency changes of -25% and 0% were noted for blades S/N 16 and S/N 18, respectively. First torsion frequency changed -13% and 1.5% . Second bending frequency changed -8% and -5.8% . The degree of delamination was more significant in blade S/N 16 than in S/N 18 since the initial spin-up of blade S/N 16 was to 110 percent speed while blade S/N 18 was spun only to 90 percent speed. The higher degree of delamination in blade S/N 16 qualitatively explains the blades larger frequency drop.

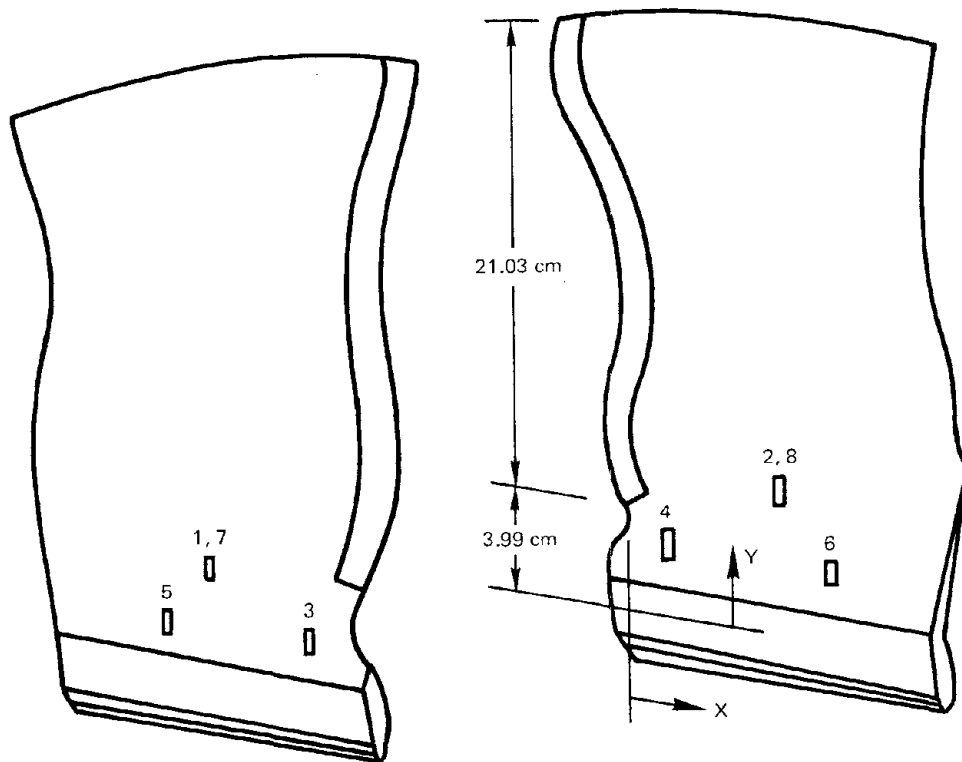
Strain-gage measurements were taken on blades S/N 16 and S/N 18. Table I-III shows the location of the gages and summarizes the strain measurements at 10,600 rpm. All gages were linear at least to 10,660 rpm. Some gages exhibited nonlinear behavior at higher speeds, indicating that some internal change had occurred in the blade. The strains measured by back-to-back gages indicated significant bending in the blades. Some of this can be attributed to the axial and tangential tilt of the blade which would normally be reduced by gas bending loads not present in the spin pit. The highest measured strain occurred at location 3, the area of the leading edge hook analytically predicted to be the highest stress region.

The spin test history of each blade is summarized in Table I-IV. Figures I-1 and I-2 show the results of P&WA ultrasonic and visual inspections at various stages in the evaluation.

Prior to testing, blade S/N 16 had core radial cracks which were detected by radiography, but no delamination at the leading edge hook area. The delamination progressed at 90 and 110 percent speeds, as shown in Figure I-1. The blade was then subjected to LCF cycles with a speed excursion from 1000 rpm to 16,7200 rpm (110% speed). The blade failed catastrophically after 11 cycles.

TABLE I-III – BLADE STRAIN-GAGE RESULTS

Gage Number	Strain at 10,660 rpm (μ cm/cm)	
	Blade S/N 16	Blade S/N 18
1	1300	1450
2	400	500
3	3000	3100
4	800	400
5	300	---
6	2400	2600
7	1500	---
8	300	300



GAGE LOCATIONS (cm)

GAGE	X	Y
1,7	7.62	4.32
2,8	7.62	4.32
3	2.54	1.27
4	2.54	1.27
5	10.16	1.27
6	10.16	1.27

TABLE I-IV BLADE SPIN-TEST RESULTS

Blade S/N	Pretest Condition	Initial Spin + Ultrasonic Inspection					LCF/HFF Cycles
		70%	80%	90%	100%	110%	
16	No delamination Core radial cracks	Delam.		Delam. growth		Delam. Growth	Catastrophic failure in 11 cycles at 110% speed.
17	No delamination Core radial cracks	No delam. at R.T. Delam. at 350°F. Ti pads & Al wedges un- bonded					
18	No delamination Core radial cracks	No delam.	Delam.	Delam. Growth			1) 50 LCF cycles @ 90% speed. Slight growth of delam. area. 2) HFF tested at 10 ksi for 10^7 cycles. No growth. 3) 10 LCF cycles @ 90% speed. No growth. 4) 30 LCF cycles @ 100% speed. Slight growth.
20	No delamination Core radial cracks	Root & tip cracks Delam.	Delam. growth	Delam. growth	Same as 90%	Catastrophic failure at 101% speed	

Blade S/N 17 had core radial cracks but no delamination prior to testing. Initially the blade was spun to 70 percent speed at room temperature. Ultrasonic inspection showed no delamination. The test was rerun to 70 percent speed but at 177°C [350°F] and delamination occurred, as shown in Figure I-1. In addition, the titanium pads and aluminum wedges in the attachment became unbonded, terminating the test.

Blade S/N 18 was subjected to the most extensive testing of the four blades. Prior to testing the blade showed core radial cracks but no delamination. Delamination showed up initially at 80 percent speed, as shown in Figure I-2, and progressed significantly at 90 percent speed. The blade was then subjected to 50 LCF cycles at 90 percent speed with slight growth in the delaminated area. Blade S/N 18 was then high-frequency-fatigue (HFF) tested in first bending at $\pm 6,900 \text{ N/cm}^2$ [10,000 lbf/in.²] for 10^7 cycles. No growth occurred in the delaminated area. Low-cycle-fatigue testing at 90 percent speed continued for 10 cycles with no delamination growth. The LCF speed was changed from 90 to 100 percent, and the blade was cycled for 30 cycles with only a slight growth in the delaminated area. Testing was then terminated.

Blade S/N 20 was fabricated with $\pm 10^\circ$ core plies instead of 0° plies in an effort to eliminate core radial cracking. The radial cracks were reduced but not eliminated. The blade did not show delamination prior to testing. At 70 percent speed, root and tip cracks were observed visually and, as shown in Figure I-1, delamination was present. The delamination progressed at 80 percent and 90 percent speeds, and showed no progression between 90 and 100 percent speeds. The blade failed catastrophically at 101 percent speed.

CONCLUSIONS

Kerimid 601 blades in an aerodynamic rig program represent a significant structural risk. The rotor would have to be limited to 90 percent speed and inlet temperatures to -40°F .

The reduction in torsional frequency that occurs after spin-up can create a second mode, low-order-resonance problem (3E) which would further limit the rig operating range. Therefore, the use of Kerimid 601 blades in the ultra-high speed fan aerodynamic program would result in a structural configuration having only a minimal chance of success.

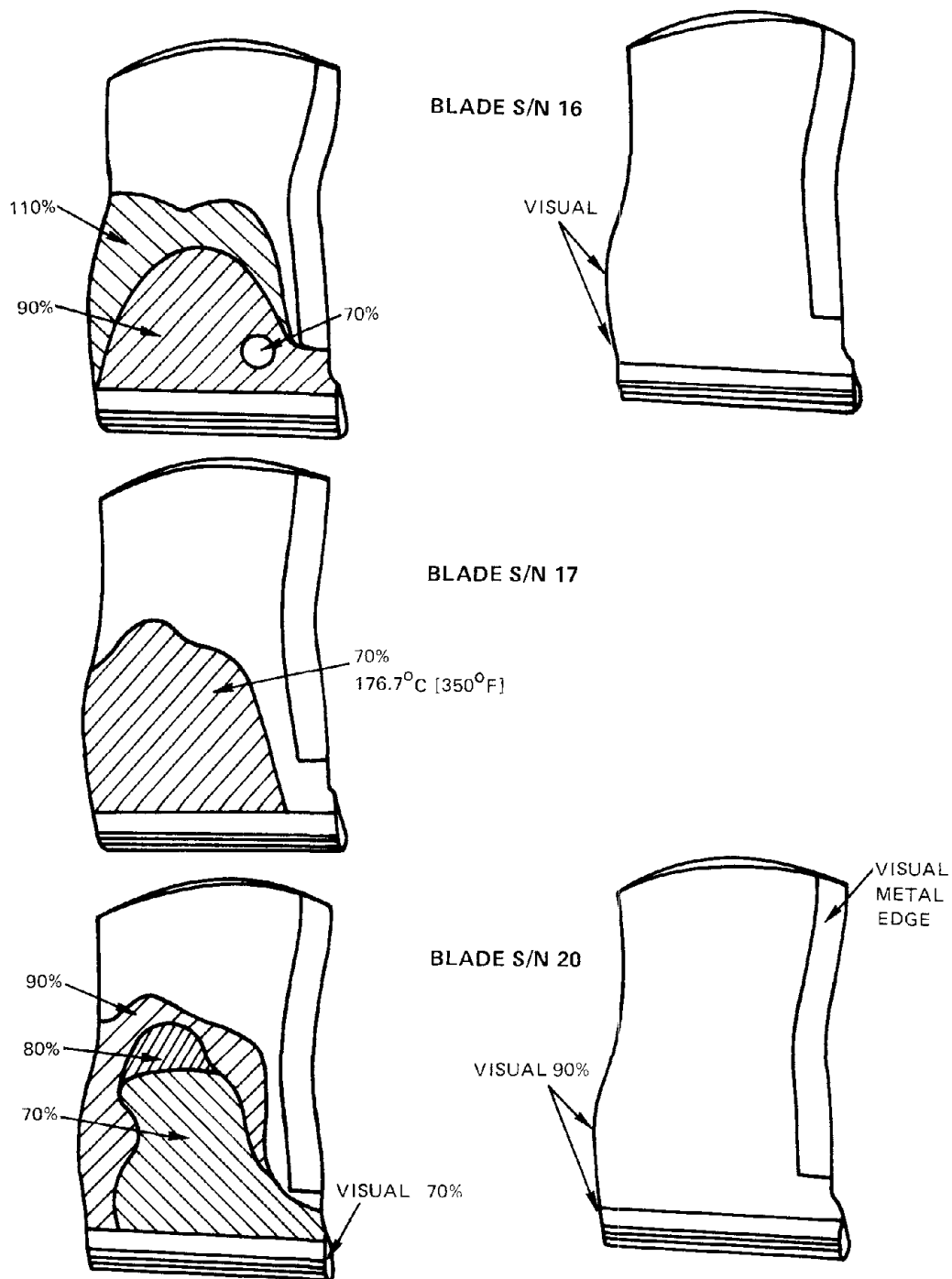
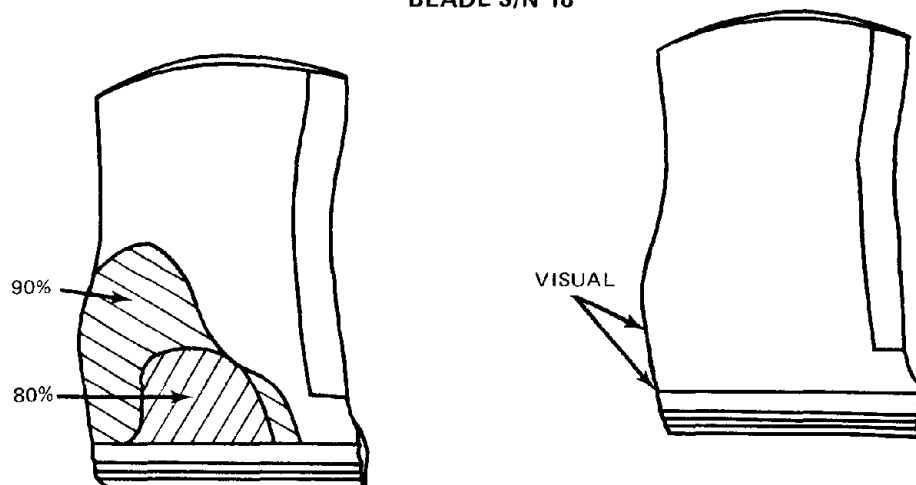


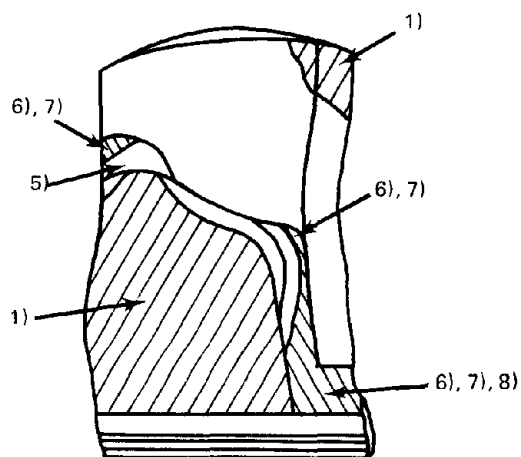
Figure I-1 Ultrasonic and Visual Inspection Results

BLADE S/N 18



AFTER INITIAL SPIN-UP

TEST SEQUENCE



- 1) 10 CYCLES AT 90% SPEED
- 2) 5 CYCLES AT 90% SPEED
- 4) 35 CYCLES AT 90% SPEED
- 4) 10^7 HFF CYCLES
- 5) 10 CYCLES AT 90% SPEED
- 6) 10 CYCLES AT 100% SPEED
- 7) 10 CYCLES AT 100% SPEED
- 8) 10 CYCLES AT 100% SPEED

LCF SPIN AND HFF BENCH TESTS

Figure I-2 Ultrasonic and Visual Inspection Results

Page Intentionally Left Blank

APPENDIX J

**EVALUATION OF PMR POLYIMIDE
ULTRA-HIGH TIP SPEED FAN BLADES**

Contract NAS3-15335

Prepared by

W. E. Winters

**TRW Inc.
TRW Equipment
Cleveland, Ohio**

INTRODUCTION

This appendix describes the materials and construction of nine ultra-high tip speed fan blades and their spin test evaluation. The blades were fabricated by TRW Equipment, Cleveland, Ohio under several NASA-Lewis contracts including NAS3-17772, NAS3-18939, and Purchase Order C-65605. The blade design was developed under contract NAS3-15335 by Pratt & Whitney Aircraft, East Hartford, Connecticut where the spin testing was also accomplished. It is the purpose of this appendix to summarize the various improvements in materials, composite design and processing methods during the evaluation of the blade and to correlate these factors with performance. Specific details of the blade fabrication are found in final reports generated by TRW on the above mentioned contracts.

During the course of the development of the ultra-high speed blade, a new and unique type of polyimide resin designated PMR was developed by NASA-Lewis personnel, which provided higher temperature capability, greater ductility, and improved translation of fiber properties in graphite fiber composites than the composite matrix resin originally selected for the high speed blade. With the development of processing procedures for PMR/Gr composites by TRW under the above mentioned contracts which were appropriate for fan blade fabrication, it became appropriate to evaluate the PMR-PI composite in the very demanding application of the ultra-high tip speed fan blade. Several blades were thus fabricated and submitted for evaluation which included spin testing, low cycle fatigue and high frequency fatigue methods.

BLADE CONSTRUCTION

Table J-I defines the materials of construction and the composite ply orientation and thickness used for each of the blades evaluated. Blades S/N T-1 and S/N T-2 were of identical construction to the blades originally evaluated on NAS3-15335 with the exception of the substitution of PMR-15 polyimide resin as the composite matrix. The reinforcement was HT-S graphite fiber from Hercules and the composite construction was of a shell/core design with the $\pm 40^\circ$ shell plies separated from the 0° core plies by a single pair of $\pm 20^\circ$ transition plies. Blade S/N T-4 was modified to incorporate a $\pm 30^\circ$ shell and an interspersed $(+10^\circ, 0^\circ, -10^\circ, 0^\circ)_n$ core.

TABLE J-I – BLADE CONSTRUCTION

Blade S/N	Fiber	Resin	Ply Orientation (degrees)				Ply Thickness (mm)		
			Tip	Shell	Trans.	Core	Shell	Core	L.E. ¹
T-1	HT-S	PMR-15	± 75	± 40	± 20	0	0.127	0.254	None
T-2	HT-S	PMR-15	± 75	± 40	± 20	0	0.127	0.254	None
T-4	HT-S	PMR-15	± 75	± 30	± 30	$(10,0,-10,0)_n$	0.127	0.254	None
T-9	A-S	PMR-11	± 60		$(+40,0,-40,0)_n$		0.127	0.254	None
T-10	A-S	PMR-11	± 60		$(+40,0,-40,0)_n$		0.127	0.254	None
T-12	A-S	PMR-11	± 60		$(+40,0,-40,0)_n$		0.127	0.254	Yes
T-14	A-S	PMR-11	± 60		$(+40,0,-40,0)_n$		0.127	0.254	Yes
T-21	A-S	PMR-11	± 60		$(+40,0,-40,0)_n$		0.127	0.254	Yes
T-22	A-S	PMR-11	± 60		$(+40,0,-40,0)_n$		0.127	0.254	Yes

Note 1: L.E. = leading edge

For blades S/N T-9 and beyond, type A-S fiber was substituted for HT-S, representing a somewhat higher tensile and composite shear strength reinforcement at slight reduction of fiber modulus (30 vs. 34 msi). A PMR-11 resin was also substituted for PMR-15 which had been established on the referenced programs to provide suitable composite mechanic properties for the intended environment. A major change in these blades, however, included the use of a totally interspersed composite construction $(+40^\circ, 0^\circ, -40^\circ, 0^\circ)_n$ instead of the shell/core design used on previous blades.

Several minor changes were also incorporated into blades S/N T-9 and S/N T-10 including:

- Increased ply length (0.1016 - 0.1524 cm [0.040 - 0.060 in.]) at root and tip to better fill the idle cavity.
- Reduced the resin content by 3 percent to compensate for lower flow.
- Reduced the 0.254 mm [10 mil] core ply thickness by 5 percent.
- Replaced parts of three plies (20, 26, 56) which had been deleted earlier to accommodate an oversize condition near the root.

Blades S/N's T-12 through T-22 were further modified by substituting 0.127 mm [5 mil] prepreg, which had demonstrated improved composite properties, for the 0.254 mm [10 mil] prepreg previously used. Also, these blades incorporated a 0.0762 mm [3 mil] electroformed nickel leading edge guard secondarily bonded to the blade with a high temperature epoxy paste adhesive which was also used for the titanium pressure pad.

BLADE EVALUATION METHODS

Before shipment, all blades were radiographed and ultrasonically and dimensionally inspected. The blades were again radiographed and ultrasonically inspected at P&WA prior to spin testing. Initial evaluation in the spin pit involved acceleration to speed from 60 percent to 110 percent in 10 percent increments with ultrasonic evaluation after each increment. One hundred percent speed was at 15,200 rpm. Following initial spin-up tests, blades were subjected to fifty cycles of low cycle fatigue (LCF) by repeatedly spinning briefly to 100 to 105 percent speed with ultrasonic inspection at each 10 cycle increment.

With survival of LCF, the blades were then subjected to ten million cycles of high frequency fatigue (HFF) on a vibration table. Blades were excited at their first bending frequency mode with sufficient energy to achieve a 0.508 cm [0.200 in.] total tip amplitude displacement. A final series of tests included an additional ten cycles in LCF at the same speed as the original LCF. Natural frequency measurements were made on the blade initially and after each major type of testing. First and second bending and first torsional modes were determined. In addition to these tests, visual examinations were made at each step of the evaluation.

TABLE J-II – BLADE NATURAL FREQUENCIES, Hz

	<u>Blade S/N (speed)</u>	<u>1st Bending</u>	<u>2nd Bending</u>	<u>1st Torsion</u>
Drawing Requirements		250 ± 13	840 ± 42	845 ± 42
Initial	T-1	248	932	804
	T-4	269	997	808
	T-9	261	985	813
	T-10	258	975	815
	T-12	284	1025	789
	T-14	281	1029	777
	T-21	283	1026	768
	T-22	280	1017	766
After 1st Spin	T-12 (105%)	265	987	762
	T-22 (100%)	267	995	748
After 50 Cycles LCF	T-2 (100%)	226	889	731
	T-10 (110%)	244	953	783
	T-14 (105%)	262	988	736
After 10 ⁷ Cycles HCF	T-2	220	884	727
	T-10	238	939	777
	T-14	257	986	735
After 10 Cycles LCF	T-10 (110%)	238	938	777
	¹ T-14 (105%)	264	975	738

Note 1: Taping down of loose edge protector may have affected these frequencies.

TEST RESULTS

Three of these unusually highly stressed blades survived the entire testing procedure although not without internal damage and changes in natural frequencies. The results of the natural frequency tests are presented in Table J-II. Several observations are noted: the bending frequencies of the ±30° shell, ±10°, 0° interspersed core of blade S/N T-4 were slightly higher than the basic design (S/N T-1) while the torsional frequency indicated no change. On the other hand, the ±40°, 0° interspersed construction of blades S/N T-9 and S/N T-10 coupled with the use of A-S fiber caused little change in any mode over S/N T-4. The use of the same construction for blades S/N T-12 through S/N T-22, but with 0.127 mm [5 mil] prepreg in the core instead of 0.254 mm [10 mil] produced significant frequency changes. Increases of 8.5 percent and 4.5 percent in first and second bending, respectively, were noted while a 4.8 percent drop in torsional frequency was observed. Of interest is the reproducibility in the frequencies of like construction blades (S/N's 12, 14, 21, 22) with maximum deviation from mean values at each of the three vibrational modes of 0.7 percent, 0.7 percent, and 1.2 percent, respectively.

Reduction in natural frequencies in all three modes was noted after the completion of each test evaluation series. Major changes occurred in the original spin-up to 100 or 105 percent speed and in the first 50 cycles in LCF. Largest reductions were noted in the first bending

mode, ranging from 5 to 7 percent. Only minor frequency changes resulted from HFF, ranging from 0.1 to 2.6 percent in all modes, while essentially no additional damage was incurred in the final 10 cycles in LCF. It is interesting to note that the total change in first bending for blade S/N T-10 from before test until final evaluation was only 20 Hz or 7.8 percent while serious delamination was noted even after original spin-up to 110 percent speed.

Spin test history for each blade is tabulated in Table J-III. Figures J-1 through J-17 exhibit pictorially results of P&WA ultrasonic inspection and visual inspection at various stages in the evaluation. While a large number of maps were prepared, only those showing significant changes have been reproduced here.

Blade S/N T-1 exhibited a small, narrow, ultrasonic indication (Figure J-1) as fabricated, which was presumed to be a delamination. This indication expanded to the root area after spin-up to 90 percent speed, and blade failure was experienced at 100 percent speed.

Blade S/N T-2 survived the entire testing procedure beginning with an as-fabricated indication (Figure J-2) which grew steadily through initial spin-up and 30 cycles of LCF (Figure J-3). No further change was noted through HFF and ten additional cycles of LCF. The performance of S/N T-4 was similar to T-1 although the ultrasonic C-scan was clear initially. Likewise, S/N T-9 was clear initially, but delaminated at 100 percent speed across the full-chord width above the root, as shown in Figure J-4.

Blade S/N T-10, originally clear, survived the full test procedure and was ultrasonically clear through 100 percent speed. Local, minor fiber lifting was observed at the tip and midspan on the leading edge after 80 percent speed (Figure J-5). At 100 percent speed a crack appeared in the root leading edge face in the composite between aluminum root wedges (Figure J-6). At 110 percent, delamination occurred similar to the previous blade (Figure J-7). It was, however, further tested with no change noted in LCF, and only a slight expansion of the delaminated area was observed after HFF (Figure J-8). No additional delamination occurred in the final LCF although some additional fiber lifting was noted (Figure J-9), and one pressure pad was lifted for a 5.08 cm [2 in.] length. A view of the low pressure face is illustrated in Figure 8 along with the high pressure side of the airfoil, showing all indications. The survivability of this blade was surprising since it was deviated in machining in that the root leading edge face was machined 0.203 cm [0.080 in.] short, placing the blade in the spin arbor significantly displaced from the true stacking axis.

The performance of blade S/N T-12 was similar to blades S/N T-9 and S/N T-10, except delamination occurred at 105 percent speed (Figure J-10). No further evaluation was conducted on this blade.

Blade S/N T-14 went through the entire testing procedure. Figure J-11 illustrates an ultrasonic clear blade, but some minor imperfections were observed on the leading edge guard prior to test. Otherwise, the blade was sound except that the tip end was machined 0.203 cm [0.080 in.] short. Figure J-12, J-13, and J-14 illustrate visual indications occurring during initial spin-up although no ultrasonic indications were noted through 110 percent speed, a decided improvement over previous blades. However, after 50 cycles LCF at 105 percent speed, delamination was experienced (Figure J-15). An additional small piece (2.54 cm [1 in.] length) of the leading edge guard was lost in HFF at the tip on the low pressure face, but no additional damage was incurred in the final 10 cycles in LCF.

TABLE J-III — BLADE SPIN TEST RESULTS

Blade S/N	Before Test Sonic	Initial Spin Ultrasonic Inspection					50 Cycles LCF	10 ⁷ Cycles HCF	10 Cycles LCF
		Thru 80%	90%	100%	105%	110%			
T-1	Indication	Pass	Delam.	Blade Failed	—	—	—	—	—
T-2	Indication	Delam.	Delam. Growth	Delam. Growth	N. T.	N. T.	100% Small Delam. Growth	N. C.	N. C.
T-4	Clear	Pass	Pass	Blade Failed	—	—	—	—	—
T-9	Clear	Pass	Pass	Delam.	N. T.	N. T.	N. T.	N. T.	N. T.
T-10	Clear	Pass	Pass	Pass	N. T.	Delam.	N. C.	N. C.	Delam. Growth
T-12	Clear	Pass	Pass	Pass	Delam.	N. T.	N. T.	N. T.	N. T.
T-14	Clear	Pass	Pass	Pass	Pass	Pass	105% Delam.	L.E. Guard Missing at Tip	N. C.
T-21	Clear	Pass	Pass	Blade Failed	—	—	—	—	—
T-22	Clear	Pass	Pass	Delam.	N. T.	N. T.	N. T.	N. T.	N. T.

Notes: N. T. = Not Tested
N. C. = No Change

For blade S/N T-21, no ultrasonic indications were observed during spin-up, but blade failure occurred at 100 percent speed at the location indicated in Figure J-16. The performance of blade S/N T-22 was similar to several previous blades exhibiting delamination at 100 percent speed as shown Figure J-17.

As a post-test analysis, blade S/N T-2, which had survived the entire test procedure, was sectioned and observed microscopically at P&WA. The sections confirmed the presence of fabrication residual stress radial cracking in the core, which had been observed previously in radiographs. The number of radial cracks had, in fact, increased significantly. Of more concern was the serious amount of delamination between the shell and core members and within the core. The analysis identified a shear type failure, induced predominantly by the high stresses of spin testing, but accentuated by the core/shell residual stress concentration in the composite. Otherwise, the blade was sound with no porosity observed although some fiber dislocations were observed. This observation led to the use in subsequent blades of high density fibers strategically located for radiographic identification for fiber orientation maintenance. Processing procedures were also modified to achieve minimum fiber displacement in fabrication. The technique significantly improved blade quality.

From the test results, it is apparent that failure occurs or is initiated at or near the contour discontinuity in the airfoil about 5.08 cm [2 in.] above the root at midchord (sometimes described as the "bump" area) or at the severe leading edge curvature above the root. In the high stress loading environment of high speed spinning, these sharp contour changes appear to induce a shear stress condition beyond the capability of the laminated composite construction.

SUMMARY AND CONCLUSIONS

It was demonstrated that sound, high quality, complex fan blades could be reproducibly fabricated using PMR-11 polyimide reinforced with A-S/type graphite fiber. Very significant performance improvements were demonstrated through the use of this material combination, improved processing techniques, and improved composite construction compared with previously tested blades. The average speed at which delamination initiated was increased from 65 percent of full speed for original contract blades to 105 percent. On the basis of centrifugal loading, this represents an increase in failure initiation stress of 137 percent. However, with the current design, the blade must be considered marginal for full operation in the stress environment intended. Operation somewhat below 100 percent of full speed, 670.6 m/sec [2200 ft/sec] tip speed is fully practical.

The totally interspersed composite construction was found to eliminate residual stress cracking and the 0.127 mm [5 mil] core laminae provided improved performance over the 0.254 mm [10 mil] in the original blade design. For the totally interspersed orientation investigated ($+40^\circ$, 0° , -40° , 0°)_n, increases were noted in blade bending vibrational modes with some reduction in torsional frequency. Natural frequencies can, however, be tuned by varying fiber orientation angles and/or the ratio of radial oriented to cross plied material.

In conclusion, the PMR-11/A-S combination provides one of the highest strength and shear capability, low density composite materials of construction available at this time. Ultrasonically sound, ultra high tip speed blades fabricated with this material with accurate maintenance of composite quality and fiber alignment as determined by radiographic tracer examination have demonstrated only marginal survivability. Further blade performance improvements for this application must, therefore, be sought through improved airfoil and root retention designs. Additional considerations should include such factors as root wedge material selection and, looking forward to jet engine operation, the incorporation of a leading edge guard scheme that not only survives the spinning environment but provides the necessary degree of foreign object damage protection.

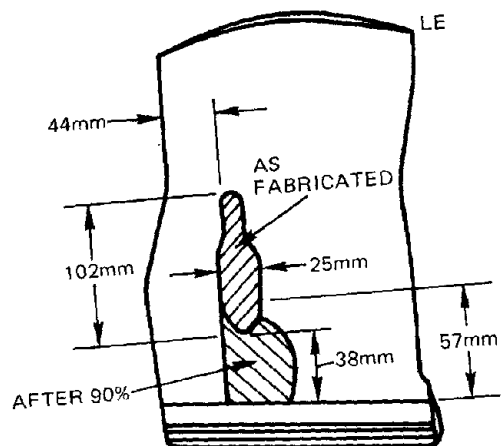


Figure J-1 Blade Inspection Results; Blade Serial No. T-1, as Fabricated.

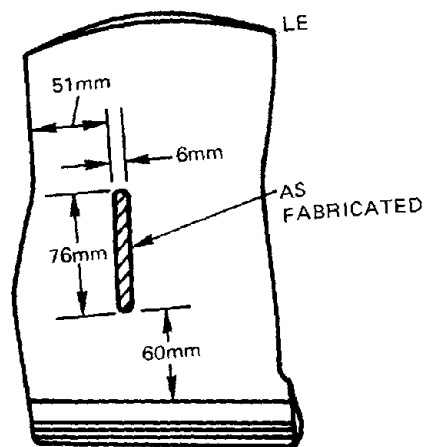


Figure J-2 Blade Inspection Results; Blade Serial No. T-2, as Fabricated.

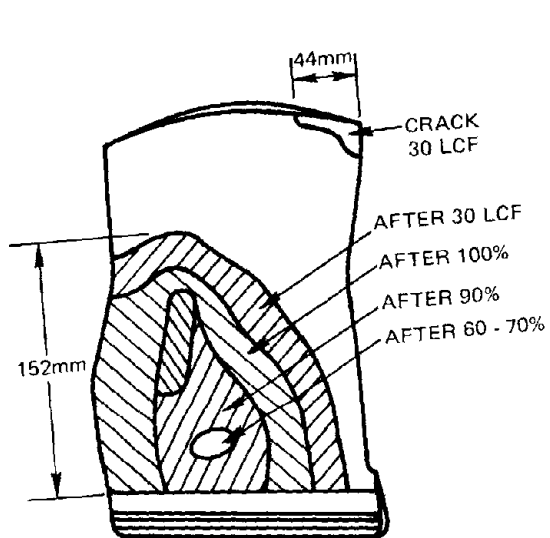


Figure J-3 Blade Inspection Results; Blade Serial No. T-2, After Progressive Speeds and 30 LCF Cycles.

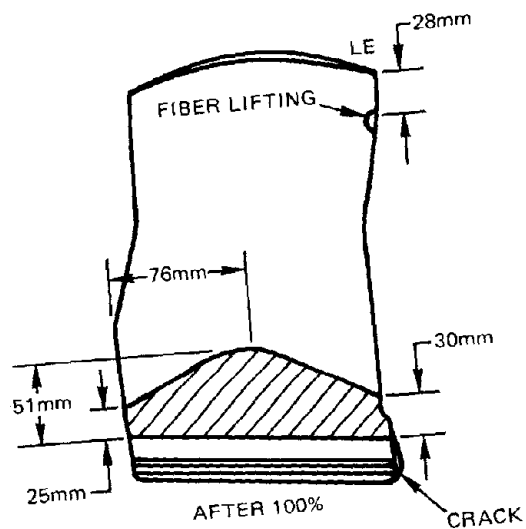


Figure J-4 Blade Inspection Results; Blade Serial No. T-9, After 100 Percent Speed.

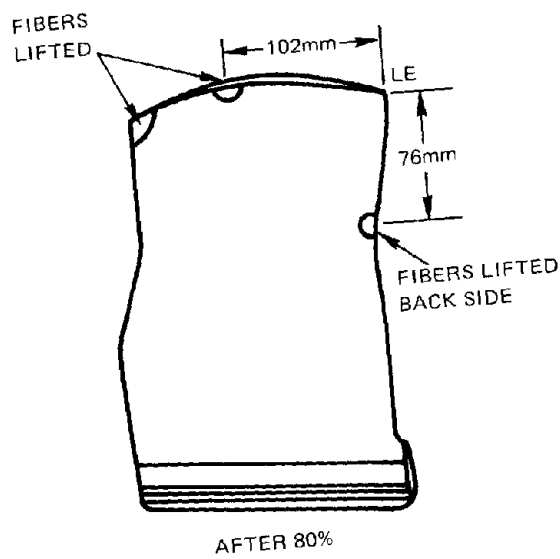


Figure J-5 Blade Inspection Results; Blade Serial No. T-10, After 80 Percent Speed.

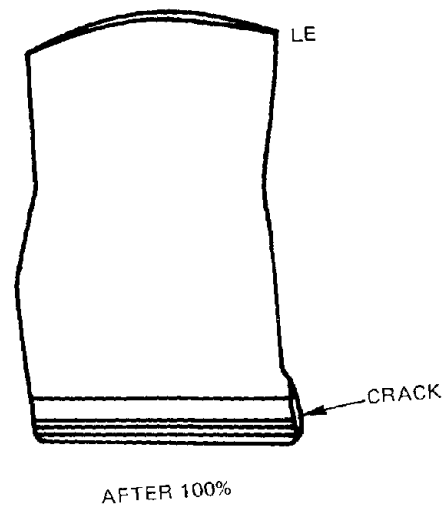


Figure J-6 Blade Inspection Results; Blade Serial No. T-10, After 100 Percent Speed.

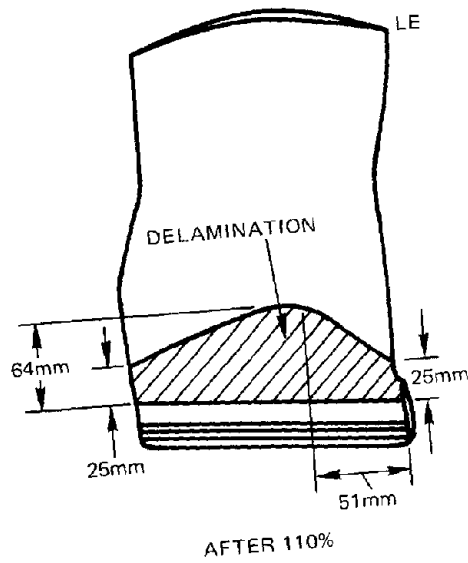


Figure J-7 Blade Inspection Results; Blade Serial No. T-10, After 110 Percent Speed.

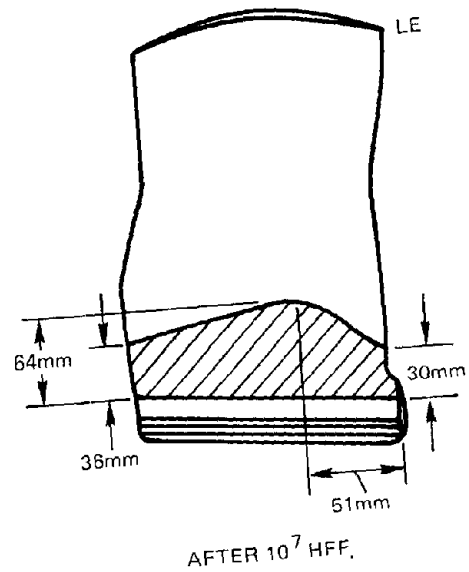


Figure J-8 Blade Inspection Results; Blade Serial No. T-10, After 10^7 HFF Cycles.

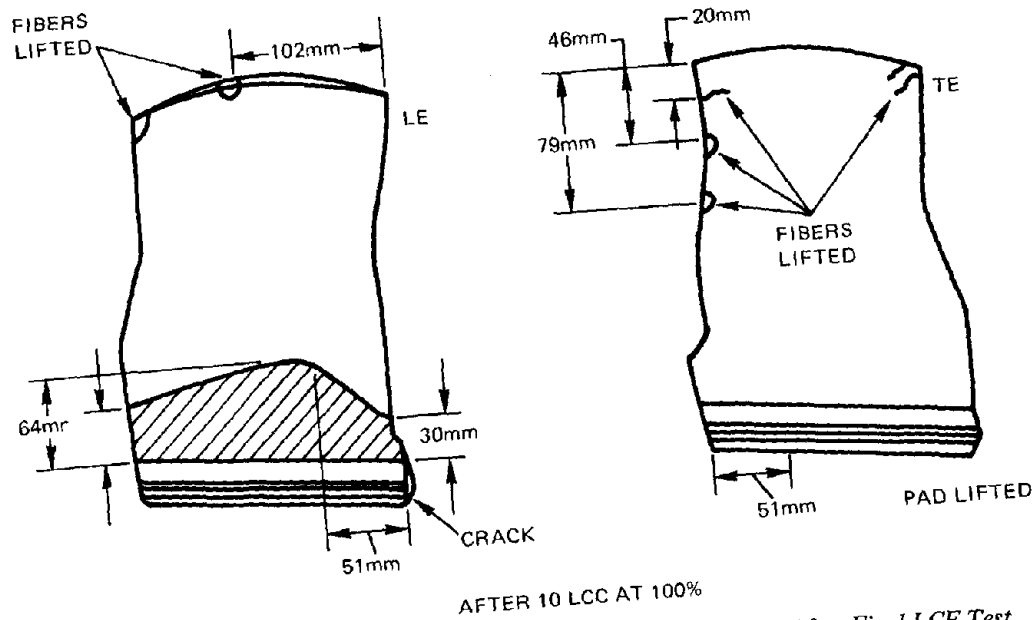


Figure J-9 Blade Inspection Results; Blade Serial No. T-10, After Final LCF Test.

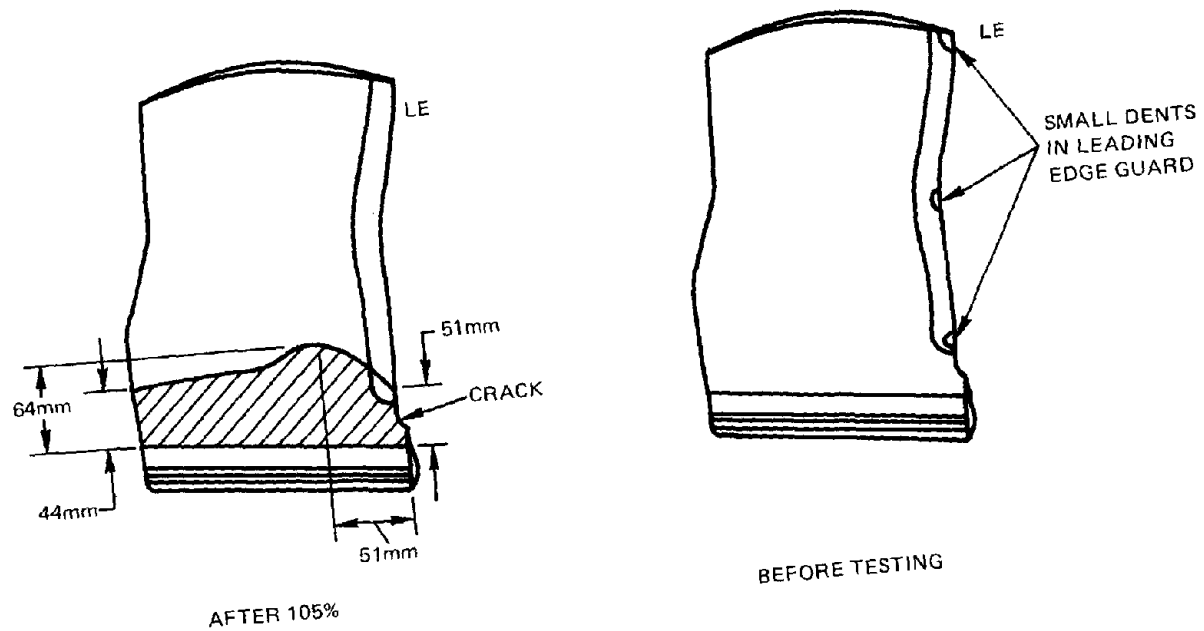


Figure J-10 Blade Inspection Results; Blade Serial No. T-12, After 105 Percent Speed.

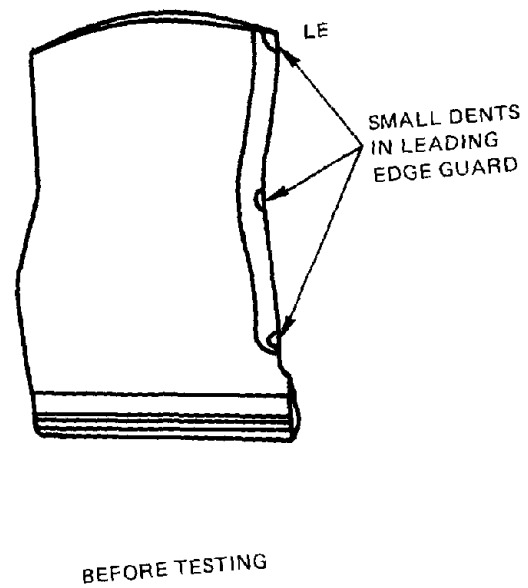
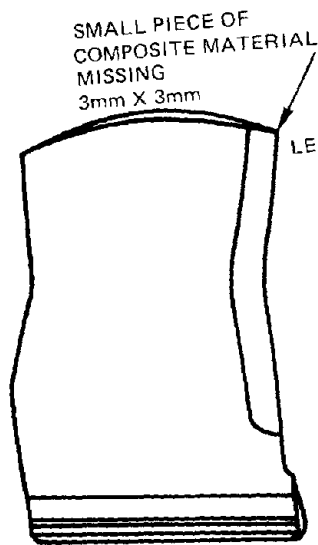
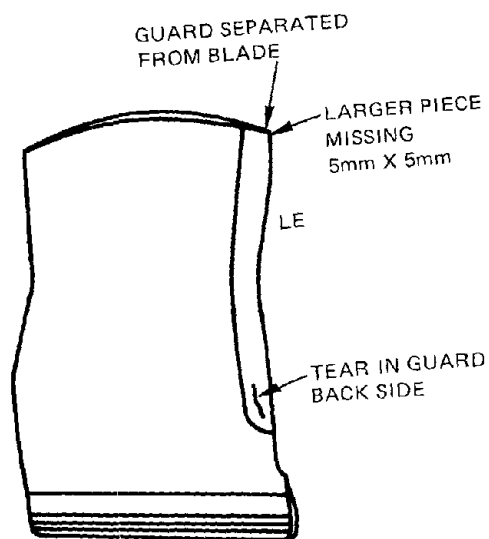


Figure J-11 Blade Inspection Results; Blade Serial No. T-14, Before Testing.



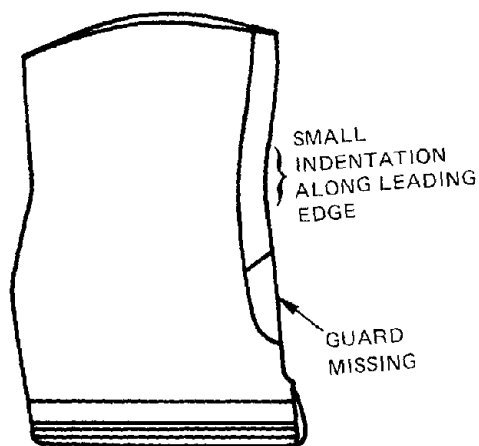
AFTER 80%

Figure J-12 Blade Inspection Results; Blade Serial No. T-14, After 80 Percent Speed.



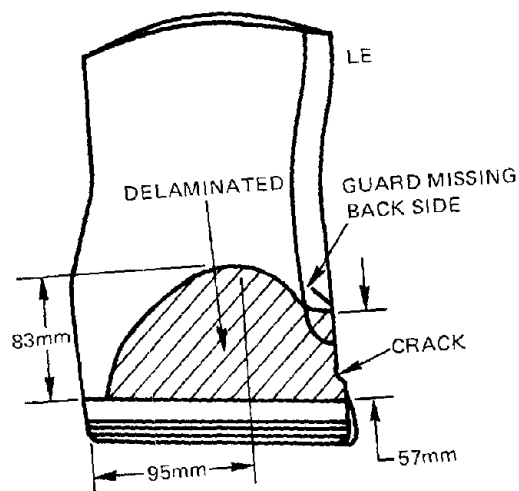
AFTER 105%

Figure J-13 Blade Inspection Results; Blade Serial No. T-14, After 105 Percent Speed.



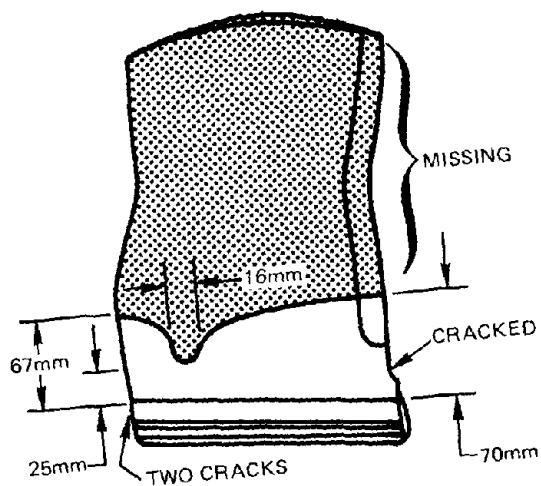
AFTER 110%

Figure J-14 Blade Inspection Results; Blade Serial No. T-14, After 110 Percent Speed.



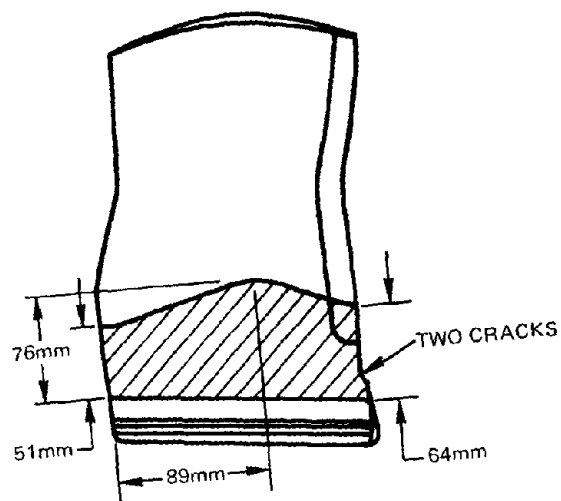
AFTER 50 LCF 105%

Figure J-15 Blade Inspection Results; Blade Serial No. T-14, After 50 LCF Cycles at 105 Percent Speed.



AFTER 7 SEC AT 100%

Figure J-16 Blade Inspection Results; Blade Serial No. T-21, After 7 Seconds at 100 Percent Speed.



AFTER 100%

Figure J-17 Blade Inspection Results; Blade Serial No. T-22, After 100 Percent Speed.

REFERENCES

1. Sulam, D. H., Keenan, M. J., and Flynn, J. T.; "Single-Stage Evaluation of Highly Loaded, High Mach Number Compressor Stages-II. Data and Performance, Multiple Circular-Arc Rotor," NASA CR-72694, 1970.
2. Morris, A. L., and Sulam, D. H.; "High Loading 1800 Ft/Sec Tip Speed Transonic Compressor Fan Stage-II – Final Report," NASA CR-120991, December 1972.
3. Morris, A. L., Halle, J. E., Kennedy, E.; "High Loading, 1800 Ft/Sec Tip Speed Transonic Compressor Fan Stager I. Aerodynamic and Mechanical Design," NASA CR-120907, 1972.
4. Marsh, H.; "A Digital Computer Program for the Through-Flow Fluid Mechanics in an Arbitrary Turbomachine Using a Matrix Method," (Ministry of Technology Reports and Memoranda No. 3509).
5. Wu, Chung Hua; "A General Theory of Three-Dimensional Flow in Subsonic and Supersonic Turbomachines of Axial, Radial, and Mixed-Flow Types," (NACA TN 2604).
6. Messenger, H. E. and Keenan, M. J.; "Two-Stage Fan – II. Data and Performance With Redesigned Second-Stage Rotor, Uniform and Distorted Inlet Flows," NASA CR-134710, 1974.
7. Reshotko, E., and Tucker, M.; "Approximate Calculation of Compressible Turbulent Boundary Layer with Heat Transfer and Arbitrary Pressure Gradient," NACA Report 4154, 1957.
8. Keenan, M. J., and Bartok, J. A.; "Experimental Evaluation of Transonic Stators," NASA CR-72298, 1969.
9. Harley, K. G., and Burdsall, E. A.; "High Loading Low-Speed Fan Study-II Data and Performance, Unslotted Blades and Vanes," NASA CR-72667, 1970.
10. Fottner, L., "A Semi-Empirical Approach of the Transonic Flow Past Cascades Including Shock and Viscous Effects," AGARD CP 34 (Advanced Components for Turbojet Engines), 1968.